5-2020

Understanding Ice Mixtures under Pluto Simulated Conditions and their Implications for Geophysical Processes

Caitlin Joannah Ahrens
University of Arkansas, Fayetteville

Understanding Ice Mixtures under Pluto Simulated Conditions and their Implications for Geophysical Processes

A dissertation submitted in partial fulfillment
of the requirements for the degree of
Doctor of Philosophy in Space and Planetary Sciences

by

Caitlin Joannah Ahrens
West Virginia University
Bachelor of Science in Physics, 2015
West Virginia University
Bachelor of Science in Geology, 2015

May 2020
University of Arkansas

This dissertation is approved for recommendation to the Graduate Council.

_____
Vincent Chevrier, Ph.D.
Dissertation Director

_____
Larry Roe, Ph.D.
Committee Member

_____
Feng Wang, Ph.D.
Committee Member

_____
Bret Lehmer, Ph.D.
Committee Member

Abstract

New Horizons at Pluto has given the planetary science community the first images of Pluto's surface, including geologic wonders and compositional variability. Methane, nitrogen, and carbon monoxide make up the bulk of the volatile plutonian surface along with water ice. In this work, these three main volatiles are specifically investigated in the laboratory setting to understand the spectral properties and behavior of binary and ternary mixtures. The spectra are taken in the near-infrared wavelengths (1 – 2.5 μm) using Fourier transform infrared (FTIR) spectroscopy techniques utilizing the Pluto Simulation Chamber housed at the University of Arkansas, which can reach conditions relevant to Pluto (10 – 50 K; 14- 25 μbar). Here updated investigations of the methane-nitrogen and nitrogen-carbon monoxide binary systems are developed, along with the creation of an entirely new methane-carbon monoxide binary phase diagram. The second part of this dissertation is the study of certain geophysical processes. This includes compressional folds at the Baret Montes glacier, collapsing from putative cryovolcanism at Hekla Cavus, and fault construction in the southwestern close-encounter hemisphere of Pluto. Both the experimental spectroscopy and theoretical geology expand the knowledge of Pluto and other icy bodies of the outer solar system and could perhaps expand our knowledge of the interactions of different combinations of ices at low temperatures to understand surface evolution or surface-atmosphere relations.

Acknowledgements

The research completed in this project was funded by NASA Solar System Workings grant #80NSSC19K0163.

I would like to thank my advisor, Dr. Vincent Chevrier, for all his support and for allowing me to work on this project. I would also like to thank my committee members Dr. Larry Roe, Dr. Feng Wang, and Dr. Bret Lehmer for their support and guidance throughout my graduate career. A special thank you to Walter Graupner for his invaluable insight and assistance while working at the University of Arkansas W.M. Keck Laboratory for Planetary Simulations and Zachary McMahon for his amazing construction of the Pluto Simulations Chamber. I would also like to thank Dr. Paul Byrne for allowing me to intern with him at North Carolina State University.

I also greatly appreciate Dr. Alan Stern, Dr. William Grundy, and the New Horizons team for the availability of the New Horizons mission data and helpful comments given at Pluto (and other planetary) workshops and conferences.

Lastly, I would like to express my gratitude to all the reviewers for their invaluable insight and commentary on my papers.

Dedication

This dissertation is dedicated to my loving mother and husband; my amazing family; as well as all my friends and professors who helped and supported me at West Virginia University and the University of Arkansas. This work is also in honor and memoriam of my father, who inspired me to pursue science – *ad astra per aspera*.

Table of Contents

List of Figures

Chapter 1:

Chapter 2:

Chapter 3:

Chapter 4:

Chapter 5:

Chapter 6:

Chapter 7:

Chapter 8:

Chapter 9:

List of Tables

Chapter 3:

Chapter 6:

Chapter 9:

List of Published Chapters

Chapter 2 and 3:

Ahrens, C., Chevrier, V., High-resolution near-IR investigation of N_2-CH_4 ices under simulated plutonian conditions. *Under review in Planetary Space Science Journal.*

Chapter 5:

Ahrens, C., Chevrier, V., (2019) Compressional ridges on Baret Montes, Pluto as observed by New Horizons. *Geophysical Research Letters*, 46 (24), 14328-14335. doi:10.1029/2019GL085648

Chapter 6:

Ahrens, C., Chevrier, V., Investigation of the morphology and interpretation of Hekla Cavus, Pluto. *Under review in Icarus.*

Chapter 7:

Ahrens, C., Byrne, P., Chevrier, V., Geometry, shear stress, and roughness of faults in central Cthulhu Macula, Pluto. *Under review in Icarus.*

Chapter 1

Introduction

1.1 Background

1.1.1. Plutonian Ices

Pluto is the largest Trans-Neptunian Object (TNO) and known Kuiper Belt Object (KBO) located at the inner region of the icy Kuiper disk. Pluto has a proposed differentiated interior, complex surface interactions, and tenuous atmosphere, each playing a key role for our understanding of the outer Solar System and evolution of icy dwarf planets. Each role, however, presents its own set of challenges to quantify. Complicating these challenges include heterogeneous volatile ices, sublimation-condensation cycles, local and global seasonal evolution, and photochemical processes in the atmosphere (Spencer et al. 1997; Madey et al. 2002; Schmitt et al. 2017).

The Linear Etalon Imaging Spectral Array (LEISA) onboard the New Horizons probe has been ideal for observing complex icy surface geology at the 1.25 μm – 2.5 μm wavelength range (Young et al. 2008; Stern et al. 2015) at the Close Encounter Hemisphere and has determined the distributions of Pluto's main volatile constituents.

CH_4, CO, and N_2 are the three main constituents observed on Pluto's surface through telescopic (and eventually New Horizons) observations (Cruikshank et al. 1976; Owen et al. 1993). These molecules interact and form molecular mixtures with variable stratigraphic and geographic abundances (Doute et al. 1999; Olkin et al. 2007) as seen in Figure 1 (Schmitt et al. 2017). This variability can be comparable to other large KBOs and Triton with segregated phases and spatial locations of compounds (Quirico et al. 1999; Merlin et al. 2009; Guilbert et al. 2009). Water ice is also known to be observed in rather small abundances, except for the (informally named) Cthulhu

Macula region where water ice is the dominant component, but the nature and importance to the overall structure of Pluto is still tentative (Grundy and Buie, 2002). Figure 2 displays a variety of spectra across the surface of Pluto, as observed from New Horizons (Grundy et al. 2016).

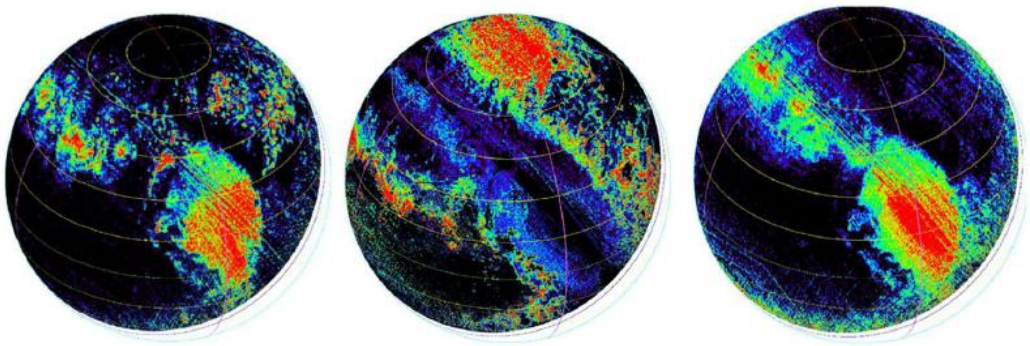

Figure 1: Ice variations across Pluto taken from the New Horizons flyby. (Left to right): Nitrogen, methane, carbon monoxide from the LEISA instrument onboard the New Horizons (From Schmitt et al. 2017).

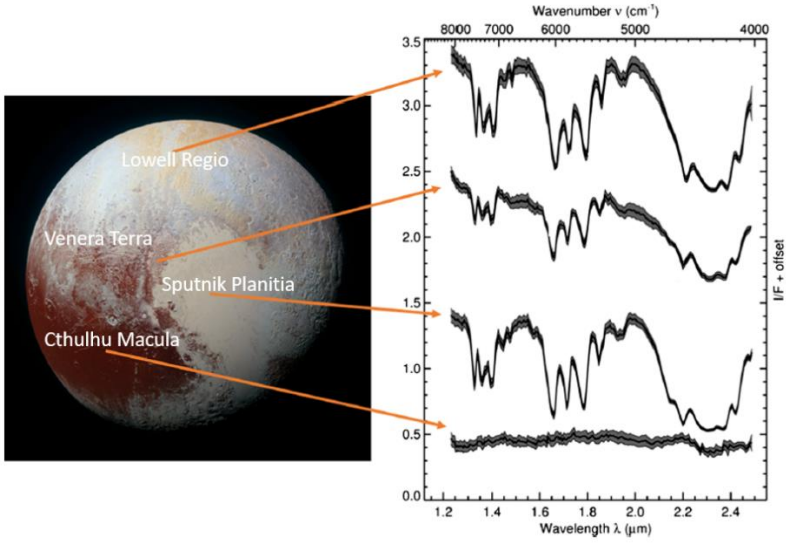

Figure 2: Regions of Pluto with spectral characterizations to highlight spectral diversity. Pluto's northern pole shows strong CH_4 ice absorptions. The edge of Sputnik Planitia also shows CH_4 absorptions and weak H_2O ice bands at 1.5 and 2 μm. The center of Sputnik Planitia shows strong signals in CH_4, N_2, and CO. The Cthulhu Regio in the southwestern region shows weak H_2O ice absorptions at 1.5 and 2 μm, but with possible hydrocarbon features at 2.3 μm. Adapted from Grundy et al. (2016).

Ground-based observations and the NASA New Horizons fly-by have advanced our understanding of Pluto's surface composition and geochemistry. This also warranted the need for laboratory measurements to interpret such mission data and improve physical and chemical modeling (Ahrens et al. 2018). Laboratory work gives these observations a better context, such as providing spectral or chemical properties of specific ice mixtures (at various ratios) and the behavior of such mixtures when subjected to varying temperatures, both discussed in this paper. The characterization of plutonian materials requires the capability to create controlled samples, characterize their composition and behavior, and verify the reproducibility of the measurements under cryogenic and vacuum conditions reproducing the environment on the surface of Pluto.

Ice behaves in various ways depending on the compositions and environmental conditions, therefore playing various roles in the development of mineral, geological, and climatological processes on icy planetary surfaces (Roush 2001; Cruikshank et al. 2015; Grundy et al. 2016; Moore et al. 2016).

However, if the major compounds have been identified, the effects of binary or ternary mixtures remain poorly understood. Few of these binary or ternary phase interactions have been characterized experimentally in the near-infrared (NIR), but rather using other techniques such as X-ray diffraction (XRD), Raman, or mid-infrared wavelengths (Angwin and Wasserman 1966; Prokhvatilov and Yantsevich 1983; Strazzulla and Palumbo 1998).

Previous experiments have been done to explain the phase behavior of methane and nitrogen (Prokhvatilov and Yantsevich 1983; Tryka et al. 1993; Brunetto et al. 2008). Experimental NIR spectra of solid N_2, CO, or mixtures thereof have also been previously studied (Angwin and Wassermann 1966; Grundy et al. 1993; Quirico and Schmitt 1997; Vetter et al. 2007; Tegler et al. 2019), though mostly in the range 30 K – 80 K. It has been investigated that CO

spectral bands are significantly sensitive to the phase present of solid N_2 in the crystalline matrix (Quirico and Schmitt 1997).

No current experimental work has currently been done for a complete CO-CH_4 binary phase diagram. Most background work to lead into this study, specifically for Pluto or other TNOs, have been investigating: CH_4 spectral bands and gaseous CO in Pluto's atmosphere (Lellouch et al. 2011); CO clathrates in H_2O ices (Palumbo 1997); or irradiation products of CO and CO-CH_4 binary ice mixtures (Bennett et al. 2005; Jamieson et al. 2006; Hudson et al. 2008; Maity et al. 2014). I present the first study of CH_4-CO crystalline ice mixture phases and characterize their spectral behavior to complete a binary phase diagram (see Chapter 5).

Ternary mixtures, similar to previous work done for CO-CH_4 mixtures, have mostly been investigated for electron irradiation by-products at low temperatures < 40 K (Moore and Hudson 2003; Hudson et al. 2008; Kim and Kaiser 2012). Douté et al. (1999) recorded NIR spectra of Pluto's surface through ground-based telescopic data and derived an N_2-dominant ternary mixture. Tegler et al. (2010) also reported CH_4-enriched N_2 ices on the surface of Pluto as well. However, experimental work for varying molar concentrations of these ices and the spectral behavior of such constituents are not yet known. I present the spectral behavior (e.g., mixture- and temperature-dependent spectral bands) of a variety of N_2-CH_4-CO mixtures (see Chapter 6). This is also a first step to creating a ternary phase diagram.

1.1.2. Geophysical Processes

The New Horizons Long Range Reconnaissance Imager (LORRI) obtained images of the Pluto surface during the spacecraft's targeted fly-by in 2015. These images obtained revealed Pluto to be a very geologically complex Kuiper Belt body (Moore et al. 2016). Pluto offers a wide variety

of geologic structures, from glaciers to mountain ranges to fault likes. Each of these geologic formations presents several implications, namely (i) strength of the ice material present; (ii) subsurface or rheological processes; and (iii) behavior of the ice to influence the process.

There are several large floating (or partially submerged) mountainous glaciers, namely Hillary, Al-Idrisi, and Baret Montes (Howard et al., 2017; White et al., 2017). These glaciers are located on the western lobe of Sputnik Planitia, a large, elongated impact basin consisting of currently-active convective processes (Roberts and Nimmo, 2008; Trowbridge et al., 2016; Hammond et al., 2016; McKinnon et al., 2016a, b). I explore the glacial dynamics of Baret Montes and relate the ridges to an estimated time frame < 10 My (in Chapter 7).

Cryovolcanism (i.e., eruption of molten material from within icy bodies) has been proposed for several worlds, namely Europa, Ganymede, Enceladus, Titan, and Triton (Lopes et al. 2007; Jaumann et al. 2009). Cryovolcanic activity then, according to Kargel (1995), includes eruptions of partly crystallized slurries derived by partial melting of ice-bearing materials (i.e., the addition of ammonia to form an ammonia-water ice cryo-magma material). In the case of Pluto, it has also been suggested that there is evidence for a subsurface fluid layer (Nimmo et al. 2016; Moore et al. 2016) and inferred presence of cryovolcanoes (Singer et al. 2018; Schenk et al. 2018) or cryovolcanic subsurface materials (Cruikshank et al. 2019). With the knowledge of this subsurface material, there is evidence for potentially collapsing of the lithosphere from subsurface material movement and/or depletion, which I explore at Hekla Cavus, Pluto (see Chapter 8).

Pluto also displays a range of faulted areas, where Cthulhu Macula (one of the largest water-ice based regions) consists of some of the widest extensional features > 200 km in length. Understanding the geometry of these faults can provide insight to variations and distributions of localized stresses, and possibly, how interactions (i.e. overlapping) of such faults may influence

displacement and stresses. I measure the geometry of four main faults in Cthulhu Macula and investigate their cross-cutting relationships and shear stresses to essentially show how diverse the icy lithosphere is across Cthulhu Macula (in Chapter 9).

1.2 Advancements and Motivations of Pluto Experimental Research

The outer reaches of the Solar System house the myriad of Kuiper Belt Objects, with Pluto being the largest, where materials are thought to be varied in radiation and material concentration. KBOs are exposed to various materials and solar radiation; consequently, KBOs surface and atmosphere are interactive, which is a challenge to understand even today.

Laboratory measurements of planetary surface and atmosphere compositions provide crucial support to science instrument measurements from ground-based, orbital, and lander observations; instrument design; calibrations; future mission planning; and interpretation of data. In most situations, theoretical models are a primary source of parameterization to address geophysical modules which otherwise cannot be directly measured (i.e. subsurface layers, tidal physics, etc.). Currently, there are a deficient number of laboratories to measure the properties over the range of conditions and materials relevant to Pluto and KBOs. Extremely low conditions and exotic ice materials have been little studied due to challenging experimental constraints, maintenance, and funding limitations.

In a general sense, the interpretation of geophysical and atmospheric techniques in terms of plutonian formation, evolution, and current state, relies on the knowledge and constraints of physical properties of the materials detected or expected at those conditions. Samples synthesized in the laboratory are necessary for comparison to observational measurements.

The need for continuous use and improvement of laboratory facilities in the analysis of Pluto and other KBOs opens new studies for KBO material properties. Ground-based and space

fly-bys provide key starting points for such studies, but are limited for time constraints, conditions, and amount of data for a specific purpose. Laboratory work gives these observations a wider range of possible scenarios for interpreting those observations.

(a) Development of phase relationships

This is an important case for extremely low temperatures and pressures for phases of materials relevant to Pluto. There is a need to fill in the gaps in planetary material and ice databases, especially amorphous ice, cubic ice, slurries, multiphase, and volatile compositions. Additionally, stability and vapor pressures of such phases and transitions are lacking.

(b) Mineralogical and chemical roles for simulations

Microstructures and chemical constituents relate to the complexity of icy bodies defined by texture; grain shape, size, and growth; crystallographic orientations; lattice-preferred orientations; distribution of phases, especially grain boundaries and polarity; porosity; intrinsic and extrinsic diffusion; etc.; that can all have major effects on flows, localization of constituents, cyclicity or seasonality of materials, transitions, and transport properties of plutonian materials. Learning the fundamental rheology, heat transport, and other dynamical processes are key to understanding Pluto's evolution and ice behavior over time.

1.2.1 FTIR Background

Fourier Transform Infrared (FTIR) spectroscopy is a technique used for qualitative features of IR-active molecules in solid, liquid, or gas samples. It is considered a rapid and inexpensive method for crystalline/ microcrystalline, amorphous, or films of solids. This technique is mainly used for the geochemistry or mineralogy of ices regarding several qualities, including: structure (van der Marel & Beutelspacher 1976); volatile concentrations (Rossman 1988; King et al. 2004);

thermodynamic and transport properties (Hofmeister 2004). Remote sensing also uses laboratory FTIR to calibrate data obtained from mineral mixtures and/or produce spectra that can be applied to remote sensing algorithms (Crowley 2004; Swayze et al. 2003).

Fourier-transform infrared spectroscopy works by passing a light beam through a Michelson interferometer. As the length of one arm of the interferometer changes, light interferes with itself destructively, then constructively, then destructively, and so on, oscillating at a rate that depends on its wavelength. Different wavelengths in the beam produce different frequencies in the interferogram that is recorded while the arm moves, and the intensity as a function of wavelength can be extracted through a Fourier transform.

It is necessary to choose the appropriate IR source, detection, and accessories. Different facilities have defined the near-, mid-, and far-IR regions differently depending on the practicality of their instrumentation (Hirschmugl 2004). Once the range has been established, the sampling setup could be set in a variety of ways, including setting in an atmospheric environment, restrictions or limitations on sample size, and complexity of mixture, if any presented. It is then necessary to choose an optimal sample chamber, interferometer unit, sample geometry with the detector, and data acquisition methodology (King et al. 2004).

1.3 Dissertation Science Goals and Objectives

1.3.1 Goals

The primary goal of this dissertation is to study the (i) spectral behavior of phases in binary ice mixtures; (ii) spectral behavior and creation of the CH_4-N_2-CO ternary phase diagram; (iii) investigate the geophysical processes observed on Plutonian glaciers, subsurface collapses, and fault structures in terms of compositional differences.

Mixtures of ices and their respective near-IR spectral analyses have shown that the observance of certain spectral bands depend heavily on temperature and molar ratio of the constituents involved. In that case, this has mineralogical implications for crystallization processes, and on a macro-scale, influence the geophysical processes on Pluto's icy surface.

While water ice was not part of the experimental tasks, modeling water ice behavior along with the knowledge of the crystallization behavior of CH_4, N_2, and CO, enhanced the geophysical modeling of the glaciers, subsurface collapsing, and fault mechanisms.

1.3.2 Objectives and Tasks

In order to investigate the goals of this dissertation, the following objectives and corresponding tasks are established:

1) Study the binary mixtures of CH_4, N_2, and CO
    a. Experimental conditions at 10 – 60 K temperatures and < 25 μbar pressures relevant to Pluto surface environmental conditions.
    b. Observe and document any temperature, molar ratio, or binary-dependent spectral bands
    c. Compare to previous experimental work (if applicable) and improve (or create) phase diagrams of the binary mixtures
2) Study the ternary mixture $CH_4 – N_2 – CO$
    a. Same experimental conditions apply from binary mixtures
    b. Observe and document how the molar concentrations of each constituent influence certain spectral band strengths
    c. Create a new ternary phase diagram

3) Investigate glacial folding

a. Develop a model to relate the folding wavelengths observed on the Baret Montes glacier

b. Use model to estimate age of the folding based on rheological properties of the CH_4 ice present

4) Evaluate tectonic-related processes

a. Map the Cthulhu Macula region for large subsurface cavities (cavi) and faults (fossae)

b. Investigate the presence of a large subsurface cavity not related to sublimation or impact cratering, and find evidence for subsurface glacio-volcanism collapsing

c. Develop a model to determine the shear stress and fault roughness (thus relative age) of Cthulhu Macula faults depending on the geometry of the fault.

The objectives and tasks of this dissertation meet several criterions from the Planetary Science Decadal Survey. Cross cutting themes, as defined within Vision and Voyages (V&V) for Planetary Science in the Decade 2013-2022, addressed here are within the scope of "Workings of Solar Systems – revealing planetary processes through time." This dissertation addresses the mineralogical and geophysical changes across the surface of Pluto in global (ices) and localized (Cthulhu Macula) scales. The workings of the solar system are addressed by simulating the Plutonian surface environment to investigate the evolution of ice mixtures and their possible surface impacts. A major objective within this scope included the question: "*How have the myriad chemical and physical processes that shaped the solar system operated, interacted, and evolved over time?*" The V&V also stated that in order to maximize the scientific return from NASA space

missions and ground-based observations alike, that materials and processes must be studied in the laboratory.

In studying the current state of spectral analyses of binary and ternary mixtures for relevant Plutonian conditions, it is possible to better understand the spectral behavior of such ices using higher resolution and lower temperatures than previous (or current) experimental studies, thus building upon current phase diagrams, or creating entirely new phase diagrams. Then by determining the effects of ice on the surface of Pluto, the glacial processes and tectonism can be better constrained.

1.4 Dissertation Outline

This dissertation consists of an Introduction (Chapter 1), Methods (Chapter 2), seven research chapters (Chapters 3 – 9), and a Conclusion (Chapter 10). The methods section summarizes all instruments used over the course of this dissertation and experimental protocol. The research chapters 3 – 5 will discuss the experiments and results of the binary mixtures between CH_4, N_2, and CO ices at simulated Plutonian conditions using near-IR FTIR spectroscopy. These series of papers have been submitted to various planetary science and planetary chemistry journals. The sixth chapter examines the CH_4 – N_2 – CO ternary phases and creation of a phase diagram. The seventh chapter investigates the Baret Montes glacial folding and estimates the age of the folding regarding the rheological properties of the CH_4 and H_2O ices. This has been accepted in Geophysical Research Letters. The eighth chapter looks at Hekla Cavus, a possible collapse pit from subsurface material (submitted to Icarus). The ninth and final research chapter models the shear stresses across large Cthulhu Macula faults (from my internship at North Carolina State University; submitted to Icarus).

1.5 References

Ahrens, C., Grundy, W., Mandt, K., Cooper, P., Umurhan, O., Chevrier, V., (2018) Recent advancements and motivations of simulated Pluto experiments. Space Science Reviews, 214(8), id. 130. https://doi.org/10.1007/s11214-018-0558-6

Ahrens, C., Chevrier, V. (2019) Compressional ridges on Baret Montes, Pluto as observed by New Horizons. GRL, 46 (24), 14328-14335. https://doi.org/10.1029/2019GL085648

Angwin, M. J., Wasserman, J., (1966). Nitrogen-Carbon Monoxide Phase Diagram. The Journal of Chemical Physics. 44(1), 417-418. https://doi.org/10.1063/1.1726486

Bennett, C., Jamieson, C., Osamura, Y., Kaiser, R. (2005) A combined experimental and computational investigation on the synthesis of acetaldehyde in interstellar ices. Astrophysical Journal, 624 (2), 1097. https://doi.org/10.1086/429119

Brunetto, R., Caniglia, G., Baratta, G. A., Palumbo, M. E., (2008) Integrated near-infrared band strengths of solid CH4 and its mixtures with N2. The Astrophysical Journal. 686(2), 1480. https://doi.org/10.1086/591509

Crowley, J. (2004) Hydrothermal mineral zoning within an eroded stratocone: Remote sensing spectral analysis of Brokeoff Volcano, California. In Infrared Spectroscopy in Geochemistry, Exploration Geochemistry and Remote Sensing (P. King, M. Ramsey, G. Swayze, ed.), Mineral. Assoc. Canada, Short Course 33, 215-226.

Cruikshank, D., Pilcher, C., Morrison, D. (1976) Pluto-Evidence for methane frost. Science 194, 835-837. Doi: https://doi.org/10.1126/science.194.4267.835-a

Cruikshank, D., W. Grundy, W., W. DeMeo, W., et al. (2015) The surface compositions of Pluto and Charon. Icarus 246, 82-92. Doi: http://dx.doi.org/10.1016/j.icarus.2014.05.023.

Cruikshank, D., Umurhan, O., Beyer, R., et al., (2019) Recent cryovolcanism in Virgil Fossae on Pluto. Icarus, 330, 155-168. 10.1016/j.icarus.2019.04.023

Douté, S., Schmitt, B., Quirico, E., et al. (1999) Evidence for methane segregation at the surface of Pluto. Icarus 142(2), 421-444. Doi: https://doi.org/10.1006/icar.1999.6226

Grundy, W., Buie, M. (2002) Spatial and Compositional Constraints on Non-ice Components and H2O on Pluto's Surface. Icarus 157(1), 128-138. Doi: 10.1006/icar.2002.6833

Grundy, W., Binzel, R., Buratti, B., et al. (2016) Surface compositions across Pluto and Charon. Science 351(6279), aad9189. Doi: 10.1126/science.aad9189

Guilbert, A., Alvarez-Candal, A., F. Merlin, F., M. Barucci, M., et al. (2009) ESO-large program on TNOs: near-infrared spectroscopy with SINFONI. Icarus 201, 272-283. Doi: https://doi.org/10.1016/j.icarus.2008.12.023

Hammond, N., A. Barr, A., E. Parmentier, E. (2016) Recent tectonic activity on Pluto driven by phase changes in the ice shell. Geophys. Res. Lett. 43 (13), 6775-6782. Doi: 10.1002/2016GL069220

Hirschmugl, C. (2004) An Introduction to Infrared Spectroscopy for Geochemistry and Remote Sensing. In Infrared Spectroscopy in Geochemistry, Exploration Geochemistry and Remote Sensing (P. King, M. Ramsey, G. Swayze, ed.), Mineral. Assoc. Canada, Short Course 33, 1-16.

Hofmeister, A. (2004) Thermal and thermodynamic properties from infrared spectra. In Infrared Spectroscopy in Geochemistry, Exploration Geochemistry and Remote Sensing (P. King, M. Ramsey, G. Swayze, ed.), Mineral. Assoc. Canada, Short Course 33, 135- 154.

Howard, A., Moore, J., Umurhan, O., et al. (2017) Present and past glaciation on Pluto. Icarus, 287, 287-300. DOI: https://doi.org/10.1016/j.icarus.2016.07.006

Hudson, R., Palumbo, M., Strazzulla, G., Moore, M., Cooper, J., Sturner, S. (2008) Laboratory studies of the chemistry of transneptunian object surface materials. *In: The Solar System Beyond Neptune*, 507-523.

Jamieson, C., Mebel, A., Kaiser, R., (2006) Understanding the kinetics and dynamics of radiation-induced reaction pathways in carbon monoxide ice at 10 K. Astrophysical Journal, 163, 184-206. doi.org/10.1086/499245.

Jaumann, R., et al., (2009) Icy satellites: geological evolution and surface processes: Saturn from Cassini-Huygens: Springer, p. 637-681. https://doi.org/10.1007/978-1-4020-9217-6_20

Kargel, J., (1995) Cryovolcanism on the Icy Satellites: Earth Moon Planets, v. 67, p.101-113. https://doi.org/10.1007/978-94-017-1092-3_12

Kim, Y., Kaiser, R. (2012) Electron irradiation of Kuiper Belt surface ices: ternary N2-CH4-CO mixtures as a case study. Astrophysical Journal, 758 (37), pp. 6. 10.1088/0004-637X/758/1/37.

King, P., McMillan, P., Moore, G. (2004) Infrared spectroscopy of silicate glasses with application to natural systems. In Infrared Spectroscopy in Geochemistry, Exploration Geochemistry and Remote Sensing (P. King, M. Ramsey, G. Swayze, ed.), Mineral. Assoc. Canada, Short Course 33, 93-133.

Lellouch, E., de Bergh, C., Sicardy, B., Kaufl, H., Smette, A. (2011) High resolution spectroscopy of Pluto's atmosphere: detection of the 2.3 um CH4 bands and evidence for carbon monoxide. A&A, 530, L4. https://doi.org/10.1051/0004-6361/201116954

Lopes, R., et al., (2007) Cryovolcanic features on Titan's surface as revealed by the Cassini Titan Radar Mapper. Icarus, 186, 395-412. https://doi.org/10.1016/j.icarus.2006.09.006

Madey, T., Johnson, R., Orlando, T. (2002) Far-out surface science: radiation-induced surface processes in the solar system. Surface Science 500 (1-3), 838-858. Doi: 10.1016/S0039-6028(01)01556-4

Maity, S., Kaiser, R., Jones, B. (2014) Formation of Ketene (H2CCO) in interstellar analogous methane (CH4)-carbon monoxide (CO) ices: A combined FTIR and reflectron time-of-flight mass spectroscopic study. Astrophysical Journal, 789 (1), https://doi.org/10.1088/0004-637X/789/1/36

McKinnon, W. et al., (2016a) Thermal Convection in Solid Nitrogen, and the Depth and Surface Age of Cellular Terrain Within Sputnik Planum, Pluto. In: 47th Lunar and Planetary Science Conference, Abstract 2921.

McKinnon, W. et al., (2016b) Convection in a volatile nitrogen-ice-rich layer drives Pluto's geological vigour: Nature, 534 (7605), 82-85. https://doi.org/10.1038/nature18289

Merlin, F., Alvarez-Candal, A., Delsanti, A., et al. (2009) Stratification of methane ice on Eris' surface. The Astronomical Journal, 137 (1). Doi: https://doi.org/10.1088/0004-6256/137/1/315

Moore, J., McKinnon, W., Spencer, J., et al. (2016) The geology of Pluto and Charon through the eyes of New Horizons. Science 351(6279), 1284-1293. Doi: 10.1126/science.aad7055

Moore, J., Hudson, R. (2003) Infrared study of ion-irradiated N2-dominated ices relevant to Triton and Pluto: formation of HCN and HNC. Icarus, 161 (2), 486-500. https://doi.org/10.1016/S0019-1035(02)00037-4

Nimmo, F., Hamilton, D., McKinnon, W., et al. (2016) Reorientation of Sputnik Planitia implies a subsurface ocean on Pluto. Nature 540, 94-96. Doi: 10.1038/nature20148

Olkin, C., Young, E., Young, L., et al. (2007) Pluto's Spectrum from 1.0 to 4.2 μm: Implications for Surface Properties. The Astronomical Journal 133 (2). Doi: https://doi.org/10.1086/509616

Owen, T., Roush, T., Cruikshank, D., et al. (1993) Surface ices and the atmospheric composition of Pluto. Science 261 (5122), 745-748. Doi: 10.1126/science.261.5122.745

Palumbo, M. (1997) Infrared spectra and nature of the principal CO trapping sites in amorphous and crystalline H2O ice. J. Phys. Chem. A, 101, 23, 4298-4301. https://doi.org/10.1021/jp962462y

Prokhvatilov, A., Yantsevich, L., (1983) X-ray investigation of the equilibrium phase diagram of CH4-N2 solid mixtures. Sov. J. Low Temp. Phys. 9(2), 94-98.

Quirico, E., Doute, S., Schmitt, B., et al. (1999) Composition, physical state, and distribution of ices at the surface of Triton. Icarus, 139 (2), 159-178. Doi: https://doi.org/10.1006/icar.1999.6111

Roberts, J., and Nimmo, F., (2008) Tidal heating and the long-term stability of a subsurface ocean on Enceladus: Icarus 194, 675-689. https://doi.org/10.1016/j.icarus.2007.11.010

Rossman, G. (1988) Vibrational spectroscopy of hydrous components. In Spectroscopic Methods in Mineralogy and Geology (F. Hawthorne, ed.) Rev. Mineral. 18, Mineral. Soc. Am., Blacksburg, VA, 193-206.

Roush, T. L., (2001). Physical state of ices in the outer solar system. Journal of Geophysical Research: Planets. 106(E12), 33315-33323. https://doi.org/10.1029/2000JE001334

Schenk, P., Beyer, R., McKinnon, W., et al., (2018) Basins, fractures and volcanoes: Global cartography and topography of Pluto from New Horizons. Icarus, 314, 400-433. https://doi.org/10.1016/j.icarus.2018.06.008

Schmitt, B., Philippe, S., Grundy, W., et al. (2017) Physical state and distribution of materials at the surface of Pluto from New Horizons LEISA imaging spectrometer. Icarus 287, 229-260. Doi: https://doi.org/10.1016/j.icarus.2016.12.025

Singer, K., et al., (2018) Cryovolcanism on Pluto and Charon. EGU General Assembly, 20, Geophysical Research Abstracts 5761.

Spencer, J., Stansberry, J., Trafton, L., et al. (1997) Volatile transport, seasonal cycles, and atmospheric dynamics on Pluto. *In: Pluto and Charon* (S. Stern, D. Tholen, Eds.), University of Arizona Press, Tucson, 435-473.

Stern, S., Bagenal, F., Ennico, K., et al. (2015) The Pluto system: Initial results from its exploration by New Horizons. Science 350(6258), aad1815. Doi: 10.1126/science.aad1815

Strazzulla, G., Palumbo, M. E., (1998) Evolution of icy surfaces: an experimental approach. Planetary and Space Science. 46(9-10), 1339-1348. https://doi.org/10.1016/S0032-0633(97)00210-9

Swayze, G., Clark, R., Goetz, A. et al. (2003) Effects of spectrometer band pass, sampling, and signal-to-noise ratio on spectral identification using the Tetracorder algorithm. J. Geophys. Res. 108(E9), 5105. Doi:1029/2002JE001975

Tegler, S., et al. (2010) Methane and nitrogen abundances on Pluto and Eris. ApJ, 725 (1), 1296. https://doi.org/10.1088/0004-637X/725/1/1296

Trowbridge, A., Melosh, H., Steckloff, J., Freed, A. (2016) Vigorous convection as the explanation for Pluto's polygonal terrain. Nature 534, 79-81. Doi: 10.1038/nature18016

Tryka, K. A., Brown, R. H., Anicich, V., Cruikshank, D. P., Owen, T. C., (1993) Spectroscopic Determination of the Phase Composition and Temperature of Nitrogen ice on Triton. Science. 261(5122), 751-754. 10.1126/science.261.5122.751

Van der Marel, H., Beutelspacher, H. (1976) Atlas of Infrared Spectroscopy of Clay Minerals and their Admixtures. Elsevier, Amsterdam.

White, O., Moore, J., McKinnon, W., et al. (2017) Geological mapping of Sputnik Planitia on Pluto. Icarus 287, 261-286. Doi: https://doi.org/10.1016/j.icarus.2017.01.011

Young, L. A., et al., (2008) New Horizons: Anticipated Scientific Investigations at the Pluto System. Space Science Reviews 140, 93–127. https://doi.org/10.1007/s11214-008-9462-9

Chapter 2

Chamber Setup

2.1 Chamber description

The Pluto Simulation Chamber is a horizontal cryo-vacuum vessel designed to test ice components under temperatures and pressures comparable to Pluto surface conditions (Figure 1). The vessel is constructed from stainless steel with external dimensions of 1.31 m in length (1.18 m length internally) and 0.45 m in diameter, but the working volume is smaller due to space taken up by a GoPro camera and lighting system (40 W bulb) for monitoring purposes and optical observations of the coldhead (Figure 2). Low pressure is achieved by an Alcatel Pascal vacuum pump for the roughing stage to the instrumental minimum of 14 ± 3 μbar. Monitoring of pressure is achieved by using a combination of a Granville-Phillips Series 375 Convectron and an ionization gauge with an accuracy of 10^{-8} Pa. To reach the temperatures of Pluto, we use a Janis Special CSS DE-204SL Cryogenic Cryocooler Closed Cycle Refrigerator System. The coldhead is coupled with a HC-2 compressor unit by APD Cryogenics. The minimum temperature reached by the cryocooler is 10 ± 1 K.

Temperature measurements are made in three locations in the chamber. One thermocouple (type T) is placed directly on the coldhead stage and another two at the sides < 1 cm from the coldhead. The stage is a flat 2-inch diameter vertical platform attached below the coldhead, where inserted gases are condensed, and is located 0.6 cm from the spectroscopic line of sight. The chamber has 22 points of access for instrumentation, mainly insertion of pre-mixed gases, FTIR probe, and the optical camera. Twelve of these access ports are CF275 type flanges: four of the flanges are located at the back end of the chamber, four on the lid, and the final four on the sides near the top. Seven of the access ports are CF600 type flanges: two of these flanges are located

on each side, two on the top, and one on the far end opposite the lid. Finally, one CF800 type flange is located on the bottom. The chamber has been fitted with an adapter to CF275 to fit to the lines of the pressure system. Finally, one CF1000 type flange is located on the main door to encompass the entire 0.45 m diameter of the chamber.

An 8.5-liter pre-mixing chamber is used for preparing the gas mixtures. Gas are injected in this chamber and the measurement of the partial pressures of each gas component via pressure gauge readings provides the molar ratios of each component. Once the selected mixture of gases is complete, it is vacuum pumped into the main simulation chamber.

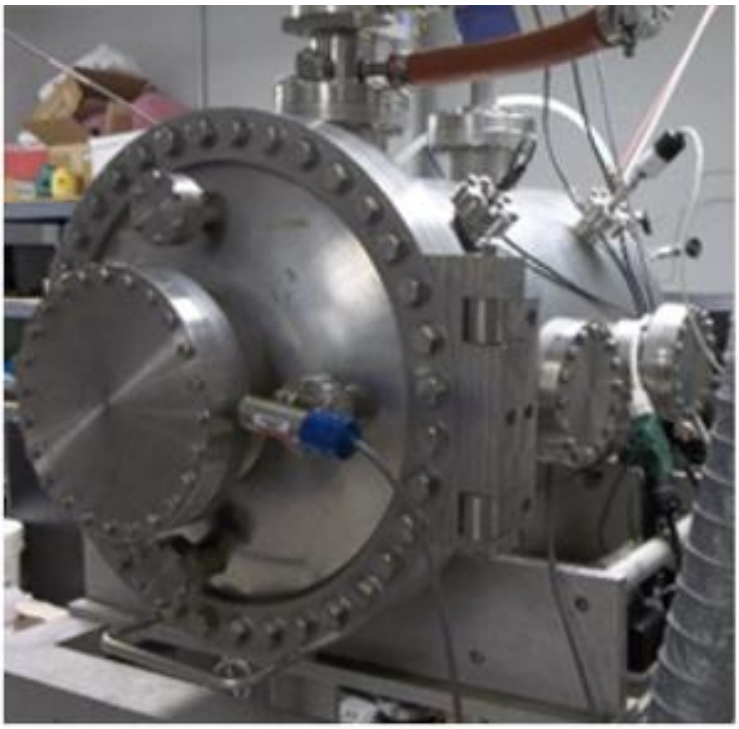

Figure 1: Exterior of the Pluto simulation chamber at the W.M. Keck Laboratory for Planetary Simulations, Arkansas Center for Space and Planetary Sciences, showing the front and side panels. The diameter of the front panel is 45 cm.

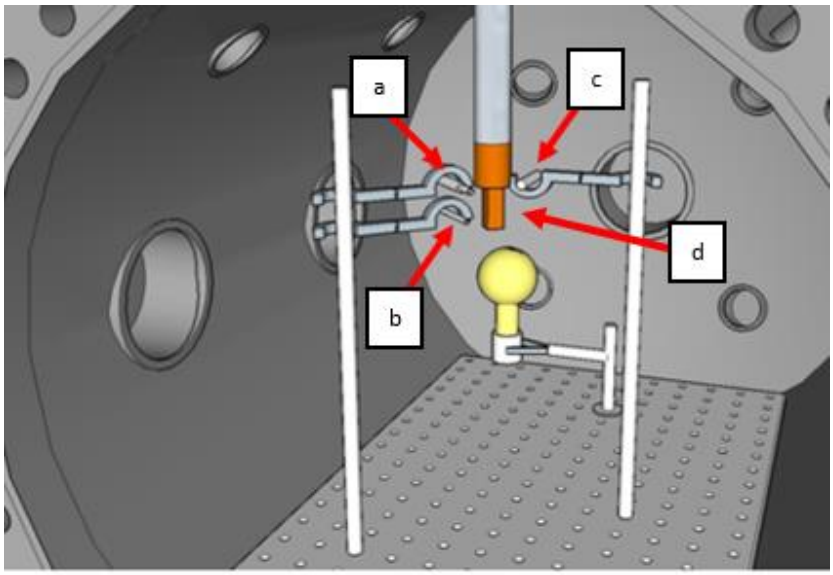

Figure 2: Schematic of the simulation chamber interior. a. FTIR probe; b. gas line; c. camera; d. coldhead stage.

2.2 Sample Preparation

The experimental protocol for sample preparation is as follows: each gas constituent is mixed as partial pressure using pressure gauge readings, and use of Dalton's Law of partial pressures, with a second (or third) constituent within the 8.5 L mixing manifold connected to the Pluto simulation chamber. This manifold is pre-vacuumed to 14 ± 3 µbar. Once the pressure is obtained in the main chamber, it is then purged with nitrogen before insertion of gas to ensure no water vapor or gas residue will affect the mixture. The resulting mixture within the manifold is then flow-controlled at 0.1 psi/second through a 2 mm diameter copper hose placed 20 mm in front of the cryostat coldhead stage. The mixture then condenses onto the vertical helium-cooled coldhead at the starting temperature of 10 ± 1 K.

2.3 Pressure and Temperature Tests

The lowest pressure achieved with just the roughing pump when sealed off from the chamber was 32 µbar, typically after 13 consecutive hours of pumping. With the addition of the coolant for the cold head function of the chamber, most of the gas could be evacuated with the roughing pump and then cryopump the chamber down to approximately 14 µbar.

To provide more direct control over the temperature, a heater was connected to the temperature indicator/controller. With this controller, a set point and a max wattage for the heater power can be defined. Once a set point is defined, the controller can reach the corresponding temperature and maintain it if required within 60 minutes.

Primary bench tests were undertaken to ensure the durability of the system over longer periods of time (> 6 hours). A test experiment where a CH_4:N_2= 0.5:0.5 molar mixture was condensed at 40 K and 17 µbar pressure. The chamber was able to maintain temperature and pressure conditions after sample preparation for up to 12 hours, as shown in Figure 3.

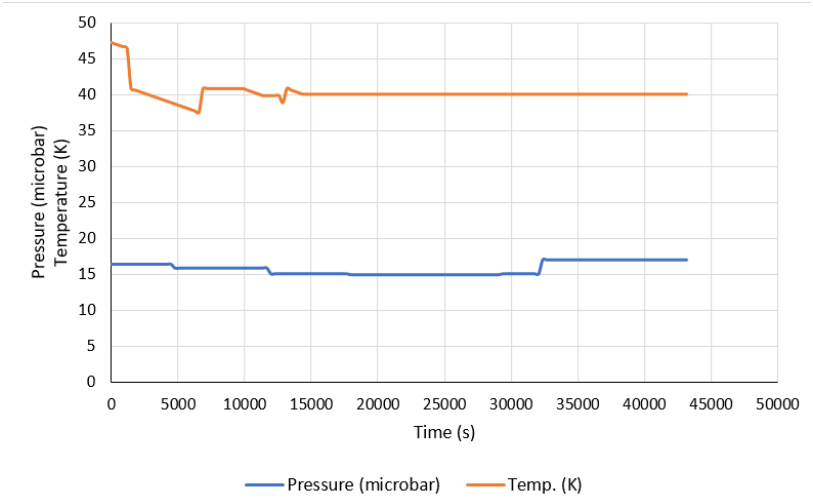

Figure 3: Pressure-temperature monitoring as a function of time during a preliminary experiment with a molar ratio N_2:CH_4: 0.5: 0.5 showing the ability of the chamber to maintain pressure (bottom curve) and temperature (upper curve) for up to 12 hours.

2.4 Light bulb Test

The 40 W light bulb placed in the chamber is solely used for verification of the ice sample condensation, alignment of the FTIR detector, recording of sublimation processes as the temperature is increased, and observe any residual ice to be purged before the next experiment. The lighting system is placed 19 cm away from the coldhead and thermocouples. Tests have been made to verify that no interference from the 40 W light source is causing heating or pre-sublimation processes in both temperature-pressure readouts. During a typical experiment, the temperature and pressure are lowered to the required 20 K and 14 μbar respectively. As the temperature is raised to 50 K, the pressure rises as a response. The results, shown in Figure 4, show that during two chamber tests with 100% N_2 starting at 20 K and 2000 seconds, one with the light bulb on and one in complete darkness, the temperature after 3600 seconds remains virtually identical within < 4 K. Therefore, the lightbulb does not significantly affect the temperature or pressure during an experiment or hinder sample production and behavior.

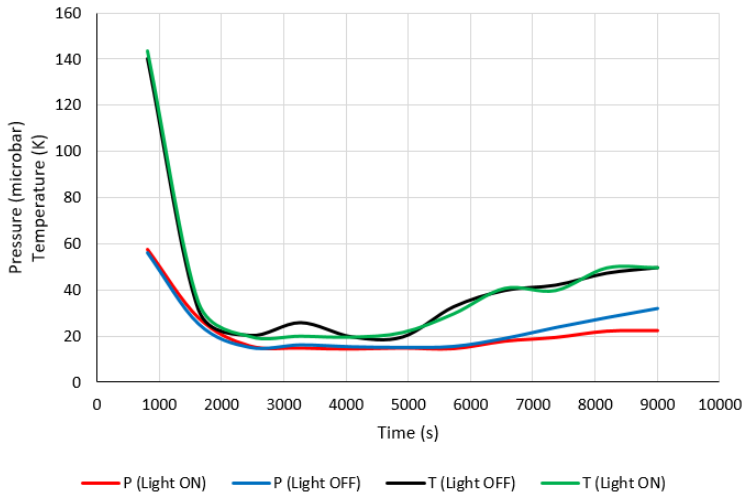

Figure 4: Coldhead temperature and pressure as a function of time during an experimental simulation of the effect of the 40 W light source on the environmental conditions in the chamber.

2.5 Data Acquisition

Once the gas mixture is condensed, FTIR spectral recording and visual observations with a macroscopic GoPro camera begins. The mixture is then heated by 10 K increments up to the experimental maximum of 60 K to determine the temperature of phase transitions or destabilization. This results in a pressure increase of 2.5 μbar increments. Therefore, this is considered as a passive-pressure chamber (the pressure is controlled by adiabatic gradient). An advantage of these *in situ* experiments is that we can explore a range of temperature increments, typically 10 K but down to 1 K for better resolution of the phase transitions.

The IR spectra of ice samples are obtained using a Nicolet 6700 FTIR spectrometer (equipped with a TEC InGaAs 2.6 μm detector and a CaF_2 beam-splitter) operating from 1 to 2.5 μm, with a spectral sampling of 4 cm^{-1} and connected to a fiber optic probe located just in front of the vertical coldhead condenser stage. Spectra are collected at a 450 second interval per spectral reading. Such long acquisition times allow a higher resolution to identify and separate more complex mixtures, especially for spectral and/or phase transitions. FTIR spectra of the samples are automatically normalized to a previously-taken background spectrum taken at 40 K using Spectralon© (a fluoro-polymer that has its highest diffuse reading within the infrared portion of the spectrum) during the acquisition.

An optical GoPro USB camera is located inside the chamber on the opposite side of the coldhead and is used for verification of ice condensation onto the coldhead and imaging throughout the experimental procedure. The GoPro system is connected via USB to the main computer, and used mainly for verification of sample condensation, monitoring of the sample, and verification of behavior with respect to sublimation or other destabilization processes (including textural changes). Both the FTIR and GoPro data can be taken simultaneously, which is beneficial for

verifying physical changes of the ice sample. All temperature and pressure data are continuously monitored and collected by computer utilizing Microsoft Excel. The infrared spectra are acquired using OMNIC© software.

2.6 Summary of technical specifications

- Total pressure ranges from (instrumental minimum) 14 μbar to 25 μbar.
- Temperature ranges from 10 K to 60 K (up to 100 K)
- Gas mixtures are regulated by partial pressures into pre-mixing manifold
- Flow rate of mixed gas is controlled by pressure regulators
- Techniques for *in situ* analysis: FTIR spectroscopy, optical imaging

Chapter 3

High-resolution near-IR investigation of N_2-CH_4 ices under simulated plutonian conditions

C. J. Ahrens[1], V. F. Chevrier[1]

[1]University of Arkansas, Center for Space and Planetary Sciences, Fayetteville, AR 72701

3.1 Abstract

With the images and spectra of Pluto's surface environment acquired by the 2015 New Horizons fly-by mission, there is now a significant need for lab measurements to advance mission data interpretation and understand the dynamics and chemical interactions of ice mixtures found on Pluto and other Kuiper Belt Objects. To that aim, we developed a simulation chamber for the purpose of *in situ* Fourier Transform Infrared Spectroscopy (FTIR) and characterization of composition, stability, and phase transitions of various ice samples at conditions relevant to the surface of Pluto at higher resolutions than those of previous experiments. We present 1 – 2.4 μm infrared spectra of pure CH_4 and N_2:CH_4 solid mixtures at temperatures from 10 K – 60 K, well within the scope of Pluto's natural seasonal variations. We compare the reflectance bands of CH_4 in N_2 with those of pure CH_4. Changes in band positions with temperature are presented, particularly regarding the known phase transitions of α-N_2 - β-N_2 and CH_4 II (α)– CH_4 I (β) and mixtures thereof. Our experiments show the CH_4 α to CH_4 β transition at 21 K is characterized by the disappearance of the 2.194 μm band, which nevertheless remains in mixture with N_2. There is also an unidentified transition at ~ 24 K where the 2.185 μm CH_4 band disappears, implying a spectral relationship with the molar ratio of N_2 present in the ice sample. Pure N_2 shows a 2.137 μm vibrational mode < 40 K, and in mixture with CH_4 produces a 2.149 μm vibrational mode > 40 K, which is the approximate temperature for the α-N_2 - β-N_2 lattice transition. A weak 1.485

μm CH_4 band also appears only when in mixture with N_2, revealing binary ice interactions. Thus, the high-resolution spectral results obtained using the Pluto simulation chamber can be used to infer mineralogical composition of Pluto's surface as well as other Kuiper Belt Objects (KBOs).

3.2 Introduction

Although Pluto does not currently have *in situ* observations, ground-based observations and the NASA New Horizons fly-by advanced our understanding of Pluto's surface composition and geochemistry. This also warranted the need for laboratory measurements to interpret such mission data and improve physical and chemical modeling (Ahrens et al. 2018). Laboratory work gives these observations a better context, such as providing spectral or chemical properties of specific ice mixtures (at various ratios) and the behavior of such mixtures when subjected to varying temperatures, both discussed in this paper. The characterization of plutonian materials requires the capability to create controlled samples, characterize their composition and behavior, and verify the reproducibility of the measurements under cryogenic and vacuum conditions reproducing the environment on the surface of Pluto.

Ice behaves in various ways depending on the compositions and environmental conditions, therefore playing various roles in the development of mineral, geological, and climatological processes on icy planetary surfaces (Roush 2001; Cruikshank et al. 2015; Grundy et al. 2016; Moore et al. 2016). Pluto's conditions are in a temperature range of 30-50 K, but have the potential to have certain areas be below 30 K due to seasonal variation and indirect sun angle (Buie et al. 1992; Hansen and Paige 1996). The compositional variability of the surface of Pluto has been well known since early ground based and Hubble observations (Owen et al. 1993; Douté et al. 1999;

Benecchi et al. 2015), mainly observing regional compositional differences and possibly related to ice mixtures.

The observations by NASA New Horizons of Pluto's surface have evidenced a striking compositional variability, essentially dominated by nitrogen (N_2), methane (CH_4) and carbon monoxide (CO) ices but in various distributions and abundances (Protopapa et al. 2017; Schmitt et al. 2017). The Linear Etalon Imaging Spectral Array (LEISA) onboard the New Horizons probe has been ideal for observing complex icy surface geology at the 1.25 μm – 2.5 μm wavelength range (Young et al. 2008; Stern et al. 2015) at the Close Encounter Hemisphere and has determined the distributions of Pluto's main volatile constituents.

Most of the proposed volatile mixtures for the various compositional regions on the surface of Pluto involve some form of geological processes (Grundy et al. 2016; McKinnon et al. 2016) or seasonal interactions with the thin atmosphere (Greaves et al. 2011; Gladstone et al. 2016). However, if the major compounds have been identified, the effects of binary or ternary mixtures remain poorly understood. Few of these binary or ternary phase interactions have been characterized experimentally in the near-infrared, but rather using other techniques such as X-ray diffraction (XRD) and higher infrared wavelengths (Angwin and Wasserman 1966; Prokhvatilov and Yantsevich 1983; Strazzulla and Palumbo 1998). Previous experiments have been done to explain the phase behavior of methane and nitrogen (Prokhvatilov and Yantsevich 1983; Tryka et al. 1993; Brunetto et al. 2008) and have identified various phases depending on the temperature and molar ratio (Figure 1). At approximately 21 K, CH_4 undergoes a transition from CH_4 α: N_2 to CH_4 β: N_2 (Prokhvatilov and Yantsevich 1983; Calvani et al. 1992; Tegler et al. 2010). N_2 itself undergoes an α to β transition at a temperature around 35 K (Prokhvatilov and Yantsevich 1983; Grundy et al. 1993). Prokhvatilov and Yantsevich (1983) used XRD to determine the transitions

of CH_4 and N_2 from changes in the crystal structure at certain experimental molar ratios and low temperatures at 5 K - 90 K. We used these transitions as a guideline for our near-IR studies.

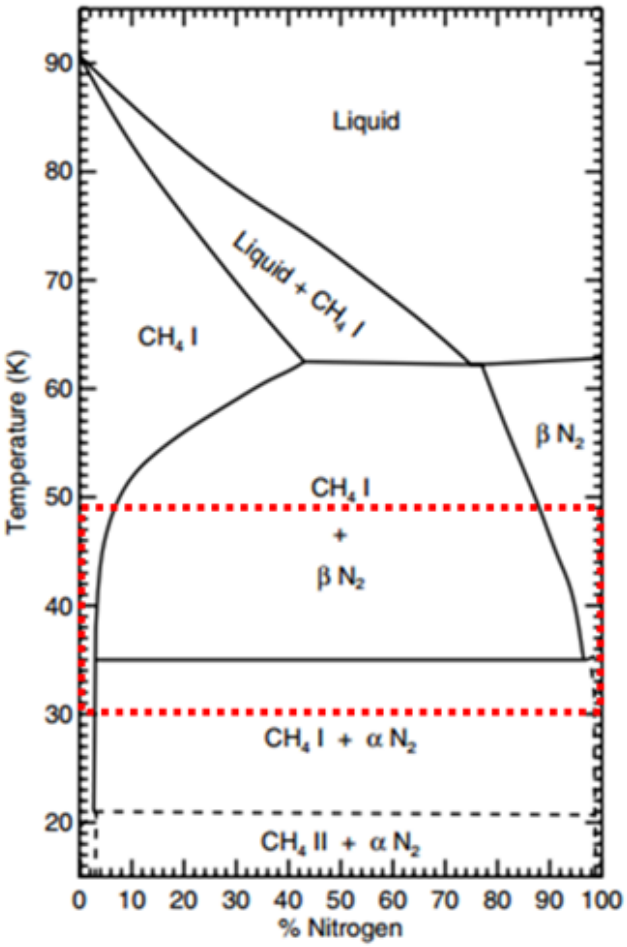

Figure 1: Phase diagram of the methane-nitrogen binary system and the respective crystalline phases (from Tegler et al. 2010). The dotted box indicates observed normal Pluto surface conditions. Extreme seasonal conditions can extend from 10 K to 60 K, encompassing a variety of phases.

These potential phase changes (Buie and Fink 1987; Grundy and Buie 2002; Tegler et al. 2010) can be of various physical and chemical nature (solid-solid transitions, or atmospheric-seasonal interaction through condensation or sublimation, and even liquefaction). Another issue is the location of the ices regarding seasonality-obliquity dynamics or cold-trap process from Sputnik

Planitia (Earle et al. 2017, 2018). These could influence any of the abundance ratios of the nitrogen and methane ices, particularly stratification or sublimation processes (Bertrand et al. 2018; Shi and Ip 2018; Schmitt et al. 2018). The proposed presence of these various phases of methane and nitrogen suggest transitions during slow seasonal changes and the potential for studying the evolution of Pluto's thin nitrogen atmosphere (Cruikshank and Silvaggio 1980; Hubbard et al. 1988; Lellouch et al. 2009, 2011). These mixture characteristics will also help determine Pluto's localized compositions where some regions are more N_2 or CH_4 dominant (Schmitt et al. 2017). This study can also apply to the case of Triton, where longitudinal variations of pure CH_4 and layers of N_2 have been observed (Merlin et al. 2018).

Therefore, the purpose of this work is to investigate the stability of Pluto's main ices constituents and mixtures thereof in conditions corresponding to the surface temperature range (30-50 K) and extreme seasonal range (10-60 K) at a pressure range of 14-25 μbar. The results of these experiments help characterize the observed phases and the mechanisms of destabilization related to seasonal processes and volatile interactions with the surrounding geology leading to a better understanding of the evolution of the surface of Pluto and methane-nitrogen dominant icy bodies in the outer Solar System.

3.3 Results

The reflectance bands are determined for each recorded spectrum, to provide two main aspects: 1) temporal evolution of the mixture behavior through the Pluto seasonal extremes (10 K – 60 K); 2) evolution of the mixture behavior through varying gas ratios in a binary-mixture. Two sets of data analyses were carried out: (1) compare spectra of a single ice mixture at various temperatures; (2) compare spectra of a single temperature at various ice mixture ratios.

Nitrogen, which is the dominant constituent on Pluto's surface, is not an IR-active compound, so the spectrum of pure (100 mol%) N_2 appears relatively flat, except for the distinct 2.149 µm band (Figure 2), which is a temperature-dependent reflectance band (Figure 3; Grundy et al. 1993). This pure N_2 band displays a very weak temperature-dependent 2.137 µm mode alongside the 2.149 µm band at temperatures < 40 K (Figure 3). This appearance of the 2.137 µm N_2 band < 30 K is presumed to be the α-β N_2 spectral phase change indicator.

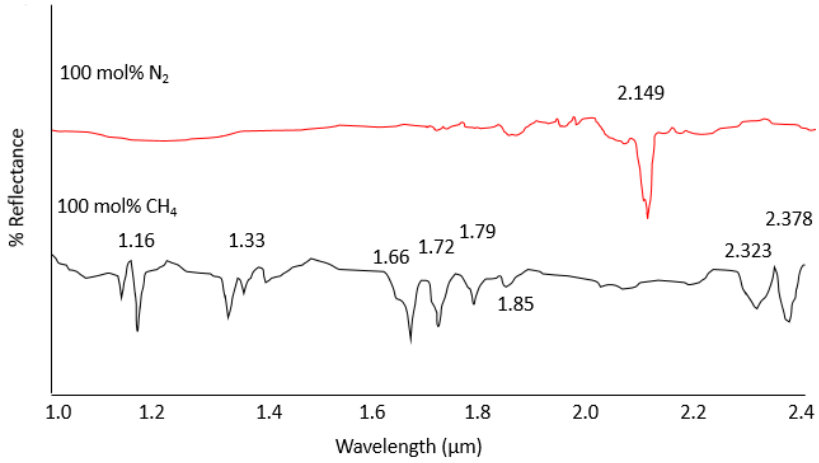

Figure 2: 1.0 – 2.4 µm IR spectra of 100 mol% N_2 and 100 mol% CH_4 at 40 K. Spectra have been offset for clarity.

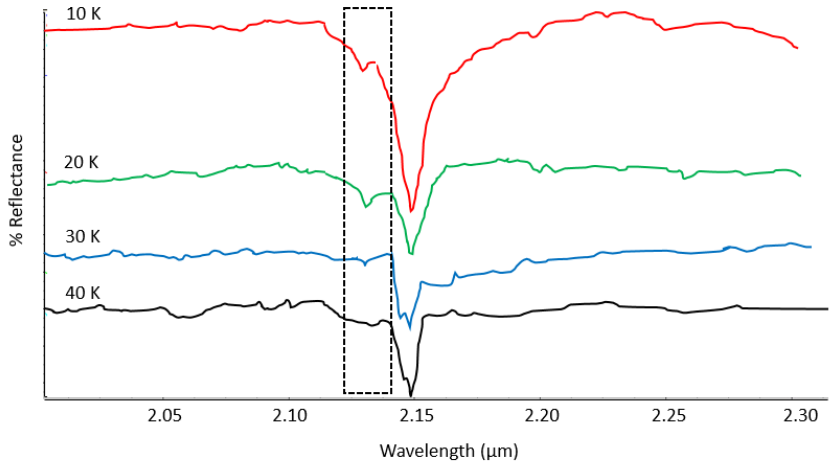

Figure 3: Nitrogen spectral profile (2.05 – 2.30 µm) of its dominant 2.149 µm band with associated 2.137 µm observed at temperature conditions < 30 K, below the β-N_2 transition.

Methane is the second most dominant constituent found on Pluto with IR bands centered at 1.16, 1.33, 1.66, 1.72, 1.79, 1.85, 2.323, and 2.378 μm (Figure 4; Clark et al. 2009; Grundy et al. 2011; Schmitt et al. 2017). At 10 K, the 1.16, 1.33, 1.66, 1.72, 1.79, 1.85 (weak), 2.185, 2.194, 2.323 and 2.378 μm bands are prominent (Figure 4). At 20 K, there is a clear shift (< 0.02 microns) of the 2.323 μm band and a widening of the 2.185 and 2.194 μm bands. At 30 K, the 1.16, 1.33, 1.66, 1.72, 1.79, 1.85, 2.323, 2.378 μm bands remain unchanged while the 2.185 and 2.194 μm bands have disappeared. With increasing temperature, the 2.323 and 2.378 μm bands are decreasing in depth. At increased temperatures > 50 K, the sublimation of the methane ice sample begins as marked by visual cracking of the ice sample (Figure 5).

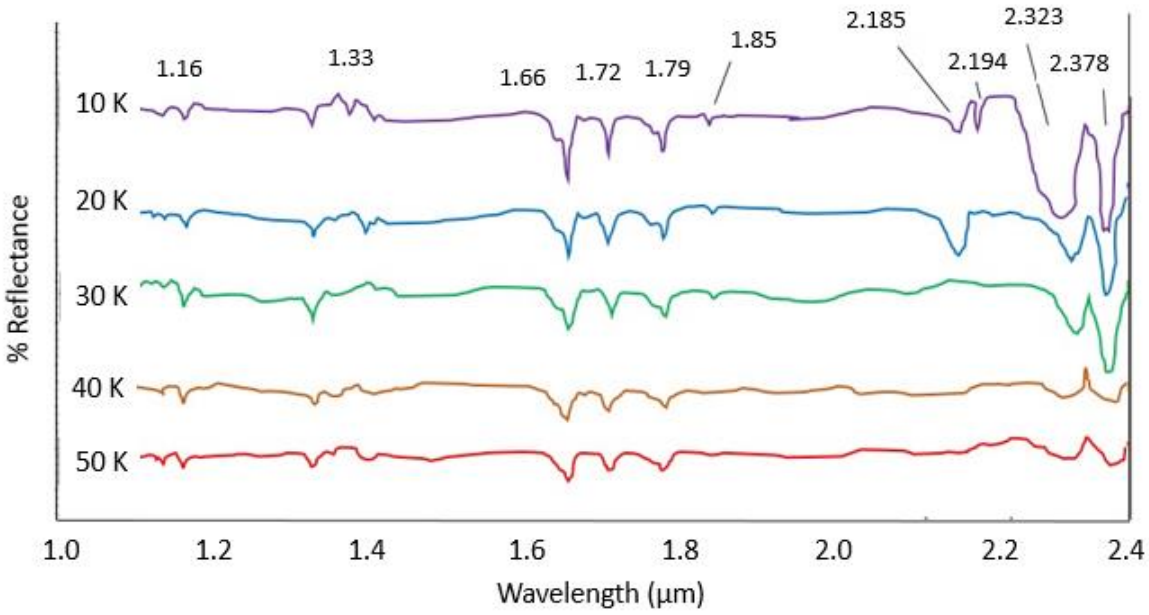

Figure 4: Near-IR spectra of pure CH_4 at various temperatures (minimum 10 K on top, 10 K increments). Note the 2.185 and 2.194 μm band changes from 10 K – 30 K. Spectra have been offset for clarity.

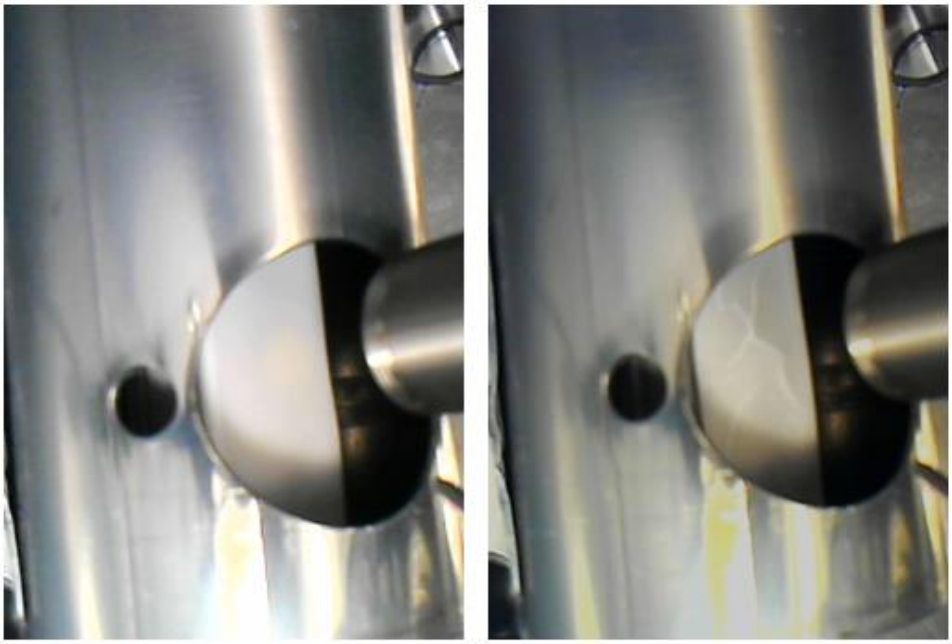

Figure 5: (Left): Pure CH_4 ice sample at 10 K within the Pluto simulation chamber. (Right): Cracks showing on the surface of the same ice sample, marking the beginning of the sublimation process and immediate breakage of the sample away from the coldhead stage.

Further investigation into the 2.185 + 2.194 and 2.323 + 2.378 μm CH_4 bands was completed with 1 K increment experiments to refine the transition (Figure 6). Past 21 K, the 2.194 μm band is to either have disappeared entirely or merged with the 2.185 μm band. From the FWHM measurements of the 2.185 μm band, this residual band disappears > 24 K (Figure 7). This dynamic temperature-dependent response of the absorption bands implies an additional transition within 19 – 24 K. The 2.185 μm FWHM band shape shifts within temperatures 19 – 24 K (Figures 7, 8). The positions of 2.323 and 2.378 μm CH_4 bands shift by approximately < 0.03 microns to shorter wavelengths (Figure 8) with increasing temperatures.

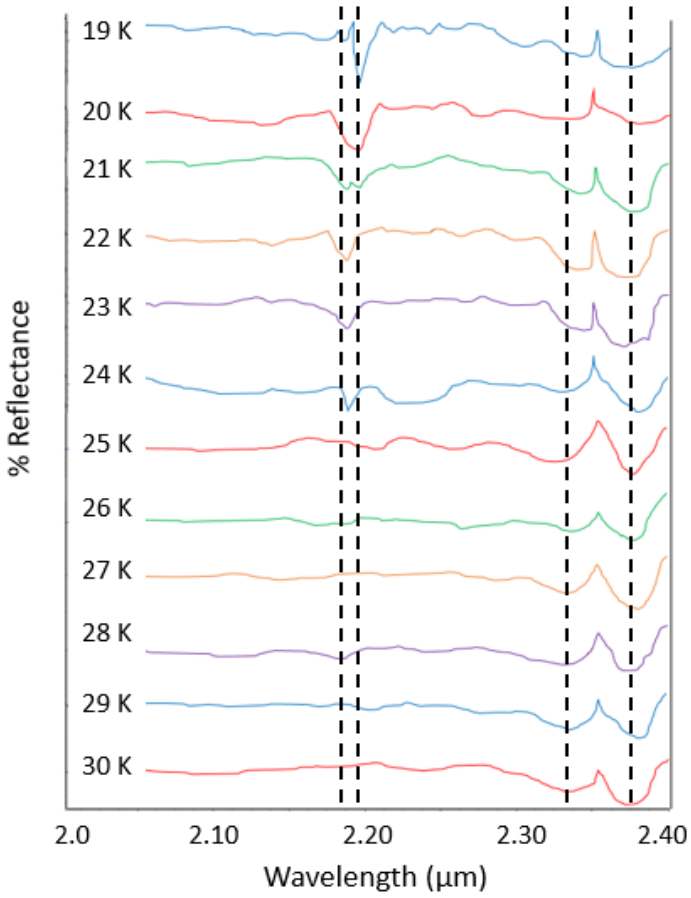

Figure 6: Near-IR spectra from 2.0 – 2.40 µm of 100 mol% CH_4 at 19 K – 30 K in 1 K increments. Dotted lines show 2.185, 2.194, 2.323, and 2.378 µm band placements respectively. Spectra has been offset for clarity.

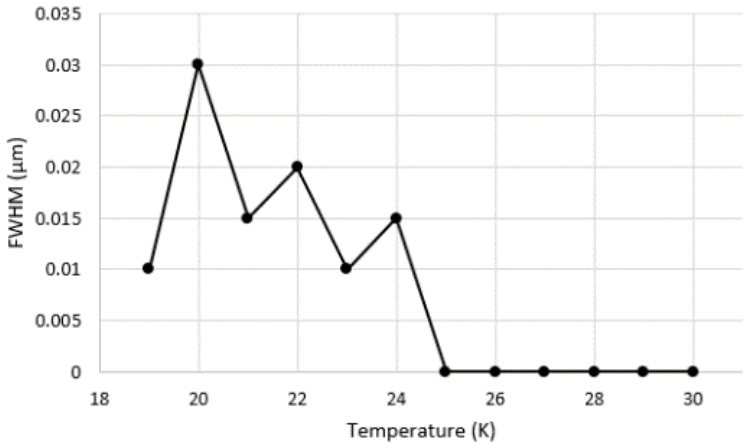

Figure 7: FWHM vs temperature for the 2.185 µm CH_4 band from a pure ice sample. The band widths are observed to be shifting variably from 19 K – 24 K, then undetectable at 25 K.

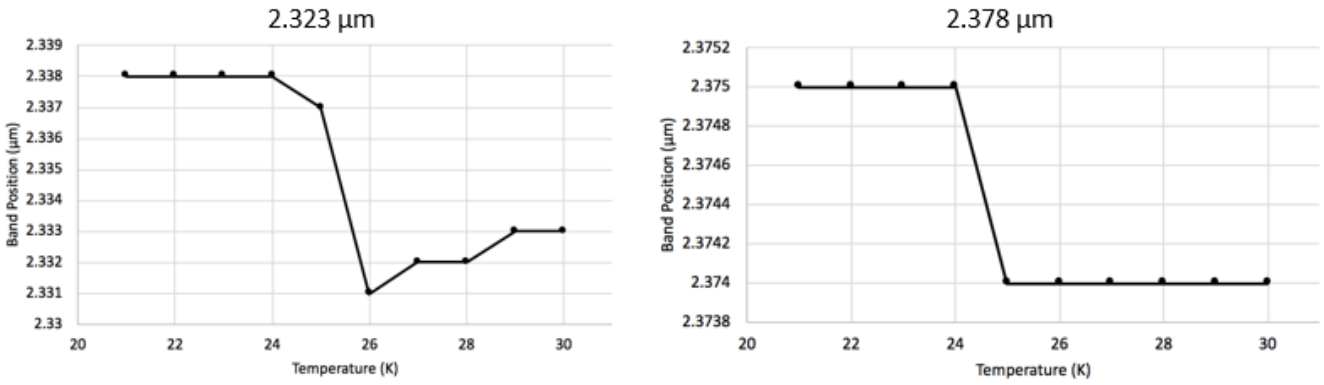

Figure 8: Band positions of 2.323 µm (left) and 2.378 µm (right) as a function of temperature for 1 K increments between 19 K and 30 K.

In N_2:CH_4 = 0.5:0.5 mixtures, as shown in Figure 9, the 2.149 µm N_2 band is observed at temperatures ≥ 40 K. However, no minor 2.137 µm N_2 band was detected (as observed in Figure 3), implying this minor mode to be only associated with the pure N_2 ice. The appearance of the 2.149 µm at these relatively higher temperatures in mixture with CH_4 suggests the β-N_2 transition.

The 2.185 and 2.194 µm methane bands are interesting to observe at temperatures > 30 K due to their absence in pure CH_4 ice samples above this temperature as previously discussed, which may imply a mixture effect when nitrogen is present. The methane band at 2.185 µm deepens and widens with increasing temperature while the 2.194, 2.323, and 2.378 µm bands shorten and only slightly widen (as instrumentation measurements permit), in Figure 9.

Three new bands not shown within the pure CH_4 or N_2 spectra are also observed within the binary ice mixtures (Figure 9). A 1.485 µm band can be found at the 10 – 60 K temperature range, with an additional 1.458 µm vibrational mode at temperatures > 40 K, which widens with increasing temperatures. Another band to appear in N_2:CH_4 mixtures is the 1.935 µm band in the 10 – 60 K range. The third CH_4 band in mixture with N_2 is the 2.21 µm.

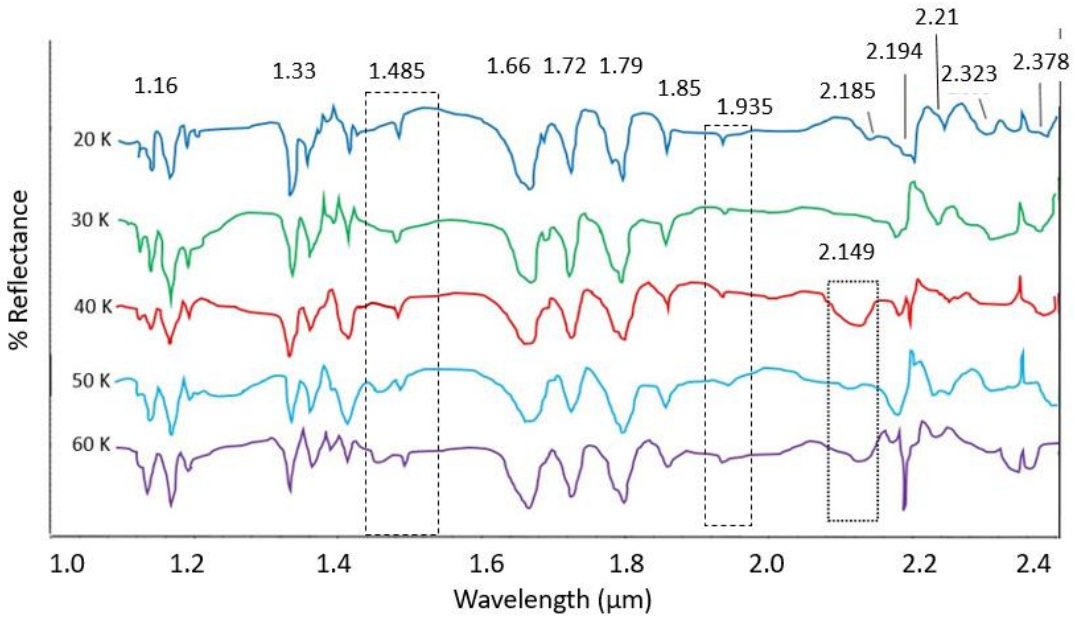

Figure 9: Near-IR spectra (1.0 – 2.4 μm) of binary mixture CH_4:N_2 = 0.5:0.5 mol ratio at various temperatures (20 K top spectrum, increase in 10 K increments). The boxes outline specific spectral signatures discussed within the text, most notable the 1.485 and 1.935 μm CH_4 bands and the 2.149 μm N_2 band observable at ≥ 40 K. Spectra has been offset for clarity.

Varying the molar ratios of N_2 and CH_4 can characterize band activity dependent on molar concentrations and compare to band dynamics to temperature-dependency, specifically from 10 – 60 K. Below, the spectra of CH_4:N_2 in varying molar concentration ratios are compared within specific temperatures (20, 30, 40, and 50 K).

Figure 10 displays varying molar ratios of CH_4:N_2 at 20 K. The 1.485 μm CH_4 band is observed (Figure 10 box a), but not the 1.458 μm partner mode. The 1.485 μm band is only observed at molar concentrations 70 mol% of CH_4. There is a slight shifting of the 1.485 μm to shorter wavelengths at smaller CH_4 molar ratios. The 1.935 μm band also appears at 20 K, but seemingly prominent in the 50 – 70 mol% CH_4 mixtures. No N_2 spectral band at 2.149 μm is observed, which is to be expected since this is below the 35 K α-β N_2 transition. The 2.185 + 2.194 μm CH_4 band pairing is very prominent in this set, especially with the 2.194 μm band being the more dominant of the pair. The 2.21 μm CH_4 band appears at 20 K for molar concentrations of

CH_4 < 70 mol %. The 2.323 µm CH_4 band appears to shift across the compositional range, mainly to shorter wavelengths at higher molar concentrations of CH_4, and vice versa to longer wavelengths with higher concentrations of N_2.

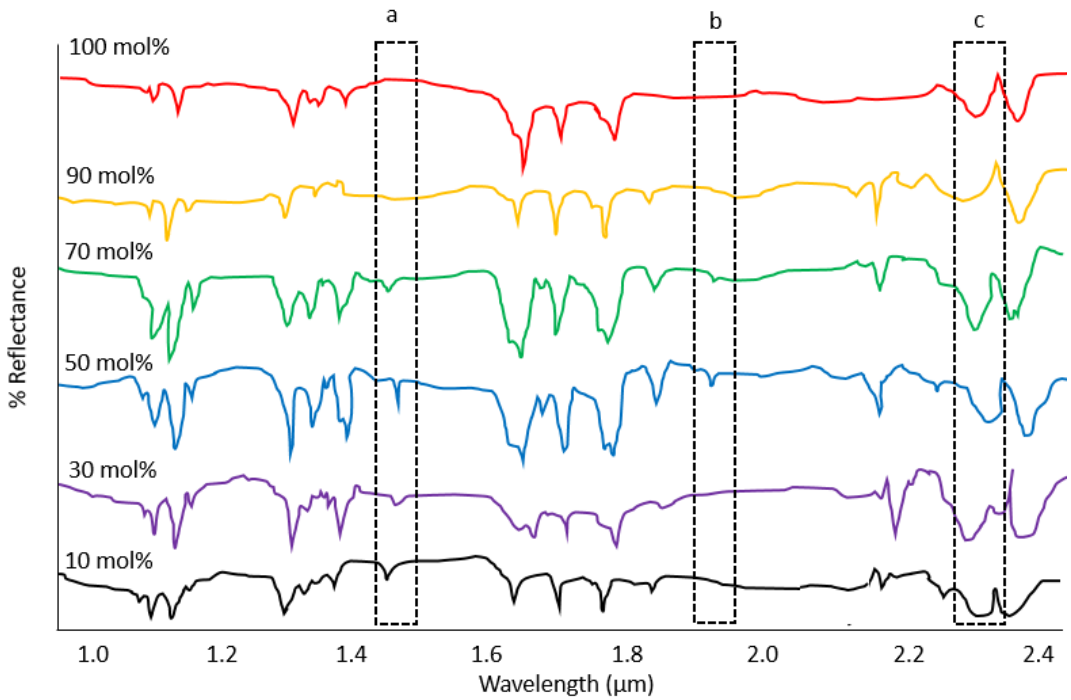

Figure 10: Near-IR spectral observations at 20 K over a range of N_2-CH_4 molar concentrations (in CH_4 mol %). Specific spectral bands are indicated for convenience: a) 1.485 µm; b) 1.935 µm; c) 2.323 µm.

When comparing the different mixtures to 30 K temperatures (Figure 11), the 1.485 µm CH_4 band is observed again, with no vibrational mode at 1.458 µm (Figure 11 box a). Similar to 20 K, this band is observed at molar ratios < 70 mol% of CH_4. The 1.935 µm CH_4 band also appears, although very weak, and detectable in the 50 – 70 mol% CH_4, similar to the 20 K temperature conditions (Figure 11 box b). Again, the 2.149 µm N_2 spectral band is not observed. The 2.185 + 2.194 µm CH_4 band pairing is observed, but the 2.185 µm band is now the dominant band in the pair. The 2.194 µm CH_4 band, however, does not seem present in the 90 mol% CH_4

and 10 mol% CH_4. The 2.21 µm CH_4 band appears at 30 K for molar concentrations of CH_4 < 90 mol %, with slight shifting to shorter wavelengths in the smaller concentrations of CH_4.

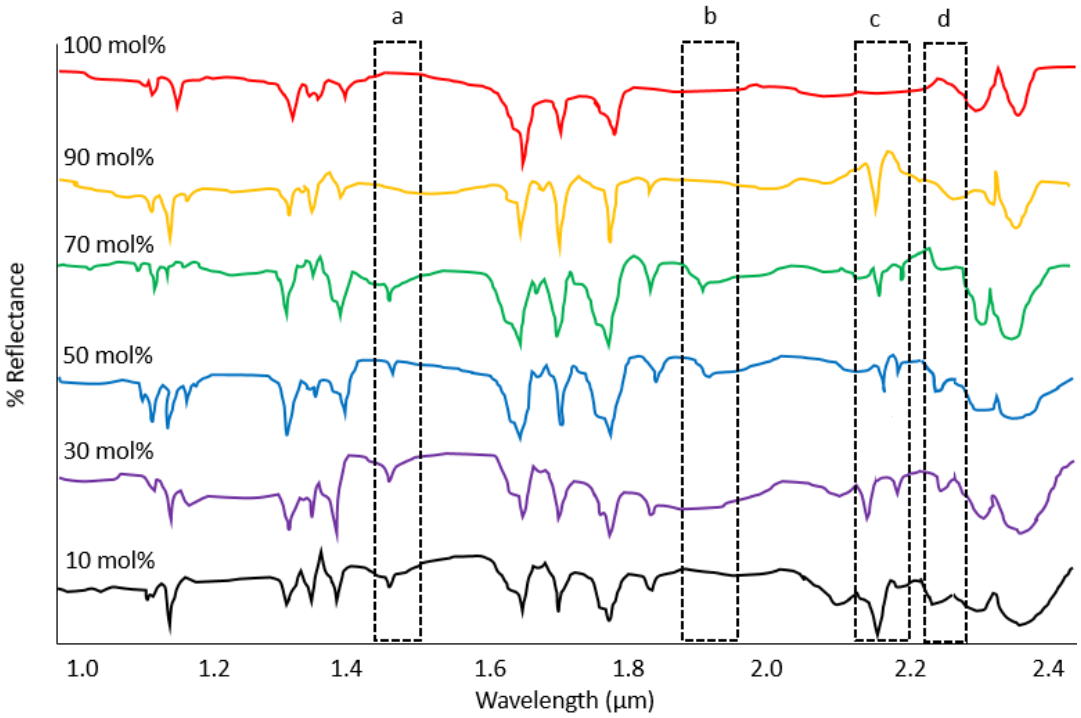

Figure 11: Near-IR spectral observations at 30 K over a range of molar concentrations (in CH_4 mol %). Specific spectral bands are indicated for convenience: a) 1.485 µm; b) 1.935 µm; c) 2.185 – 2.194 µm; d) 2.21 µm.

In 40 K temperatures (Figure 12), the 1.485 µm CH_4 is present at molar concentrations < 70 mol%, again with no 1.458 µm mode (Figure 12 box a). The 1.935 µm CH_4 band also appears, again only within the 50 – 70 mol% CH_4. The N_2 spectral band at 2.149 µm is observed, past the 35 K α-β transition, mainly in molar concentrations where N_2 > 50 mol%. The 2.185 + 2.194 µm CH_4 band pairing is now only showing the 2.185 µm band, with shifting to longer wavelengths at concentrations < 90 mol% of CH_4. The 2.21 µm CH_4 band appears at 40 K for molar concentrations < 90 mol% CH_4.

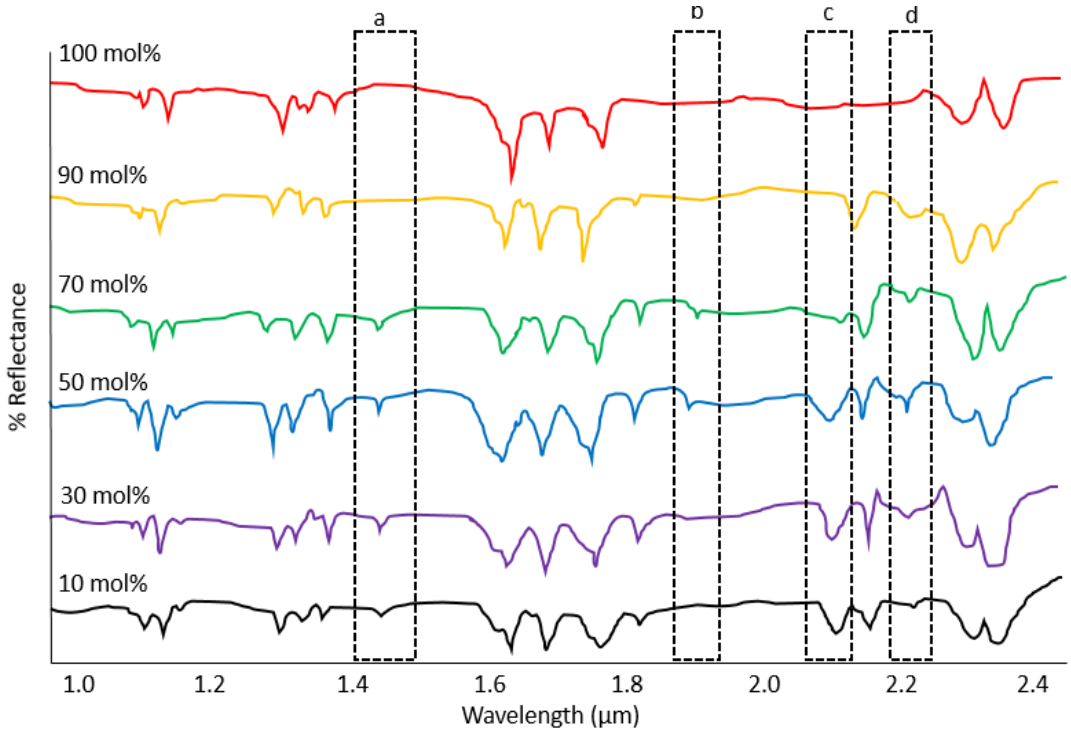

Figure 12: Near-IR spectral observations at 40 K over a range of molar concentrations (in CH_4 mol %). Specific spectral bands are indicated for convenience: a) 1.485 µm; b) 1.935 µm; c) 2.149 µm; d) 2.21 µm.

Figure 13 displays molar concentrations at 50 K. The 1.485 µm CH_4 band is observed at molar concentrations < 90 mol%, including the accompanying 1.458 µm band at molar concentrations < 50 mol% CH_4. There is a slight shifting of the 1.485 µm to shorter wavelengths at smaller CH_4 molar ratios. The 1.935 µm CH_4 band is now present in molar concentrations < 70 mol % CH_4. The 2.149 µm N_2 band is very prominent at all molar CH_4:N_2 molar concentration mixtures. The 2.185 µm CH_4 is observed, with shifting to shorter wavelengths within the 30 – 50 mol% CH_4 ratios. The 2.21 µm CH_4 band (Figure 13 box d) is observable as a very broad band, though not detectable at other molar concentrations of CH_4.

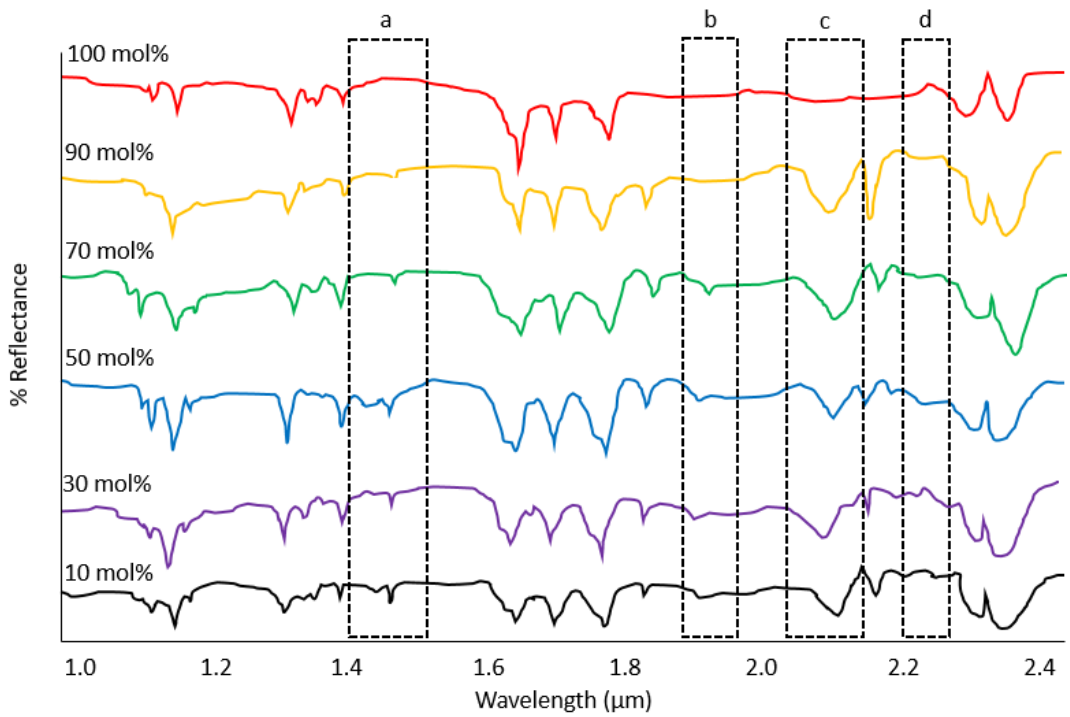

Figure 13: Near-IR spectral observations at 50 K over a range of molar concentrations (in CH_4 mol %). Specific spectral bands are indicated for convenience: a) 1.485 μm with associated 1.458 μm band; b) 1.935 μm; c) 2.149 μm; d) 2.21 μm.

3.4 Discussion

We have observed that the appearances, positions, and relative band widths in the near-IR of CH_4 in N_2 differ from those of pure CH_4 and N_2 ices, mainly the introduction of different binary mixture bands not produced in the pure CH_4 or N_2 ice samples. The differences in the band positions in the pure CH_4 spectra vs CH_4 in N_2 solid mixtures can be compared to previous experimental spectral studies of these constituents (Prokhvatilov and Yantsevich 1983; Calvani et al. 1992; Tryka et al. 1993; Quirico and Schmitt 1997; Grundy et al. 2002; Brunetto et al. 2008). The CH_4 spectral evaluations from Grundy et al. (2002) has given a wide overview of the spectral placements and vibrational modes (as listed in Table 1), and the analyses from Grundy et al. (1993) also show similar N_2 band formations. However, the proposed shifting that we have observed (namely the CH_4 2.185 μm) and the appearance of the N_2 mode at 2.137 μm both being previously

unidentified by numerous CH_4-N_2 studies shows that these discrepancies depend mostly on the spectral resolution (e.g., 0.01 cm^{-1} for this study compared to ~1 cm^{-1} from Grundy et al. 2002), along with the molar ratio of the crystalline matrix and temperature gradients subjected on the ice sample. The differences in CH_4 band behavior depending on N_2 molar concentrations and temperatures should allow one to recognize the conditions based on band positions.

The central positions of the CH_4 ($\nu_3 + \nu_4$) and ($\nu_1 + \nu_4$) combination modes (at 2.323 and 2.378 μm, respectively) in N_2 were slightly shifted and broader than their positions in pure CH_4 in our spectra, also observed in Quirico and Schmitt (1997).

We have observed the 2.185 and 2.194 μm ($\nu_2 + \nu_3$) bands of CH_4 to shift to shorter wavelengths and increasing bandwidth with increasing temperature (< 30 K) for pure CH_4. In the pure CH_4 case, these bands are significant to the evidence of the CH_4 α – CH_4 β phase transition at ~21 K with the 2.194 μm band disappearing. However, the 2.185 μm band shows a prominent (and previously unidentified) change at 24 K with the disappearance of the band entirely. This 2.185 μm band, as observed in Figure 3.1.12, shows that shifting of the 2.194 μm band after the 21 K CH_4 α – CH_4 β transition, implying this transition to be rather complex under a range of temperatures (19 K – 24 K) rather than a single transitional boundary. When mixed with N_2, the 2.185 and 2.194 μm bands become deeper as temperatures increase, with the shifting of dominance from the 2.194 μm in pure and higher molar concentrations of CH_4 to the 2.185 μm band in lower concentrations of CH_4 and higher temperatures.

An interesting feature observed in our CH_4:N_2mixtures is the N_2 2.149 μm band when in mixture with CH_4 in different temperatures and appearing at temperatures > 30 K (Figure 14). This may be indicative of the α-N_2 - β-N_2 transition at ~ 35 K (Cruikshank et al. 1993; Douté et al. 1999). Detection of this N_2 band gives rise to the implications of how N_2 can be detected depending

on CH_4 concentration and temperature setting, mainly with temperature conditions > 35 K and higher molar concentrations of N_2 (> 50 mol%) in the mixture.

Although the 1.485 μm band has been observed in previous spectral studies (Cruikshank et al. 1993; Douté et al. 1999), the conditions for this band regarding ice mixture behavior is yet identified. Such a CH_4 band to appear only in mixture with N_2 is considered "parasitic" as coined by Prokhvatilov and Yantsevich (1983). That is, the behavior of CH_4 in N_2 ice samples reveal different and affected vibrational modes in the near-IR due to this binary interaction. This 1.485 μm CH_4 band also shows a possible vibrational mode at 1.458 μm (Figure 14) above 40 K temperatures, nearing solubility levels for N_2 and CH_4 (Prokhvatilov and Yantsevich 1983). The 1.485 μm CH_4 band is observed in molar concentrations < 70 mol % CH_4, then observed at much higher CH_4 concentrations at temperatures ~50 K (Figure 14). The corresponding 1.458 μm mode was only observed in concentrations < 50 mol% CH_4 at temperatures > 40 K. The change in the 1.485 μm and the associated 1.458 μm bands imply another possible transitionary range between 40 – 50 K, giving the possibility of a new CH_4-N_2 phase not previously identified.

The 2.21 μm CH_4 band is observable with molar concentrations < 70 mol% CH_4. Once beyond the 21 K α-β CH_4 transition, this band is present until ≥ 50 K temperatures, where it is more prevalent in higher concentrations of N_2 again. This change in band appearance confirms the dependence on ratio concentrations of CH_4:N_2. However, the lack of presence in higher CH_4 concentrations at 20 K temperatures may be due to the phase changes of CH_4 and N_2 (Figure 14).

The 1.935 μm CH_4 band is observable within the limited molar concentrations of 50 – 70 mol% CH_4 at temperatures ≤ 40 K (Figure 14). However, at 50 K temperatures, this band is apparent with higher molar concentrations of CH_4. This implies a transitionary period between 40 – 50 K temperatures dependent on CH_4 molar concentrations in the sample. However, the lack of

its presence in molar concentrations > 70 mol% CH_4 could imply a saturation range where this weak band is overtaken by stronger CH_4 bands.

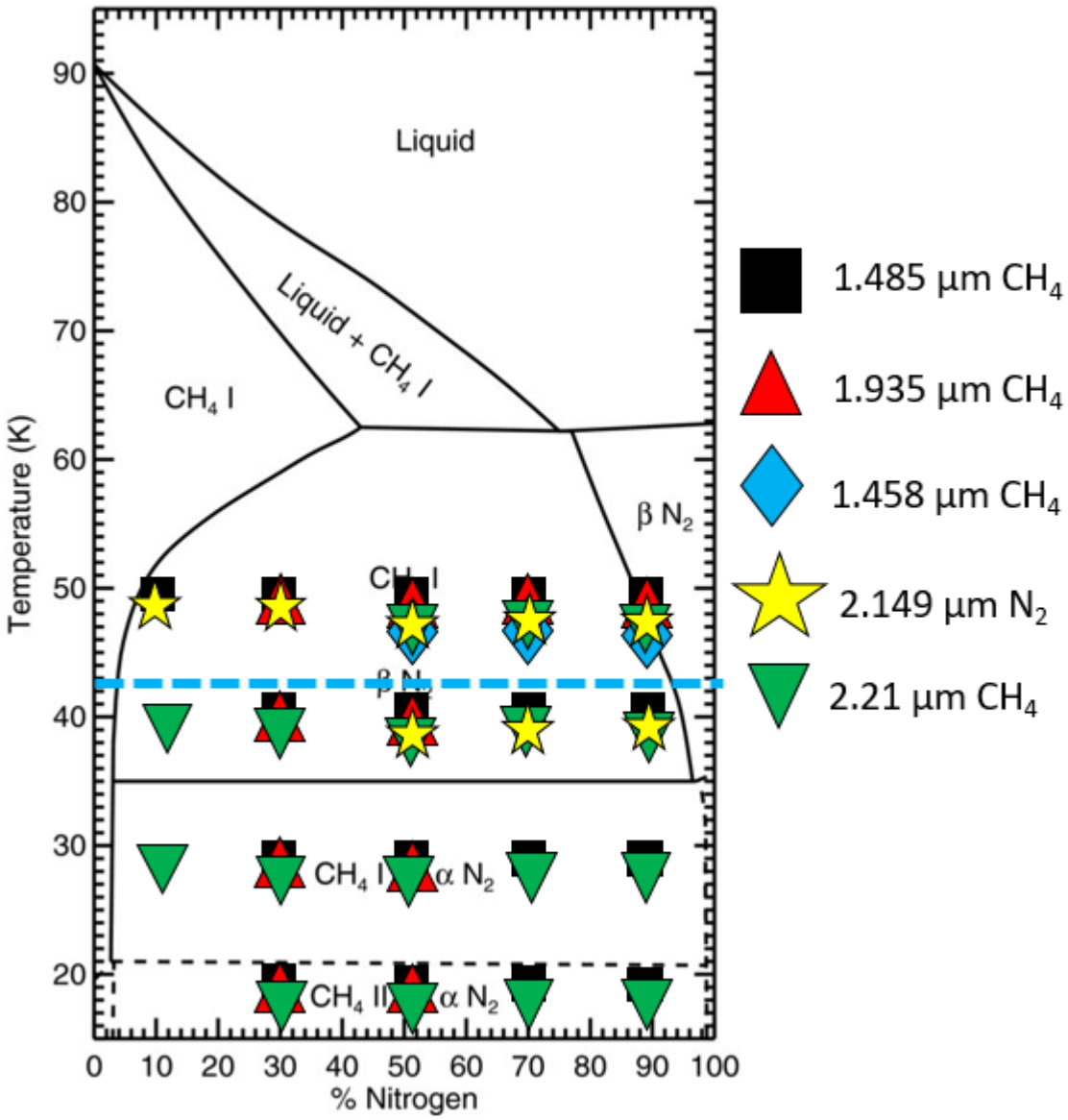

Figure 14: Data points indicating the presence of certain CH_4 and N_2 spectral bands overlain on the CH_4:N_2 binary phase diagram developed by Prokhvatilov and Yantsevich (1983). The presence of the 2.149 μm N_2 band above > 40 K temperatures verifies the α-β phase transition. Several CH_4 spectral bands depend on both temperature and molar concentrations within the ice sample, such as the 1.458 μm vibrational mode, indicated by the blue dotted line.

Table 1: Band assignments and respective vibrational modes as identified from the Grenoble Astrophysics and Planetology Solid Spectroscopy and Thermodynamics (GhoSST) spectral database. [a]Indicates molar concentration dependence; [b]Indicates temperature dependence.

Band (μm)	**Vibrational mode**	**Pure CH_4 or CH_4:N_2-Mixed Spectral Band**
1.16	$2\nu_1+\nu_2+\nu_4$	Pure
1.33	$\nu_2+2\nu_3$	Pure
1.458	ν3+3ν4	Mixed[a,b]
1.485	ν1+3ν4	Mixed[a]
1.66	$2\nu_3$	Pure
1.72	$\nu_2+\nu_3+\nu_4$	Pure
1.79	$2\nu_2+2\nu_4$	Pure
1.85	$\nu_2+3\nu_4$	Pure
1.935	4ν4	Mixed[a]
2.185 – 2.194	$\nu_2+\nu_3$	Mixed[a]
2.21	ν2+ν3	Mixed[a]
2.323	$\nu_3+\nu_4$	Pure
2.378	$\nu_1+\nu_4$	Pure

In the case of Pluto, efforts to research the spectra obtained from ground-based telescopes and the New Horizons LEISA instrument versus the state of ices in the laboratory have several important issues. The first concerns the state of CH_4 ice observed on Pluto's surface. Seen at high spectral resolution (Schmitt et al. 2018), the CH_4 bands in Pluto's spectrum are shifted toward shorter wavelengths compared to the central wavelengths of pure CH_4 (obtained in the laboratory setting), implying CH_4 being dissolved in a matrix of solid N_2 (Quirico and Schmitt, 1997;

Protopapa et al. 2015, 2017). The LEISA instrument did detect the same methane bands from our study and are categorized into "spectral zones", as follows: 1.30 – 1.43 μm (medium bands); 1.59 – 1.83 μm (medium-strong bands); 1.90 – 2.00 μm (weak bands); 2.09 – 2.48 μm (strong bands) (Schmitt et al. 2017). However, the 1.485 μm CH_4 fall in between medium to medium-strong bands, though not in any particular spectral zone. In comparison, Douté et al. (1999) observed similar methane and nitrogen bands from ground-based telescopic spectra (Figure 15). This spectrum showed the 1.485 μm CH_4 (though the associated vibrational mode at 1.458 μm was not observable) and the 2.149 μm N_2 band. The appearance of these bands from our studies implies that this spectra from Douté et al. (1999) was taken at Pluto conditions > 35 K with higher observable concentrations of methane. However, it should be noted that the behavior of the normal and parasitic CH_4 bands need to be further explored due to the possible influence of carbon monoxide (Ahrens and Chevrier 2019).

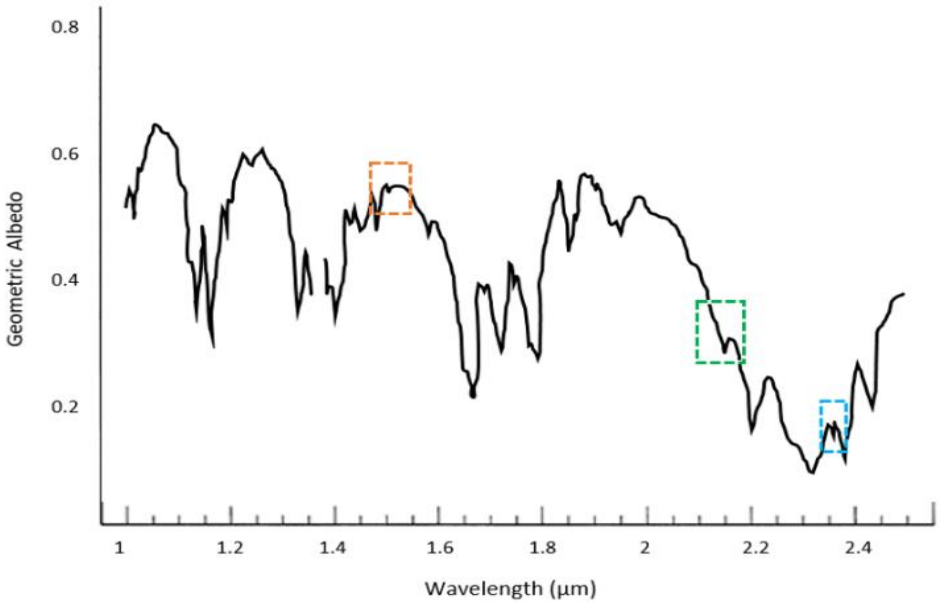

Figure 15: Pluto spectrum from the United Kingdom Infrared Telescope (UKIRT) telescope. Orange dotted box outlines the 1.485 μm CH_4 band. Green dotted box shows the 2.149 μm N_2

band. Blue dotted box outlines the weak CO signature. All other unmarked areas mark dominant CH_4 bands. Adapted from Douté et al. (1999).

While CH_4 could be affected by the matrix into which it is frozen, it is hoped that the binary systematic changes of widths, relative band positions and shape recorded here will help New Horizons data analysts ascertain whether CH_4 is pure or intimately mixed with N_2 on the surface of Pluto, or other icy bodies in the outer solar system. Based on the latest LEISA spectrometer data on Pluto (Schmitt et al. 2017) one might characterize the level of mixture behavior representative in certain regional areas on Pluto (Grundy et al. 2016; Schmitt et al. 2017; Earle et al. 2018). For example, 40°N latitude near the Sputnik Planitia basin has a great overlap of CH_4 and N_2 spectral signatures from LEISA. According to Earle et al. (2017), this area (with an albedo of 0.3) has a temperature range of 15 – 60 K within the current Pluto orbit (Figure 16). This temperature range then implies a large variability of CH_4-N_2 phases, including the α-β CH_4 crystalline phases.

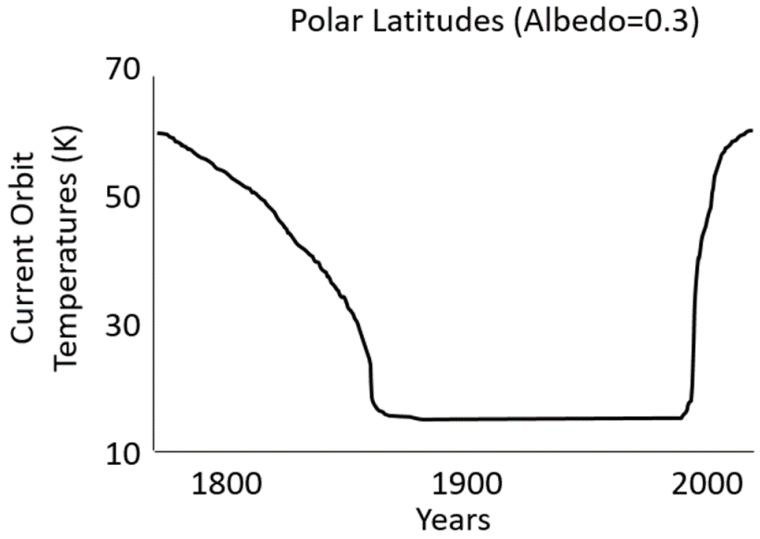

Figure 16: Local equilibrium temperatures for polar latitudes (30°N – 90°N), where greater areas of CH_4-N_2 mixtures are detected from LEISA. Adapted from Earle et al. (2017).

3.5 Conclusions

The Pluto simulation chamber was developed to be a useful tool in several scientific areas of knowledge, such as ice chemistry, spectroscopy, and ice mixture behavior. These in turn would relate to the geophysics, geomorphology, and volatility evolution studies of Pluto. It is hoped that this work of concentration ratios and temperature variations will help observers ascertain whether CH_4 is pure or intimately mixed with N_2 on icy surfaces, like Pluto and other Kuiper Belt objects (Grundy and Buie 2001; Cruikshank et al. 2015; Schmitt et al. 2017; Merlin et al. 2018).

The facility we designed meets the goals of condensing ice mixture constituents relevant to Pluto conditions, continually measuring spectrum and physical behavior, and performing *in situ* near-IR investigations of Pluto ices. We have observed the near-IR activity of N_2-CH_4 mixtures at various molar ratios and temperatures. We also observed the transitions of CH_4-α to CH_4-β at ~21 K with a previously unidentified residual band change at ~24 K. We also observed the N_2-α to N_2-β at > 30 K when in mixture with CH_4. The identification of a 1.485 μm CH_4 band (with a possible 1.458 μm mode transition at > 40 K) and the "reappearance" of the 2.185 and 2.194 μm CH_4 bands when in mixture with N_2 could imply a spectral relationship with the concentration of N_2 present in the ice sample. The changes of the 1.935 μm CH_4 band appearance dependent on both molar concentrations and temperatures gives us insight to the complexity of binary ices. Verifying these transitions and ratios of ice mixtures with our methodology advances our understanding of ice mixture phases for the two most abundant volatiles on Pluto.

3.6 References

Ahrens, C., Chevrier, V., 2018. Spectral characteristics of carbon monoxide in nitrogen and methane mixtures in simulated Pluto conditions. Lunar and Planetary Science Conference, Vol. XLIX, The Woodlands, Houston, TX, Abstract 2833.

Ahrens, C., Grundy, W., Mandt, K., Cooper, P., Umurhan, O., Chevrier, V., 2018. Recent advancements and motivations of simulated Pluto experiments. Space Science Reviews, 214(8), id. 130. https://doi.org/10.1007/s11214-018-0558-6

Ahrens, C., Chevrier, V., 2019. Spectral behavior of methane in binary and ternary icy mixtures in experimental Pluto conditions. Pluto System After New Horizons Workshop, Laurel, MD, Abstract 7034.

Angwin, M. J., Wasserman, J., 1966. Nitrogen-Carbon Monoxide Phase Diagram. The Journal of Chemical Physics. 44(1), 417-418. https://doi.org/10.1063/1.1726486

Benecchi, S. D., Noll, K. S., Weaver, H. A., Spencer, J. R., Stern, S. A., Buie, M. W., Parker, A. H., 2015. New Horizons: Long-range Kuiper Belt targets observed by the Hubble Space Telescope. Icarus. 246, 369-374. https://doi.org/10.1016/j.icarus.2014.04.014

Bernstein, M. P., Cruikshank, D. P., Sandford, S. A., 2006. Near-infrared spectra of laboratory H2O-CH4 ice mixtures. Icarus 181, 302-308. https://doi.org/10.1016/j.icarus.2005.10.021

Bernstein, M.P., Cruikshank, D.P., Sandford, S.A., 2005. Near-infrared laboratory spectra of solid H2O/CO2 and CH3OH/CO2 ice mixtures. Icarus 179, 527–534. https://doi.org/10.1016/j.icarus.2005.07.009

Bertrand, T., Forget, F., Umurhan, O., Grundy, W., Schmitt, B., Protopapa, S., Zangari, A., White, O., Schenk, P., Singer, K., Stern, A., Weaver, H., Young, L., Ennico, K., Olkin, C., 2018. The nitrogen cycles on Pluto over seasonal and astronomical timescales. Icarus, 309, p. 277-296. https://doi.org/10.1016/j.icarus.2018.03.012

Brunetto, R., Caniglia, G., Baratta, G. A., Palumbo, M. E., 2008. Integrated near-infrared band strengths of solid CH4 and its mixtures with N2. The Astrophysical Journal. 686(2), 1480. https://doi.org/10.1086/591509

Buie, M. W., Tholen, D. J., Horne, K., 1992. Albedo maps of Pluto and Charon: Initial mutual event results. Icarus. 97(2), 211-227. https://doi.org/10.1016/0019-1035(92)90129-U

Buie, M. W., Fink, U., 1987. Methane absorption variations in the spectrum of Pluto. Icarus. 70(3), 483-498. https://doi.org/10.1016/0019-1035(87)90090-X

Calvani, P., Cunsolo, S., Lupi, S., Nucara, A., 1992. The near-infrared spectrum of solid CH4. J. Chem. Phys., 96, 7372. https://doi.org/10.1063/1.462440

Clark, R.N., Curchin, J.M., Hoefen, T.M., Swayze, G.A., 2009, Reflectance spectroscopy of organic compounds: 1. alkanes. J. Geophys. Res. 114, E03001. https://doi.org/10.1029/2008JE003150

Cornelison, D., Tegler, S., Grundy, W., Abernathy, M., 2008. Near-infrared laboratory spectroscopy of CH4/N2 ice mixtures: Implications for icy dwarf planets. Science of Solar System Ices Workshop, Abstract 9089.

Cruikshank, D. P., Silvaggio, P. M., 1980. The surface and atmosphere of Pluto. Icarus. 41(1), 96-102. https://doi.org/10.1016/0019-1035(80)90162-1

Cruikshank, D., P., Roush, T. L., Owen, T. C., Geballe, T. R., de Bergh, C., Schmitt, B., Brown, R. H., Bartholomew, M. J., 1993. Ices on the surface of Triton. Science. 261 (5122), 742-745. 10.1126/science.261.5122.742

Cruikshank, D. P., Grundy, W. M., DeMeo, F. E., Buie, M. W., Binzel, R. P., Jennings, D. E., Olkin, C. B., Parker, J. W., Reuter, D. C., Spencer, J. R., Stern, S. A., Young, L. A., Weaver, H. A., 2015. The surface compositions of Pluto and Charon. Icarus. 246, 82-92. https://doi.org/10.1016/j.icarus.2014.05.023

Douté, S., Schmitt, B., Quirico, E., Owen, T. C., Cruikshank, D. P., de Bergh C., Geballe, T. R., Roush, T. L., 1999. Evidence for Methane Segregation at the Surface of Pluto. Icarus, 142 (2), 421-444. https://doi.org/10.1006/icar.1999.6226

Earle, A., Binzel, R., Young, L., Stern, S., Ennico, K., Grundy, W., Olkin, C., Weaver, H., New Horizons Geology and Geophysics Imaging Team, 2017. Long-term surface temperature modeling of Pluto. Icarus, 287, 37-46. https://doi.org/10.1016/j.icarus.2016.09.036

Earle. A. M., Grundy, W. M., Howett, C., Olkin, C., Parker, A., Scipioni, F., Binzel, R., Beyer, R., Cook, J., Cruikshank, D., Dalle Ore, C., Ennico, K., Protopapa, S., Reuter, D., Schenk, P., Schmitt, B., Stern, S., Weaver, H., Young, L., New Horizons Surface Composition Theme Team, 2018. Methane distribution on Pluto as mapped by the New Horizons Ralph/MVIC instrument. Icarus, 314, 195-209. https://doi.org/10.1016/j.icarus.2018.06.005

Gladstone, G. R., Stern, S. A., Ennico, K., Olkin, C. B., Weaver, H. A., Young, L. A., Summers, M. E., Strobel, D. F., Hinson, D. P., Kammer, J. A., Parker, A. H., Steffl, A. J., Linscott, I. R., Parker, J. W., Cheng, A. F., Slater, D. C., Versteeg, M. H., Greathouse, T. K., Retherford, K. D., Throop, H., Cunningham, N. J., Woods, W. W., Singer, K. N., Tsang, C. C. C., Schindhelm, E., Lisse, C. M., Wong, M. L., Yung, Y. L., Zhu, X., Curdt, W., Lavvas, P., Young, E. F., Tyler, G. L., team, N. H. S., 2016. The atmosphere of Pluto as observed by New Horizons. Science. 351(6279). https://doi.org/10.1126/science.aad8866

Greaves, J. S., Helling, C., Friberg, P., 2011. Discovery of carbon monoxide in the upper atmosphere of Pluto. Monthly Notices of the Royal Astronomical Society: Letters. 414(1), L36-L40. https://doi.org/10.1111/j.1745-3933.2011.01052.x

Grundy, W. M., Schmitt, B., Quirico, E., 1993. The Temperature-Dependent Spectra of α and β Nitrogen Ice with Application to Triton. Icarus. 105(1), 254-258. https://doi.org/10.1006/icar.1993.1122

Grundy, W. M., Buie, M. W., 2001. Distribution and evolution of CH4, N2, and CO ices on Pluto's surfaces: 1995 to 1998. Icarus 153, 248-263. https://doi.org/10.1006/icar.2001.6684

Grundy, W. M., Buie, M. W., 2002. Spatial and Compositional Constraints on Non-ice Components and H_2O on Pluto's Surface. Icarus. 157(1), 128-138. https://doi.org/10.1006/icar.2002.6833

Grundy, W., Schmitt, B., Quirico, E., 2002. The temperature-dependent spectrum of methane ice I between 0.7 and 5 um and opportunities for near-infrared remote thermometry. Icarus 155, 486-496. https://doi.org/10.1006/icar.2001.6726

Grundy, W., Morrison, S., Bovyn, M., Tegler, S., Cornelison, D., 2011. Remote sensing D/H ratios in methane ice: Temperature-dependent absorption coefficients of CH3D in methane ice and in nitrogen ice. Icarus. 212(2), 941-949. https://doi.org/10.1016/j.icarus.2011.01.034

Grundy, W. M., Binzel, R. P., Buratti, B. J., Cook, J. C., Cruikshank, D. P., Dalle Ore, C. M., Earle, A. M., Ennico, K., Howett, C., Lunsford, A. W., Olkin, C. B., A. H. Parker, A. H., Philippe, S., Protopapa, S., Quirico, E., Reuter, D. C., Schmitt, B., Singer, K. N., Verbiscer, A. J., Beyer, R. A., Buie, M. W., Cheng, A. F., Jennings, D. E., Linscott, I. R., Parker, J., Schenk, P. M., Spencer, J. R., Stansberry, J. A., Stern, S. A., Throop, H. B., Tsang, C., Weaver, H. A., Weigle II, G. E., Young, L. A., and the New Horizons Science Team, 2016. Surface compositions across Pluto and Charon. Science. 351, aad9189. https://doi.org/10.1126/science.aad9189

Hansen, C. J., Paige, D. A., 1996. Seasonal Nitrogen Cycles on Pluto. Icarus. 120(2), 247-265. https://doi.org/10.1006/icar.1996.0049

Hubbard, W. B., Hunten, D. M., Dieters, S. W., Hill, K. M., Watson, R. D., 1988. Occultation evidence for an atmosphere on Pluto. Nature. 336(6198), 452-454. https://doi.org/10.1038/336452a0

Lellouch, E., Sicardy, B., De Bergh, C., Kaufl, H. U., Kassi, S., Campargue, A., 2009. Pluto's lower atmosphere structure and methane abundance from high-resolution spectroscopy and stellar occultations. Astronomy & Astrophysics. 495(3), L17-L21. https://doi.org/10.1051/0004-6361/200911633

Lellouch, E., De Bergh, C., Sicardy, B., Käufl, H. U., Smette, A., 2011. High resolution spectroscopy of Pluto's atmosphere: detection of the 2.3 μm CH4 bands and evidence for carbon monoxide. Astronomy & Astrophysics. 530, L4. https://doi.org/10.1051/0004-6361/201116954

McKinnon, W. B., Nimmo, F., Wong, T., Schenk, P. M., White, O. L., Roberts, J. H., Moore, J. M., Spencer, J. R., Howard, A. D., Umurhan, O. M., Stern, S. A., Weaver, H. A., Olkin, C. B., Young, L. A., Smith, K. E., the New Horizons Geology, G., Imaging Theme, T., 2016. Convection in a volatile nitrogen-ice-rich layer drives Pluto's geological vigour. Nature. 534(7605), 82-85. https://doi.org/10.1038/nature18289

McMahon, Z., 2016. Development of a Pluto Chamber for Surface Simulations. Master's Thesis. http://scholarworks.uark.edu/etd/1812

Merlin, F., Lellouch, E., Quirico, E., Schmitt, B., 2018. Triton's surface ices: Distribution, temperature and mixing state from VLT/SINFONI observations. Icarus, 314, 274-293. https://doi.org/10.1016/j.icarus.2018.06.003

Moore, J. M., McKinnon, W. B., Spencer, J. R., Howard, A. D., Schenk, P. M., Beyer, R. A., Nimmo, F., Singer, K. N., Umurhan, O. M., White, O. L., 2016. The geology of Pluto and

Charon through the eyes of New Horizons. Science. 351(6279), 1284-1293. https://doi.org/10.1126/science.aad7055

Moores, J., Smith, C., Toigo, A., Guzewich, S., 2017. Penitentes as the origin of the bladed terrain of Tartarus Dorsa on Pluto. Nature. 541(7636), 188-190. https://doi.org/10.1038/nature20779

Owen, T. C., Roush, T. L., Cruikshank, D. P., Elliot, J. L., Young, L., De Bergh, C., Schmitt, B., Geballe, T., Brown, R., Bartholomew, M., 1993. Surface ices and the atmospheric composition of Pluto. Science. 261(5122), 745-748. https://doi.org/10.1126/science.261.5122.745

Prokhvatilov, A., Yantsevich, L., 1983. X-ray investigation of the equilibrium phase diagram of CH_4-N_2 solid mixtures. Sov. J. Low Temp. Phys. 9(2), 94-98.

Protopapa, S., Grundy, W., Tegler, S., Bergonio, J., 2015. Absorption Coefficients of the Methane-Nitrogen Binary Ice System: Implications for Pluto. Icarus, 253, 179-188. https://doi.org/10.1016/j.icarus.2015.02.027

Protopapa, S., Grundy, W. M., Reuter, D. C., Hamilton, D. P., Dalle Ore, C. M., Cook, J. C., Cruikshank, D. P., Schmitt, B., Philippe, S., Quirico, E., 2017. Pluto's global surface composition through pixel-by-pixel Hapke modeling of New Horizons Ralph/LEISA data. Icarus. 287, 218-228. https://doi.org/10.1016/j.icarus.2016.11.028

Quirico, E., Schmitt, B., 1997. Near-infrared spectroscopy of simple hydrocarbons and carbon oxides diluted in solid N2 and as pure ices: Implications for Triton and Pluto. Icarus 127, 354–378. https://doi.org/10.1006/icar.1996.5663

Roush, T. L., 2001. Physical state of ices in the outer solar system. Journal of Geophysical Research: Planets. 106(E12), 33315-33323. https://doi.org/10.1029/2000JE001334

Schmitt, B., Philippe, S., Grundy, W. M., Reuter, D. C., Côte, R., Quirico, E., Protopapa, S., Young, L. A., Binzel, R. P., Cook, J. C., Cruikshank, D. P., Dalle Ore, C. M., Earle, A. M., Ennico, K., Howett, C. J. A., Jennings, D. E., Linscott, I. R., Lunsford, A. W., Olkin, C. B., Parker, A. H., Parker, J. W., Singer, K. N., Spencer, J. R., Stansberry, J. A., Stern, S. A., Tsang, C. C. C., Verbiscer, A. J., Weaver, H. A., 2017. Physical state and distribution of materials at the surface of Pluto from New Horizons LEISA imaging spectrometer. Icarus. 287, 229-260. https://doi.org/10.1016/j.icarus.2016.12.025

Schmitt, B., Gabasova, L., Philippe, S., Bertrand, T., Grundy, W., Quirico, E., Forget, F., Stansberry, J., Lewis, B., Protopapa, S., Dhingra, R., Young, L., Olkin, C., Dennis, C., Stern, S., Weaver, H., New Horizons Competition Team, 2018. Evidence of local CH4 stratification on Pluto from New Horizons LEISA data and a complete N2 ice map. AAS-DPS meeting #50, id.506.02.

Shi, H., Ip, W., 2018. A study of the seasonal variation of the sublimation rate of the Sputnik Planum ice sheet on Pluto. Serendipities in the Solar System and Beyond. ASP Conference Series, Vol. 513, Astronomical Society of the Pacific, p.275.

Smith, K., 2018. Methane ice dunes on Pluto. Science. 360 (6392), p. 976-978. 10.1126/science.360.6392.976-j

Stern, S. A., Bagenal, F., Ennico, K., Gladstone, G. R., Grundy, W. M., McKinnon, W. B., Moore, J. M., Olkin, C. B., Spencer, J. R., Weaver, H. A., 2015. The Pluto system: Initial results from its exploration by New Horizons. Science. 350(6258), aad1815. https://doi.org/10.1126/science.aad1815

Strazzulla, G., Palumbo, M. E., 1998. Evolution of icy surfaces: an experimental approach. Planetary and Space Science. 46(9-10), 1339-1348. https://doi.org/10.1016/S0032-0633(97)00210-9

Tegler, S. C., Cornelison, D. M., Grundy, W. M., Romanishin, W., Abernathy, M. R., Bovyn, M. J., Burt, J. A., Evans, D. E., Maleszewski, C. K., Thompson, Z., Vilas, F., 2010. Methane and Nitrogen Abundances on Pluto and Eris. The Astrophysical Journal. 725(1), 1296. https://doi.org/10.1088/0004-637X/725/1/1296

Tryka, K. A., Brown, R. H., Anicich, V., Cruikshank, D. P., Owen, T. C., 1993. Spectroscopic Determination of the Phase Composition and Temperature of Nitrogen ice on Triton. Science. 261(5122), 751-754. 10.1126/science.261.5122.751

Young, L. A., et al., 2008. New Horizons: Anticipated Scientific Investigations at the Pluto System. Space Science Reviews 140, 93–127. https://doi.org/10.1007/s11214-008-9462-9

Chapter 4

A possible polycrystalline phase from near-IR spectral analyses of CO-N_2 ice with implications toward Pluto

C. J. Ahrens[1], V. F. Chevrier[1]

[1]University of Arkansas, Center for Space and Planetary Sciences, Fayetteville, AR 72701

4.1 Abstract

Pluto has latitudinal concentrations of solid nitrogen (N_2) and carbon monoxide (CO), with increased levels at the Sputnik Planitia basin, as observed by New Horizons. Here, we provide near-infrared spectra of pure N_2 and CO, and binary mixtures thereof at various molar ratios and temperatures. We use a Pluto simulation chamber capable of reproducing Plutonian surface conditions (10 – 50 K, 14 – 25 μbar). Experimental samples were analyzed using Fourier transform infrared (FTIR) spectroscopy within 1 – 2.4 μm. We confirmed the cubic to hexagonal crystalline transition of the binary mixture, though we have noted several spectral bands that only appear in the binary mixture of N_2-CO and not in the pure spectra. A possible polycrystalline phase has been detected through near-IR observations of the 2.318-2.38 μm CO bands and lack of the 2.337 μm band, including a physical fracturing pattern on the ice sample at < 30 mol% CO and ≤ 20 K temperatures.

4.2 Introduction

Carbon monoxide (CO) and nitrogen (N_2) are two abundant ices on Pluto's surface, aside from methane (CH_4) and water ice (H_2O), as observed by the New Horizons Linear Etalon Imaging Spectral Array (LEISA), which mapped Pluto's spectral signatures from 1 – 2.5 μm (Grundy and Buie 2001; Merlin 2010; Stern et al. 2015; Grundy et al. 2016; Protopapa et al. 2017; Schmitt et

al. 2017) . LEISA also observed the concentrations of such ices to be variable across the plutonian surface, where N_2 and CO are most prevalent in the Tombaugh Regio region and Venera Terra to the northwest (Schmitt et al. 2017), where surfaces are considered sublimation-driven or heavily cratered. Although in relatively smaller concentrations on the surface at Pluto, CO is considered an important factor for atmospheric processes (Greaves et al. 2011; Lellouch et al. 2017; He et al. 2017) and cryovolcanism (Neveu et al. 2015).

Even though the range in surface temperatures on Pluto (40 - 45 K) is in the solid stability field of both N_2 and CO, with surface pressures at 10 - 25 microbar (Zalucha and Gulbis 2012; Stern et al. 2015), the formation and stability in extreme seasonal conditions (10 K – 50 K) is possible in past and current processes (Young et al. 1997; Caracas 2013; Gladstone et al. 2016). This 10 – 50 K temperature range gives rise to variations in the crystalline state, especially the α-β phase transitions of N_2 (at 35.6 K) (Grundy et al. 1993; Quirico and Schmitt 1997a); and α-β CO at 61.6 K (Giauque and Clayton 1933; Angwin and Wassermann 1966; Quirico and Schmitt 1997a, b; Vetter et al. 2007; de Bergh et al. 2008).

In the binary N2:CO binary phase diagram, first created by Angwin and Wassermann (1966) through X-ray diffraction, the cubic crystalline orientation phase is within the range 35.6 K – 60 K, depending on the molar concentration of CO (e.g., higher concentrations of CO require relatively higher temperatures ~60 K for achieve a phase transition). Above this temperature range is the hexagonal-cubic-packed (hcp). Angwin and Wassermann (1966) also observed a lens phase domain within the N_2:CO binary phase diagram, where a crystalline mixture of hexagonal and cubic (hcp + cubic) co-exists. However, this phase diagram is still poorly defined, mainly due to laboratory constraints in the previous experimental studies, so experiments < 30 K are not well-defined.

Experimental near-IR (NIR) spectra of solid N_2, CO, or mixtures thereof have been previously studied (Angwin and Wassermann 1966; Dubost 1976; Nelander 1976; Grundy et al. 1993; Tryka et al. 1995; Quirico and Schmitt 1997a; Xia and McKellar 2000; Vetter et al. 2007; Tegler et al. 2019), though mostly in the range 30 K – 80 K and showed very weak IR bands (Schmitt et al. 1990; Green et al. 1991; de Bergh et al. 2008). CO spectral bands are sensitive to the phase of solid N_2 in the crystalline matrix (Quirico and Schmitt 1997a). It has also been noted by Quirico and Schmitt (1997a) that the α-CO phase is isotropic and organized lattice, but that the α-phase is not precisely oriented and may present a variety of orientations. Moreover, it is interesting that contrary to N_2 and CH_4 having an inter-lattice mixture due to their nonpolar attributes, CO is a weakly polar molecule which could lead to interesting effects in this range of temperatures. Temperatures below the α-N_2 at 35.6 K are still cause for analysis for extreme Pluto conditions, including the investigation of the polarity (CO) and non-polarity (N_2) interactions during condensation.

In this work, we investigate the NIR reflectance spectra of N_2 and CO in pure and binary mixture samples condensed in laboratory-prepared environments simulating plutonian conditions (10 – 50 K and ≤ 25 μbar). We use FTIR spectroscopy to investigate spectral bands in the NIR wavelength range, and to detect possible N_2-CO specific band variations dependent on molar concentrations within the ice matrix, or previously unknown phases.

4.3 Results

In this section we show in detail the differences in spectral characteristics between pure N_2 and CO ice samples and binary mixtures. We also deduce from the NIR spectra observed phase changes and an optical observance of fractures on the ice sample. Because the edges of our

wavelength range using our current FTIR setup show significant noise at longer wavelengths, we focus on the spectral range 1 – 2.4 μm for clarity. Spectral band identification was verified by the Grenoble Astrophysics and Planetology Solid Spectroscopy and Thermodynamics (GhoSST) database.

Nitrogen is not necessarily an IR-active compound, but does have several key spectral features, namely the prominent 2.149 μm band (Figure 1) (Grundy et al. 1993; Vetter et al. 2007; de Bergh et al. 2008). This pure N_2 band displays a very weak temperature-dependent 2.137 μm mode alongside the 2.149 μm band at temperatures < 40 K (Figure 2), presumed to be the α-β N_2 spectral phase change indicator expected to be at 35.6 K (Prokvatilov and Yantsevich 1983). Another interesting feature to note is the 2.149 um N_2 band forming a doublet structure at temperatures > 30 K.

Carbon monoxide has several identified NIR spectral bands at 1.577 (3ν), 1.61 (3ν), 2.318 (2ν), 2.337 ([ν]+[ν]), 2.35 (2ν), 2.38 ([ν]+[ν]) and 2.405 (2ν) μm (Plyler et al. 1958; Fink and Sill 1982; Quirico and Schmitt 1997 a, b; Lellouch et al. 2017). In the pure CO NIR-spectra (Figure 3), we observe the dominant 2.35 μm with accompanying 2.318 and 2.38 μm bands from 10 – 50 K, with the 2.35 μm band decreasing strength with increasing temperatures.

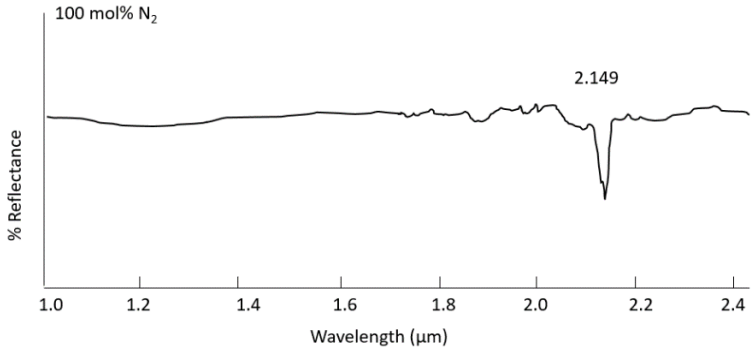

Figure 1: Pure nitrogen NIR spectra in the range 1.0 – 2.4 μm at 40 K, showing the prominent 2.149 μm band.

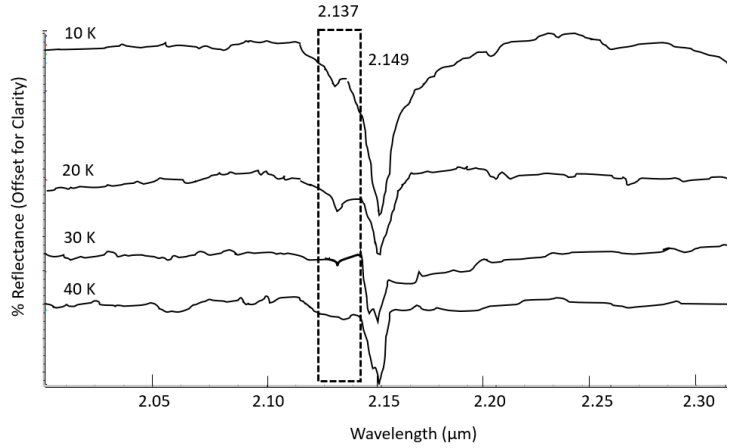

Figure 2: Nitrogen N_2 spectra (2.05 – 2.30 μm) of the 2.149 μm band with associated 2.137 μm (dashed box) observed at temperature conditions < 30 K, below the β-N_2 transition.

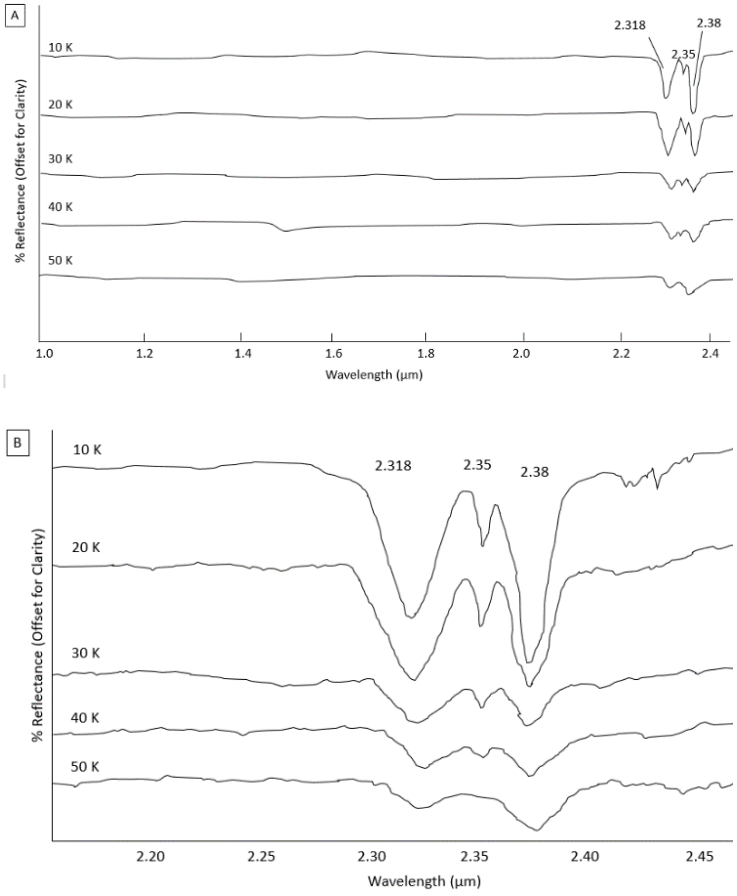

Figure 3: A) Carbon monoxide CO NIR spectra (1.00 – 2.4 μm) showing the dominant 2.35 μm and accompanying 2.318 and 2.38 μm bands in the temperature range 10 – 50 K. **B)** Close up of the pure CO spectral bands from 2.20 – 2.45 μm.

Here, the spectra of CO:N_2 in varying molar concentrations are compared with different temperature conditions (20 - 40 K). It should be noted that at 50 K, ice samples began to sublimate and were no longer in crystalline solid form to obtain a proper spectrum reading.

Figure 4 displays varying molar ratios of CO:N_2 at 20 K. The 1.88 µm band is observed (box A), but only within molar concentrations of 10 – 80 mol% CO. The combination CO:N_2 band at 2.239 µm (box B) is observed at molar concentrations of CO > 50 mol%. The 2.35 µm CO band (box C) with accompanying 2.318 and 2.38 µm bands shows an interesting variability where the central 2.35 µm band is prominent < 30 mol% CO. The 2.318 and 2.38 µm bands appear at relatively increased molar ratios of CO, though interesting to note that the 2.318 µm band is not as prominent in mixture as it was with pure CO ice samples. We observe the 2.337 µm CO band (Figure 4B) at ≥ 50 mol% CO. The 2.405 µm band (Figure 4A box D) is also observed at all molar concentrations of CO.

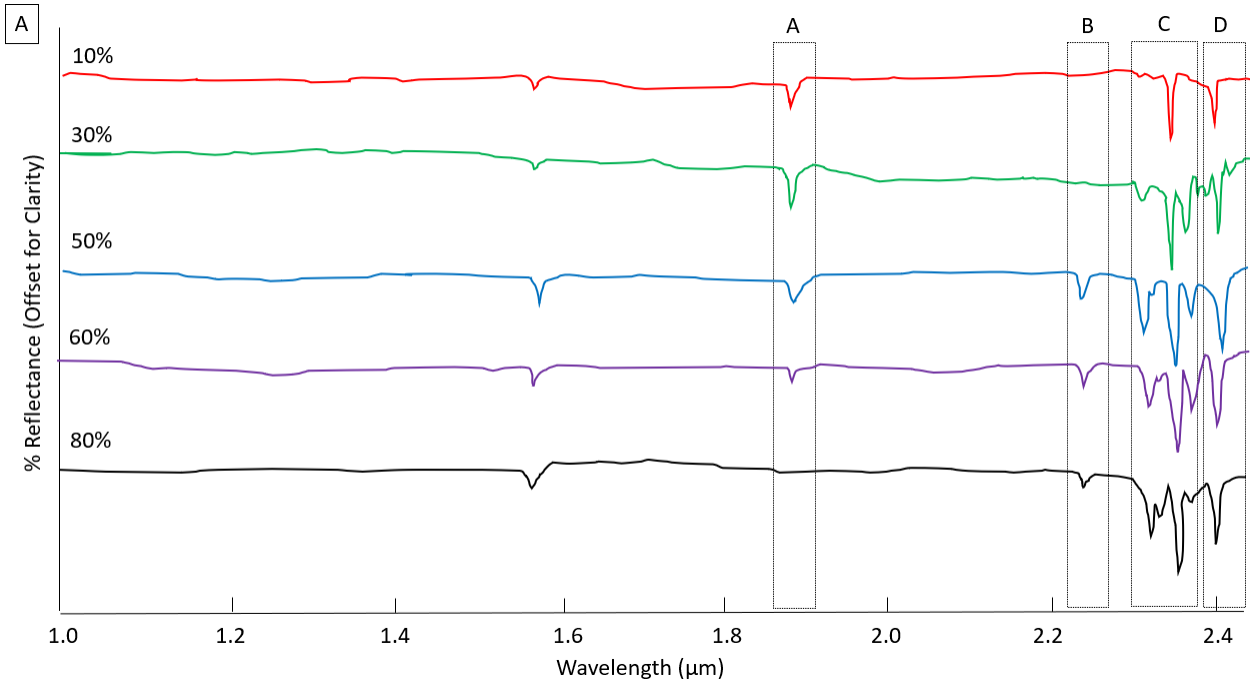

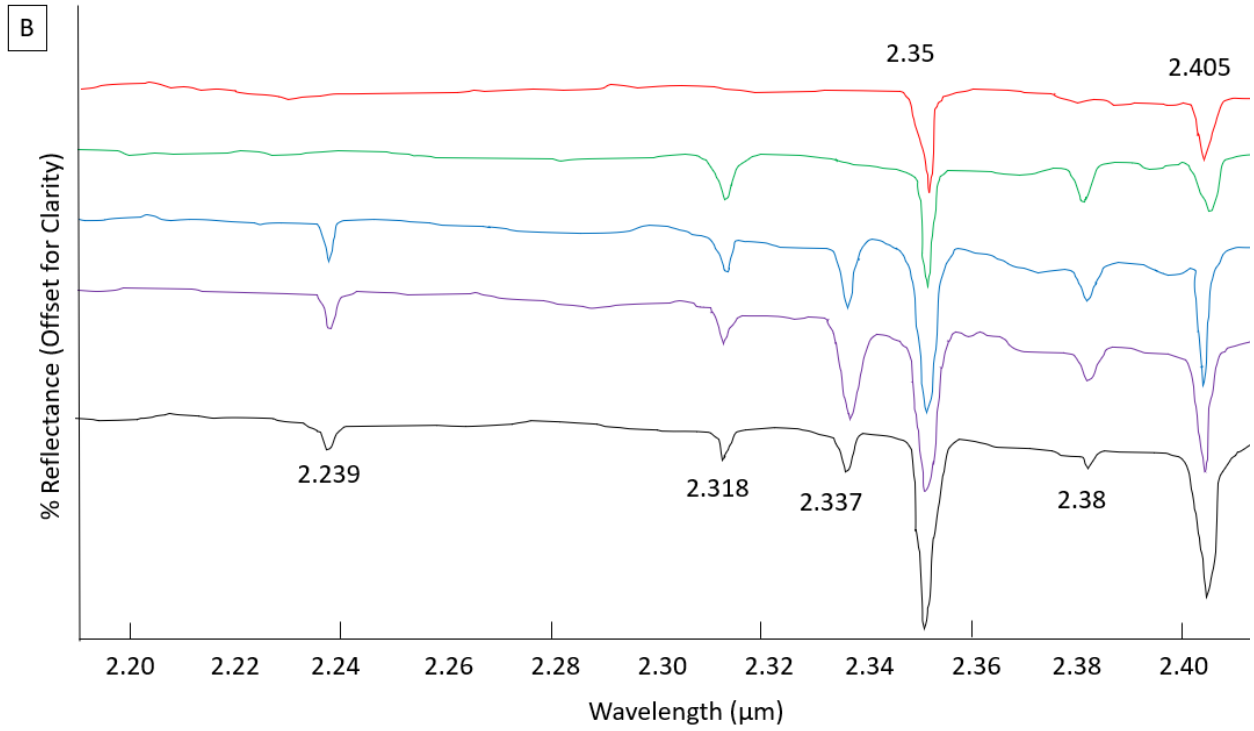

Figure 4: A) NIR spectral observations at 20 K over a range of N_2-CO molar concentrations (in CO mol %). Specific spectral bands are indicated for convenience: A) 1.88 μm; B) 2.239 μm; C) 2.318 – 2.38 μm; D) 2.405 μm. **B)** Close-up of boxes B-D from (**A**) to identify notable CO spectral bands.

When comparing the same molar concentrations at 30 K (Figure 5), the 1.88 μm band is observed again within the 10 – 60 mol% CO range (Figure 5 box A). The combination band at 2.239 μm is observed at CO molar concentrations 10 – 80 mol%, being weaker at smaller CO molar concentrations (box B). The central 2.35 μm CO band is observed in all the ratios at 30 K, with the accompanying 2.318, 2.337, and 2.38 μm bands at ≥ 50 mol% CO (box C). In Figure 5 (box D), the 2.405 μm band also remains to be detected at all molar concentrations of CO.

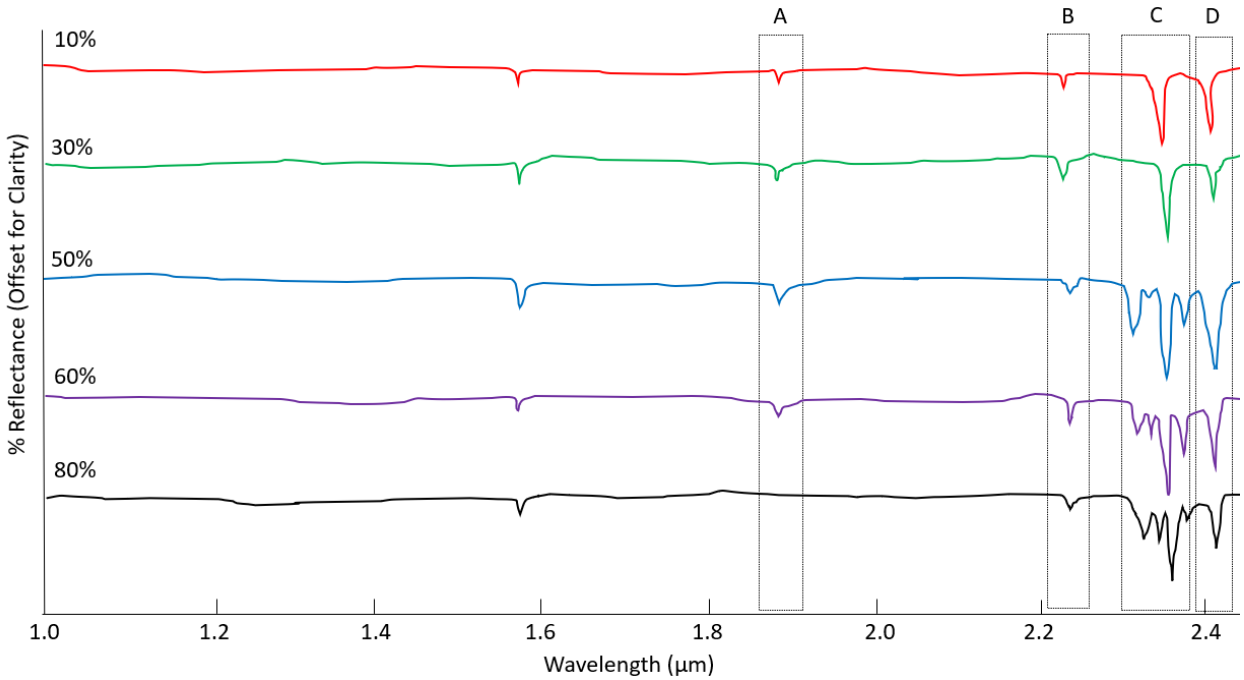

Figure 5: NIR spectral observations at 30 K over a range of N_2-CO molar concentrations (in CO mol %). Specific spectral bands are indicated for convenience: A) 1.88 μm; B) 2.239 μm; C) 2.318 – 2.38 μm; D) 2.405 μm.

At 40 K (Figure 6), the 1.88 μm band is no longer observed (box A) at any CO:N_2 molar ratio. The 2.239 and 2.405 μm bands are observed at concentrations ≥ 50 mol% CO (box B, D). The 2.35 μm CO band is present at all molar ratios (box C), though noticeably more prominent at higher concentrations ≥ 50 mol% CO. The accompanying 2.318, 2.337, and 2.38 μm CO bands (box C) are present at lower concentrations of CO ≤ 50 mol%.

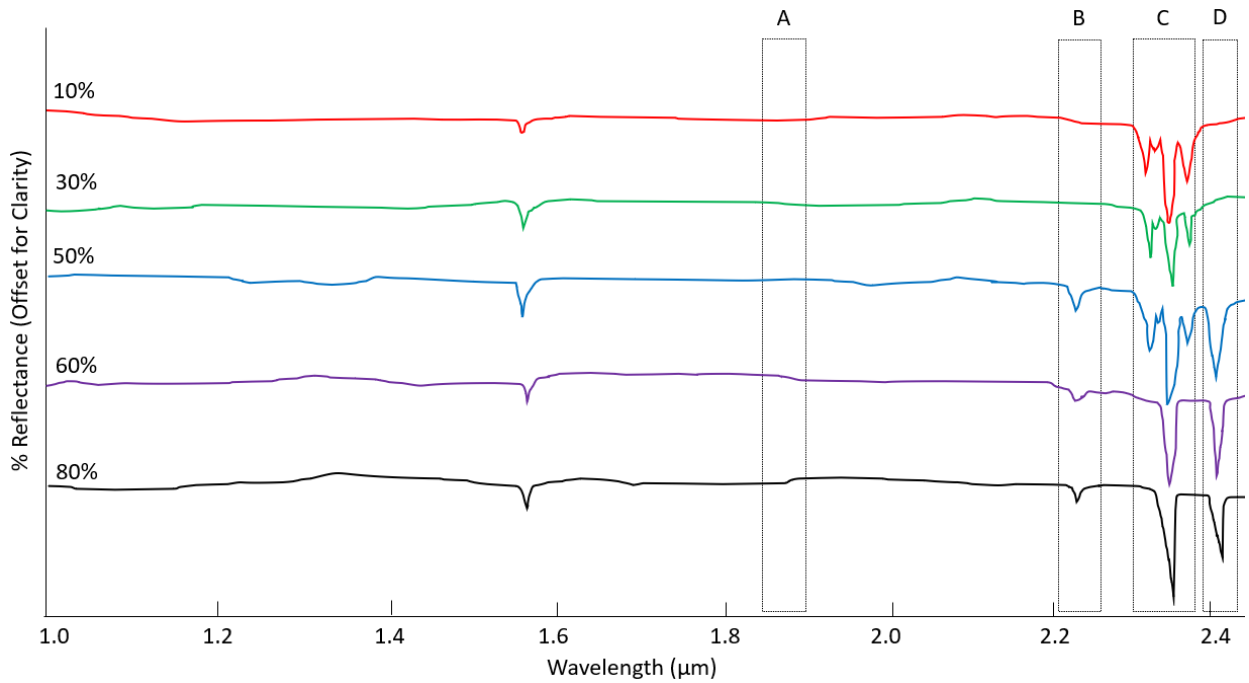

Figure 6: NIR spectral observations at 40 K over a range of N_2-CO molar concentrations (in CO mol %). Specific spectral bands are indicated for convenience: A) 1.88 μm; B) 2.239 μm; C) 2.318 – 2.38 μm; D) 2.405 μm.

Ice samples analyzed using the camera optics system installed in the Pluto Simulation Chamber revealed fracture patterns on the ice sample surface after deposition. These fractures only appear for molar ratios ≤ 30 mol% CO and temperature conditions ≤ 20 K. We have taken spectra at 15 K to investigate the NIR behavior in this low CO ratio, low temperature regime. From Figure 7, the 2.35 μm band is dominant with 10 and 15 mol% CO, unobservable at 20 mol%, instead showing the 2.318 and 2.38 μm CO bands, then reappearing at 30 mol% CO. It is interesting to note that the 2.405 μm band is not present at these conditions compared to the 50 mol% CO spectrum (Figure 7).

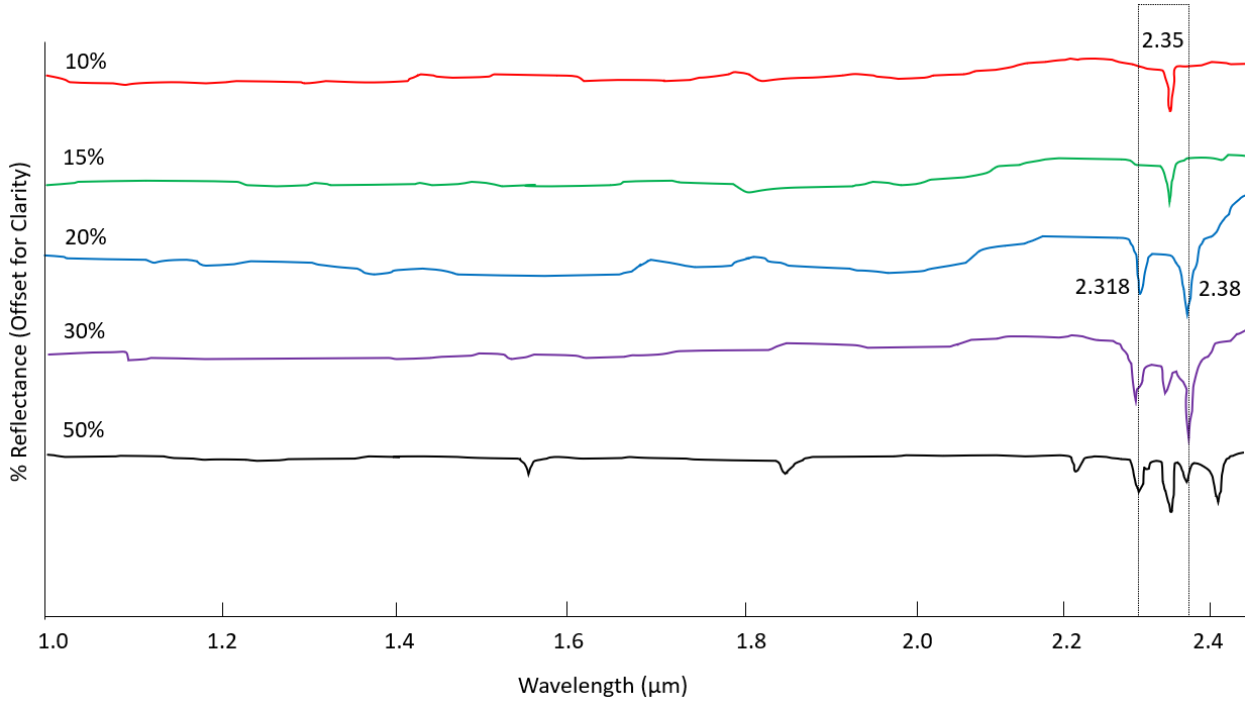

Figure 7: NIR spectral observations at 15 K over a range of N_2-CO molar concentrations (in CO mol %). Dotted lines indicate alignment of 2.318 and 2.38 µm CO bands. The black (bottom) spectrum shown is 50 mol% CO at 20 K for comparison.

Using images from the camera system (Figure 8), we determined a simple fracture intensity variable at different ratios of CO-N_2 at 15 K. The area of the ice sample measured is 25 cm^2. Using the equation I = F/A, where *F* is the number of fractures in a given area (*A*) to solve for the fracture intensity (*I*), plotted in Figure 9, where it is observed that *I* increases at conditions < 15 mol% CO, levels off between 15 – 30 mol%, then the fractures are not observed at ratios > 30 mol% CO.

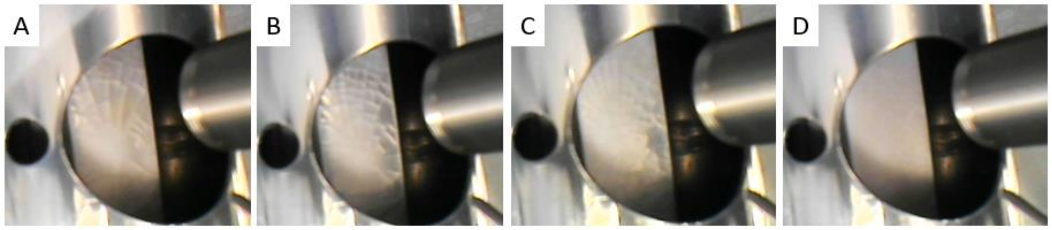

Figure 8: Visuals of the condensed N_2:CO ice samples at 15 K to show the varying degrees of micro-fracturing effect on the surface of the sample at different ratios. A) 10 mol% CO; B) 20 mol% CO; C) 30 mol% CO; D) 50 mol% CO (no cracks visible).

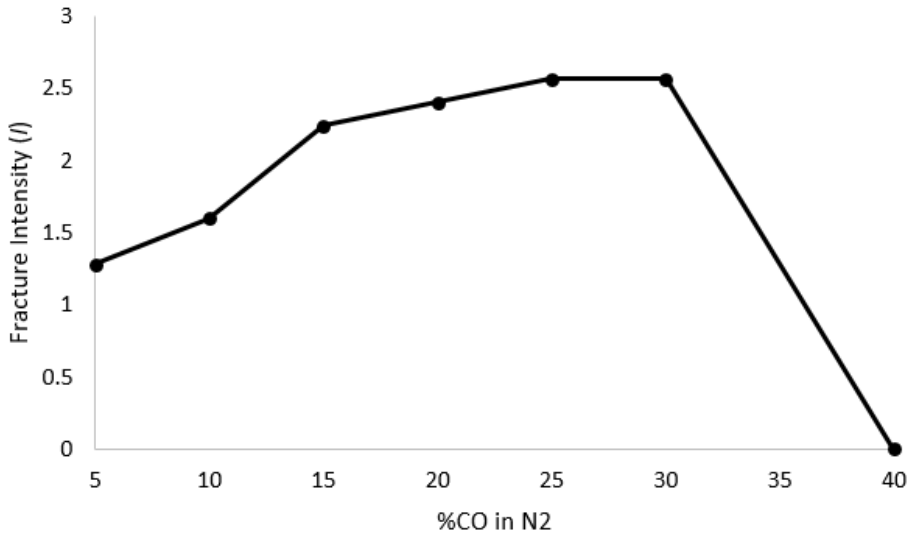

Figure 9: Fracture intensity (*I*) across different molar concentrations of CO in N_2. Note that the number of fractures plateau approaching 30 mol% until fractures disappear entirely at higher concentrations of CO.

4.4 Discussion

We have observed in the NIR wavelength relative band appearances and positions of CO in N_2 differ from those of pure CO and N_2 ices, and analysis of binary-mixture spectral bands. We note that the 1.577, 1.61, 2.337, and 2.405 μm bands were not present in the pure CO spectra we obtained due to these bands probably being too spectrally weak for our instrumentation resolution.

Differences in the band positions in the CO - N_2 solid mixtures can be compared to previous experimental spectral studies of these constituents (Angwin and Wassermann 1966; Quirico and Schmitt 1997 a, b; Vetter et al. 2007; Tegler et al. 2019), although our methodology investigates a larger range of molar concentrations and relatively lower temperature and pressure conditions than most previous work. Vetter et al. (2007) experiments have observed similar band changes, including the pure N_2 vibrational mode at 2.137 μm and the 2.337 μm CO band at certain temperatures (≥ 30 K) and molar ratios. However, there were no investigations of the 2.337 μm CO band at lower CO molar ratios (< 30 mol%) at ≤ 20 K temperatures (where we observe our

unidentified polycrystalline phase). Their methodology included a different condensation technique (e.g., liquefied sample from the gas phase and slower cooling) and growth of larger polycrystalline samples (which gives an uncertainty in the homogeneity of the binary ice growth). This difference in techniques is crucial to comparing spectral analyses and crystalline behavior of an N_2-CO ice sample.

The 2.35 μm CO band changing depth (and thus spectral strength in detection) depends on the molar ratio concentration in the ice sample, as observed by Vetter et al. (2007), and temperature conditions gives us several insights to the dynamics of CO in N_2 compounds, namely (i) lower temperatures (< 30 K) have increased NIR signal strength of the 2.35 μm CO band, even though the molar concentration of CO is < 10 mol%; and (ii) at even lower temperatures < 20 K, the 2.35 μm CO band is observed to disappear and reappear at molar concentrations < 30 mol% CO. The observation of the 1.577 μm CO band being only observed in mixtures and not pure CO relates to the spectral relationships of CO diluted in N_2. We note that the 1.61 μm CO band was not detected in the pure or binary samples, however Qurico and Schmitt (1997b) labeled this CO band vvw (very-very-weak) strength and may not be clearly identified in the resolution of our instrumentation.

The 2.318 and 2.38 μm CO bands display several interesting spectral morphologies, indicating possible phase changes in the CO-N_2 matrix. The first indication of the 2.318 and 2.38 μm band changes occur when these accompanying CO bands are observed at 15 K at lower CO molar concentrations ≤ 30 mol%, then observed at higher molar concentrations to temperatures ≥ 20 K. These spectral bands are observed mainly in the cubic CO-N_2 phase, then shifts again ≥ 40 K, where 2.318 and 2.38 μm are observed at lower concentrations of CO again, outlining the hcp + cubic lens (Figure 10). The 2.337 μm CO band follows similar displays as the 2.318 μm band at

molar concentrations ≥ 50 mol% CO, though it is not observed at the polycrystalline regime at lower temperatures (Figure 11). This could be due to where the 2.337 μm band is dependent on the 2.318 and 2.38 μm bands present, especially at temperatures ~ 40 K, where these more dominant CO bands outline the hcp + cubic lens phase and increased molar concentrations of CO does not have the 2.318 and 2.38 μm bands (thus no appearance of the 2.337 μm band). At ~ 40 K is also the change in the α-β N_2 crystallinity, which also changes the detection (or lacking the observance of) the 1.88 μm band, as displayed in Figure 10.

Although the 2.35 and 2.239 μm bands have been previously identified by Tegler et al. (2019), noting some saturation effects at lower molar concentrations of CO (< 4 mol%) and at comparatively lower spectral resolution (0.6 cm^{-1}), their experimental regime did not reach temperatures < 30 K. We were able to verify the observation of the 2.239 μm at 30 K. However, only at lower temperatures ≤ 30 K and slightly higher molar concentrations of CO would there be detection of several CO-N_2 bands and no observance of the 2.239 μm band. Note that this spectral band was not identified within the proposed polycrystalline regime, furthering the argument that a previously unidentified phase is present in this section of the N_2-CO binary phase diagram.

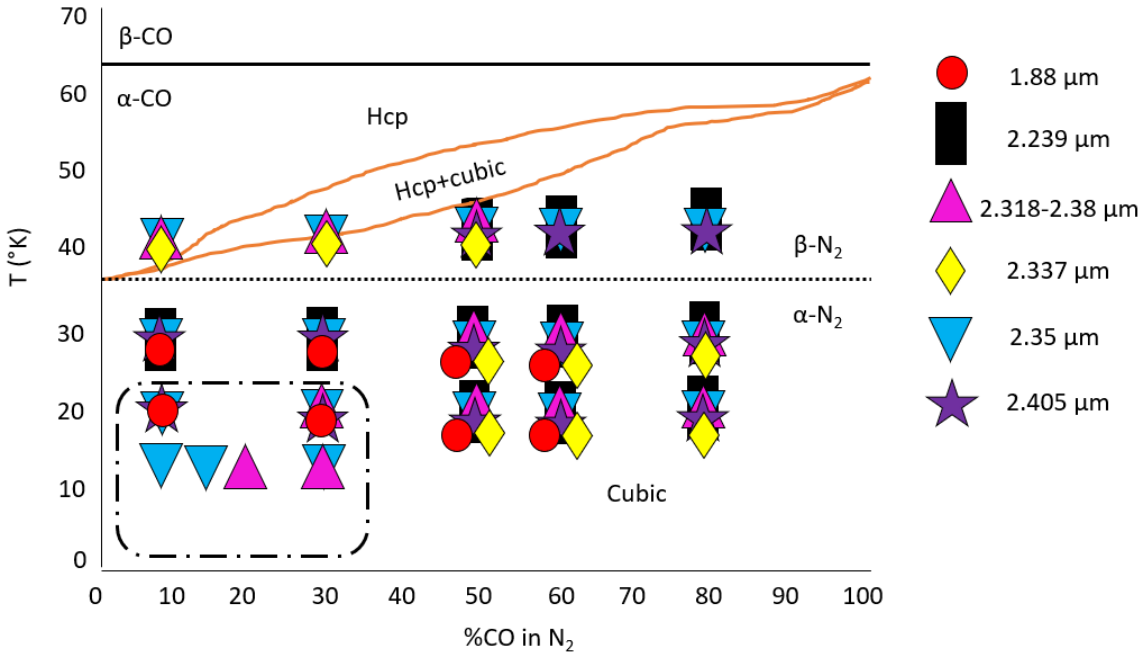

Figure 10: Data points indicating the presence of certain CO and N_2 spectral bands overlain on the CO:N_2 binary phase diagram developed by Angwin and Wassermann (1966). The presence of the 2.239 and 2.405 µm bands verify the cubic phase, and not present in the hcp + cubic or hcp regimes. The dot-dash box indicates the polycrystalline phase as observed by the detection or molar concentration shifts of certain CO:N_2 bands.

With the observation of fractures also in this low temperature - low molar concentration regime, it can be suspected that a polycrystalline effect is forming, possibly due to a reaction to the condensation of a polar (CO) and non-polar (N_2) ice. Fractures were not observed from Quirico and Schmitt[16] or Tegler et al. (2019) due to their experimental setup of CO molar concentrations being < 4.2 mol%, which according to our study would have a stronger presence of the 2.35 µm CO band (as we verify in our study), but the observed shifting of the 2.318 - 2.38 µm CO and 1.88 µm N_2:CO bands occur at relatively increased CO molar concentrations. N_2 and CO have similar molecular size, though N_2 is more porous (Mikhal'chenko et al. 1972) and denser (Bar-Cohen et al. 2016) at temperatures < 60 K (1,022 kg/m^3) whereas CO at ~65 K is 929 kg/m^3. We propose that the crystallinity of the CO within a porous N_2 matrix is forming differentiating crystalline orientations (e.g., polycrystalline), forming microfractures in the ice sample, with CO (as being

less dense than N_2 with a different molecular polarity) concentrating at the top of the ice matrix (Figure 11). As the molar concentration and temperature increase, the crystallinity of CO and N_2 stabilize into a more uniform cubic orientation.

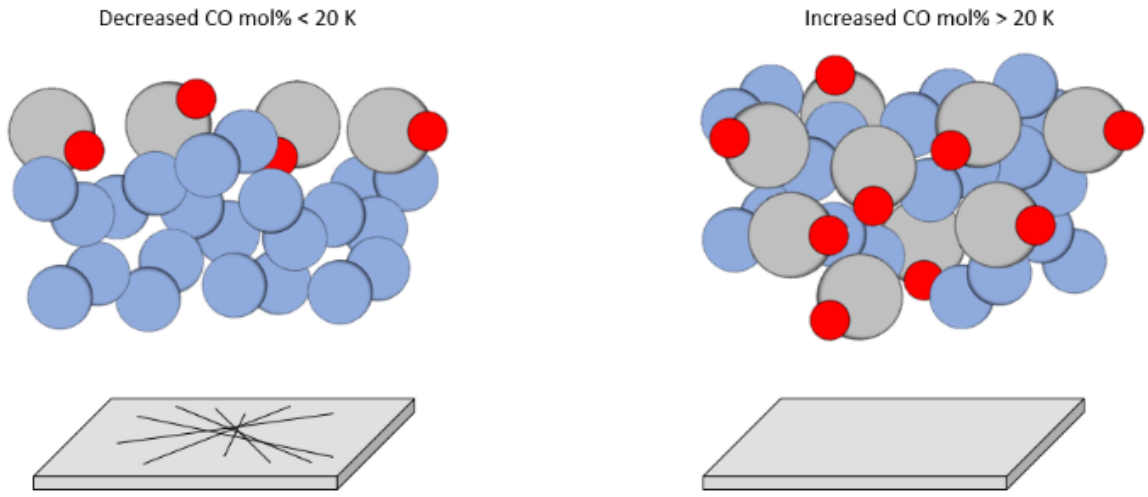

Figure 11: Illustration of the proposed polycrystalline phase at conditions < 20 K and higher molar concentrations of N_2 where CO molecules condense at the top of the ice sample. When CO concentration is increased, the crystallinity of the sample becomes more stable (and less porous), thus diminishing the micro-fracturing effect.

The New Horizons LEISA instrument detected strong CO signatures mainly in the Sputnik Planitia and Voyager Terra. On a global scale, the extent of CO distribution appears well correlated with N_2 abundance (Schmitt et al. 2017), with some latitudinal differences in the northwestern close-encounter hemisphere. Strong CO signatures are located mainly within the 40° - 60° latitudes, whereas N_2 abundance in this same region is within 20° - 40°. The boundary between these latitudes marks an area of rougher, polygonal terrain to the north (possibly CO as a top layer). It should be noted that band depth determination of CO (at 1.577 μm) from LEISA was modified to be readable against stronger CH_4 signatures (Grundy et al. 2014; Grundy et al. 2016; Schmitt et

al. 2017). That is, CH_4 is also strong at the 2.32-2.37 μm range, so the 2.35 μm CO dominant band might otherwise be saturated from the CH_4 spectral signature from LEISA.

The observation of the polycrystalline phase brings about interesting geomorphological and seasonal implications (Hansen and Paige 1996; Grundy et al. 2016). That is, if this phase is only with higher concentrations of N_2 with CO and lower temperatures than Pluto's average surface temperature of 44 K, it could be possible for this phase to be present in N_2-rich craters at or near CO concentrated latitudes (e.g., Venera Terra) with potential permanent shadow regions having accumulated CO at the bottom. This could also have implications of micro-fracturing at the sublimation pitting on the Sputnik Planitia basin, where trapped (with relatively low) concentrations of CO in the N_2-dominant basin could be mineralogically unstable within these deep sublimation pits. For example, Venera Terra at 48°N latitude has a latitudinal overlap of N_2 and CO observed by LEISA. According to Earle et al. (2017), this area is estimated with an albedo of 0.3 and a temperature range of 15 – 60 K within the current Pluto orbit (Figure 12). In contrast, the N_2-CO rich areas of Sputnik Planitia have an albedo of 0.6 and have a much narrower temperature range of 27 – 38 K. This temperature range then implies a relatively larger variability of N_2-CO phases at the more solid lithospheric areas like Venera Terra (including the polycrystalline phase) compared to the Sputnik Planitia slurry, which would have a dominant cubic CO-N_2 crystalline.

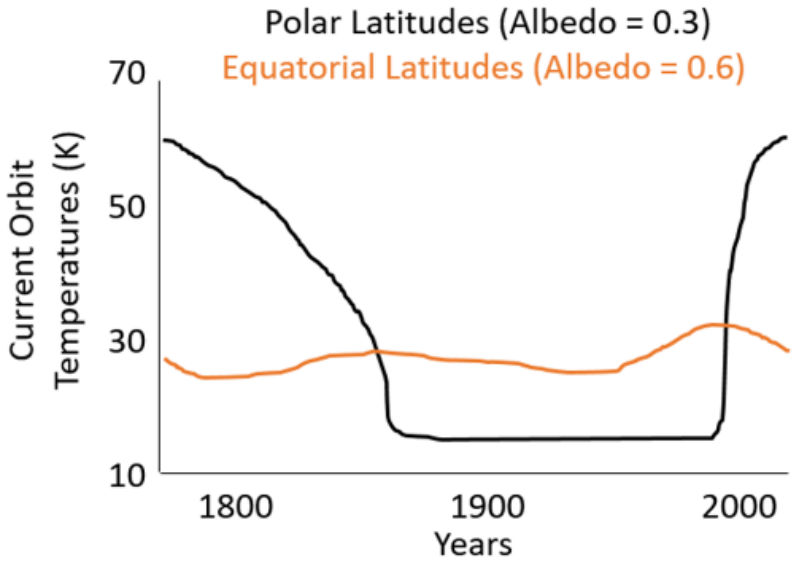

Figure 12: Local equilibrium temperatures for polar latitudes (30°N – 90°N), and equatorial/Sputnik Planitia latitudes where greater areas of CO-N_2 mixtures are detected from LEISA. Adapted from Earle et al. (2017).

While the CO crystallinity could be affected by the molar ratio of N_2 in the matrix into which it is frozen, it is hoped that the binary systematic changes recorded here will help New Horizons data analysts ascertain whether CO is pure or intimately mixed with N_2 on the surface of Pluto, or other icy bodies in the outer solar system. The differences in CO band behavior depending on N_2 molar concentrations and temperature conditions should allow one to recognize the conditions based on band positions or observing of specific bands present in the spectra.

4.5 Conclusions

The Pluto Simulation Chamber allows us to study relevant low temperature and pressure conditions to that of Pluto. Several types of experiments were conducted: pure N_2 and CO, various ratios of N_2 and CO binary mixtures, and observations of a proposed polycrystalline phase region. Through analysis of the NIR spectra using an FTIR, we report that lack of certain CO spectral bands confirmed the hcp + cubic phase transition at ~40K. We identify a previously unknown

phase change with the 2.318 and 2.38 μm CO bands within the specific conditions of ≤ 20 K and ≤ 30 mol% CO, including a physical fractured pattern of the ice sample, which lack the 2.239 and 2.337 μm bands indicative of the cubic phase. We propose this section of the phase diagram to be a polycrystalline structure between N_2 and CO. The observation of varying conditions (and thus probably phases) of N_2 and CO on Pluto (i.e., Sputnik Planitia versus Venera Terra) gives rise to hypotheses of the mixture capabilities and latitudinal limits of these ices, more specifically if the polycrystalline structure can be found in deep, shadowed craters or sublimation pits (where temperatures are considerably lower than the average surface temperature) and where there is a stronger presence of N_2 in mixture with CO. This previously unknown polycrystalline phase gives insight to the mixture dynamics of such simple compounds at low temperature conditions and mineralogical effects implied on Pluto and other KBOs.

4.6 References

Angwin, M. and Wassermann, J. (1966) Nitrogen-Carbon monoxide phase diagram, Journal of Chemical Physics, 44 (1), p417-418. 10.1063/1.1726486.

Bar-Cohen, Y., ed. (2016) Low Temperature Materials and Mechanisms. CRC Press.

Caracas, R. (2013) First-Principles Calculations of Physical Properties of Planetary Ices. In: M. S. Gudipati, J. Castillo-Rogez, (Eds.), The Science of Solar System Ices. Springer New York, New York, NY, pp. 149-169.

De Bergh, C., et al. (2008) Laboratory data on ices, refractory carbonaceous materials, and minerals relevant to transneptunian objects and Centaurs. In: The Solar System Beyond Neptune, pp. 483-506.

Dubost, H. (1976) Infrared absorption spectra of carbon monoxide in rare gas matrices. Chem. Phys., 12 (2), 139-151. https://doi.org/10.1016/0301-0104(76)87051-6

Earle, A., Binzel, R., Young, L., Stern, S., Ennico, K., Grundy, W., Olkin, C., Weaver, H., New Horizons Geology and Geophysics Imaging Team, 2017. Long-term surface temperature modeling of Pluto. Icarus, 287, 37-46. https://doi.org/10.1016/j.icarus.2016.09.036

Fink, U., Sill, G. (1982) The infrared spectral properties of frozen volatiles. In Comets (L. L. Wilkening, ed.), pp. 164–202. Univ. of Arizona, Tucson.

Giauque, W., Clayton, J. (1933) The heat capacity and entropy of nitrogen. Heat of vaporization. Vapor pressures of solid and liquid. The reaction ½ N2 + ½ O2 = NO from spectroscopic data. J. Am. Chem. Soc., 55 (12), 4875-4889. 10.1021/ja01339a024.

Gladstone, G. R., et al. (2016) The atmosphere of Pluto as observed by New Horizons. Science. 351(6279). 10.1126/science.aad8866

Greaves, J. S., Helling, C., Friberg, P. (2011) Discovery of carbon monoxide in the upper atmosphere of Pluto. Monthly Notices of the Royal Astronomical Society: Letters. 414(1), L36-L40. https://doi.org/10.1111/j.1745-3933.2011.01052.x

Green, J., Brown, R., Cruikshank, D., Anicich, V. (1991) The absorption coefficient of nitrogen with application to Triton (abstract). Bull. Am. Astron. Soc., 23, 1208.

Grundy, W. M., Schmitt, B., Quirico, E. (1993) The Temperature-Dependent Spectra of α and β Nitrogen Ice with Application to Triton. Icarus. 105(1), 254-258. https://doi.org/10.1006/icar.1993.1122

Grundy, W. M., Buie, M. W. (2001) Distribution and evolution of CH4, N2, and CO ices on Pluto's surface: 1995 to 1998. Icarus. 153(2), 248-263. https://doi.org/10.1006/icar.2001.6684

Grundy, W.M. , Olkin, C.B. , Young, L.A. , Holler, B.J. (2014) Near-infrared spectral monitoring of Pluto’s ices: recent decline of CO and N2 ice absorptions. Icarus 235, 220–224. https://doi.org/10.1016/j.icarus.2014.02.025

Grundy, W. M., et al. (2016) Surface compositions across Pluto and Charon. Science. 351(6279), aad9189. 10.1126/science.aad9189

Hansen, C. J., Paige, D. A. (1996) Seasonal Nitrogen Cycles on Pluto. Icarus. 120(2), 247-265. https://doi.org/10.1006/icar.1996.0049

He, C., et al. (2017) Carbon monoxide affecting planetary atmospheric chemistry. Astrophys. Journ. Letters, 841:L31. https://doi.org/10.3847/2041-8213/aa74cc

Lellouch, E., Gurwell, M., Butler, B. et al. (2017) Detection of CO and HCN in Pluto’s atmosphere with ALMA. Icarus, 286, 289-307. https://doi.org/10.1016/j.icarus.2016.10.013

McMahon, Z. M. (2016). Development of a Pluto Chamber for Surface Simulations. Theses and Dissertations Retrieved from https://scholarworks.uark.edu/etd/1812

Merlin, F., (2010) Chemical and physical properties of the variegated Pluto and Charon surfaces. Icarus 210, 930–943. https://doi.org/10.1016/j.icarus.2010.07.028

Mikhal'chenko, R., Getmanets, V., Arkhipov, V. (1972) Peculiarities of heat transfer in porous solid nitrogen. Journal of engineering physics, 23 (3), 1075-1081. https://doi.org/10.1007/BF00832213

Nelander, B. (1976) On the infrared spectrum of a carbon dioxide containing nitrogen matrix. Chem. Phys. Lett., 42, 187–189. https://doi.org/10.1016/0009-2614(76)80582-9

Neveu, M., Desch, S., Shock, E., Glein, C. (2015) Prerequisites for explosive cryovolcanism on dwarf planet-class Kuiper belt objects. Icarus, 246, 48-64. http://dx.doi.org/10.1016/j.icarus.2014.03.043

Pavlenko, Y., Jones, H. (2002) Carbon monoxide bands in M dwarfs. A&A, 396 (3), 967-975. https://doi.org/10.1051/0004-6361:20021454

Plyler, E., Allen, H., Tidwell, E. (1958) Emission spectrum of carbon monoxide from 2.3 to 2.5 microns. Journal of Research of the National Bureau of Standards, 61 (1), 2883.

Prokvatilov, A., Yantsevich, L., (1983) X-ray investigation of the equilibrium phase diagram of CH4-N2 solid mixtures. Sov. J. Low Temp. Phys., 9(2), 94-98.

Protopapa, S., et al. (2017) Pluto's global surface composition through pixel-by-pixel Hapke modeling of New Horizons Ralph/LEISA data, Icarus, 287, 218-228. https://doi.org/10.1016/j.icarus.2016.11.028

Quirico, E., Schmitt, B. (1997a) A spectroscopic study of CO diluted in N2 ice: Applications for Triton and Pluto. Icarus, 128, 181–188. https://doi.org/10.1006/icar.1997.5710

Quirico, E., Schmitt, B. (1997b) Near-infrared spectroscopy of simple hydrocarbons and carbon oxides diluted in solid N2 and as pure ices: Implications for Triton and Pluto. Icarus, 127, 354–378. https://doi.org/10.1006/icar.1996.5663

Schmitt B., Oehler A., Calvier R., Haschberger P., Lindermeier E. (1990) The near infrared absorption features of solid nitrogen and methane on Triton (abstract). Bull. Am. Astron. Soc., 22, 1121

Schmitt, B., et al. (2017) Physical state and distribution of materials at the surface of Pluto from New Horizons LEISA imaging spectrometer, Icarus, 287, 229-260. https://doi.org/10.1016/j.icarus.2016.12.025

Stern, S. A., et al. (2015) The Pluto system: Initial results from its exploration by New Horizons. Science. 350(6258), aad1815. 10.1126/science.aad1815

Tegler, S., et al. (2019) A new two-molecule combination band as a diagnostic of carbon monoxide diluted in nitrogen ice on Triton. Astronomical Journal, 158 (1), 17. https://doi.org/10.3847/1538-3881/ab199f

Tryka, K., Brown, R., Anicich, V. (1995) Near-infrared absorption coefficients of solid nitrogen as a function of temperature. Icarus, 116, 409–414. https://doi.org/10.1006/icar.1995.1133

Vetter, M., Jodl, J. Brodyanski, A. (2007) From optical spectra to phase diagrams-the binary mixture N2 –CO. Low Temp. Phys. 33, 1052. https://doi.org/10.1063/1.2747091

Xia, C., McKellar, A. (2000) Infrared spectrum of the CO-N2 van der Waals complex: Assignments for CO-para N2 and observation of a bending state for CO-ortho N2. J. Chem. Phys., 113 (2), p 525. https://doi.org/10.1063/1.481912

Young, L. A., Elliot, J. L., Tokunaga, A., de Bergh, C., Owen, T. (1997) Detection of gaseous methane on Pluto. Icarus. 127(1), 258-262. https://doi.org/10.1006/icar.1997.5709

Zalucha, A., Gulbis, A. (2012) Comparison of a simple 2-D Pluto general circulation model with stellar occultation light curves and implications for atmospheric circulation. Journal of Geophysical Research, 117, E05002. https://doi.org/10.1029/2011JE003957

Chapter 5

Binary phase diagram of CH_4-CO from laboratory experiments at 20 – 50 K: Implications for Pluto

C. J. Ahrens[1], V. F. Chevrier[1]

[1]University of Arkansas, Center for Space and Planetary Sciences, Fayetteville, AR 72701

5.1 Abstract

Methane (CH_4) and carbon monoxide (CO) are present at the surface of Pluto and other Kuiper Belt Objects (KBOs). Both CH_4 and CO, in previous experimental spectral investigations, have shown to have varying crystallinity, thus different spectral band behaviors, depending on temperature and molar concentration in the ice matrix present. However, the binary phase diagram of CH_4-CO is unknown. Here we show that the spectral bands of CH_4 and CO vary depending on the molar concentration of CO present in temperatures relevant to Pluto's surface 20 – 50 K. We found in experimentally simulated Pluto conditions using Fourier Transform Infrared (FTIR) in the near-infrared wavelengths (1 – 2.4 μm) that there are five distinct phase regimes, each displaying certain spectral bands, especially the 1.243 μm CH_4 band, which is only present in the β-CH_4 crystalline phase at molar concentrations of < 60 mol% CO. Furthermore, we found that molar ratios ≥ 70 mol% display the 2.32 μm CH_4 and 2.38 μm CO bands at all recorded temperature conditions, which we have labeled as a separate phase (Phase III). Our results demonstrate how the crystallinity of the CH_4 or CO are likely to influence the presence of certain spectral bands. We anticipate our developed binary phase diagram would not only define the spectral behavior of a previously-unknown binary mixture in the near-infrared wavelengths, but

also characterize the level of impurity of CO and CH_4 relevant for the surface of Pluto and KBOs based on retrieved mission spectral data.

5.2 Introduction

Methane (CH_4) and carbon monoxide (CO) are two abundant ices on the surface of Pluto, as observed by the New Horizons Linear Etalon Imaging Spectral Array (LEISA) (Grundy and Buie 2001; Merlin 2010; Stern et al. 2015; Grundy et al. 2016; Schmitt et al. 2017; Protopapa et al. 2017), and found on other outer solar system objects, such as Triton and comets (Schmitt et al. 1990; de Bergh et al. 2008 Tegler et al. 2019). On Pluto, specifically, CH_4 and CO are geographically variable, both as separate and mixed concentrations, and could lead to significant crystalline changes depending on Pluto's orbit (e.g., seasonal temperature changes). The temperature range on the surface of Pluto is at 40 – 45 K, this range is in the solid stability field of both CH_4 and CO, with surface pressures at 10 - 25 microbar (Zalucha and Gulbis 2012; Stern et al. 2015). However, extreme seasonal conditions (down to 20 K) is possible in past and current processes (Grundy et al. 1993; Young et al. 1997; Caracas 2013; Grundy et al. 2014; Gladstone et al. 2016). This 20 – 50 K temperature range gives rise to variations in the crystalline state, especially the α-β phase transitions of CH_4 at 21 K (Grundy et al. 1993; Quirico and Schmitt 1997); and α-β CO at 61.6 K (Giauque and Clayton 1933; Angwin and Wassermann 1966; Calvani et al. 1992; Quirico and Schmitt 1997; Vetter et al. 2007).

Experimental near-IR (NIR) spectra of solid CH_4 and CO have been previously studied, either as: pure samples (Calvani et al. 1992; Vetter et al. 2007); in mixture with other constituents (e.g., N_2, H_2O) (Prokvatilov and Yantsevich 1983; Tryka et al. 1995; Palumbo 1997); or irradiation studies in the range 30 K – 80 K (Kim and Kaiser 2012; He et al. 2017).

CO when in mixture with N_2 displays a variety of crystalline orientations (Angwin and Wassermann 1966), depending on the concentration of CO and temperature, and CO spectral bands are sensitive to the phase of solid N_2 in the crystalline matrix (Quirico and Schmitt 1997). We propose that this is the case for CO and CH_4 in that the spectral signatures of these constituents depend on the crystalline orientation of CH_4 and molar concentrations of CO. We therefore chose to focus on a sample of molar ratios over a range of temperatures at an atmospheric pressure of < 25 μbar.

We use FTIR spectroscopy to investigate spectral bands in the NIR (1 – 2.4 μm) wavelength and investigate spectral band variations dependent on molar concentrations and temperature. This work reports the first results of laboratory measurements of CO-CH_4 binary mixtures to create a low-temperature phase diagram.

5.3 Results

Pure CH_4 has numerous NIR bands: 1.16 ($2\nu_1+\nu_2+\nu_4$), 1.33 ($\nu_2+2\nu_3$), 1.66 ($2\nu_3$), 1.72($\nu_2+\nu_3+\nu_4$), 1.79($2\nu_2+2\nu_4$), 1.856 ($\nu_2+3\nu_4$), 2.185 (v2+v3), 2.194 (v2+v3), 2.323 ($\nu_3+\nu_4$) and 2.378 ($\nu_1+\nu_4$) μm (Grundy and Buie 2001; Schmitt et al. 2017). Pure CO has NIR bands at 2.318 (2ν), 2.35 (2ν), and 2.38 (2ν) μm (Plyler et al. 1958; Lellouch et al. 2017; Tegler et al. 2019).

As shown in Figure 1a, the CH_4 bands at 10 K change as temperature increases, namely the shifting (< 0.02 microns) of the 2.323 μm band. Past the 21 K α-β transition, the 2.185 and 2.194 μm bands have disappeared. With increasing temperature, the 2.323 and 2.378 μm bands decrease in spectral strength. The pure CO spectra (Figure 1b) displays the 2.35 μm with accompanying 2.318 and 2.38 μm absorption bands from 10 – 50 K, with the 2.35 μm band shortening with increasing temperatures.

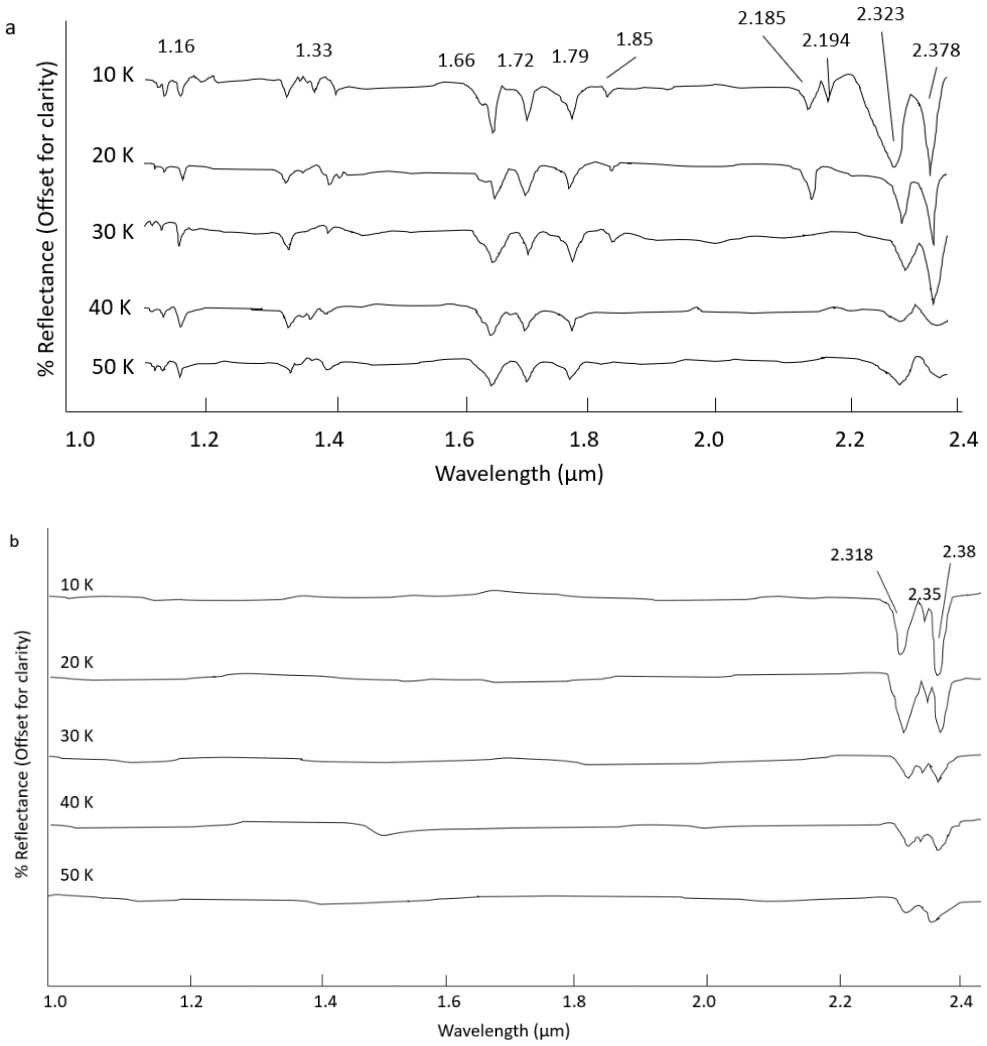

Figure 1: Experimental NIR spectra of pure ice samples. **a.** NIR spectra of CH_4 from 1 – 2.4 μm from 10 – 50 K. **b.** NIR spectra of CO from 1 – 2.4 μm from 10 – 50 K. Spectra is offset for clarity.

Other CH_4 spectral bands that have been detected when in mixture with other compounds (e.g., N_2 or H_2O) are the 1.243 ($\nu_1+4\nu_4$), 1.485 ($\nu_1+3\nu_4$), 1.856 ($\nu_2 + 3\nu_4$), 1.935 ($4\nu_4$), and 2.204 ($\nu_2+\nu_3$) μm bands (Grundy et al. 2016; Calvani et al. 1992). The CO band at 1.577 (3ν) μm also has this trait when in mixture with N_2 (Vetter et al. 2007), which is observed in all retrieved spectra in this study. We specifically investigate the observed changes in the 1.243, 1.935, 2.323, and 2.38 μm bands of the CO-CH_4 binary mixtures.

At 20 K temperatures (Figure 2a), there are no observances with the 1.243 μm CH_4 band. The 1.935 μm CH_4 band is present at 10 – 60 mol% CO. From 30 – 90 mol% CO, both the 2.323 μm CH_4 and 2.38 μm CO bands are detected. The 2.323 μm band shows slight shifting (< 0.2 microns) to longer wavelengths at 70 mol% CO. The 2.38 μm band displays a double mode at smaller molar ratios of CO (< 50 mol%).

When comparing the same molar concentrations at 30 K temperatures (Figure 2b), the 1.243 μm is observed from 10 – 60 mol% CO, same as the 1.935 μm CH_4 band. The 2.323 μm CH_4 band remains detected from 30 – 90 mol% CO, again with a slight shift at > 70 mol% to longer wavelengths. The 2.38 μm CO band is also present from 30 – 90 mol% CO.

At 40 K temperatures (Figure 2c), the 1.243 and 1.935 μm CH_4 bands are detected from 10 – 60 mol% CO. The 2.323 μm band is observed from 30 – 90 mol%, with a widening of the band at ≥ 70 mol%. The 2.38 μm CO band is also at 30 – 90 mol%.

Finally at the 50 K temperature conditions (Figure 2d), both 1.243 and 1.935 μm CH_4 bands are seen from 10 – 60 mol%. This increase in temperature also shows the 2.323 μm CH_4 and 2.38 μm CO bands present at all observed molar ratios. Both bands show a shift (< 0.2 microns) at ≥ 70 mol% CO.

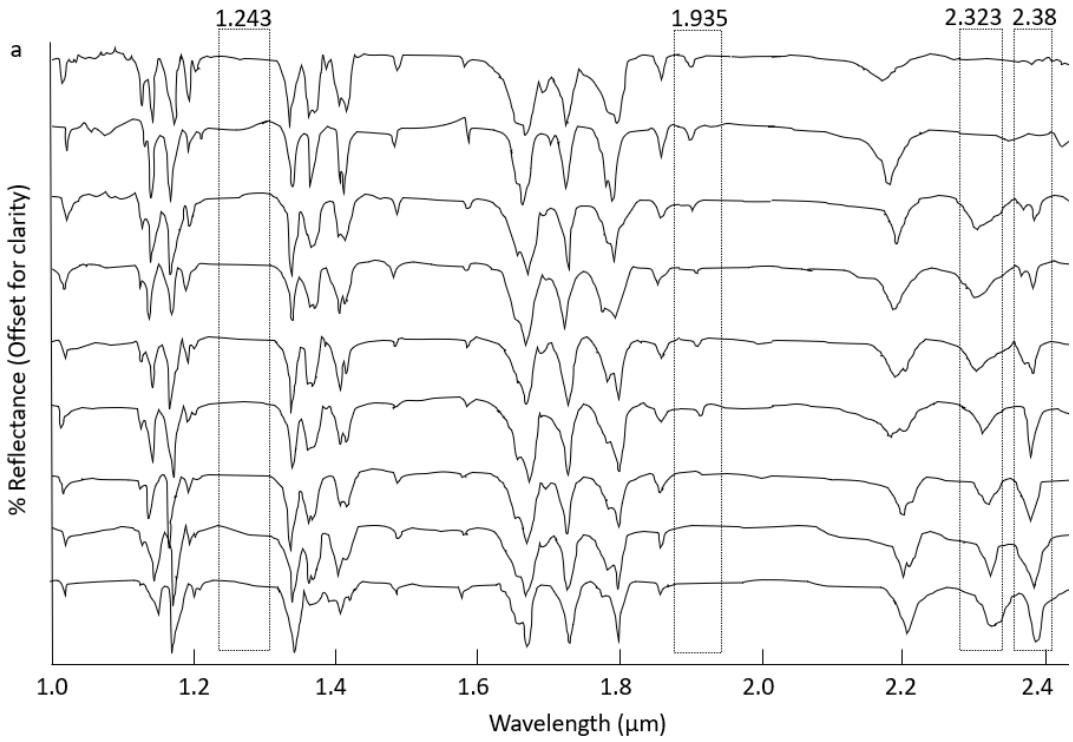
a
1.243
1.935
2.323
2.38
% Reflectance (Offset for clarity)
1.0
1.2
1.4
1.6
1.8
2.0
2.2
2.4
Wavelength (μm)

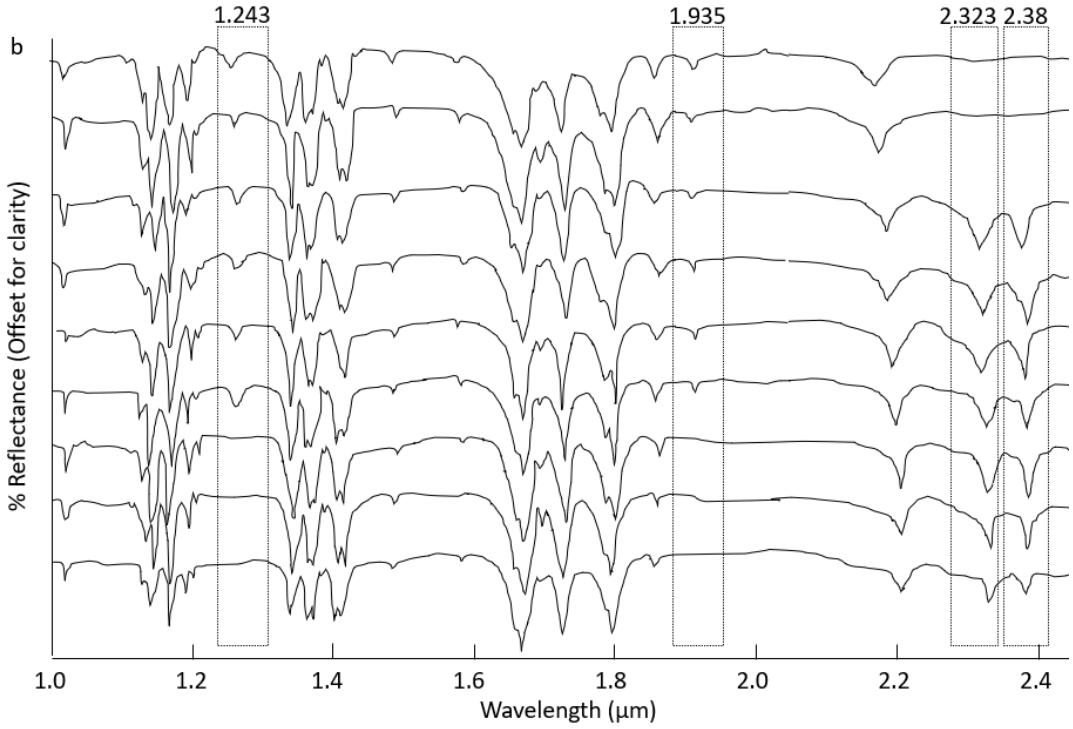
b
1.243
1.935
2.323
2.38
% Reflectance (Offset for clarity)
1.0
1.2
1.4
1.6
1.8
2.0
2.2
2.4
Wavelength (μm)

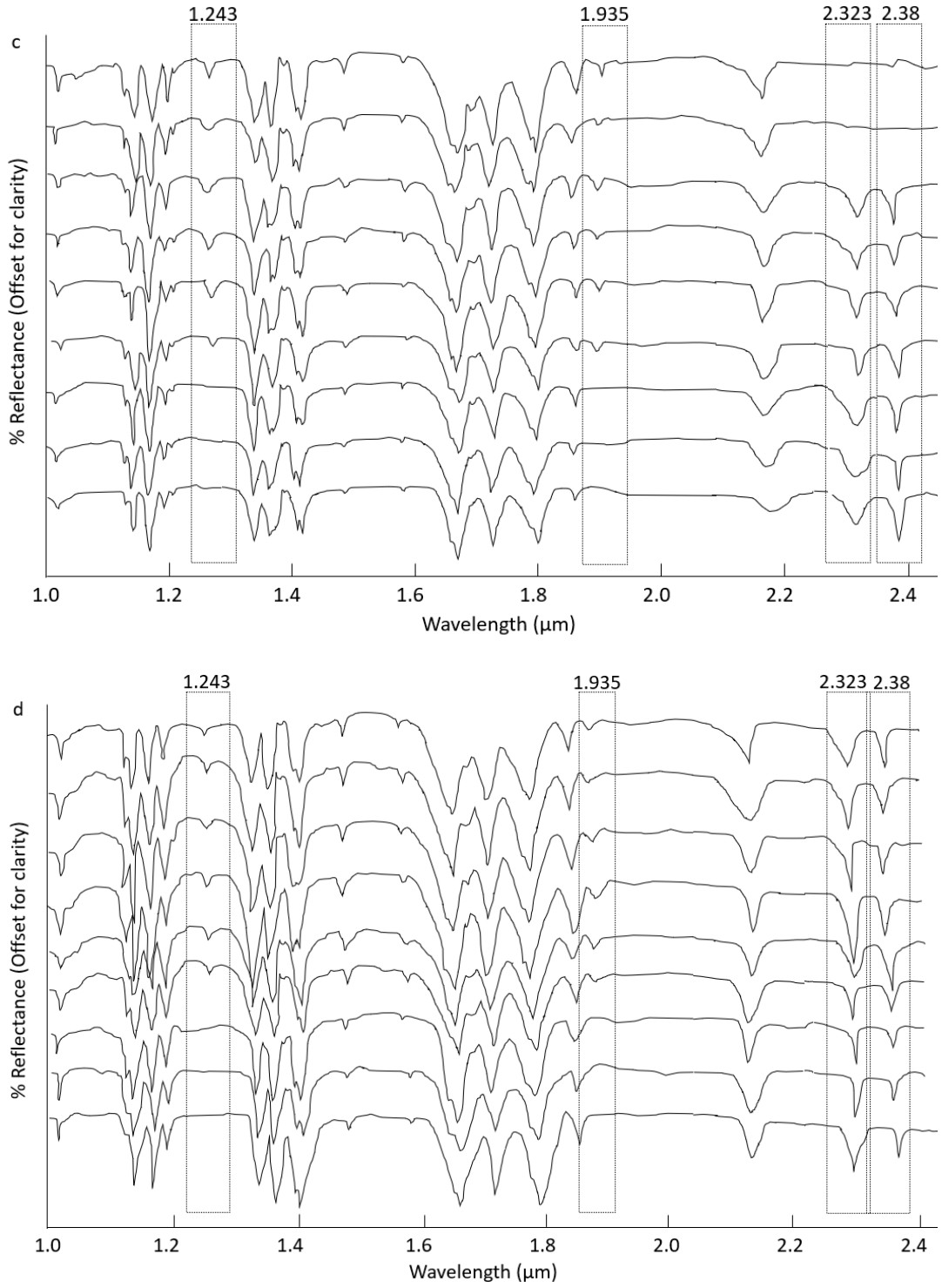

Figure 2: Experimental NIR spectra (1 – 2.4 μm) of CO-CH_4 binary ice samples in 10 mol% CO increments, starting with 10 mol% CO at the top and increasing downward. **a.** NIR spectra at 20 K conditions. **b.** Spectra at 30 K. **c.** Spectra at 40 K. **d.** Spectra at 50 K. Boxes mark specific band changes to outline the binary phase diagram.

5.4 Discussion

Investigating these band observances and shifting in the CO-CH_4 ice mixtures can help create a newly created solid binary phase diagram (Figure 3). We suspect that the α-β CH_4 transition at ~21 K could be relevant to the presence of the 1.243 μm CH_4 band at temperatures ≥ 30 K and not observed at 20 K. The 1.935 μm CH_4 is present in both α and β, except at molar ratios > 60 mol% CO, which we have designated as phase III. Phase III at relatively higher molar concentrations of CO only display the 2.323 μm CH_4 and 2.38 μm CO bands (and spectral shifting thereof) at all recorded temperatures. Phase Iβ is interesting to note in that it does not extend to the 50 K range due to the presence of the 2.323 and 2.38 μm bands. This may be due to a CO crystallization change at lower molar ratios in which the CO crystalline orientation changes from cubic to hexagonal ~ 40 K, as observed from the CO-N_2 binary phase diagram (Angwin and Wassermann 1966).

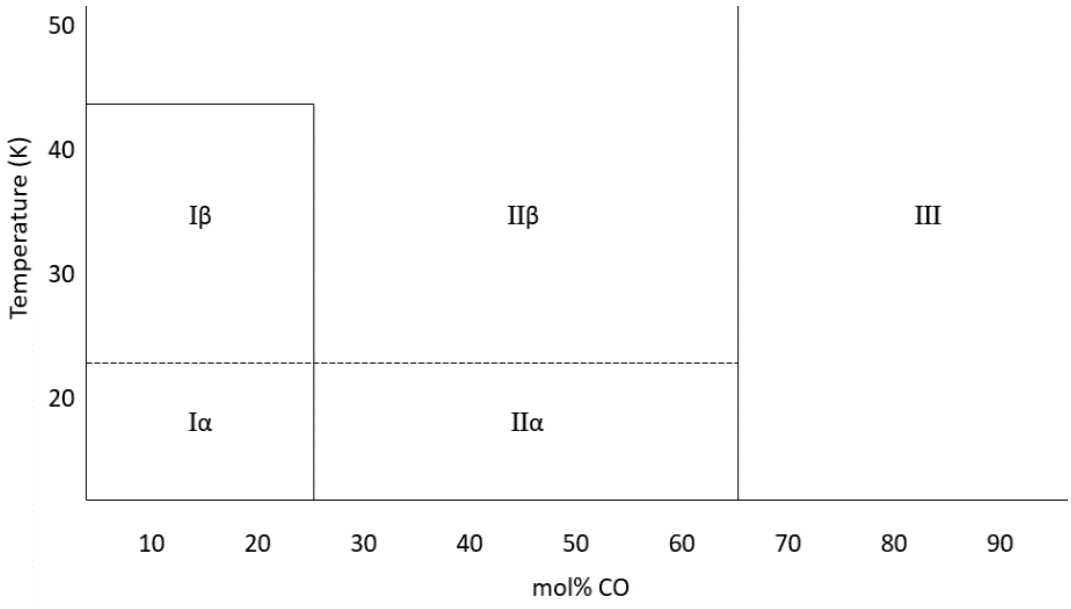

Figure 3: Solid CO-CH_4 binary phase diagram. α and β designate the CH_4 crystalline phases. Each section is representative of the spectral bands present (or shifts observed) from this study.

A newly created CO-CH_4 binary phase diagram would be essential for studying the ice properties at icy bodies, such as Pluto and other KBOs. From the New Horizons LEISA instrument, the band depth determination of CO (at 1.577 μm) was modified to be readable against stronger CH_4 signatures at similar micron wavelengths (Grundy et al. 2016; Schmitt et al. 2017) to prevent CH_4 saturation. However, the spectral behavior observed in our study suggest that CO and CH_4 hold a variety of phases, which would be crucial to understanding the CO-CH_4 dominant regions of Pluto. For example, Krun Macula (informal name) in the southeastern close-encounter hemisphere, and northwestern Voyager Terra above 60°N all have strong detections of CO and CH_4 as detected by LEISA. However, the geology at each of these sites are vastly different. That is, Krun Macula displays very ridged terrain, and northwestern Voyager Terra has polygonal features (Moore et al. 2016; Ahrens and Chevrier 2019). Voyager Terra at 70°N latitude has a latitudinal overlap of CH_4 and CO observed by LEISA. According to Earle et al. (2017), this area (with an albedo of 0.3) has a climatological temperature range of 15 – 60 K within the current Pluto orbit (Figure 4). In contrast, the Krun Macula region (at 4°N with an albedo of 0.1) has a relatively limited temperature range of ~30 – 40 K. This temperature range then implies a relatively larger variability of CH_4-CO phases at Voyager Terra. Having a limited range at Krun Macula, however, shows that this region would specifically only have the β-CH4 or phase III within the phase diagram (Figure 3), which may lead to assumptions of sublimation formations and lithosphere evolution over seasonal time accounting for the spikiness at Krun Macula rather than the smoother, polygonal features at Voyager Terra.

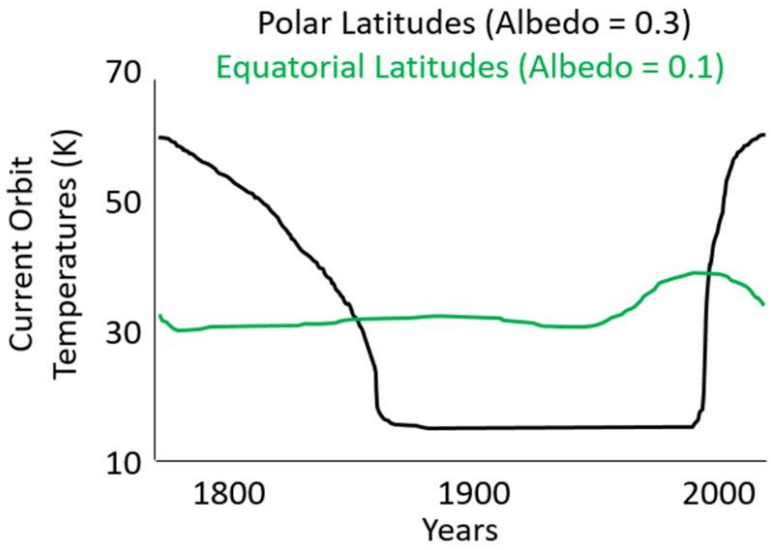

Figure 4: Local equilibrium temperatures for polar latitudes (30°N – 90°N), where greater areas of CH_4-CO mixtures are detected from LEISA. Krun Macula is located at the equatorial latitudes with an albedo of 0.1. Adapted from Earle et al. (2017).

Even though CO is not as abundant at Pluto's surface, it is an important factor for atmospheric processes (e.g., volatile transport) (Greaves et al. 2011), and cryovolcanism (Neveu et al. 2015). While the CO could be affected by the molar ratio and crystallinity of the CH_4 in the matrix into which it is frozen, it is hoped that the created binary phase diagram recorded here will help New Horizons data analyses (and future missions) ascertain the level of molar concentration and impurity of the CO and CH_4 ice at Pluto (and other icy bodies in the outer solar system).

5.5 Conclusions

These ice mixtures were compositionally distinct depending on the molar concentrations and temperature conditions. This approach in investigating the NIR spectral band behaviors provides insight into crystallinity and temperature dependence on certain spectral bands, thereby enabling a newly created solid binary phase diagram. The complexities of the crystalline behavior of both CH_4 and CO at temperatures < 50 K, as compared to previous studies of CO and CH_4 with

other volatile constituents, provide guidance on which spectral bands (and thus crystalline orientation) are more likely to result from concentration and temperature conditions. Further work is necessary to clarify the phase boundaries responsible for these spectral band behaviors. Although CH_4 has been studied numerous times, more so than CO, the interactions of their solid binary formations are incomplete. Laboratory production of such solid mixtures is a crucial step to properly characterize these ices on the surface of Pluto and KBOs.

5.6 References

Ahrens, C., and Chevrier, V. (2019) Spectral and surface characteristics of carbon monoxide on Pluto. 50th LPSC, Abstract #1552.

Angwin, M. and Wasserman, J. (1966) Nitrogen-Carbon monoxide phase diagram, Journal of Chemical Physics, 44 (1), p417-418. 10.1063/1.1726486.

Calvani, P., Cunsolo, S., Lupi, S., Nucara, A., 1992. The near-infrared spectrum of solid CH4. J. Chem. Phys., 96, 7372. https://doi.org/10.1063/1.462440

Caracas, R. (2013) First-Principles Calculations of Physical Properties of Planetary Ices. In: M. S. Gudipati, J. Castillo-Rogez, (Eds.), The Science of Solar System Ices. Springer New York, New York, NY, pp. 149-169.

Clark, R.N., Curchin, J.M., Hoefen, T.M., Swayze, G.A., 2009, Reflectance spectroscopy of organic compounds: 1. alkanes. J. Geophys. Res. 114, E03001. https://doi.org/10.1029/2008JE003150

De Bergh, C., et al. (2008) Laboratory data on ices, refractory carbonaceous materials, and minerals relevant to transneptunian objects and Centaurs. In: The Solar System Beyond Neptune, pp. 483-506.

Earle, A., Binzel, R., Young, L., Stern, S., Ennico, K., Grundy, W., Olkin, C., Weaver, H., New Horizons Geology and Geophysics Imaging Team, 2017. Long-term surface temperature modeling of Pluto. Icarus, 287, 37-46. https://doi.org/10.1016/j.icarus.2016.09.036

Fink, U., Sill, G. (1982) The infrared spectral properties of frozen volatiles. In Comets (L. L. Wilkening, ed.), pp. 164–202. Univ. of Arizona, Tucson.

Giauque, W., Clayton, J. (1933) The heat capacity and entropy of nitrogen. Heat of vaporization. Vapor pressures of solid and liquid. The reaction ½ N2 + ½ O2 = NO from spectroscopic data. J. Am. Chem. Soc., 55 (12), 4875-4889. 10.1021/ja01339a024.

Gladstone, G. R., et al. (2016) The atmosphere of Pluto as observed by New Horizons. Science. 351(6279). 10.1126/science.aad8866

Greaves, J. S., Helling, C., Friberg, P. (2011) Discovery of carbon monoxide in the upper atmosphere of Pluto. Monthly Notices of the Royal Astronomical Society: Letters. 414(1), L36-L40. https://doi.org/10.1111/j.1745-3933.2011.01052.x

Grundy, W. M., Schmitt, B., Quirico, E. (1993) The Temperature-Dependent Spectra of α and β Nitrogen Ice with Application to Triton. Icarus. 105(1), 254-258. https://doi.org/10.1006/icar.1993.1122

Grundy, W. M., Buie, M. W. (2001) Distribution and evolution of CH4, N2, and CO ices on Pluto's surface: 1995 to 1998. Icarus. 153(2), 248-263. https://doi.org/10.1006/icar.2001.6684

Grundy, W., Morrison, S., Bovyn, M., Tegler, S., Cornelison, D., (2011) Remote sensing D/H ratios in methane ice: Temperature-dependent absorption coefficients of CH3D in methane ice and in nitrogen ice. Icarus. 212(2), 941-949. https://doi.org/10.1016/j.icarus.2011.01.034

Grundy, W.M. , Olkin, C.B. , Young, L.A. , Holler, B.J. (2014) Near-infrared spectral monitoring of Pluto's ices: recent decline of CO and N2 ice absorptions. Icarus 235, 220–224. https://doi.org/10.1016/j.icarus.2014.02.025

Grundy, W. M., et al. (2016) Surface compositions across Pluto and Charon. Science. 351(6279), aad9189. 10.1126/science.aad9189

He, C., et al. (2017) Carbon monoxide affecting planetary atmospheric chemistry. Astrophys. Journ. Letters, 841:L31. https://doi.org/10.3847/2041-8213/aa74cc

Kim, Y., and Kaiser, R. (2012) Electron irradiation of Kuiper Belt surface ices: Ternary N2-CH4-CO mixtures as a case study. ApJ, 758, 37, https://doi.org/10.1088/0004-637X/758/1/37

Lellouch, E., Gurwell, M., Butler, B. et al. (2017) Detection of CO and HCN in Pluto's atmosphere with ALMA. Icarus, 286, 289-307. https://doi.org/10.1016/j.icarus.2016.10.013

Merlin, F., (2010) Chemical and physical properties of the variegated Pluto and Charon surfaces. Icarus 210, 930–943. https://doi.org/10.1016/j.icarus.2010.07.028

Moore, J. M., McKinnon, W. B., Spencer, J. R., Howard, A. D., Schenk, P. M., Beyer, R. A., Nimmo, F., Singer, K. N., Umurhan, O. M., White, O. L., 2016. The geology of Pluto and Charon through the eyes of New Horizons. Science. 351(6279), 1284-1293. https://doi.org/10.1126/science.aad7055

Neveu, M., Desch, S., Shock, E., Glein, C. (2015) Prerequisites for explosive cryovolcanism on dwarf planet-class Kuiper belt objects. Icarus, 246, 48-64. http://dx.doi.org/10.1016/j.icarus.2014.03.043

Palumbo, M. E. (1997) Infrared spectra and nature of the principal CO trapping sites in amorphous and crystalline H2O ice. J. Phys. Chem. A, 101 (23), 4298-4301. https://doi.org/10.1021/jp962462y

Plyler, E., Allen, H., Tidwell, E. (1958) Emission spectrum of carbon monoxide from 2.3 to 2.5 microns. Journal of Research of the National Bureau of Standards, 61 (1), 2883.

Prokvatilov, A., Yantsevich, L., (1983) X-ray investigation of the equilibrium phase diagram of CH4-N2 solid mixtures. Sov. J. Low Temp. Phys., 9(2), 94-98.

Protopapa, S., et al. (2017) Pluto's global surface composition through pixel-by-pixel Hapke modeling of New Horizons Ralph/LEISA data, Icarus, 287, 218-228. https://doi.org/10.1016/j.icarus.2016.11.028

Quirico, E., Schmitt, B. (1997) A spectroscopic study of CO diluted in N2 ice: Applications for Triton and Pluto. Icarus, 128, 181–188. https://doi.org/10.1006/icar.1997.5710

Schmitt B., Oehler A., Calvier R., Haschberger P., Lindermeier E. (1990) The near infrared absorption features of solid nitrogen and methane on Triton (abstract). Bull. Am. Astron. Soc., 22, 1121

Schmitt, B., et al. (2017) Physical state and distribution of materials at the surface of Pluto from New Horizons LEISA imaging spectrometer, Icarus, 287, 229-260. https://doi.org/10.1016/j.icarus.2016.12.025

Stern, S. A., et al. (2015) The Pluto system: Initial results from its exploration by New Horizons. Science. 350(6258), aad1815. 10.1126/science.aad1815

Tegler, S., et al. (2019) A new two-molecule combination band as a diagnostic of carbon monoxide diluted in nitrogen ice on Triton. Astronomical Journal, 158 (1), 17. https://doi.org/10.3847/1538-3881/ab199f

Tryka, K., Brown, R., Anicich, V. (1995) Near-infrared absorption coefficients of solid nitrogen as a function of temperature. Icarus, 116, 409–414. https://doi.org/10.1006/icar.1995.1133

Vetter, M., Jodl, J. Brodyanski, A. (2007) From optical spectra to phase diagrams-the binary mixture N2 –CO. Low Temp. Phys. 33, 1052. https://doi.org/10.1063/1.2747091

Young, L. A., Elliot, J. L., Tokunaga, A., de Bergh, C., Owen, T. (1997) Detection of gaseous methane on Pluto. Icarus. 127(1), 258-262. https://doi.org/10.1006/icar.1997.5709

Zalucha, A., Gulbis, A. (2012) Comparison of a simple 2-D Pluto general circulation model with stellar occultation light curves and implications for atmospheric circulation. Journal of Geophysical Research, 117, E05002. https://doi.org/10.1029/2011JE003957

Chapter 6

Ternary Ice Mixtures

C. J. Ahrens[1], V. F. Chevrier[1]

[1]University of Arkansas, Center for Space and Planetary Sciences, Fayetteville, AR 72701

6.1 Abstract

Compositional analyses from ground-based observations and the New Horizons mission of Triton and Pluto include large variations in methane (CH_4), nitrogen (N_2), and carbon monoxide (CO). Fourier transform infrared (FTIR) spectroscopy was utilized to monitor the various concentrations created in this study at extremely low temperatures and pressures relevant to Pluto surface conditions (15 – 50 K, 14 – 25 μbar). The results from this study ultimately achieved the goal of creating a newly defined ternary phase diagram based on the spectral behavior of the ternary mixtures. We have found that the 1.484 μm CH_4 band is not present in the N_2- or CO-dominant mixtures. The 2.207 μm CH_4 is also not observed in the CO-dominant mixtures. The 1.88 μm CO-N_2 combined band was only detected in temperatures > 30 K. The ternary phase diagram we have created shows CO- and CH_4-dominant phase regimes, with three additional phase boundaries depending on the spectral bands detected from varying molar ratios of the three constituents. Pluto's spectrum shows certain bands relevant to our CH_4-dominant mixtures, whereas Triton's spectrum does not harbor the 1.484 CH_4 band as strongly, which suggests a more N_2-dominant surface. We anticipate our developed ternary phase diagram would not only define the spectral behavior of a wide range of concentrations, but also characterize the dominant ice for the surface of Pluto, Triton, and other outer solar system bodies.

6.2 Introduction

Methane (CH_4), nitrogen (N_2), carbon monoxide (CO) ices have been detected on the surface of many outer solar system bodies, including Pluto (Cruikshank et al. 1976; Owen et al. 1993; Grundy et al. 1993; Douté et al. 1999; Grundy et al. 2013; Schmitt et al. 2017) and Triton (Cruikshank et al. 1993; Quirico et al. 1999; Tegler et al. 2019). Methane-enriched nitrogen ices were reported at Pluto (Tegler et al. 2010) and a nitrogen-rich surface composition for Triton (Tryka et al. 1993; Holler et al. 2016). Since the images retrieved by Voyager 2 at Triton and Pluto from the New Horizons mission, both of these icy bodies display a variety of geology, thus diversity in the spatial variability in the relative abundance of ice species (Douté et al. 1999; Grundy and Buie 2001, 2002; Grundy et al. 2013). This includes band variations latitudinally, which can vary seasonally, as observed for Pluto (Grundy et al. 2013; Earle et al. 2017; Binzel et al. 2017). Understanding the CH_4, N_2, and CO across an icy surface can prove useful in determining volatile mobility, seasonal behavior, and surface-atmosphere interactions. For example, CH_4 on Pluto is a marker for most sublimation landforms, such as the bladed terrain at Tartarus Dorsa (Moores et al. 2017), but as condensation on high-altitude mountains (Moore et al. 2016). CO is also a clue to cryovolcanism (Neveu et al. 2015) and is found in larger quantities with N_2 at Sputnik Planitia (Schmitt et al. 2017).

In this work, we investigate the NIR reflectance spectra of CH_4-N_2-CO mixtures condensed in a laboratory-prepared environment simulation chamber under relevant plutonian conditions (10 – 50 K and ≤ 25 μbar). We investigate CH_4-, N_2-, and CO-dominant mixtures under a range of temperatures (15 – 50 K) to simulate extreme plutonian seasons. We utilize *in situ* FTIR spectroscopy to investigate certain spectral bands in the NIR wavelength (1 – 2.45 μm) range.

6.2.1 CH_4-N_2 subsystem

CH_4 has several IR bands within the range 1 – 2.5 μm (Khanna 1990; Clark et al. 2009; Grundy et al. 2002; Grundy et al. 2011; Schmitt et al. 2017) as listed in Table 1. N_2, however, is IR-inactive, but does display certain spectral bands when in mixture with CH_4 (Table 1). Previous experiments have been done to explain the phase behavior of methane and nitrogen (Prokhvatilov and Yantsevich 1983; Tryka et al. 1993; Brunetto et al. 2008) and have identified various phases depending on the temperature and molar ratio. At ~ 21 K, CH_4 undergoes a transition from $CH_4\alpha$ to $CH_4\beta$ (Prokhvatilov and Yantsevich 1983; Calvani et al. 1992; Tegler et al. 2010). N_2 itself undergoes an α to β transition at a temperature ~ 35 K (Prokhvatilov and Yantsevich 1983).

6.2.2 N_2-CO subsystem

Experimental NIR spectra of solid N_2, CO, or mixtures thereof have been previously studied (Angwin and Wassermann 1966; Grundy et al. 1993; Quirico and Schmitt 1997a; Xia and McKellar 2000; Vetter et al. 2007; Tegler et al. 2019), though mostly in the range 30 K – 80 K and stated to be very weak IR bands (Tegler et al. 2019). CO has several identified NIR spectral bands at 2.337, 2.352, 2.38 μm, with a combined CO-N_2 band at 1.88 μm (Plyler et al. 1958; Fink and Sill 1982; Quirico and Schmitt 1997b; Pavlenko and Jones 2002). With N_2 diluted in CO, the α-phase below 35.6 K is in the cubic crystalline orientation and above 35.6 K, the β-phase is hexagonal and orientationally disordered (Quirico and Schmitt 1997a). It has been previously investigated that CO spectral bands are significantly sensitive to the phase present of solid N_2 in the crystalline matrix (Quirico and Schmitt 1997a). Specifically, the α-CO phase is isotropic, but is not precisely oriented and may present a variety of orientations. Angwin and Wassermann

(1966) through x-ray diffraction studies observed a lens phase within the N_2:CO binary phase diagram, where a crystalline mixture of hexagonal and cubic (hcp + cubic) exists.

6.2.3 CO-CH_4 subsystem

Our previous experimental work (Ahrens and Chevrier 2019) have observed that there are five distinct phases in CO-CH_4 binary mixtures. They have also noted that certain spectral bands depend on the CH_4 crystalline phase, notably the 1.243 μm CH_4 band, which is only present in the β-CH_4 crystalline phase at molar concentrations of < 60 mol% CO.

Table 1: Spectral bands from this study in microns. Also shown is the respective vibrational modes and related compound. Vibrational modes are documented from the Grenoble Astrophysics and Planetology Solid Spectroscopy and Thermodynamics (GhoSST) database.

Band (μm)	Vibrational mode	Spectral Band
1.164	$2\nu_1+\nu_2+\nu_4$	CH_4
1.243	$\nu_1+4\nu_4$	CH_4
1.362	$\nu_1+\nu_2+\nu_3$	CH_4
1.41	$\nu_2+\nu_3+2\nu_4$	CH_4
1.484	$\nu_1+3\nu_4$	CH_4
1.66	$2\nu_3$	CH_4
1.72	$\nu_2+\nu_3+\nu_4$	CH_4
1.79	$2\nu_2+2\nu_4$	CH_4
1.857	$\nu_2+3\nu_4$	CH_4
1.88	$4\nu_4$	CO-N_2
2.185	$\nu_2+\nu_3$	CH_4-N_2

Table 1 Cont.: Spectral bands from this study in microns. Also shown is the respective vibrational modes and related compound. Vibrational modes are documented from the Grenoble Astrophysics and Planetology Solid Spectroscopy and Thermodynamics (GhoSST) database.

Band (μm)	Vibrational mode	Spectral Band
2.337	ν+ν	CO
2.352	2ν	CO
2.38	2ν	CO
2.428	ν_2+2ν_4	CH_4

6.3 Results

In this section we show in detail the differences in spectral characteristics between CH_4, N_2, and CO dominant mixtures in the following ratios (in molar %): 90:5:5, 60:20:20, 50:40:10. Because the edges of our wavelength range using our current FTIR setup show significant noise at longer wavelengths, we focus on the spectral range 1 – 2.45 μm for clarity.

6.3.1 CH_4-dominant ternary mixtures

At 15 K (Figure 1a), bands are observed at 1.484, 1.88, 2.207, and 2.337 μm. The 1.484 μm CH_4 band is only observed at ≥ 60 mol% CH_4. The 1.88, 2.207, and 2.337 μm bands are only present at CH_4 molar concentrations of 50 mol% and variability in N_2 and CO concentration ~ 40 mol%. Heating the sample to 20 K (Figure 1b), the 1.243 μm band appears at all tested molar ratios of CH_4. All five notable bands remain stable at temperatures from 30 – 40 K (Figure 1c, d) as observed at 20 K. At 50 K, the 1.484 μm band becomes undetected (Figure 1e). The 1.243 μm is present in all observable ratios, but mostly dominant in ratios > 60 mol% CH_4. The 1.88 and 2.207 μm bands are also present, but only detected at molar ratios 50 mol% CH_4.

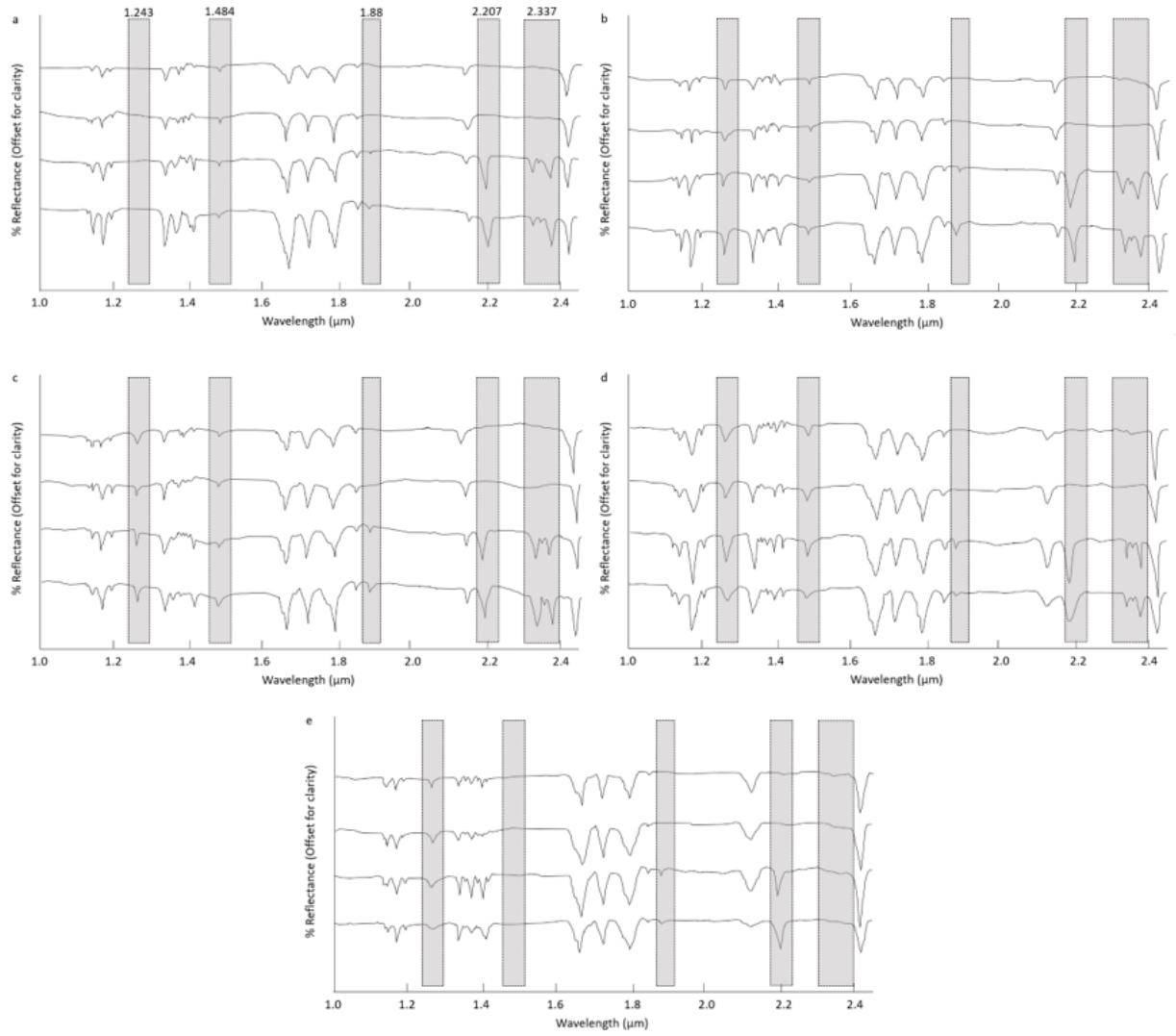

Figure 1: NIR spectral observations of CH_4-dominant ice mixtures (from top to bottom in CH_4:N_2:CO molar ratios): 90:5:5, 60:20:20, 50:40:10, and 50:10:40. Temperature conditions are: **a)** 15 K; **b)** 20 K; **c)** 30 K; **d)** 40 K; **e)** 50 K. Shaded regions are specific spectral bands: 1.243, 1.484, 1.88, 2.207, and 2.337 μm. Spectra has been offset for clarity.

6.3.2 N_2-dominant ternary mixtures

At 15 K (Figure 2a), bands are observed at 1.243, 1.88, 2.207, 2.337 μm. The 2.207 μm CH_4 band is only observed at ≥ 60 mol% N_2 and 50:40:10 CH_4:N_2:CO mixtures. This behavior also stays the same from 20 - 40 K (Figure 2b, c, d). Heating the sample to 50 K (Figure 2e), the

1.243 and 1.88 μm bands remain detectable at all tested molar ratios. However, there is an observed transition where the 2.337 μm CO band is no longer detected.

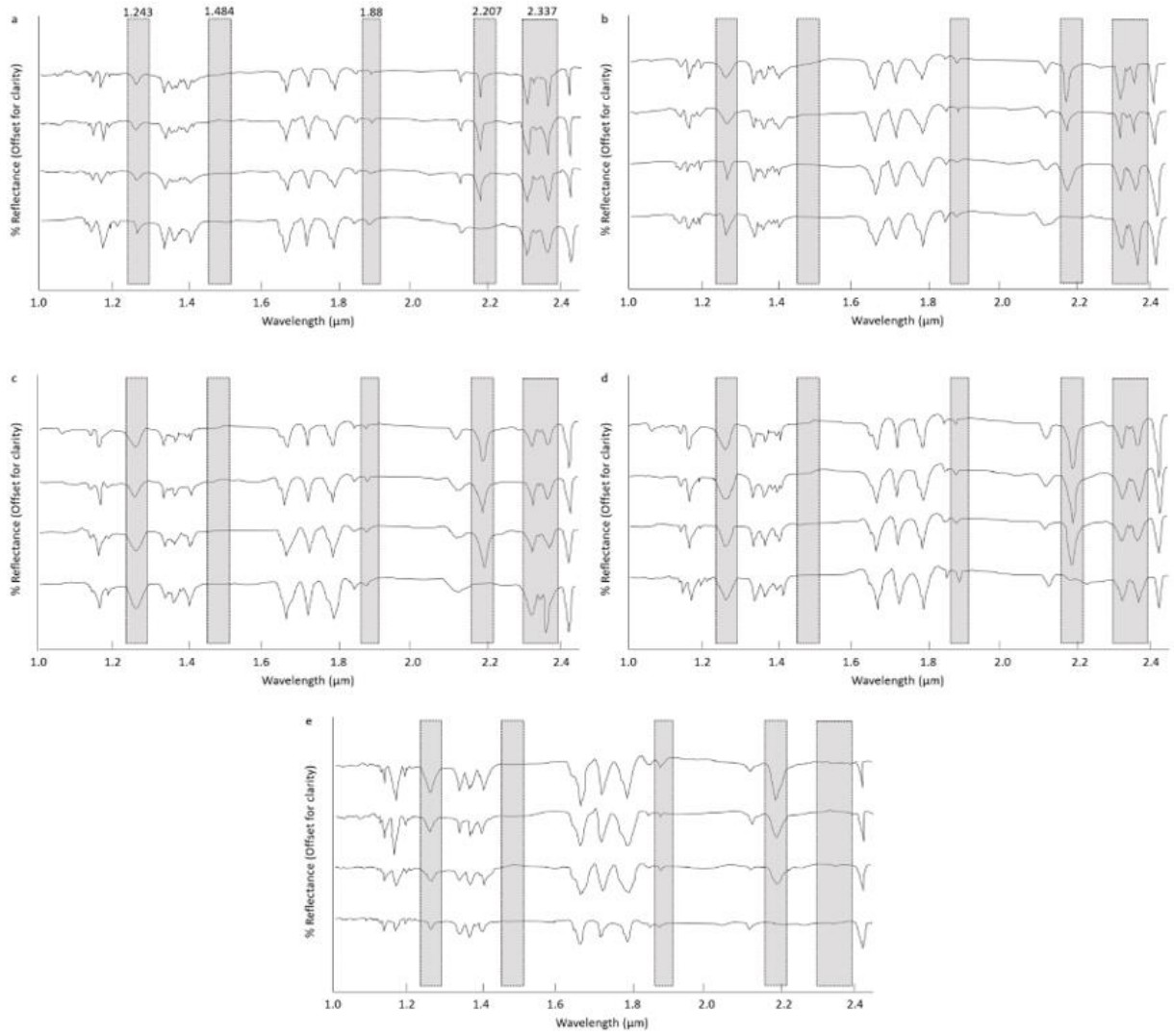

Figure 2: NIR spectral observations of N_2-dominant ice mixtures (from top to bottom in CH_4:N_2:CO molar ratios): 5:90:5, 20:60:20, 40:50:10, and 10:50:40. Temperature conditions are: **a)** 15 K; **b)** 20 K; **c)** 30 K; **d)** 40 K; **e)** 50 K. Shaded regions are specific spectral bands: 1.243, 1.484, 1.88, 2.207, and 2.337 μm. Spectra has been offset for clarity.

6.3.3 CO-dominant ternary mixtures

At 15 K (Figure 3a), the only bands observed are the 2.337-2.352-2.38 μm triplet. At 20 K (Figure 3b), the 1.243 μm CH_4 band is present. Heating the sample to 30 K (Figure 3c), the 1.88 μm band appears alongside the 1.243 and 2.337 μm bands. These remain detectable at 40 K (Figure 3d). Several transitions happen at 50 K temperatures, such as the disappearance of the 1.88 μm CO-N_2 combination band.

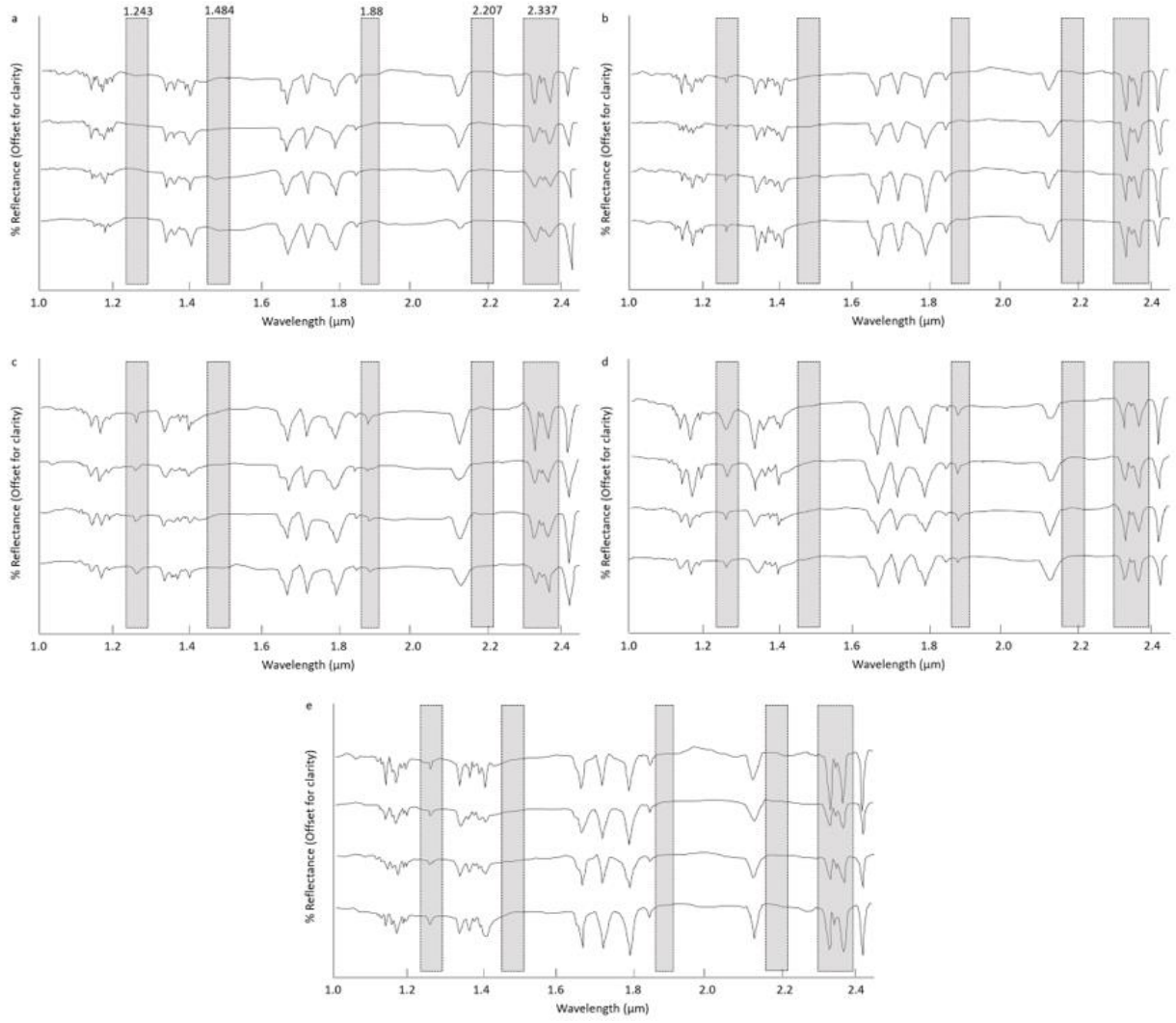

Figure 3: NIR spectral observations of CO-dominant ice mixtures (from top to bottom in CH_4:N_2:CO molar ratios): 5:5:90, 20:20:60, 40:10:50, and 10:40:50. Temperature conditions are: **a)** 15 K; **b)** 20 K; **c)** 30 K; **d)** 40 K; **e)** 50 K. Shaded regions are specific spectral bands: 1.243, 1.484, 1.88, 2.207, and 2.337 μm. Spectra has been offset for clarity.

6.4 Discussion

6.4.1 Construction of the ternary phase diagram

Investigating these band observances and behavior (notably the 1.243, 1.484, 1.88, 2.207, 2.337 μm) can help create a more defined solid ternary phase diagram (Figure 4). We note that these transitions happen at certain temperature conditions, so the relative abundances over the temperature range 15 – 50 K is taken into consideration for the making of the ternary diagram. From the CH_4-dominant ices (≥ 50 mol% CH_4), we observe the 1.484 μm CH_4 band mostly within temperatures ≤ 40 K, but not present in N_2- or CO-dominant ice mixtures. The CO-dominant phase (≥ 50 mol% CO) of the ternary diagram (Figure 4) constitutes mostly the 2.337 μm CO triplet bands, where other bands would otherwise transition in and out of this part of the ternary diagram, such as the 1.243 μm CH_4 band that only becomes detectable at > 15 K conditions.

Phase I constitutes the 1.88 CO-N_2 band with the 2.207 μm CH_4 band. Both bands also occur in Phase II, with the added 1.243 μm CH_4 band. Phase III consists of the 1.88 and 1.243 μm bands but does not have the 2.207 μm band present.

From the designations of the phases that we propose, these transitions of CH_4, N_2, and CO phases depend on temperature and the crystallization of the dominant ice. For example, the 1.243 μm CH_4 band is observed at all observed temperatures within in the N_2-dominant ices. However, it is only observed in the CH_4 and CO ices > 20 K, possibly marking the crystalline phase change from CH_4-α to CH_4-β at ~21 K. Another instance is the 1.88 μm CO-N_2 band, where this band is detected in CO-dominant ices from 30 – 40 K, the range where both CO and N_2 have crystalline transitions from cubic – hexagonal and α-β, respectively.

While the crystallinity of the dominant constituent could be affected by the molar ratio of the other two volatiles in the matrix into which it is frozen, it is hoped that this ternary study recorded here will help ground-based and mission data analyses of Pluto and other outer solar system icy surfaces.

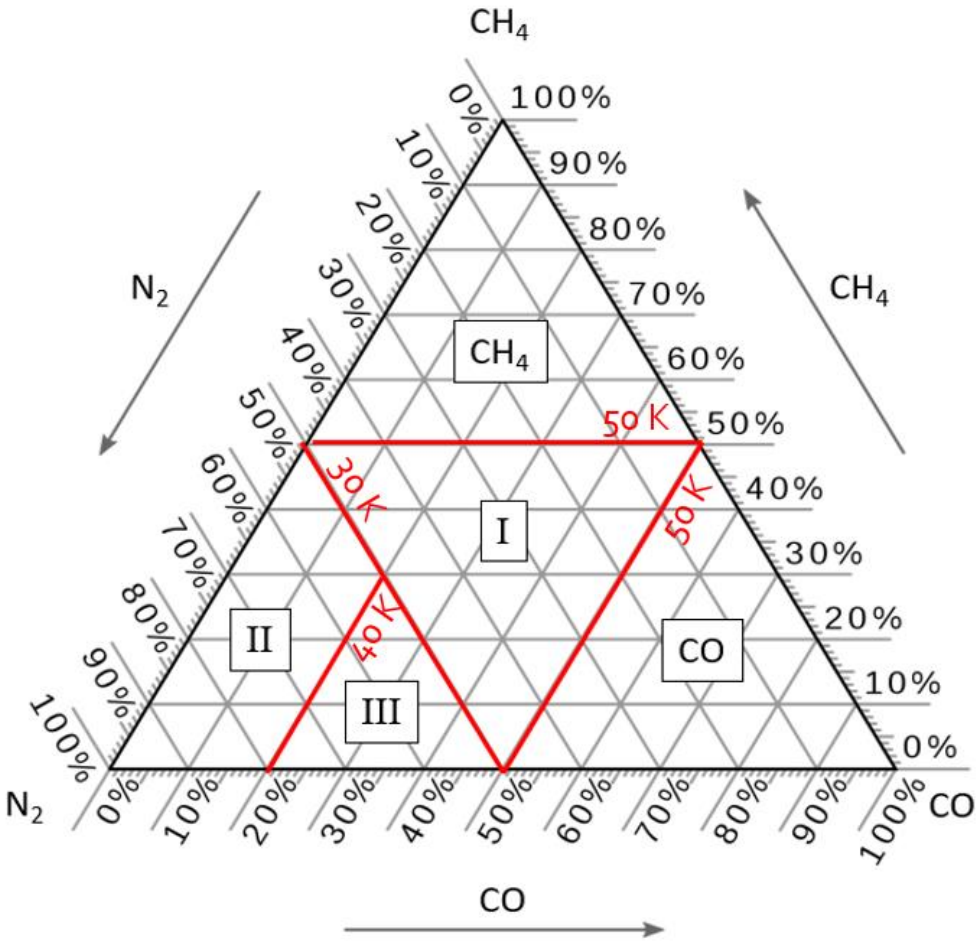

Figure 4: Proposed phase regimes based on our observations of certain spectral band phase transitions from 15 – 50 K temperatures. Phases I, II, and III have a mixture of CH_4-N_2-CO, but harbor specific spectral band phases only within that region of the ternary diagram.

6.4.2 Implications for Pluto and Triton

The New Horizons Linear Etalon Imaging Spectral Array (LEISA) instrument detected variable CH_4, N_2, and CO signatures across the surface of Pluto, mostly showing localized

concentrations of the three volatiles (Schmitt et al. 2017). Along with ground-based observations, the state of ices in the laboratory setting have several important factors.

The first concerns the state of CH_4 ice observed on Pluto's surface. From Schmitt et al. (2017), the CH_4 bands in Pluto's spectrum are shifted toward shorter wavelengths compared to the central wavelengths of pure CH_4, implying CH_4 being dissolved in a matrix of solid N_2 (Quirico and Schmitt, 1997; Protopapa et al. 2015, 2017). Schmitt et al. (2017) also grouped CH_4 into "spectral zones' depending on the spectral signal strength: 1.30 – 1.43 μm (medium bands); 1.59 – 1.83 μm (medium-strong bands); 1.90 – 2.00 μm (weak bands); 2.09 – 2.48 μm (strong bands).

In comparison, Douté et al. (1999) observed similar CH_4 and N_2 bands from ground-based telescopic spectra (Figure 5). This Pluto spectrum displays all of the spectral bands dependent on the CH_4-, N_2-, and CO-dominance of the matrix. Observing all these bands narrows down the possibility of the mixture, specifically the dominant ice at the time the spectrum was taken. From our laboratory work and the bands present in the Douté et al. (1999) spectrum gives us a range of 20 – 40 K in CH_4 dominant ice, which matches observations of Pluto being a CH_4-dominant dwarf planet (Stern et al. 2015; Schmitt et al. 2017).

Also in comparison is the spectrum of Triton taken from the NASA Infrared Telescope Facility by Holler et al. (2016). Although mostly within the 1.4 – 2.5 μm range, the observed bands still give us a clue as to the dominant ice, namely the lack of the 1.484 μm band. This narrows down the possibility that the spectrum shows a N_2-dominant ice, with > 50 mol% N_2 and < 20 mol% CO. Triton being an N_2-dominant body is confirmed in (Cruikshank et al. 1984; Grundy et al. 1993; Quirico and Schmitt 1997a). Why Triton is not CO-dominant, according to our laboratory spectra, is that our CO-dominant mixtures do not display the 2.207 μm band, which both Triton and Pluto have from ground-based spectra.

From our laboratory work compared to ground-based telescopic spectra and verifying the main constituents of ices on Pluto and Triton, one might characterize the level of mixture representative in certain areas on Pluto at more localized scales, or future spectral datasets of icy bodies in general.

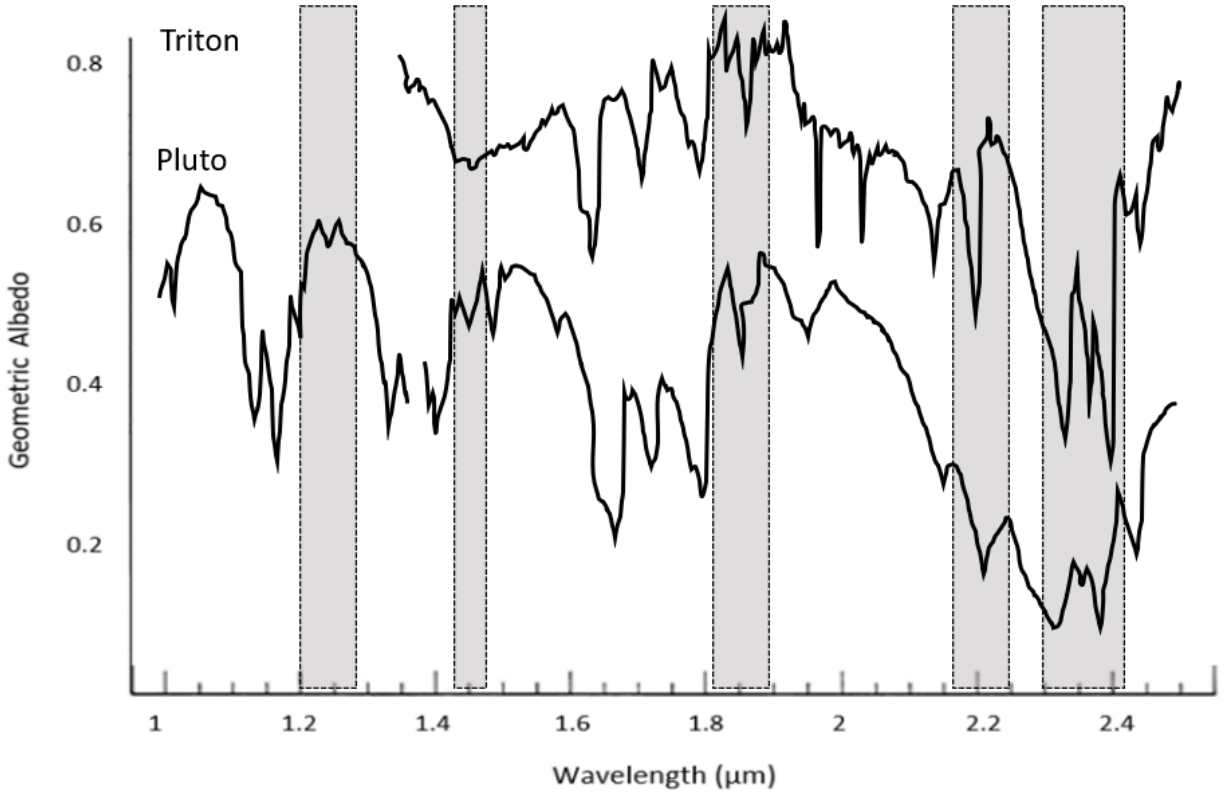

Figure 5: Ground-based telescope spectra of Triton (top) and Pluto (bottom). Triton spectrum was obtained by the NASA Infrared Telescope Facility (Holler et al. 2016). Pluto spectrum processed from the United Kingdom Infrared Telescope (UKIRT) telescope (Douté et al. 1999). Shaded regions indicate spectral bands from this study.

6.5 Conclusion

Methane, nitrogen, and carbon monoxide are observed on many outer solar system icy bodies, especially Pluto and Triton. The various molar concentrations of these ices at relevant

temperatures was simulated in the laboratory. Using in situ FTIR spectroscopy, the formation of varying phases depending on the dominant constituent provided a means to create phase boundaries within a ternary diagram. Our created ternary phase diagram shows separate methane and carbon monoxide dominant phase regimes, along with three different methane-nitrogen-carbon monoxide- mixture phases depending on the spectral bands present and molar concentrations of the dominant ice. It is interesting to note that the 1.484 μm CH_4 band is not observed in nitrogen or carbon monoxide dominant mixtures. Carbon monoxide dominant ices has a lack of the 2.207 μm CH_4 band. Comparing our study to obtained ground-based spectra, the methane-dominant mixtures matched certain spectral bands found in Pluto spectra, whereas nitrogen-dominant mixtures were more relevant to Triton spectra. This newly-defined ternary phase diagram can be helpful toward understanding dominant ice mixtures from ground-based and fly-by spectra.

6.6 Acknowledgements:

The authors greatly acknowledge the New Horizons team for their outstanding spectral data of Pluto. The authors would also like to thank W. Graupner for his contributions in the laboratory. This research is supported by NASA Solar System Workings (SSW) Research Program #80NSSC19K0163.

6.7 References

Ahrens, C., and Chevrier, V. (2019) Spectral and surface characteristics of carbon monoxide on Pluto. 50th LPSC, Abstract #1552.

Angwin, M. and Wasserman, J. (1966) Nitrogen-Carbon monoxide phase diagram, Journal of Chemical Physics, 44 (1), p417-418. 10.1063/1.1726486.

Binzel, R., et al. (2017) Climate zones on Pluto and Charon. Icarus, 287, 30-36. http://dx.doi.org/10.1016/j.icarus.2016.07.023

Brunetto, R., Caniglia, G., Baratta, G. A., Palumbo, M. E., 2008. Integrated near-infrared band strengths of solid CH4 and its mixtures with N2. The Astrophysical Journal. 686(2), 1480. https://doi.org/10.1086/591509

Calvani, P., Cunsolo, S., Lupi, S., Nucara, A., 1992. The near-infrared spectrum of solid CH4. J. Chem. Phys., 96, 7372. https://doi.org/10.1063/1.462440

Clark, R.N., Curchin, J.M., Hoefen, T.M., Swayze, G.A., 2009, Reflectance spectroscopy of organic compounds: 1. alkanes. J. Geophys. Res. 114, E03001. https://doi.org/10.1029/2008JE003150

Cruikshank, D. P., Pilcher, C. B., Morrison, D., 1976. Pluto - Evidence for methane frost. Science 194, 835–837. www.jstor.org/stable/1743489

Cruikshank, D., P., Roush, T. L., Owen, T. C., Geballe, T. R., de Bergh, C., Schmitt, B., Brown, R. H., Bartholomew, M. J., 1993. Ices on the surface of Triton. Science. 261 (5122), 742-745. 10.1126/science.261.5122.742

Douté, S., Schmitt, B., Quirico, E., Owen, T. C., Cruikshank, D. P., de Bergh C., Geballe, T. R., Roush, T. L., 1999. Evidence for Methane Segregation at the Surface of Pluto. Icarus, 142 (2), 421-444. https://doi.org/10.1006/icar.1999.6226

Earle, A., Binzel, R., Young, L., Stern, S., Ennico, K., Grundy, W., Olkin, C., Weaver, H., New Horizons Geology and Geophysics Imaging Team, 2017. Long-term surface temperature modeling of Pluto. Icarus, 287, 37-46. https://doi.org/10.1016/j.icarus.2016.09.036

Fink, U., Sill, G. (1982) The infrared spectral properties of frozen volatiles. In Comets (L. L. Wilkening, ed.), pp. 164–202. Univ. of Arizona, Tucson.

Grundy, W. M., Buie, M. W. (2001) Distribution and evolution of CH4, N2, and CO ices on Pluto's surface: 1995 to 1998. Icarus. 153(2), 248-263. https://doi.org/10.1006/icar.2001.6684

Grundy, W. M., Buie, M. W., 2002. Spatial and Compositional Constraints on Non-ice Components and H_2O on Pluto's Surface. Icarus. 157(1), 128-138. https://doi.org/10.1006/icar.2002.6833

Grundy, W. M., Schmitt, B., Quirico, E. (1993) The Temperature-Dependent Spectra of α and β Nitrogen Ice with Application to Triton. Icarus. 105(1), 254-258. https://doi.org/10.1006/icar.1993.1122

Grundy, W., Schmitt, B., Quirico, E., 2002. The temperature-dependent spectrum of methane ice I between 0.7 and 5 um and opportunities for near-infrared remote thermometry. Icarus 155, 486-496. https://doi.org/10.1006/icar.2001.6726

Grundy, W., Morrison, S., Bovyn, M., Tegler, S., Cornelison, D., 2011. Remote sensing D/H ratios in methane ice: Temperature-dependent absorption coefficients of CH3D in methane ice and in nitrogen ice. Icarus. 212(2), 941-949. https://doi.org/10.1016/j.icarus.2011.01.034

Grundy, W. M., Olkin, C. B., Young, L. A., Buie, M. W., Young, E. F., 2013. Near-infrared spectral monitoring of Pluto's ices: Spatial distribution and secular evolution. Icarus 223, 710–721. https://doi.org/10.1016/j.icarus.2013.01.019

Holler, B., et al. 2016. On the composition of Triton's southern latitudes. Icarus, 267, 255-266. https://doi.org/10.1016/j.icarus.2015.12.027

Khanna, R., and Ngoh, M. (1990) Crystal field effects on the infrared spectra of phases I and II of crystalline CH4. Spectrochemica Acta Part A: Molecular Spectroscopy, 46 (7), 1057-1063. https://doi.org/10.1016/0584-8539(90)80222-K

McMahon, Z. M. (2016). Development of a Pluto Chamber for Surface Simulations. Theses and Dissertations Retrieved from https://scholarworks.uark.edu/etd/1812

Moore, J. M., McKinnon, W. B., Spencer, J. R., Howard, A. D., Schenk, P. M., Beyer, R. A., Nimmo, F., Singer, K. N., Umurhan, O. M., White, O. L., 2016. The geology of Pluto and Charon through the eyes of New Horizons. Science. 351(6279), 1284-1293. https://doi.org/10.1126/science.aad7055

Moores, J., Smith, C., Toigo, A., Guzewich, S., 2017. Penitentes as the origin of the bladed terrain of Tartarus Dorsa on Pluto. Nature. 541(7636), 188-190. https://doi.org/10.1038/nature20779

Neveu, M., Desch, S., Shock, E., Glein, C. (2015) Prerequisites for explosive cryovolcanism on dwarf planet-class Kuiper belt objects. Icarus, 246, 48-64. http://dx.doi.org/10.1016/j.icarus.2014.03.043

Owen et al. 1993; Owen, T. C., Roush, T. L., Cruikshank, D. P., Elliot, J. L., Young, L., De Bergh, C., Schmitt, B., Geballe, T., Brown, R., Bartholomew, M., 1993. Surface ices and the atmospheric composition of Pluto. Science. 261(5122), 745-748. https://doi.org/10.1126/science.261.5122.745

Pavlenko, Y., Jones, H. (2002) Carbon monoxide bands in M dwarfs. A&A, 396 (3), 967-975. https://doi.org/10.1051/0004-6361:20021454

Plyler, E., Allen, H., Tidwell, E. (1958) Emission spectrum of carbon monoxide from 2.3 to 2.5 microns. Journal of Research of the National Bureau of Standards, 61 (1), 2883.

Prokvatilov, A., Yantsevich, L., (1983) X-ray investigation of the equilibrium phase diagram of CH4-N2 solid mixtures. Sov. J. Low Temp. Phys., 9(2), 94-98.

Protopapa, S., Grundy, W., Tegler, S., Bergonio, J., 2015. Absorption Coefficients of the Methane-Nitrogen Binary Ice System: Implications for Pluto. Icarus, 253, 179-188. https://doi.org/10.1016/j.icarus.2015.02.027

Protopapa, S., et al. (2017) Pluto's global surface composition through pixel-by-pixel Hapke modeling of New Horizons Ralph/LEISA data, Icarus, 287, 218-228. https://doi.org/10.1016/j.icarus.2016.11.028

Quirico, E., Schmitt, B. (1997a) A spectroscopic study of CO diluted in N2 ice: Applications for Triton and Pluto. Icarus, 128, 181–188. https://doi.org/10.1006/icar.1997.5710

Quirico, E., Schmitt, B. (1997b) Near-infrared spectroscopy of simple hydrocarbons and carbon oxides diluted in solid N2 and as pure ices: Implications for Triton and Pluto. Icarus, 127, 354–378. https://doi.org/10.1006/icar.1996.5663

Quirico, E., et al., 1999. Composition, Physical State, and Distribution of Ices at the Surface of Triton. Icarus 139, 159–178. https://doi.org/10.1006/icar.1999.6111

Schmitt, B., et al. (2017) Physical state and distribution of materials at the surface of Pluto from New Horizons LEISA imaging spectrometer, Icarus, 287, 229-260. https://doi.org/10.1016/j.icarus.2016.12.025

Stern, S. A., et al. (2015) The Pluto system: Initial results from its exploration by New Horizons. Science. 350(6258), aad1815. 10.1126/science.aad1815

Tegler, S. C., Cornelison, D. M., Grundy, W. M., Romanishin, W., Abernathy, M. R., Bovyn, M. J., Burt, J. A., Evans, D. E., Maleszewski, C. K., Thompson, Z., Vilas, F., 2010. Methane and Nitrogen Abundances on Pluto and Eris. The Astrophysical Journal. 725(1), 1296. https://doi.org/10.1088/0004-637X/725/1/1296

Tegler, S., et al. (2019) A new two-molecule combination band as a diagnostic of carbon monoxide diluted in nitrogen ice on Triton. Astronomical Journal, 158 (1), 17. https://doi.org/10.3847/1538-3881/ab199f

Tryka, K. A., Brown, R. H., Anicich, V., Cruikshank, D. P., Owen, T. C., 1993. Spectroscopic Determination of the Phase Composition and Temperature of Nitrogen ice on Triton. Science. 261(5122), 751-754. 10.1126/science.261.5122.751

Vetter, M., Jodl, J. Brodyanski, A. (2007) From optical spectra to phase diagrams-the binary mixture N2 –CO. Low Temp. Phys. 33, 1052. https://doi.org/10.1063/1.2747091

Xia, C., McKellar, A. (2000) Infrared spectrum of the CO-N2 van der Waals complex: Assignments for CO-para N2 and observation of a bending state for CO-ortho N2. J. Chem. Phys., 113 (2), p 525. https://doi.org/10.1063/1.481912

Chapter 7

Compressional ridges on Baret Montes, Pluto as observed by New Horizons

C. J. Ahrens[1], V. F. Chevrier[1]

[1]University of Arkansas, Center for Space and Planetary Sciences, Fayetteville, AR 72701

7.1 Abstract

Distinct compressional folding patterns may be an important aspect in shaping icy body surfaces in the outer Solar System and revealing their folding processes and stress histories. Baret Montes on Sputnik Planitia is possibly one of the most folded structures yet observed on Pluto. This glacier consists of sub-parallel ridges that display a consistent northwest-southeast orientation and is comparable to Enceladan transpression fold processes. Here, we report on mapping using images from NASA's New Horizons mission and apply ridge analysis to determine the folding characteristics and approximate the deformation duration of the folds. This leads to a discussion of the ridge formation mechanism and the possible influence of Sputnik Planitia's underlying convection. Based on the occurrence of the ridges on a water-ice based glacier with a thinner layer of methane-water ice, we conclude that the deformation rates calculated in this study implies the folding duration to be < 5.53 My.

7.2 Introduction

Glacial structures have been observed on the western lobe of Sputnik Planitia, measuring up to 30 km across and 3.5 km above the basin's relative low relief and separated from the mainland crustal surface by a few kilometers. Baret Montes has been interpreted as one of several large floating (or partially submerged) mountainous glaciers, along with Hillary and Al-Idrisi

Montes [*Howard et al.*, 2017; *Umurhan, et al.*, 2017; *White et al.*, 2017]. These glaciers are located on the western lobe of Sputnik Planitia, a large, elongated impact basin consisting of currently-active convective processes [*Roberts and Nimmo,* 2008; *Trowbridge et al.*, 2016; *Hammond et al.*, 2016; *McKinnon et al.*, 2016a, b], and is relatively young due to lack of observable craters and estimated to form within 10 My [*Singer et al.*, 2016; *Buhler and Ingersoll,* 2018].

Baret Montes is located on the encounter hemisphere of Pluto (centered at 13.81°N, 157.59°E), approximately 170.4 km ± 2.7 km in width, the tip barely in contact with the eastern shores of Cthulhu Macula (informal name) (Figure 1a, b). The latest DEM measurements from *Schenk et al.* [2018] achieved by stereo topography in this region of Pluto has a vertical precision of < 100 m. The glacier averages at about -0.85 ± 0.45 km in elevation, showing relief above Sputnik Planitia, which is roughly -2.9 km along its northwestern boundary [Figure 1c; *Moore et al.*, 2016; *White et al.*, 2019].

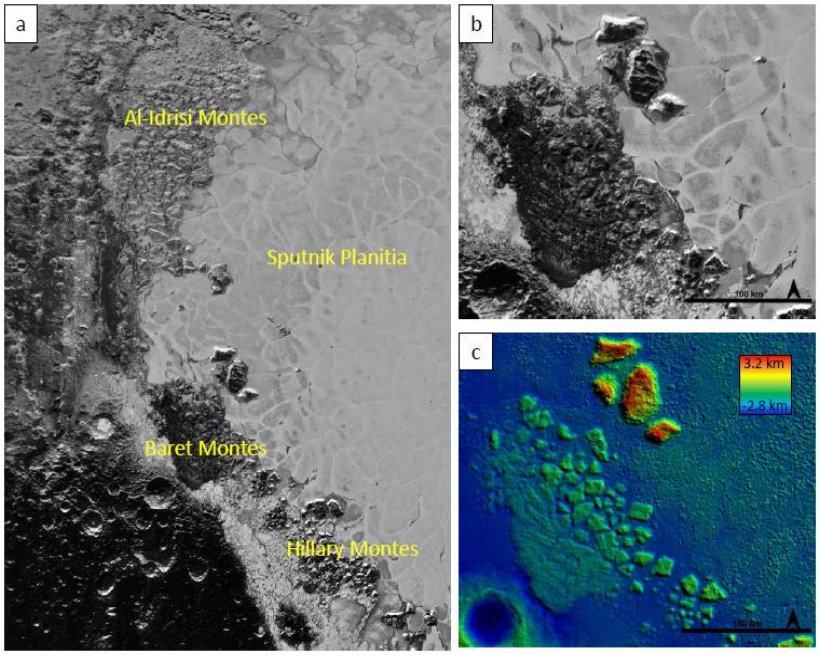

Figure 1: Baret Montes as observed using LORRI. a) Map of Baret Montes context with other labeled glacier counterparts on the western shores of Sputnik Planitia; b) Close up of Baret Montes

ridges. Scale bar equals 100 km. Arrow points north. LORRI ID: 0299175193; c) Colorized topography of Baret Montes showing relief from the surrounding Sputnik Planitia. Scale bar equals 100 km and arrow points north. The pixel resolution of these images are < 300 m/pixel.

We suspect the origin of the Baret Montes folds (Figure 2a) to be comparable to the linear ridges between Baghdad and Damascus sulci on Enceladus (Figure 2b) to have the following common geophysical characteristics: 1) collision; and 2) horizontal stress between two materials or crusts [*Twidale,* 1971; *Fink and Fletcher,* 1978]. From *Barr and Preuss* [2010], the spacing of the Enceladan sulci are relatively smaller in wavelength than the measured Baret Montes ridges. Although the sulci ridges are from geyser-like activity, the driving force from transpressions pushing the ices of different densities to ripple and collide are comparable for the purpose of this study. In the case of airless icy bodies with active geology, layers of different ice densities being dynamically forced (e.g., tiger stripes having horizontal stresses at Enceladus) has an effect of ridge preservation and mechanical distortion of the mantled ice [*Porco et al.,* 2006; *Barr and Preuss*, 2010; *Helfenstein and Porco,* 2015].

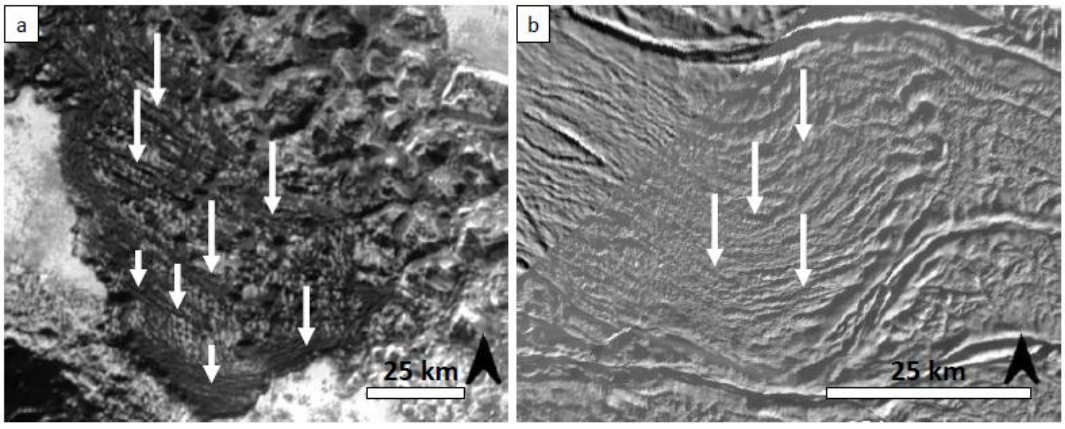

Figure 2: a) Baret Montes, Pluto. LORRI ID: 0299175193. b) Funiscular terrain at Damascus Sulci, Enceladus (centered at -85.70°N, 291.96°E). Cassini ISS ID: N1597183061. Scale bars at 25 km. White arrows indicate main ridges. Black arrows point north. These deformed ridges share common origins consisting of underlying driving forces, and that horizontal stresses influence the folding of icy material layers. Although the icy compositions are different, and the Enceladan

sulci are from geyser-like activity, the mechanical scenarios between layers of differentiating layers of ices being distorted from collisions are comparable.

The consistent linear northwest-southeast orientations of the ridges, where no other major glacial body on Sputnik Planitia holds such major ridges, suggests that these ridges are rather a geophysical remnant of the Baret Montes glacier colliding with the western crustal shores of Sputnik Planitia, resulting in accordion-like ridging. However, similar discontinuous methane-water ice-rich mountain ranges are located several kilometers north of Baret Montes on the western margin of Sputnik Planitia (Al-Idrisi Montes) [*Grundy et al.* 2016]. From *White et al.* [2017], these water-ice fragments are disruptions made by nitrogen ice from the Sputnik Planitia in-filling. Assuming that these ridges were a remnant of convective forces from the underlying geologically-young Sputnik Planitia, and hypothesizing the glacier's base and upper layer composition and densities, we can constrain the emplacement time of the ridge formations to be relatively young since the creation of the Sputnik Planitia basin and consequent in-filling. However, we briefly describe a possible alternative hypothesis of formation in the discussion section of this report. Here we identify the wavelengths of the ridges using a combination of topographic analysis and model for the formation of ridges from *Fink* [1980], allowing for an estimated timeline of Baret Montes' glacio-dynamic history.

7.3 Methods

Long Range Reconnaissance Imager (LORRI; version 3.0) images (spatially ~300 m/pixel) and respective topographic profiles were obtained and measured using the Java Mission-planning and Analysis for Remote Sensing (JMARS v.3.8.2) software (Figure 3a). Fold wavelengths were

measured from 20 elevation profiles, as seen in example Figure 3b, across the glacier to measure the dominant wavelength (from crest to crest) to be 5.17 km ± 0.45 km.

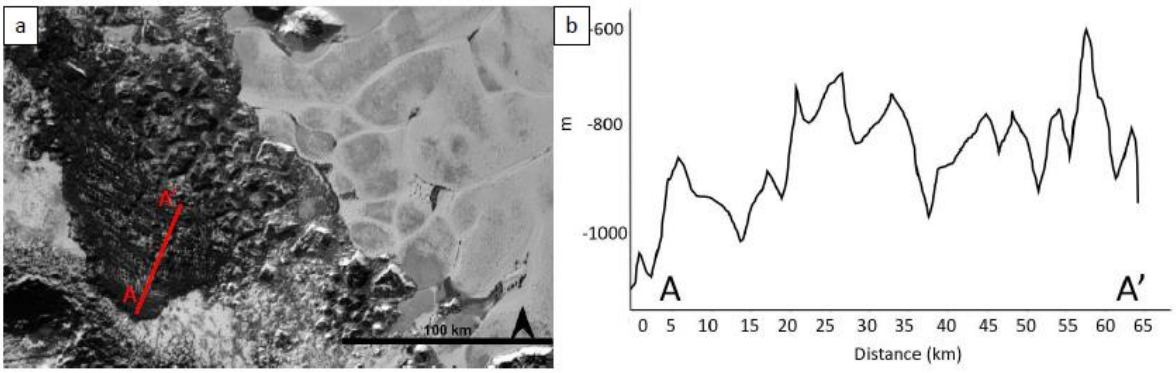

Figure 3: a) Example DEM measurement (A-A') line overlapping LORRI image. Scale bar at 100 km. Arrow points north. b) Example of a topographic profile, A-A' profile from (a).

The Linear Etalon Imaging Spectrometer Array (LEISA) has mapped the spatial distribution of volatile (N_2, CH_4, CO) surface materials as well as non-volatile H_2O ices with adequate resolution [3 km/pixel; *Reuter et al.,* 2008] to define spatial extent of materials and landform boundaries [*Moore et al.,* 2016; *Grundy et al.,* 2016; *Protopapa et al.,* 2017; *Schmitt et al.,* 2017]. It should be noted that the ridge spacing on Baret Montes cannot be entirely constrained compositionally due to this resolution, so approximations are made based on relative abundance on the glacier itself, not the surrounding Sputnik Planitia plains. Figure 4 shows LEISA data overlapping Baret Montes, observably having an abundance of methane (Figure 4a-c) and water ice (Figure 4d) where the ridges are located within the parameters marked in the figures. The 1.7-micron CH_4 band from LEISA was processed using SAOImage ds9 (v.8.0.1) software for a maximum detection threshold (Figure 4b). Methane and water ice properties were the focus in determining ridge morphology for our analysis.

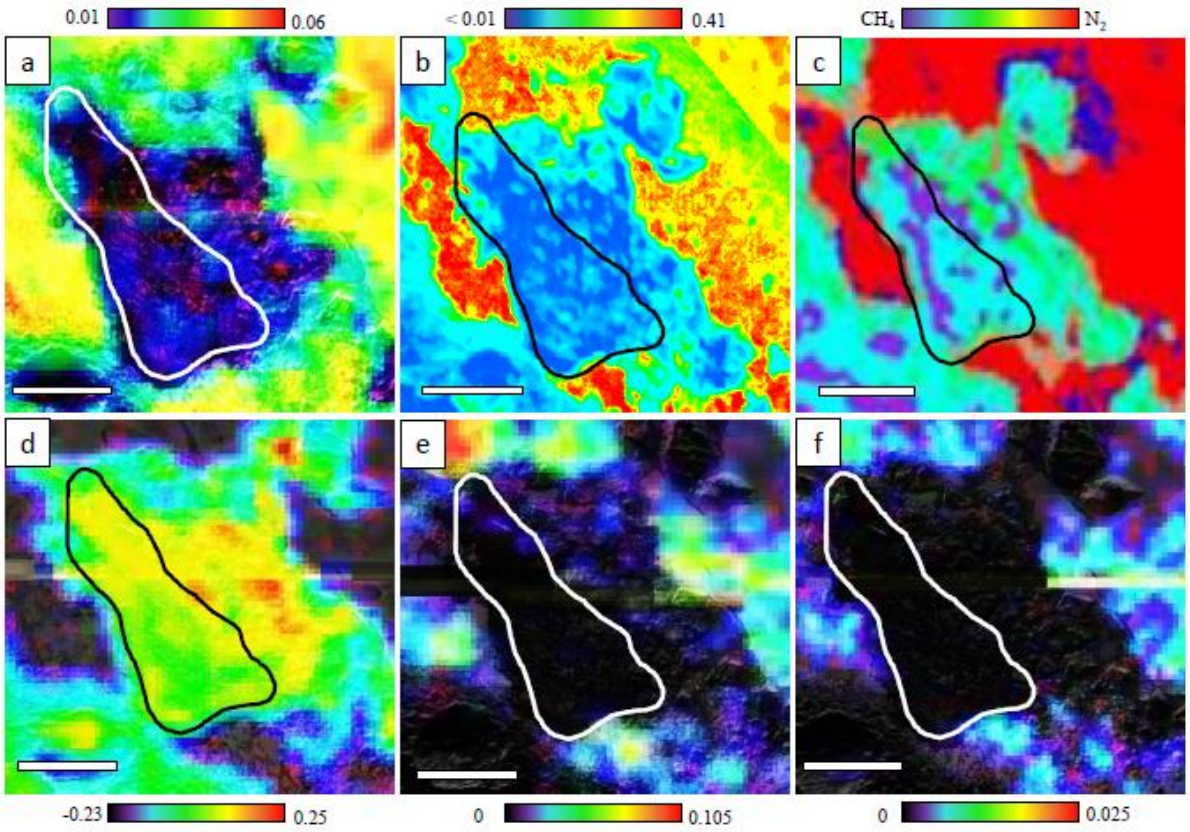

Figure 4: LEISA data overlapping LORRI images of Baret Montes and surrounding Sputnik Planitia. Bold lines indicate boundary of Baret Montes ridges. Scale bar at 50 km. a) weak abundance of CH_4 from the 1.90 - 2.00 micron CH_4 band detection; b) relatively stronger detection of CH_4 from the 1.7 micron CH_4 band detection, processed using the SAOImage ds9 software; c) CH_4-rich ice abundance at > 1 % concentrations compared to N_2 spectral bands; d) relatively high H_2O abundance; e) little to no N_2 abundance detected; f) little to no CO abundance detected. Colored scale bars (except for c) cover detection threshold to pixels at 98% positive detection. Note that (a, c-f) and respective abundance color scales adapted from *Schmitt et al.* [2017]. Readers should refer to *Schmitt et al.* [2017] for further explanation of composition abundance.

7.4 Results

Collectively, the Baret Montes folds are ~5 km wide with an average length of 70 km ± 2.7 km in a northwest-southeast direction. The dominant folding wavelength has been calculated on similar formations involving two main layers, with the upper layer susceptible to folding, proposed here to be a thin layer of methane, and the base to be water ice, based on LEISA observations [Figure 4; *Schmitt et al.,* 2017; *White et al.,* 2019]. It is noted through literature [extensively in

Protopapa et al., 2017; *Schmitt et al.,* 2017] that the LEISA spectroscopy of Pluto's surface characterizes a surface layer and that surface subjected to morphologic changes (i.e. compressional folding) may reflect bulk composition, and not accumulations (e.g., the methane-water ice dominates the entirety of the ridge composition and not merely the ridge troughs). Methane has been observed in three different wavelengths or aspects: 1.9 – 2.0-micron wavelengths (weak detection; Figure 4a); 1.7-micron wavelengths (relatively stronger detection; Figure 4b); and N_2-CH_4 band depth comparison, where CH_4 has > 1% concentrations on Baret Montes (Figure 4c). *Grundy et al.* [2016] notes that CH_4 ice spectral signatures are stronger on higher relief terrains, including the nearby glacial terrains of Al-Idrisi and Hillary Montes [see Figure 3 of *Grundy et al.,* 2016], and that mixtures of CH_4 and water ice dominate slopes, as we observe (although weak detection from different wavelengths) CH_4 on the crests of Baret Montes, and water ice being spectrally dominant on the entirety of the glacier (Figure 4d). Nonetheless, the inferred surface mineralogy of a glacially-buoyant, dominantly water-ice solid structure with a weaker upper layer (proposed in this case to be methane-water ice mixed at the crests) subjected to folding is consistent with previous interpretations made to ices moving on a larger, more volatile-based basin [*Howard et al.,* 2017; *Umurhan et al.,* 2017].

The dominant wavelength and the *Fink* [1980] folding model will infer properties of the surface, including stresses related to the folding and the deformation strain rate. This folding model has a trough-crest upper-layer thickness *H,* in which the viscosity decreases with depth as

$$\eta(z) = \eta_0 \exp(\gamma z) \quad (1)$$

where η_0 is the surface viscosity, z is depth, and γ describes the exponential decrease in viscosity. The viscosity of both layers is assumed to be Newtonian, meaning viscosity is

independent of stress [*Barr and Preuss*, 2010]. The viscosity ratio (*R*) between the base of the glacier (η_i) and surface viscosity layer of the folds (η_0) is defined by

$$R = \eta_o/\eta_i \qquad (2)$$

The thickness, *H*, is therefore defined as:

$$H = \left(\frac{1}{\gamma}\right) \ln (R) \qquad (3)$$

R is estimated to be $\leq 10^5$ estimated from the maximum activation energy estimated for Sputnik Planitia ices [*McKinnon et al.*, 2016b]. At this current time, exact viscosity values for Pluto-relevant ices and conditions are not constrained. According to *Fink's* [1980] folding model, folding occurs at the dominant wavelength L_D when L_D x γ > 28 (dimensionless unit). For the measured dominant wavelength L_D = 5.17 km, this becomes (1/γ) < 0.185 km. From this value, *H* ≈ 2.13 km. This value, however, is a magnitude larger than the observed DEM measurements (Figure 3b). R would need to be > 10^1 to match the current DEMs, though this difference could be due to viscous relaxation of the ridges in more recent geologic time, though relaxation processes of such ices are not yet known.

The basal layer of water ice on Enceladus (and noted for Pluto) can be in the range η_i ~ 10^{13} - 10^{15} Pa s [*Durham and Stern*, 2001; *Nimmo et al.*, 2016]. If the water ice below the methane upper boundary is warmed from the collision close to its melting point, we chose the maximum viscosity from *Durham and Stern* [2001] of η_i ~ 10^{15} Pa s, implying from Equation 2 that η_o ~ 10^{20} Pa s.

A requirement for folding is that the viscous driving stress must exceed the gravitational stress exerted by the weight of the surficial ice to bend [*Fink*, 1980]. The ratio between the driving stress and gravitational stress (*S*) is expressed as:

$$S = \rho g(\tfrac{1}{\gamma})/(4\dot{\varepsilon}\eta_o) \qquad (4)$$

Presently, no experimental CH_4-H_2O crystalline ice mixtures have been measured for density at such extreme conditions, so we propose the use of CH_4 density calculations for the upper layer. It has been observed that CH_4 is measured to have a density of ρ = 400 kg/m^3 at 45 K [*Yamashita et al.,* 2010; *McKinnon et al.,* 2016b]. For Pluto, gravity g=0.62 m/s^2. $\dot{\varepsilon}$ is the strain rate. According to the *Fink* [1980] folding model, $S \leq 0.02$ for folding to occur. Substituting $(1/\gamma)$ = 185 m gives an estimate for the driving stress $\sigma = \dot{\varepsilon}\eta_o$ calculated to be a maximum of 573.5 kPa. Comparably, this stress is moderately low compared to silicate bodies, though only slightly higher than observed normal faulting in proximity to Sputnik Planitia (≤ 290 kPa) [*Conrad et al.,* 2019]. These stresses are potentially the initial folding event on the entirety of the glacier before the proposed relaxation of the crust with relatively lesser stress.

The folded surface viscosity of η_0=10^{20} implies a maximum strain rate $\dot{\varepsilon} = \sigma/\eta_o$ = 5.735 x 10^{-15} s^{-1}. This is agreeable to the *Durham and Stern* [2001] range of strain rates for icy planetary surfaces to be $\dot{\varepsilon} \leq 10^{-14}$ s^{-1}. $\dot{\varepsilon} \geq 10^{-14}$ s^{-1} is relatively more dynamically active, mainly from immediate impact activity [*Durham and Stern*, 2001]. The time scale to resurface the Baret Montes glacier with folding T=$1/\dot{\varepsilon}$ is approximated to be a maximum 5.53 My. Note that this is not the determined age of the Baret Montes glacier in its entirety, but a relative emplacement duration of the folding process.

7.5 Discussion

The main results of this study as shown above has used the maximum viscosity variable for η_i = 10^{15} Pa s. However, *Nimmo et al.* [2016] modeled the Newtonian viscosity of the basal water ice layer at Pluto, specifically on Sputnik Planitia, to be η_i = 10^{14} Pa s. If the above instead used this secondary η_i variable for comparison, the resulting strain rate would become $\dot{\varepsilon}$ ~ 5.735 x

10^{-14} s^{-1}, which is within the strain rate range, although relatively more dynamic than the main result given above [*Durham and Stern,* 2001]. The folding duration time then becomes < 1 My, where the maximum η_i from the main results gives us a constraint on the time of creating such folds to be a maximum 5.53 My. Indeed, there is a dependence in understanding the viscosity of such ices at extreme compressional conditions to estimate the time evolution of the Baret Montes ridge formation.

Water ice is rigid over geologic time scales on Pluto and can support several kilometers of landform relief [*Stern et al.,* 2015; *Howard et al.*, 2017]. *Howard et al.* [2017] observed H_2O to be highly deformable for the purpose of glacial basal movements. CH_4 having a comparably lower deformability, the folding on Baret Montes would then greatly depend on shear stresses and compressibility against the solid water ice shores. However, we note that the rheology of these ice mixtures is still yet to be explored.

We hypothesize the basic sequence of the compressional ridge formation as follows. The glaciers described by *Umurhan et al.* [2017] have a water-ice base upon a convecting Sputnik Planitia upper surface layer (Figure 5a). This glacier is then driven towards the water ice shores in western Sputnik Planitia and Cthulhu Macula, initiating the compressional forces. This process folds the upper, weaker methane-water ice mixture layer, leaving the lower water ice layer mainly in the troughs and base of the Baret glacier (Figure 5b). However, there is a possible alternative hypothesis at play where these ridges could have formed before the Sputnik Planitia basin, then separated from the mainland from the Sputnik Planitia convective processes. A caveat in this alternative view is the presently unknown subsurface processes, especially those that would allow such ridge formations, are still being investigated.

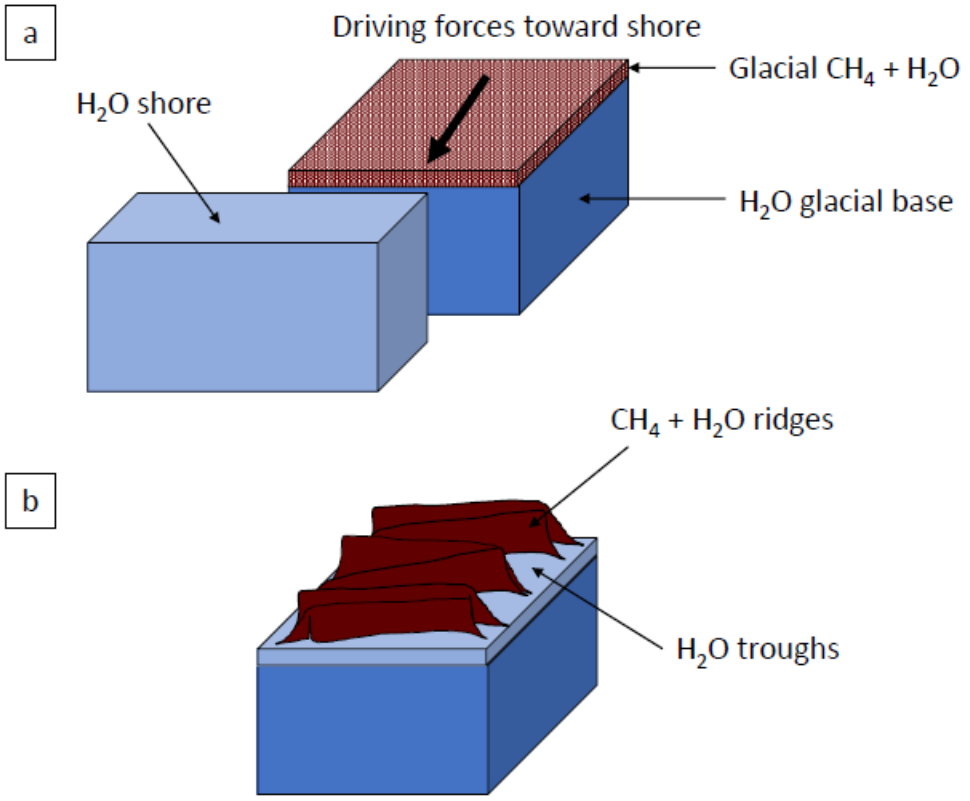

Figure 5: Schematic of the hypothesized mechanism for Baret Montes ridge formation. a) Basic components of a glacier on Sputnik Planitia with a water ice-dominant base and a weaker upper layer of methane-water ice mixtures. Convective forces from Sputnik Planitia push the glacier onto the water ice mainland, beginning the process of compressional strains. b) After the compressive forces, the remaining weaker methane-water ice layer now becomes remnant folds.

An interesting observation from LORRI images is that Baret Montes is the only major glacier on Sputnik Planitia that has a ridged surface with chaotic blocks, where the other lesser glacial structures mainly consist of blocky terrain [*Umurhan et al.,* 2017; *White et al.,* 2017]. A lack of ridges of these other glaciers would suggest that a localized convectional event occurred at the Baret glacier to force this water-ice block against the mainland after the formation of the Sputnik Planitia basin and in-filling with nitrogen ices [*Stern et al.,* 2015, 2018; *Moore et al.,* 2016; *White et al.,* 2017; *Buhler and Ingersoll,* 2018]. Other theories may be that the other glaciers do not have a layered body for the folding process, whether the glaciers are from different origins

(thus, different compositional makeup), or the convection processes across Sputnik Planitia are varying, which has been hypothesized by *Buhler and Ingersoll* [2018]. Further investigation to the strength of such ices and their role in glacial dynamics is needed.

7.6 Conclusions

While the origin of this glacier remains unknown, the folding patterns observed were analyzed for stress mechanisms and relative duration of the folds, which is estimated to be a maximum 5.53 My, within the emplacement time of the geologically young Sputnik Planitia basin at < 10 My. Based on geomorphologic and spectral observations, we infer the folded terrain observed on Baret Montes to be the remnants of a previous compressional stress process evidenced by the localization of those folds and implications of a thin upper-folding crust of methane-water ice composition. The *Fink* [1980] model uses a very simplified rheological description of the icy glacial layers in this scenario. The rheology of the glacial surfaces on Pluto is poorly constrained, so we considered it premature to include more complex viscosity-dependent deformation mechanisms. However, we note that this study may lead to promising future work on fold formation at low temperature conditions, layer mechanics of different ices (and different viscosities), and glacial processes across Sputnik Planitia specifically. Glaciers, especially with deformed, folded structures, are rare for outer solar system icy bodies. These compressional ridges may shed light on the glacio-dynamic processes on Pluto and the rheological conditions of ices.

7.7 Data

The LORRI images are archived in the Planetary Data System (PDS) Small Bodies Node at https://pds-smallbodies.astro.umd.edu/holdings/nh-p-lorri-2-pluto-v3.0/dataset.html. The

LEISA spectra are also archived in PDS at https://pds-smallbodies.astro.umd.edu/holdings/nh-p-leisa-3-pluto-v3.0/. There are no competing interests to declare.

7.8 Acknowledgements

We would like to thank the New Horizons mission for their excellent data production, Bernard Schmitt for the Pluto compositional maps, and the constructive reviews of two anonymous reviewers.

7.9 References

Barr, A., 2008, Mobile lid convection beneath Enceladus' south polar terrain: JGR 113, E07009. https://doi.org/10.1029/2008JE003114

Barr, A., and Preuss, L., 2010, On the origin of south polar folds on Enceladus: Icarus 208, 499-503. https://doi.org/10.1016/j.icarus.2010.03.038

Bland, M., McKinnon, W., Schenk, P., 2015, Constraining the heat flux between Enceladus' tiger stripes: Numerical modeling of funiscular plains formation: Icarus, 260, 232-245. https://doi.org/10.1016/j.icarus.2015.07.016

Buhler, P., and Ingersoll, A., 2018, Sublimation pit distribution indicates convection cell surface velocities of ~10 cm per year in Sputnik Planitia, Pluto: Icarus, 300, 327-240. https://doi.org/10.1016/j.icarus.2017.09.018

Conrad, J., et al., 2019, An upper bound on Pluto's heat flux from a lack of flexural response of its normal faults: Icarus, 328, 210-217. https://doi.org/10.1016/j.icarus.2019.03.028

Durham, W., and Stern, L., 2001, Rheological properties of water ice- Applications to satellites of the outer planets: Annual Review of Earth and Planetary Sciences, 29, 295-330. https://doi.org/10.1146/annurev.earth.29.1.295

Fink, J., 1980, Surface folding and viscosity of rhyolite flows: Geology 8, 250-254. https://doi.org/10.1130/0091-7613(1980)8<250:SFAVOR>2.0.CO;2

Fink, J., and Fletcher, R., 1978, Ropy pahoehoe: Surface folding of a viscous fluid: J. Volcanol. Geotherm. Res. 4, 151-170. https://doi.org/10.1016/0377-0273(78)90034-3

Grundy, W. et al., 2016, Surface compositions across Pluto and Charon: Science. 351, 6279, aad9189. 10.1126/science.aad9189

Hammond, N. et al., 2016, Recent Tectonic Activity on Pluto Driven by Phase Changes in the Ice Shell: GRL 43, 13, 6775-6782. https://doi.org/10.1002/2016GL069220

Helfenstein, P., and Porco, C., 2015, Enceladus' geysers: relation to geological features: The Astronomical Journal, 150, 96, 33 pp. doi:10.1088/0004-6256/150/3/96

Howard, A. et al., 2017, Present and past glaciation on Pluto: Icarus 287, 287-300. https://doi.org/10.1016/j.icarus.2016.07.006

McKinnon, W. et al., 2016a, Thermal Convection in Solid Nitrogen, and the Depth and Surface Age of Cellular Terrain Within Sputnik Planum, Pluto. In: 47th Lunar and Planetary Science Conference, Abstract 2921.

McKinnon, W. et al., 2016b, Convection in a volatile nitrogen-ice-rich layer drives Pluto's geological vigour: Nature, 534 (7605), 82-85. https://doi.org/10.1038/nature18289

Moore, J. et al., 2016, The geology of Pluto and Charon through the eyes of New Horizons: Science 351, 1284-1293. 10.1126/science.aad7055

Nimmo, F., et al., 2016, Reorientation of Sputnik Planitia implies a subsurface ocean on Pluto: Nature Letter, 540, 94-96. https://doi.org/10.1038/nature20148

Porco, C. et al., 2006, Cassini observes the active south pole of Enceladus. Science 311, 1393-1401. doi:10.1126/science.1123013.

Protopapa, S. et al., 2017, Pluto's global surface composition through pixel-by-pixel Hapke modeling of New Horizons Ralph/LEISA data: Icarus. 287, 218-228. https://doi.org/10.1016/j.icarus.2016.11.028

Reuter, D. et al., 2008, Ralph: A Visible/Infrared Imager for the New Horizons Pluto/Kuiper Belt Mission: Space Science Reviews, 140, 1-4, 129-154. https://doi.org/10.1007/s11214-008-9375-7

Roberts, J., and Nimmo, F., 2008, Tidal heating and the long-term stability of a subsurface ocean on Enceladus: Icarus 194, 675-689. https://doi.org/10.1016/j.icarus.2007.11.010

Schmitt, B. et al., 2017, Physical state and distribution of materials at the surface of Pluto from New Horizons LEISA imaging spectrometer: Icarus 287, 229-260. https://doi.org/10.1016/j.icarus.2016.12.025

Singer, K. et al., 2016, Craters on Pluto and Charon- surface ages and impactor populations. In 47th Lunar and Planetary Science Conference, Abstract 2310.

Singer, K. et al., 2017, Chaotic mountain blocks in Pluto's Sputnik Planitia. In: 49th AAS DPS meeting, Abstract 221.01.

Spencer, J. et al., 2009, Enceladus: An active cryovolcanic satellite. In: Saturn after Cassini-Huygens. Springer, New York, 683-722.

Stern, S., et al., 2015, The Pluto system: Initial results from its exploration by New Horizons: Science 350, 6258, aad1815. 10.1126/science.aad1815

Stern, S., et al., 2018, The Pluto system after New Horizons: Ann. Rev. Astron. Astrophys., 56, 357-392. https://doi.org/10.1146/annurev-astro-081817-051935

Trowbridge, A. et al., 2016, Vigorous convection as the explanation for Pluto's polygonal terrain: Nature, 534 (7605), 79-81. https://doi.org/10.1038/nature18016

Twidale, C., 1971, Structural Landforms. In: Australian National University Press Vol. 5.

Umurhan, O. et al., 2017, Modeling glacial flow on and onto Pluto's Sputnik Planitia: Icarus 287, 301-319. https://doi.org/10.1016/j.icarus.2017.01.017

White, O., et al., 2017, Geological mapping of Sputnik Planitia on Pluto: Icarus, 287, 261-286. doi:10.1016/j.icarus.2017.01.011.

White, O. et al., 2019, Washboard and fluted terrains on Pluto as evidence for ancient glaciation: Nature Astronomy, 3, 62-68. https://doi.org/10.1038/s41550-018-0592-z

Yamashita, Y. et al., 2010, Experimental study on the rheological properties of polycrystalline solid nitrogen and methane: Implications for tectonic processes on Triton: Icarus 207, 2, 972-977. https://doi.org/10.1016/j.icarus.2009.11.032

Chapter 8

Investigation of the morphology and interpretation of Hekla Cavus, Pluto

C. J. Ahrens[1], V. F. Chevrier[1]

[1] University of Arkansas, Center for Space and Planetary Sciences, Fayetteville, AR, 72701

8.1 Abstract

We describe and interpret the geometry and surficial characteristics of an oblong 95 km depression named Hekla Cavus in the (informally named) Cthulhu Macula, Pluto. The feature is located near the equator west of Sputnik Planitia at the Close Encounter Hemisphere. Images from the Long Range Reconnaissance Imager along with digital elevation maps reveal that the feature is part of a larger uplift system to the south, bounded by a raised rim with surficial fissures radiating from the rim. At the wall-floor contact, a mass wasting feature is also observed. The floor of the feature is asymmetric and oriented southwestward. These characteristics are not typical of craters or sublimation paterae on Pluto, suggesting this feature is of a different origin. This feature is measured to have 583 kPa of shear stress characterized with possible mechanisms of formation like that of a collapse from subsurface deflation, possibly from subglacial cryovolcanic processes. Such a feature could help define Plutonian cryo-volcanic evolution.

8.2 Introduction

On Earth, a caldera is generally regarded as a large, volcanic, quasi-circular depression, but because of the various characteristics of calderas on other planetary bodies, Wood (1984) suggested the definition to be a kilometer-scale wide, quasi-circular depression, not of impact origin, formed by collapse into a partially drained magma chamber, or release of glacial subsurface

material (e.g., glacio-volcanism). Landforms interpreted as calderas have formed on numerous terrestrial bodies, and so a variety of criteria has emerged with which to classify these landforms based on their morphology and structure (Francis 1993; Mouginis-Mark and Rowland 2001).

Cryovolcanism (i.e., eruption of molten material from within icy bodies) has been proposed for several worlds, namely Europa, Ganymede, Enceladus, Titan, and Triton (Kargel 1995; Lorenz 1996; Lopes et al. 2007; Jaumann et al. 2009). Our use of the tern cryovolcanism pertains to the transfer of subsurface materials either to the surface or movement from a depleted subsurface chamber, primarily as a result from internal processes, and excludes sublimation and condensation processes (Howard et al. 2017). Cryovolcanic activity then, according to Kargel (1995), includes eruptions of partly crystallized slurries derived by partial melting of ice-bearing materials (i.e., the addition of ammonia to form an ammonia-water ice cryo-magma material). In the case of Pluto, it has also been suggested that there is evidence for a subsurface fluid layer (Nimmo et al. 2016; Moore et al. 2016) and inferred presence of cryovolcanoes (Moore et al. 2016; Singer et al. 2018; Schenk et al. 2018) or cryovolcanic subsurface materials (Cruikshank et al. 2019).

The New Horizons Long Range Reconnaissance Imager (LORRI) obtained images of the Pluto surface during the spacecraft's targeted fly-by in 2015. These images obtained revealed Pluto to be a very geologically complex Kuiper Belt body (Moore et al. 2016). Of note, several features have already been proposed to be cryovolcanic in nature, namely the dome-like features Wright Mons and Piccard Mons (Moore et al. 2016; Singer et al. 2018). However, one feature north of these large domes (Figure 1) is a large irregular depression, named Hekla Cavus, situated on a much larger uplifted bulge (henceforth UB) outlined by mountain ranges. In this paper we discuss the possible cryovolcanic origin of this depression by considering its geological and morphometric context and providing a preliminary view on its evolution in relation to the UB.

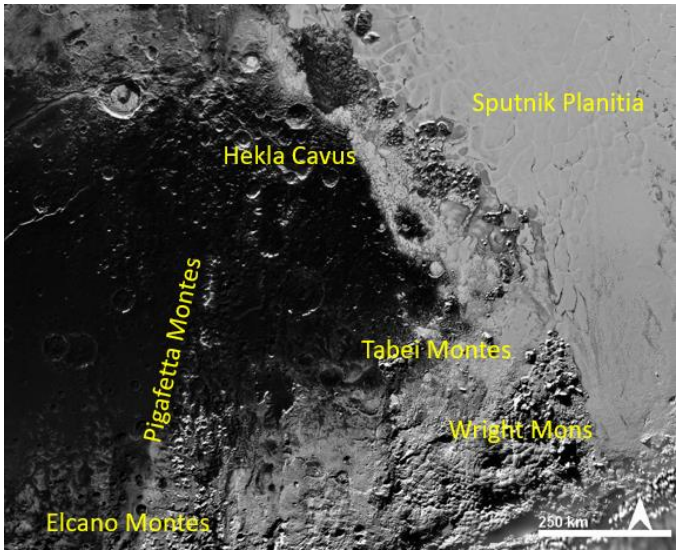

Figure 1: Context map of features mentioned throughout this report. Note that the orientation of Hekla Cavus is aligned with the mountain chains nearby. Arrow points north. Scale bar is 250 km.

8.3 Methods

Hekla Cavus and surrounding features described in this paper were identified using New Horizons Long Range Reconnaissance Orbiter (LORRI) images. High-resolution digital elevation models (DEMs) from stereographic techniques (from the MVIC hemispheric scans and LORRI mosaics) provided by Schenk et al. (2018) were used, which has a ± 100 m stereo height accuracy and a ground sample distance of <300 m/pixel. We used these DEMs for topographic profiles transecting the main cavus pit and the related morphology of the UB to the south (e.g., displacement, width). DEMs and LORRI images were processed in the Java Mission-planning and Analysis for Remote Sensing (JMARS) software (version 4.0.10) and to measure the associated UB heights and lengths. Caution was taken to measure the maximum vertical relief, as this would correspond to a minimum magnitude of erosion (Polit et al. 2009).

The Linear Etalon Imaging Spectrometer Array (LEISA) has mapped the spatial distribution of volatiles and other ice (e.g., H_2O, CH_4, CO) surface materials with adequate

resolution (3 km/pixel) to define spatial extent of materials and landform boundaries (Moore et al. 2016; Grundy et al. 2016; Schmitt et al. 2017).

8.4 Hekla Cavus Description

Hekla Cavus is an irregularly shaped depression about 95 km in diameter centered at 6.72°N, 154.41°E. From available DEMs and elevation maps (Figure 2), the feature is situated at an elevation of -1700 m relative to the Pluto datum. Note that Hekla Cavus is at the tip of the UB complex, which is outlined in arrows in Figure 2, and is observed to have a similar orientation to the UB.

We have identified and mapped a variety of units based on morphological variations in the LORRI images. Figure 3 shows an example of each morphological unit and provides a description for each unit type.

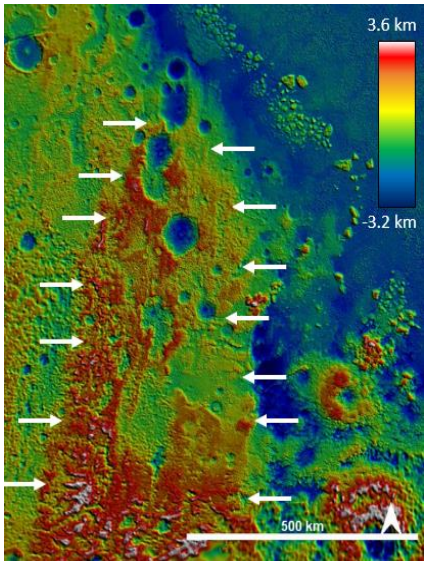

Figure 2: Colorized elevation map of the Hekla Cavus and UB area (outlined by white arrows). Scale bare at 500 km.

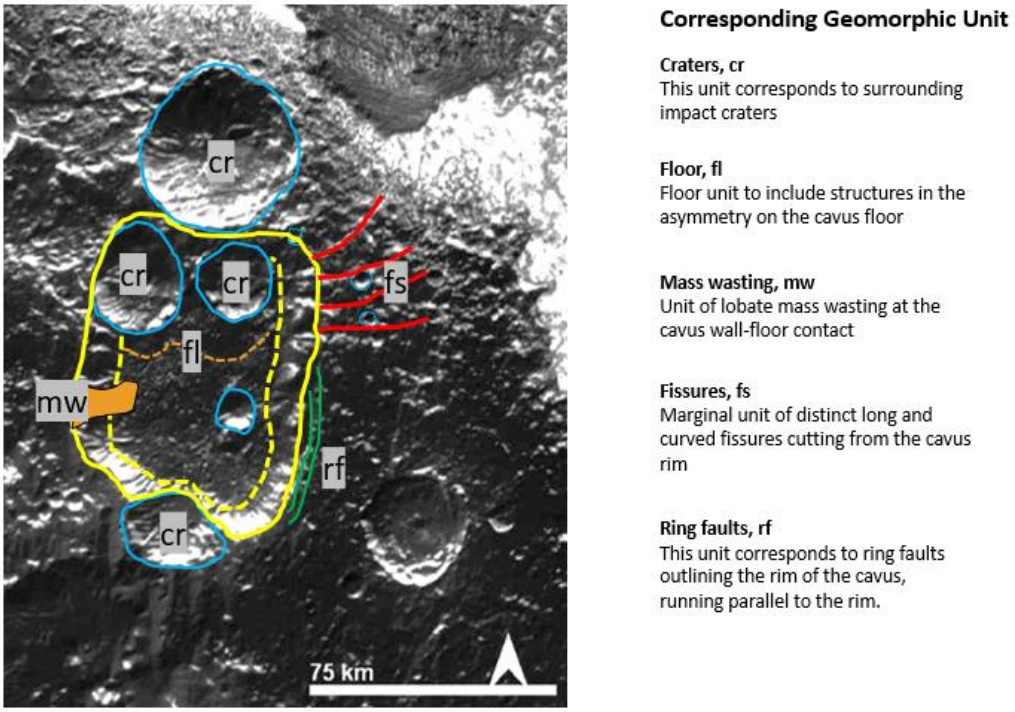

Figure 3: Overall geomorphic map of Hekla Cavus with labels indicating specific geomorphic units, listed below with descriptions of each unit.

8.4.1 Physical Setting and Uplift Bulge

Hekla Cavus is within the (informally named) Cthulhu Macula region, which is a heavily cratered and water-ice dominant region (Moore et al. 2016; Schmitt et al. 2017), implying it is an older area on Pluto as water ice is considered the base rock. To the east of Hekla Cavus is a methane-dominant slurry that outlines the western lobe of Sputnik Planitia (Schmitt et al. 2017). The Pigafetta and Elcano Montes alpine ridges are found in the southern portion of Cthulhu Macula (Figure 1), which implies an orogenic-based dynamic of uplifting (Moore et al. 2018; Schenk et al. 2018). This UB has an observable length of 950 km in a north-south orientation (though could be longer but limited by cutoff of New Horizons imaging into the dwarf planet's terminus shadow in the southern latitudes). The widest portion of the UB is 370 km, with it only being 88 km at Hekla Cavus. The eastern side of the UB has the Tabei Montes range and Wright Mons to the

southeast. This UB extends its bulge-like topography to the south, as observed in DEM traverses (Figure 4) and oblique 3D images (Figure 5).

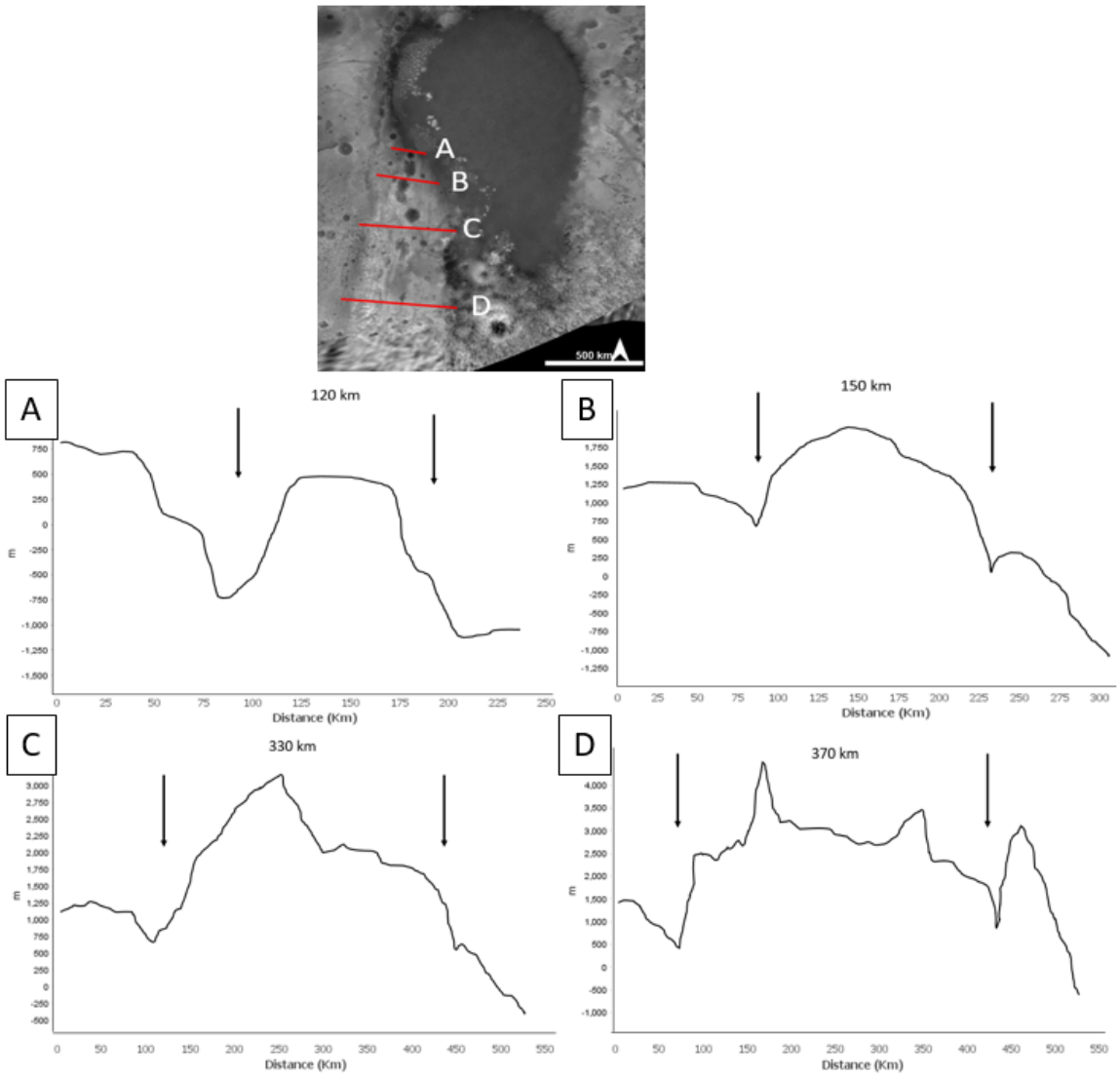

Figure 4: 300-m DEM map of the UB region with marked DEM traverses across the UB. Note the increase of extension of the UB traveling further south (edge of UB indicated by black arrows). Numbers in DEMs equal width between the black arrows.

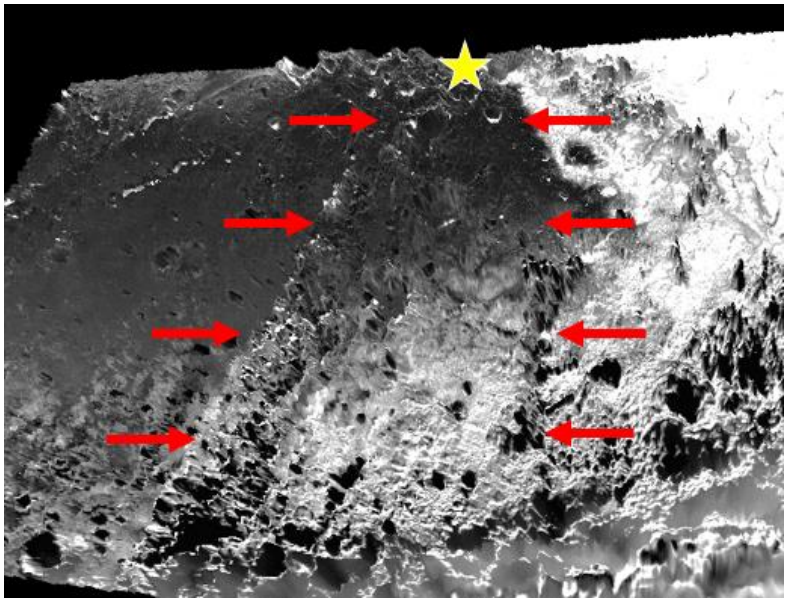

Figure 5: 3D oblique view of the Uplift Bulge (red arrows). Yellow star indicates the location of Hekla Cavus.

8.4.2 Collapse Geometry

The depression floor is relatively smooth as observed in the DEM profiles, though its northern region shows unevenness (Figure 6), possibly a secondary floor covering of material on top of the primary floor (unit *fl* in Figure 3). The distance from where the southern wall meets the primary floor to the start of the secondary floor is approximately 28 km. The depression walls show minor fluting and striations, probably due to in-fall of material. In treating Hekla Cavus as an inverted, elliptical, truncated cone, the overall volume of the landform is 10,300 km^3. On the immediate exterior of Hekla Cavus, we observed a slight bulge underlying the depression (Figure 7), showing an exterior asymmetry. This surrounding bulging is relevant to the much larger UB complex to the south.

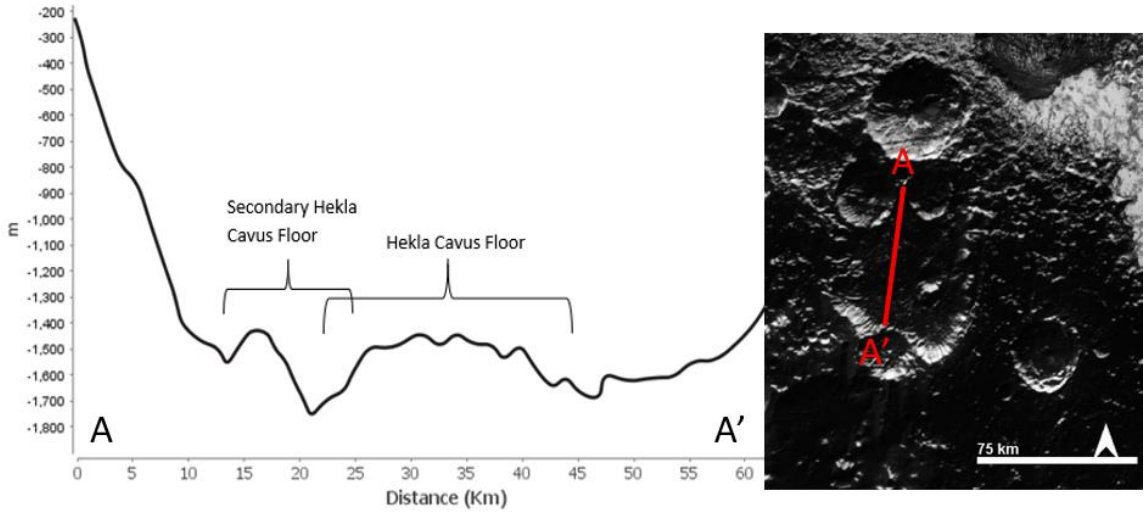

Figure 6: DEM profile of the Hekla Cavus floor showing the asymmetric main and secondary floor with respective Hekla Cavus image and marked DEM traverse.

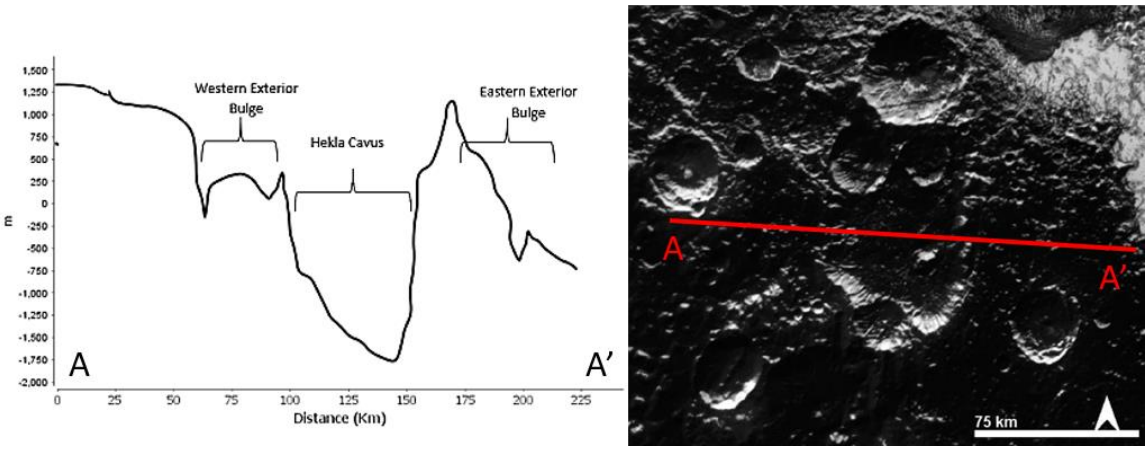

Figure 7: Exterior DEM profile of Hekla Cavus with accompanying marked DEM traverse image. Note the asymmetry of the bulge (being larger and more inclined) on the eastern side compared to the western side.

8.4.3 Fissures and Faults

To the southeast rim of Hekla Cavus are very thin ring fractures parallel to the caldera rim, oriented mainly east-northeast (Figure 8). Further up the eastern depression rim are longer fissures radiating outward with no apparent offset of geology. The longest fissure is measured at about 40

km. DEMs across these fissures show a depth of about 300 m each and are spaced ~7 km (Figure 9).

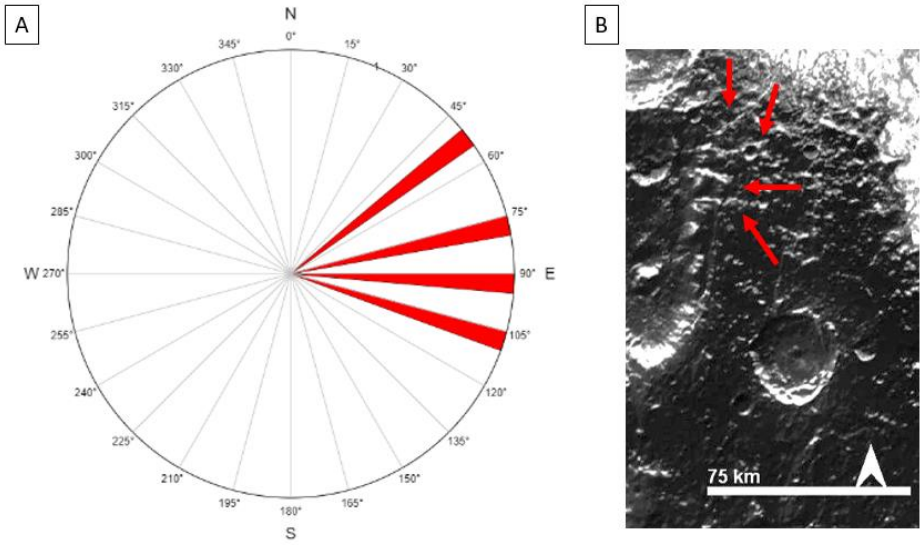

Figure 8: Rose diagram of the Hekla Cavus fissure orientation (A) with accompanying image (B) of the fissures radially outward from the depression (marked by red arrows).

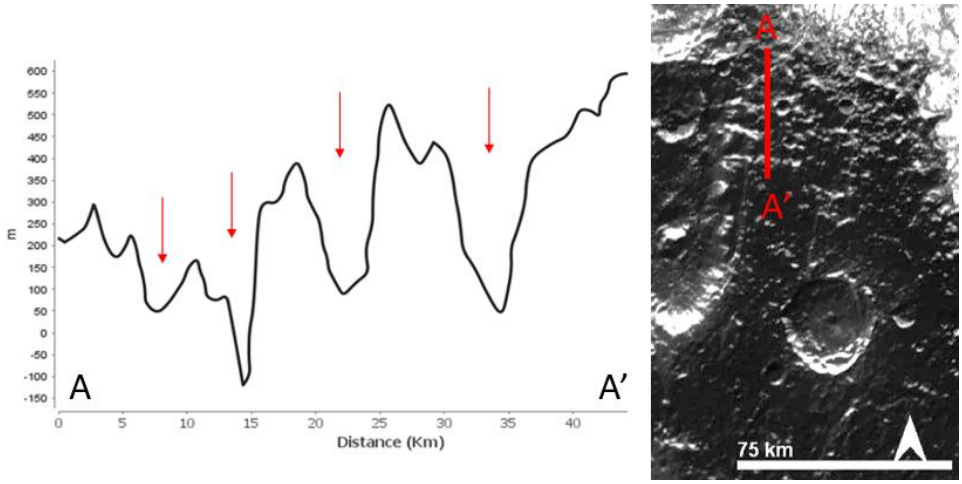

Figure 9: DEM profile showing the depth and spacing of the radial fissures, shown by the vertical red arrows with accompanying Hekla Cavus image with DEM traverse.

8.4.4 Mass Wasting

Mass wasting features also provide clues to a possible collapse activity. A lobate feature is observed at the western wall-floor contact (see Figure 1). We observed from the DEM profile

(Figure 10) a curvature from the depression wall. The lobate feature extends from the rim of Hekla Cavus to the floor at ~4 km.

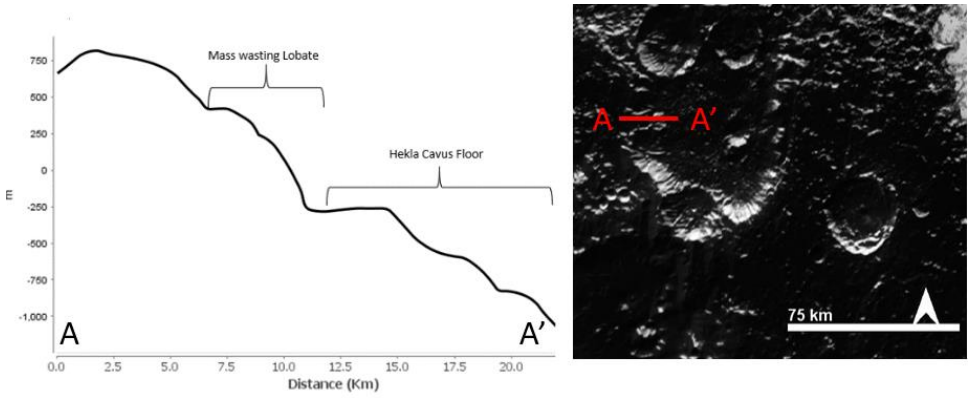

Figure 10: Lobate mass wasting DEM profile at the depression wall-floor contact with supplementary DEM traverse image.

8.4.5 Compositional setting

The volatile ices in this area (with respect to specific absorption bands from LEISA, see Schmitt et al. 2017) are water ice (H_2O; 1390 – 2060 nm), methane (CH_4; 1700 nm), and carbon monoxide (CO; 1578 nm). While the base rock in Cthulhu Macula is dominantly H_2O ice (Figure 11), CH_4 and CO have also been identified. CH_4 is observed on the Hekla Cavus rim, with spectral detections in the mass wasting feature and the fissures. CO is also mainly observed at the rim.

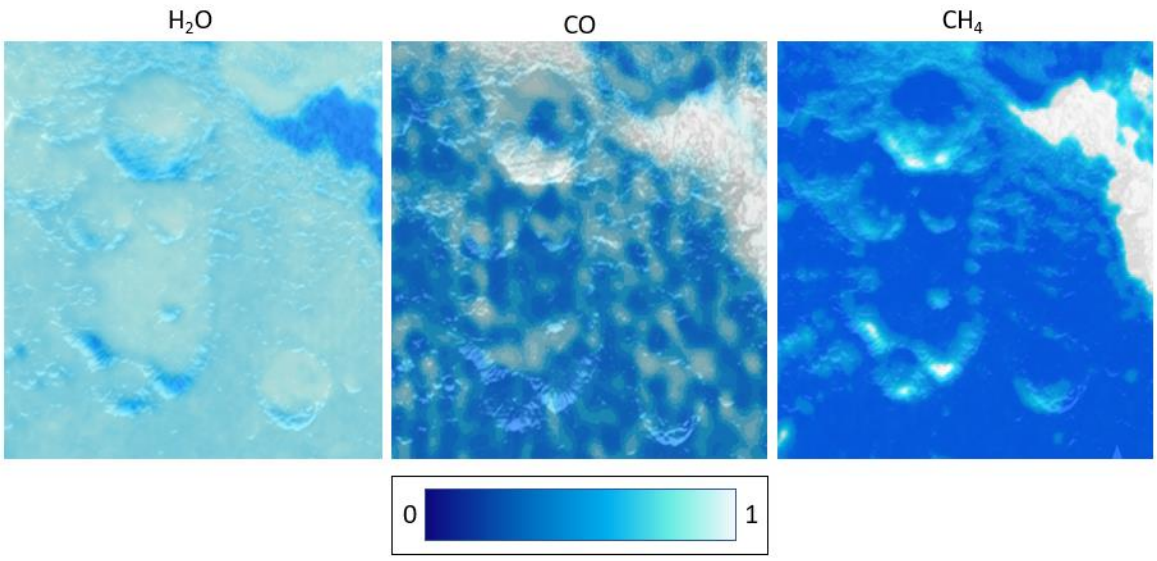

Figure 11: LEISA maps of H_2O, CO, and CH_4 at Hekla Cavus. Scale bar relates to relative abundance levels (for more information, refer to Schmitt et al. 2017).

8.5. Interpretation

8.5.1 Comparison with craters

Basin-forming impacts induce concentric features (Chapman and McKinnon 1986; Spudis 1993) that can accommodate mass wasting along the crater walls. On icy bodies, ejecta deposits can be masked from excavated ice, secondary craters, heavily eroded walls (or fluting), and in-filling on the crater floor, usually of different albedo (Dence 1972; Pappalardo and Collins 2005; Greeley 2013; Sori et al. 2019). However, craters elsewhere in water-dominant regions, such as Cthulhu Macula show substantial weathering, as evidenced by their softened rims and rugged floors (Singer et al. 2019). For Pluto, the global crater population is extremely non-uniform, displaying large variations in diameters from 15 – 200 km (Robbins et al. 2017; Singer et al. 2019). For the simple to complex crater transition on Pluto, according to Greenstreet et al. (2015), is D = 4 km. However, it should be noted that we are comparing impact craters in water-ice dominant regions, as nitrogen and methane-dominant impact craters are proposed to have different impact

scaling and erosional effects (Greenstreet et al. 2015). From the Singer et al. (2019) study, the average crater diameter in the Cthulhu Macula region (which had a survey of 902 craters) was 9.5 km. Two craters in the Cthulhu Macula region exceeded the Hekla Cavus diameter (Figure 12). For comparison purposes, these craters display central bulging (or central peaks), wide circular rims, and crosscut by relatively younger fossae. No observable bulging was observed at these Cthulhu Macula impact craters. Hekla Cavus does show preserved observable fluted walls, but no secondary crater for that size, no ejecta blanket (or halo of other icy material), and a relatively smooth, albeit an asymmetrical, floor.

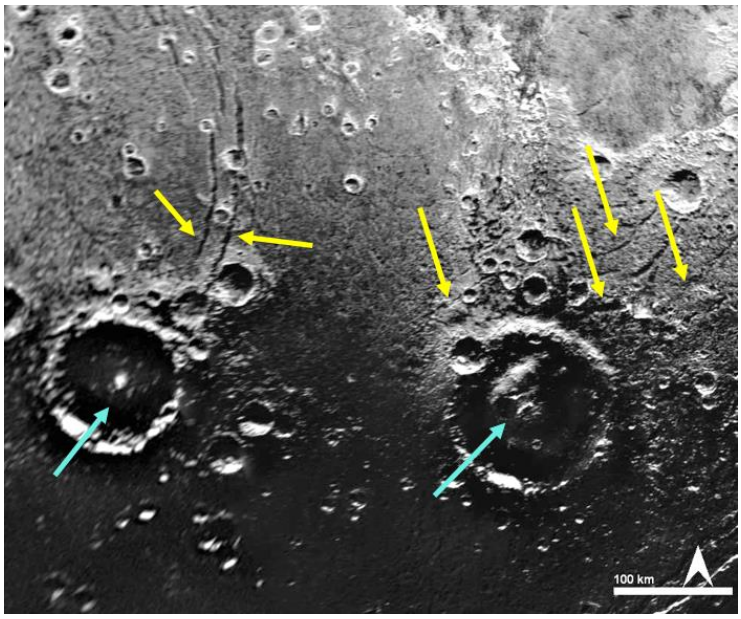

Figure 12: The two largest Cthulhu Macula craters as observed by a survey of impact craters across Pluto by Singer et al. (2019). Arrows point to specific geologic concerns, namely regional cross-cutting fossae (yellow) and central bulges or central peaks (blue). Image centered at 7.5°N, 100.6°E. Scale bar at 100 km. White arrow points north.

8.5.2 Comparison with sublimation-driven paterae

All icy satellites show evidence of mass movement and degradation, driven by several processes: mass wasting by gravity; impact bombardment; solar irradiation; or volatile sublimation

(Greeley 1985; Hartmann et al. 1981; Stephan et al. 2013). However, such externally formed depressions on icy bodies show morphological commonalities: 1) symmetrical walls, 2) smooth floors, and 3) a lack of external features (i.e., fissures). Pluto does show other types of surface depressions, namely sublimation-driven (Howard et al. 2017; Moore et al. 2017), and we consider them here, too, in comparison with Hekla Cavus (Figure 13). An example set of these other depressions are < 1,200 m deep and show heavily fluted walls, but have no evidence of fractures, fissures, or other types of strain radiating outward from their perimeters. Moreover, these depressions do not show any observable peripheral bulging that resembles the circular bulge as seen around Hekla Cavus. These pits are possibly sublimation-driven, as Howard et al. (2017) proposed the accumulation of ices in the depressions would undermine the outer walls and enlarge the pit, yet smooth crater and pit in-filling may be from cryo-volcanic in-filling (Howard et al. 2017; Sori et al. 2019).

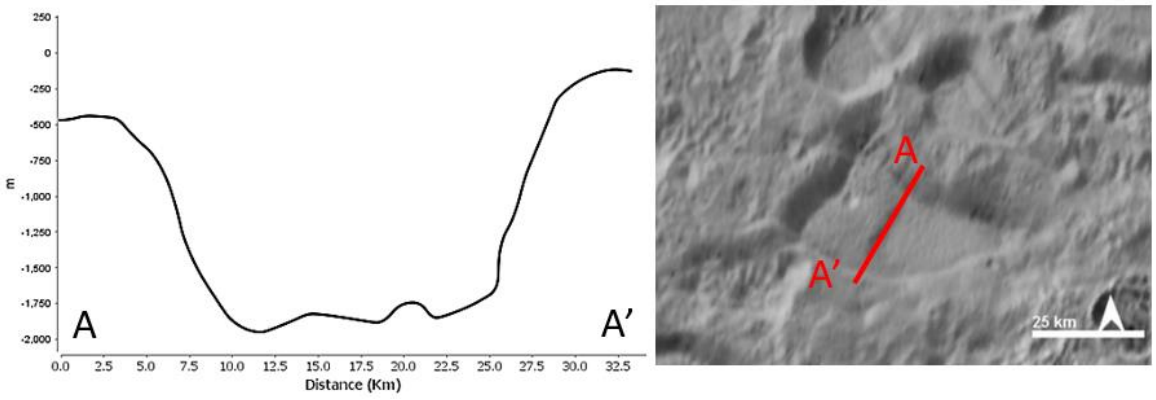

Figure 13: Example of a northern Pluto sublimation pit (57.88°N, 203.47°E) DEM profile and accompanying image with DEM traverse. Notice the relatively smooth floor and slight asymmetry of the pit rim, but not as significantly asymmetric as Hekla Cavus. Arrow points north. Scale bar at 25 km.

8.5.3 Estimates of removed ice volume

In order to evaluate the proposed subglacial volcanism model for Hekla Cavus, calorimetric estimates were made for a hypothetical eruption to determine the volume of cryo-magma material that would have been required to remove a volume of ice equal to the volume of the Hekla Cavus depression (Björnsson 1983; Pinel and Jaupart 2005). Depression volumes were determined by calculating the volume between the DEM surface and a plane defined by the average elevation around the depression rim (reported error is 1 standard deviation). The measured volume of Hekla Cavus, as previously discussed, is 10,300 km^3. We assume that all volume between the depression floor and the surrounding terrain was lost during depression formation, and that no pre-existing cavities existed or were filled during the emplacement of the cryo-magmatic substrate. The volume of cryo-magmatic material required to essentially melt (and collapse) this volume of material, assuming it is pure water ice, *Vc*, is (from Gudmundsson et al. 2004; Ghatan 2003):

$$V_c = (\rho_i L_i V_i)(\rho_c C_c \Delta T)^{-1} \quad (1)$$

where *i* indicates the surface water ice, *c* indicates cryo-magma, ρ is density, *L* is latent heat of water ice, *V* is volume, *C* is specific heat, and *T* is temperature difference between the cryo-magma and surficial water ice. We assume 100% efficiency in heat transfer between cooling cryo-magma and surface ice in order to calculate a minimum energy (cryo-magma volume) required to produce the Hekla Cavus depression.

The density of Pluto's crustal material (ρ_i) is 1,854 kg m^{-3} and the latent heat (L_i) is 333 kJ kg^{-1} (Kamata et al. 2019). From Kargel (1998), the density of an ammonia-water ice cryo-magma is 980 kg m^{-3} for temperatures < 200 K and a good estimate for ΔT with an ammonia-water ice interface is ΔT=136 K. The specific heat (C_c) for pure ammonia-water at ~40 K is 8,494 J kg^{-1} K^{-1} (Overstreet and Giauque 1937). With these references and measured volume of Hekla Cavus, the

volume of cryo-magmatic material needed to produce the Hekla Cavus depression would be 5,617 km^3. We neglect heat loss to warming of any icy debris within the depression because the ice mixing ratio is unknown as is the temperature gain.

For comparison, the case where cryo-magmatism results in the sublimation of ice to form a depression was taken into consideration. Taking a 100% sublimation case, Eq. (1) is modified such that L_i is replaced with L_{is}, the latent heat of sublimation for water ice (2.83×10^6 J kg^{-1}). The resulting cryo-magmatic volume required to sublimate the ice within the Hekla Cavus depression is then calculated to be 47,700 km^3, nearly 5 times the volume of Hekla Cavus, furthering the doubt that this depression was simply caused by only sublimation processes.

8.5.4 Shear Stresses

The strength of the lithosphere supporting the Hekla Cavus collapse and the UB topography may also be estimated from the morphometry if the elastic thickness of the lithosphere is known. The elastic thickness, *Te*, is the effective thickness in which the lithosphere can support elastic stresses over geologic timescales (Barnett and Nimmo 2002). We used *Te* = 10 km as an upper bound, as previously studied by Conrad et al. (2019). The value of predicting a maximum resolved shear stress σ_{max} is given by (Jackson and White 1989):

$$\sigma_{max} = \frac{\rho_i g h}{2e} \; if \; \frac{\lambda}{T_e} < \frac{\pi}{2} \qquad (2)$$

Where ρ_i is the density of the basement material, as previously used in Equation 1, g is the gravitational acceleration (0.62 m s^{-2}), h is the maximum vertical displacement of the Hekla Cavus depression or the UB, e is the base of natural logarithms, and λ is the wavelength (width) of the Hekla depression or UB.

Taking the *h* and λ from the elevation profiles into Eq. (2), the maximum shear stresses of the Hekla Cavus ranged from 442.3 – 583.2 kPa (Figure 14), which is within range of the low stress regime from Conrad et al. (2019) of the Inanna fault system on Pluto. These maximum shear stresses are relatively higher at the secondary floor and the southern wall. The derived maximum shear stresses of the associated UB topography shows a larger range of stresses, from 60 – 842 kPa (Figure 15), with relatively higher stresses at Hekla Cavus and further south at the bases of the Elcano and Tabei Montes mountain ranges. We take note that the other associated pits and depressions within the UB boundaries do not have observably high shear stresses compared to Hekla Cavus.

The variation in shear stresses at the UB implies several factors, namely (i) the base of mountainous structures (e.g., Elcano, Tabei, etc.) show increased shear stresses due to their proposed tectonic nature (Moore et al. 2016; Grundy et al. 2016); (ii) the base of the putative cryovolcanoes Wright and Piccard Mons show the highest levels of shear stresses at the UB edges, suggesting stresses from subsurface cryo-materials and lithospheric interactions; (iii) localized stress at Hekla Cavus, specifically the southern portion of the depression, denotes a previously active region, tectonically-speaking, in the UB.

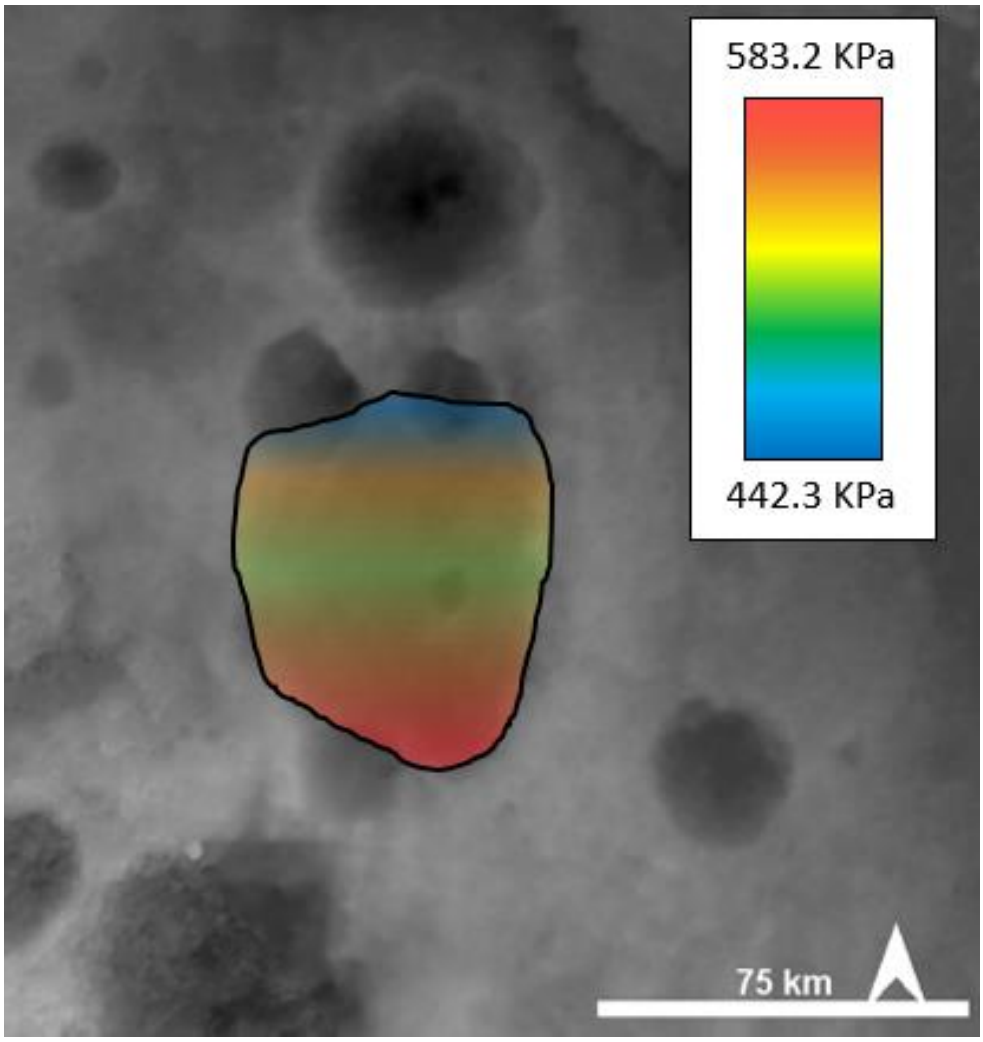

Figure 14: Colorized maximum shear stresses of Hekla Cavus overlain on a 300-m elevation map. Color bar for reference of measured shear stresses. Note that the secondary floor and the southern portion of the cavus has relatively higher shear stresses. Scale bar at 75 km. Arrow points north.

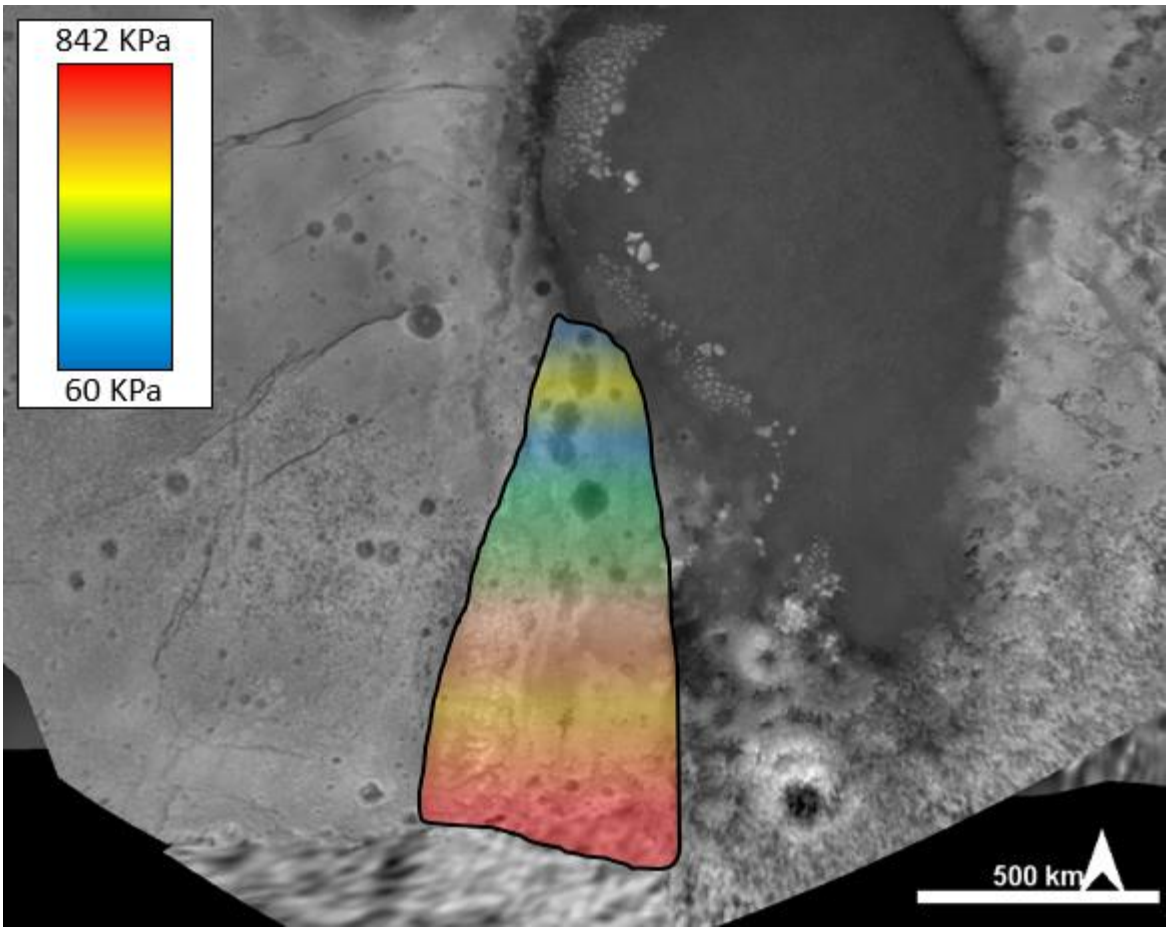

Figure 15: Colorized maximum shear stresses of the UB overlain on a 300-m elevation map. Color bar for reference of measured shear stresses. Note that Hekla Cavus and further south at the bases of Tabei and Elcano Montes mountains show relatively higher shear stresses. Scale bar at 500 km. Arrow points north.

8.5.5 Modes of Collapse Formation

Determining the process (or processes) for the origin and post-collapse evolution of Hekla Cavus is a challenge because the observations of calderas on terrestrial bodies may not directly relate to the processes at work on an icy body. The issue of the origin of the depression itself is the current lack of information on the interior of Pluto to accurately form an analysis of the subsurface movements to form the collapse event. However, we hypothesize that collapse of a caldera-like structure from a previous built-up mound, as observed from DEM profiles of a surrounding bulge,

remains basic in the dynamics, as illustrated in Figure 16. We propose that the UB, with greater stresses near the observed cryo-volcanic edifices of Wright and Piccard Mons, would have bulged upward from subsurface forces of cryo-materials (e.g., lenses of cryo-liquids). Further north toward Hekla Cavus are several large pitted formations, each possibly a collapse event from the bulging of subsurface material upward, then shifting, depleting the cryo-magmatic material, thus the lithospheric support.

Cryo-slurries also have motion in a subsurface context. On icy bodies, there are substantial reservoirs (e.g., lenses) of subsurface water (or including cryo-like materials, like ammonia) (Lopes and Carroll, 2008; Lopes et al., 2013), as we have seen several examples of depressions on other icy bodies, such as Ganymede and Triton having scalloped depressions, though their origins are still being investigated (Allison 1987; McKinnon et al. 2001; Spaun et al. 2001; Lopes and Carroll 2008). Observing fissures radially outward of a collapsed depression and circumferential ring faults along the rim show a commonality amongst collapse features associated with deflated magma chambers and caldera formation (Folch and Marti 2004; Acocella 2006; Geyer et al. 2006; Michon et al. 2009; Gudmundsson 2016). Since Hekla Cavus is observed to be near a solid-slurry interaction at Sputnik Planitia, this could give a clue to any previous activity of subsurface material movement. It is noted that most volcanic structures on terrestrial bodies are primarily found in differing compositional settings, like mantle slurry- crustal solids (Bosworth et al. 2003). Hekla Cavus also has observable CO ices at the rim (Figure 11). CO is a key volatile for gas-driven fluid ascent for cryovolcanism, according to Neveu et al. (2015).

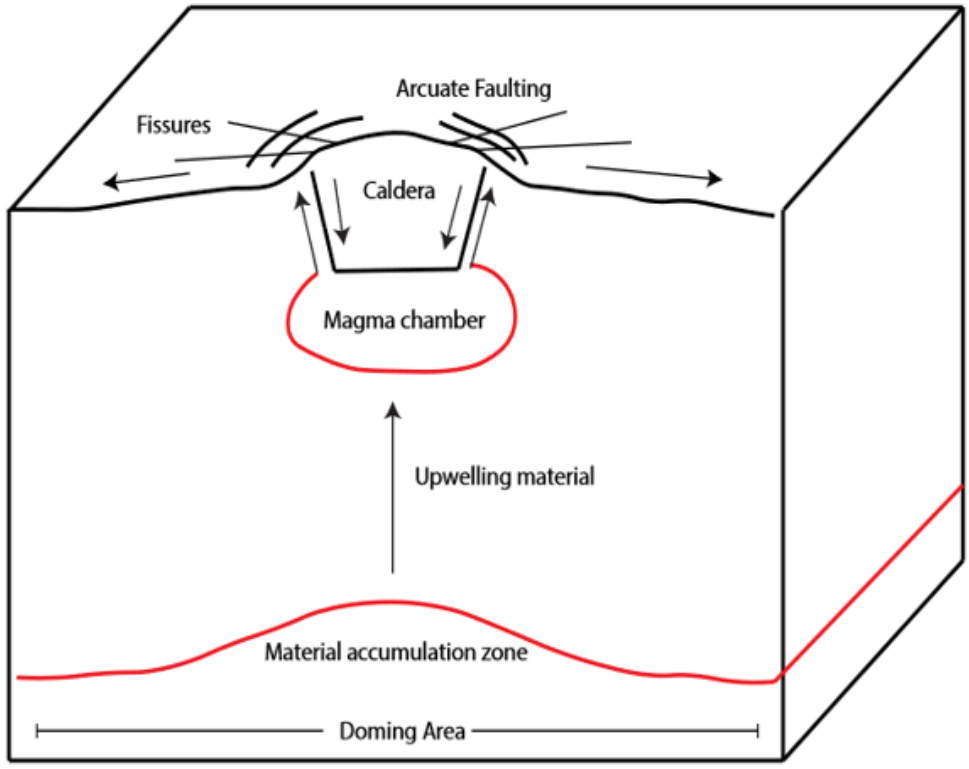

Figure 16: Cross-section of a typical caldera evolution with observed Hekla Cavus exterior features, such as the arcuate (ring) faults and fissures. The observed bulging surrounding Hekla Cavus may result from magmatic pressure that gives rise to slight doming pre-collapse. Adapted from Gudmundsson (2008).

8.6 Conclusions

Measurements of Hekla Cavus reveal differences in the maximum shear stress distribution that imply spatial variations in not only the entirety of the depression cavity, but in relation to the Uplifted Bulge system. This implies a rich, dynamic subsurface history at very localized regions in this hemisphere of Pluto, including a cryovolcanic disturbance related to a major tectonic uplifting of the icy lithosphere near putative cryovolcanic constructs.

Using an assortment of techniques, including morphometry and depression wall displacements, we suggest that Hekla Cavus is a subglacial cryo-volcanic collapse as part of the Uplifted Bulge complex of tectonic variety. The asymmetry and morphological differences, such

as fissures, of Hekla Cavus, along with an observed mass wasting lobe, also gives a clue to the displacement and collapse of material rather than influence from simply sublimation or impact. Because of its morphology, both exterior and interior, we can conclude that this depression on Pluto is of glacio-volcanic origin from a subsurface-material collapse event.

A post-collapse cryo-volcanic formation on Pluto is intriguing because it exhibits common characteristics to calderas in the solar system; yet there are significant aspects of this feature being unique to Pluto, or icy bodies in general, particularly the mass wasting lobate feature, surrounding bulge, and fissuring.

We are still in the preliminary stages of understanding geologic formations of any previous (or current) activity on Pluto. This feature may follow formation mechanisms considered for planetary glacio-volcanic calderas, yet the interaction and fluidity of subsurface material remain unanswered. Such planetary formations give insight to planetary interior processes and tectonism. Further analysis of collapse features on Pluto will lead to a better understanding of depression formation and evolution, especially on icy bodies where observational data is limited.

8.7 Acknowledgements

Support for the authors was made possible by the NASA Solar System Workings Research Program #80NSSC19K0163. We thank the New Horizons team and NASA/SwRI for their efforts in making the LORRI images available and Dr. Paul Schenk for the availability of DEMs. We also thank A. Gudmundsson (Nordic Volcanological Institute, University of Iceland), P. Byrne (North Carolina State University), and J. Olgin (University of Texas at El Paso) for their helpful comments. The LORRI images are archived in the Planetary Data System (PDS) Small Bodies Node at https://pds-smallbodies.astro.umd.edu/holdings/nh-p-lorri-2-pluto-v3.0/dataset.html. The

LEISA spectra are also archived in PDS at https://pds-smallbodies.astro.umd.edu/holdings/nh-p-leisa-3-pluto-v3.0/. There are no competing interests to declare.

8.8 References:

Acocella, V., 2006, Caldera types: How end-members relate to evolutionary stages of collapse: Geophysical Research Letters, v. 33, L181314, p. 1-5. https://doi.org/10.1029/2006GL027434

Allison, M., 1987, Ice-covered water volcanism on Ganymede: Journal of Geophysical Research, v. 92, p. 7865-7876. https://doi.org/10.1029/JB092iB08p07865

Barnett, D., Nimmo, F., 2002. Strength of faults on Mars from MOLA topography. Icarus, 157, 34-42. doi:10.1006/icar.2002.6817

Björnsson, H., 1983. A natural calorimeter at Grímsvötn: indicator of geothermal and volcanic activity. Jökull 33, 13–18.

Bosworth, W., Burke, K., Strecker, M., 2003, Effect of stress fields on magma chamber stability and the formation of collapse calderas: Tectonics, v. 22, p. 1042. https://doi.org/10.1029/2002TC001369

Chapman, C., McKinnon, W., 1986, Cratering of planetary satellites, in Buns, J., Matthews, M. (eds) Satellites: University of Arizona Press, Tuscon, p. 492-580.

Conrad, J., Nimmo, F., Schenk, P., et al., 2019. An upper bound on Pluto's heat flux from a lack of flexure response of its normal faults. Icarus, 328, 210-217. https://doi.org/10.1016/j.icarus.2019.03.028

Cruikshank, D., Umurhan, O., Beyer, R., et al., 2019. Recent cryovolcanism in Virgil Fossae on Pluto. Icarus, 330, 155-168. 10.1016/j.icarus.2019.04.023

Dence, M., 1972, The nature and significance of terrestrial impact structures, in Proceedings of the 24th International Geological Congress, v.15, p77-89.

Folch, A., Marti, J., 2004, Geometrical and mechanical constraints on the formation of ring faults calderas: Earth and Planetary Science Letters, v. 221, p. 215-225. https://doi.org/10.1016/S0012-821X(04)00101-3

Francis, P., 1993, Volcanoes: A Planetary Perspective. Oxford Univ. Press, New York, NY, pp 443.

Geyer, A., Folch, A., Marti, J., 2006, Relationship between caldera collapse and magma chamber withdrawal: An experimental approach: Journal of Volcanology and Geothermal Research, v. 157 (4), p. 375-386. https://doi.org/10.1016/j.jvolgeores.2006.05.001

Ghatan, G.J., 2003. Cavi Angusti, Mars: Characterization and assessment of possible formation mechanisms. Journal of Geophysical Research 108 (E5), 5045-19. doi:10.1029/2002JE001972.

Greeley, R., 1985, Planetary landscapes: George Allen and Unwin, London/Boston, p. 265.

Greeley, R., 2013, Introduction to planetary geomorphology: Cambridge University Press, p. 34-58.

Greenstreet, S., Gladman, B., McKinnon, W., 2015. Impact and cratering rates onto Pluto. Icarus, 258, 267-288. https://doi.org/10.1016/j.icarus.2015.05.026

Grundy, W., et al., 2016, Surface compositions across Pluto and Charon: Science, v. 351, aad9189. 10.1126/science.aad9189

Gudmundsson, A., 2008. Magma chamber geometry, fluid transport, local stresses and rock behaviour during collapse caldera formation. in Gottsmann, J. and Marti, J. (editors) Caldera Volcanism: Analysis, Modelling and Response, Amsterdam, Elsevier. p. 319

Gudmundsson, A., 2016, The mechanics of large eruptions: Earth-Science Reviews, v.163, p72-93. https://doi.org/10.1016/j.earscirev.2016.10.003

Gudmundsson, M.T., et al., 2004. The 1996 eruption at Gjalp, Vatnajokull ice cap, Iceland: efficiency of heat transfer, ice deformation and subglacial water pressure. Bull. Volcanol. 66, 46–65. https://doi.org/10.1007/s00445-003-0295-9

Hartmann, W., et al., 1981, Chronology of planetary volcanism by comparative studies of planetary cratering, in BVS Project (ed.) Basaltic volcanism on the terrestrial planets, Pergamon, Elmsford, p. 1050-1127.

Howard, A., et al., 2017. Pluto: Pits and mantles on uplands north and east of Sputnik Planitia. Icarus, 293, 218-230. https://doi.org/10.1016/j.icarus.2017.02.027

Jackson, J. A., and N. J. White 1989. Normal faulting in the upper continental crust: Observations from regions of active extension. J. Struct. Geol. 11, 15–36. https://doi.org/10.1016/0191-8141(89)90033-3

Jaumann, R., et al., 2009, Icy satellites: geological evolution and surface processes: Saturn from Cassini-Huygens: Springer, p. 637-681. https://doi.org/10.1007/978-1-4020-9217-6_20

Kamata, S., et al., 2019. Pluto's ocean is capped and insulated by gas hydrates. Nature Geoscience, 12, 407-410. https://doi.org/10.1038/s41561-019-0369-8

Kargel, J., 1995, Cryovolcanism on the Icy Satellites: Earth Moon Planets, v. 67, p.101-113. https://doi.org/10.1007/978-94-017-1092-3_12

Kargel, J., 1998. Physical chemistry of ices in the outer solar system. In: Solar System Ices Volume 1, B. Schmitt, et al. (eds.), Kluwer Academic Publishers.

Lopes, R., et al., 2007. Cryovolcanic features on Titan's surface as revealed by the Cassini Titan Radar Mapper. Icarus, 186, 395-412. https://doi.org/10.1016/j.icarus.2006.09.006

Lopes, R. and Carroll, M., 2008, Alien Volcanoes: Johns Hopkins University Press, p.99-124.

Lopes, R. et al., 2013, Cryovolcanism on Titan: New results from Cassini RADAR and VIMS: Journal of Geophysical Research Planets, v. 118, p. 416-435. https://doi.org/10.1002/jgre.20062

Lorenz, R., 1996. Pillow lava on Titan: Expectations and constraints on cryovolcanic processes. Planet. Space Sci., 44 (9), 1021-1028. https://doi.org/10.1016/0032-0633(95)00139-5

McKinnon, W., et al., 2001, Topographic and morphologic evidence for flooding of Ganymede's resurfaced terrains by 224 low-viscosity water-ice lavas: Houston, Texas, Lunar and Planetary Institute, Lunar and Planetary Science XXXII, Abstract 2179.

Michon, L., et al., 2009, How summit calderas collapse on basaltic volcanoes: New insights from the April 2007 caldera collapse of Piton de la Fournaise volcano: Journal of Volcanology and Geothermal Research, v. 184 (1-2), p. 138-151. https://doi.org/10.1016/j.jvolgeores.2008.11.003

Moore, J., et al., 2016, The geology of Pluto and Charon through the eyes of New Horizons: Science, v. 351 (6279), p. 1284-1293. 10.1126/science.aad7055

Moore, J. et al., 2017. Sublimation as a landform-shaping process on Pluto. Icarus, 287, 320-333. https://doi.org/10.1016/j.icarus.2016.08.025

Moore, J., et al., 2018. Bladed terrain on Pluto: possible origins and evolution. Icarus, 300, 129-144. https://doi.org/10.1016/j.icarus.2017.08.031

Mouginis-Mark, P., Rowland, S., 2001. The geomorphology of planetary calderas. Geomorphology, 37, 201-223. https://doi.org/10.1016/S0169-555X(00)00083-0

Neveu, M., Desch, S., Shock, E., Glein, C., 2015. Prerequisites for explosive cryovolcanism on dwarf planet-class Kuiper belt objects. Icarus, 246, 48-64. http://dx.doi.org/10.1016/j.icarus.2014.03.043

Nimmo, F., et al., 2016. Reorientation of Sputnik Planitia implies a subsurface ocean on Pluto. Nature, 540, 94-96. https://doi.org/10.1038/nature20148

Overstreet, R., Giauque, W., 1937. Ammonia: the heat capacity and vapor pressure of solid and liquid. Heat of vaporization. The entropy values from thermal and spectroscopic data. J. Am. Chem. Soc., 59 (2), 254-259. 10.1021/ja01281a008

Pappalardo, R., Collins, G., 2005, Strained craters on Ganymede: Journal of Structural Geology, v. 25, p827-838. https://doi.org/10.1016/j.jsg.2004.11.010

Pinel, V., Jaupart, C., 2005, Caldera formation by magma withdrawal from a reservoir beneath a volcanic edifice: Earth and Planetary Science Letters, v. 230, p. 273-287. https://doi.org/10.1016/j.epsl.2004.11.016

Polit, A., Schultz, R., Soliva, R., 2009. Geometry, displacement-length scaling, and extensional strain of normal faults on Mars with inferences on mechanical stratigraphy of the martian crust. Journal of Structural Geology, 31, 662-673. doi:10.1016/j.jsg.2009.03.016

Robbins, S., et al., 2017. Craters of the Pluyto-Charon system. Icarus, 287, 187-206. https://doi.org/10.1016/j.icarus.2016.09.027

Schenk, P., et al., 2018. Basins, fractures and volcanoes: Global cartography and topography of Pluto from New Horizons. Icarus, 314, 400-433. https://doi.org/10.1016/j.icarus.2018.06.008

Schmitt, B., et al., 2017. Physical state and distribution of materials at the surface of Pluto from New Horizons LEISA imaging spectrometer. Icarus, 287, 229-260. https://doi.org/10.1016/j.icarus.2016.12.025

Singer, K., et al., 2018. Cryovolcanism on Pluto and Charon. EGU General Assembly, 20, Geophysical Research Abstracts 5761.

Singer, K., et al., 2019. Impact craters on Pluto and Charon indicate a deficit of small Kuiper belt objects. Science, 363 (6430), 955-959. 10.1126/science.aap8628

Sori, M., Bapst, J., Becerra, P., Byrne, S., 2019. Islands of ice on Mars and Pluto. JGR Planets, 124, 2522-2542. https://doi.org/10.1029/2018JE005861

Spaun, N., et al., 2001, Scalloped depressions on Ganymede from Galileo G28 very high resolution imaging: Houston, Texas, Lunar and Planetary Institute, Lunar and Planetary Science XXXII, abstract 1448.

Spudis, P., 1993, The geology of multi-ring impact basins: Cambridge University Press, p. 107-108.

Stephan, K., Jaumann, R., Wagner, R., 2013, Geology of Icy Bodies, in Gudipati, M. and Castillo-Rogez, J. (eds.), The Science of Solar System Ices: Astrophysics and Space Science Library, p. 279-347.

Wood, C., 1984, Calderas: a planetary perspective. J. Geophys. Res., 89, 8391-8406. https://doi.org/10.1029/JB089iB10p08391

Chapter 9

Geometry, shear stress, and roughness of faults in central Cthulhu Macula, Pluto

C.J. Ahrens[1], P.K. Byrne[2], V.F. Chevrier[1]

[1]Arkansas Center for Space and Planetary Science, University of Arkansas, Fayetteville, AR 72701

[2] Planetary Research Group, Department of Marine, Earth, and Atmospheric Sciences, North Carolina State University at Raleigh, Raleigh, North Carolina, 27695

9.1 Abstract

We present new measurements of fault morphometry from four areas in the central Cthulhu Macula region on Pluto to investigate fault geometry and growth, displacement-length (D_{max}-L) ratio comparisons, maximum shear stresses, and roughness scaling using a variety of techniques. The Virgil Fossae and Beatrice Fossa faults exhibit a relatively higher D_{max}-L ratio (~10^{-1}) than Hermod and Kaknú Fossa (~10^{-2}), implying that Virgil and Beatrice are consistent with more deeply penetrating faults that are not restricted to depth. Beatrice Fossa also has the highest measured shear stress relative to the other central Cthulhu Macula faults, relating to a large slippage rate and higher roughness scale, implying a relatively younger faulting mechanism and more variable stress across the fault. The results suggest that fault dimensions record variations in the displacement-length ratios, maximum shear stresses, and stress field heterogeneity. We suggest that the Cthulhu Macula faults display a wide range of geologic history and fault dynamics, giving us insight to the fault evolution on Pluto.

9.2 Introduction

Geologic mapping of Pluto's surface from the techniques and mapping of previous studies (Moore et al. 2016; Schenk et al. 2018; Cruikshank et al. 2019) have shown that Pluto's surface has a variety of faulted regions. One of the largest water-ice based regions on Pluto is the Cthulhu Macula (informally named) to the southeast of Sputnik Planitia. This dark reddish region consists of some of the widest extensional features > 200 km in length.

Fault displacement dimensions and displacement-length (D_{max}-L) ratios have been used on Earth and Mars to understand fault growth (Scholz et al., 1993; Scholz, 1997; Schultz and Fossen, 2002; Soliva and Benedicto, 2005). These studies have shown that there is a linear relation between D_{max} and length (L), or width of the fault (Figure 1), in that isolated faults grow proportionally in height (here we define it as D_{max}) and width (Cowie and Scholz, 1992a,b; Dawers et al., 1993; Schlische et al., 1996; Clark and Cox, 1996; Scholz, 2002; Schultz et al., 2006, 2008). Displacement dimensions along a fault are controlled by factors such as fault shape (i.e. aspect ratio), length/width, segment linkage, localized stresses, mechanical interactions with other faults, and the elastic properties of the host rock and other variations in the lithology (Schultz and Fossen, 2002; Schultz, 1999; Soliva and Schultz, 2008). Displacement-length ratios and respective slope trends can therefore be useful in investigating how these parameters affect the growth history and evolution.

Mechanical interactions with other faults and the surrounding lithology can restrict the fault growth, such that a contiguous layer inhibits downward fault propagation (Gross et al. 1997; Wilkins and Gross, 2002; Soliva and Benedicto 2005). In plotting the D_{max}-L scaling ratios, the unit slope (slope of the linear trend in plotting length and maximum displacement) reveals possible changes in scaling from linear to nonlinear (e.g., shallower trends on the D_{max}-L diagram). Figure

1 shows this displacement-length scaling conceptually. Shallower trends indicate the nonlinerarity of the fault system, giving us insight as to the inhibition of fault growth (Soliva and Benedicto 2005; Soliva and Schultz 2008).

Confinement of the fault modulates the magnitude of shear driving stresses on the fault. The strength of the faults supporting the extensional topography can be estimated from the geometry of the topography if the elastic thickness of the lithosphere is estimated (Keane et al. 2016; Conrad et al. 2019). Understanding the geometry of these faults can provide insight to variations and distributions of localized stresses, and possibly, how interactions (i.e. overlapping) of such faults may influence displacement and stresses.

The geometric and structural heterogeneity (such as fault roughness) as well as stress distributions can influence the expected magnitude and slippage within the fault (Segall and Pollard 1980; Schorlemmer et al. 2005; Goebel et al. 2017). Measuring the fault roughness from the topographic dimensions of the fault and associated localized stresses can provide information on the crustal properties and relative age of the fault.

We present a study of four major faults in the Cthulhu Macula region on Pluto. The graben-bounded faults are within a water-ice dominant area, though possible erosional processes from the covering of the extensive reddish surface material may influence upper fault wall morphology, but not to the extent of influencing depth-length fault evolution and stresses (Grundy et al. 2018). We use fault-related topography from data acquired by the New Horizons spacecraft to analyze and interpret fault growth from D_{max}-L ratios, maximum shear stresses, and infer mechanical properties of fault slippage and roughness scaling.

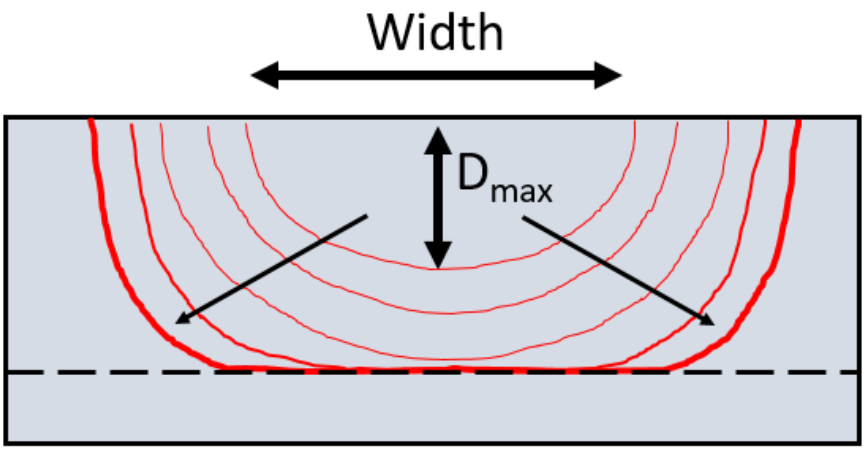

Figure 1: Conceptual illustration of fault evolution from unrestricted to restricted boundaries to influence fault growth. Adapted from Figure 1 of Polit et al. (2009).

9.3 Study Areas

The four study areas are in the western and central portion of the Cthulhu Macula province on Pluto (Figure 2a; Moore et al. 2016, Schenk et al. 2018). This dark-brown region spans longitudinally from ~ 20°E to ~ 160°E, covering an equatorial zone from 15°N to 20°S (Moore et al 2016; Cruikshank 2019). This region shows a variety of topographical and geological terrains, mantled by a layer of reddish-brown, low-albedo material (Grundy et al. 2018). From previous studies, (see Imanaka et al. 2004; Cruikshank et al. 2005; Materese et al. 2015) this dark coloring results from UV/charged-particle radiolysis/photolysis of atmospheric gases and surface ices, converting methane and nitrogen to complex organic molecules. While this mantling material may be thin enough to preserve fossae structures, some observations have been made to indicate localized thicknesses of material to obscure some crater features, or that other resurfacing processes are at work (Singer et al. 2016; Robbins et al. 2017; Cruikshank et al. 2019).

Virgil Fossae is a 798.3 km graben complex on the northern portion of Cthulhu Macula (5.56 °N, 123.37°E; Figure 2a). The complex set of graben are hypothesized to be a combination

of extensional stresses from a number of processes, including the global expansion of Pluto from a subsurface ocean freezing (Hammond et al. 2016; Moore et al. 2016), loading and consequent reorientation from the Sputnik Planitia basin (Nimmo et al. 2016; Keane et al. 2016). Virgil Fossae is in a NE-SW orientation, with the largest graben trough intersecting the northern rim of Elliot crater. The center of this 798.3 km main trough has a complex arrangement of strike-slip component branches. The largest graben trough in Virgil Fossae was the main portion used in this study with an average depth of elevation at 1.13 km (Figure 2b).

Beatrice Fossa (informal name) is a similar 358.7 km NE-SW oriented graben sub-parallel to Virgil Fossae, centered at 0.25°S, 128.66°E (Figure 2a). The origins of this fault are from similar processes as Virgil Fossae (Conrad et al. 2019). However, the lack of a more complex strike-slip like Virgil Fossae may give insight to a different localized stress field in that portion of Cthulhu Macula. Beatrice has a prominent segmented break of the main trough near a crater at the eastern part of the fault, with an average elevation depth at 1.25 km (Figure 2b). Beatrice intersects the VB fossae at its southern portion.

Hermod Fossae is observably the second-largest graben trough (712.1 km; 4.56°S, 120.47°E) in Cthulhu Macula (Figure 2a). Two main branches make up these fossae in an N-S orientation, notably intersecting the Virgil Fossae to the north. The intersecting nature of these fossae can give us insight to the relative age compared to both Virgil and Beatrice and could provide insight to the dynamics of overlapping graben, mainly localized stresses involved. The longest branch in the western section of this graben complex was the focus in this study and has an average depth elevation of 0.68 km (Figure 2b).

Kaknú Fossa is a 259.1 km graben on the southern portion of Cthulhu Macula (Figure 2a). This large graben, centered at 30.41°S, 120.47°E, shows numerous, smaller, parallel grabens, but

this study only focuses on the main graben, with an average elevation at 0.7 km (Figure 2b). Kaknú is oriented in a NW-SE direction, opposite to the other three large grabens. This graben also intersects a small crater to the east.

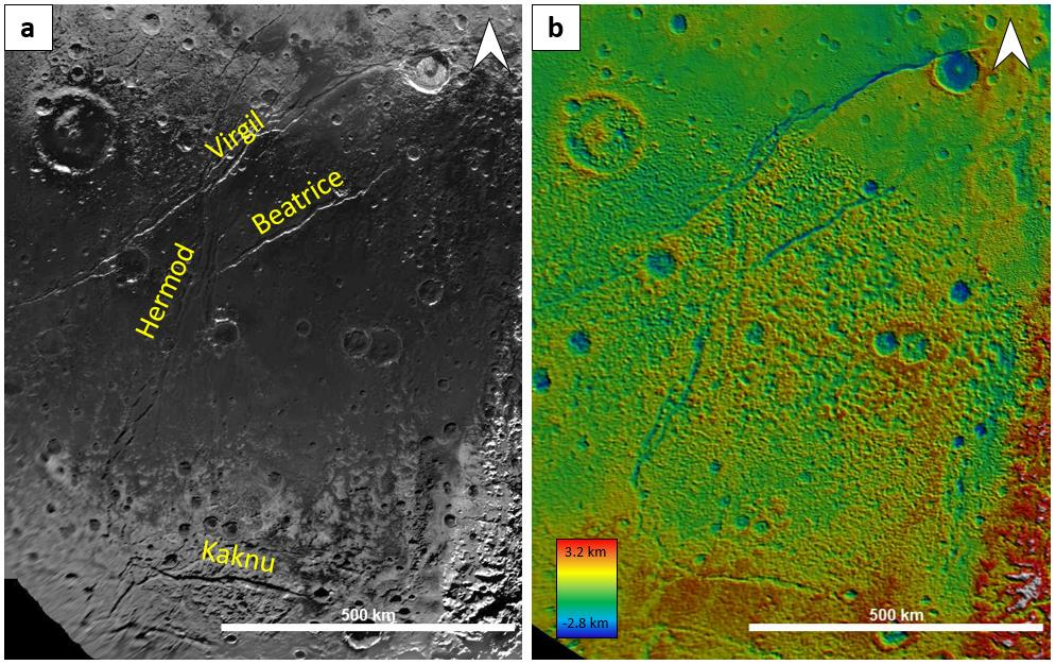

Figure 2: Context map of study area from LORRI images (a) and elevation (b). Scale bar at 500 km. Arrow points north.

9.4 Methods and Equations

The faults in this paper were identified using New Horizons Long Range Reconnaissance Orbiter (LORRI) images. High-resolution digital elevation models (DEMs) from stereographic techniques (from the MVIC hemispheric scans and LORRI mosaics) provided by Schenk et al. (2018), which has a ± 100 m stereo height accuracy and a ground sample distance of <300 m/pixel. While the southern portion of Hermod Fossae and the location of Kaknú Fossa are not in the highest resolution areas compared to Virgil and Beatrice Fossae, these areas appear in high enough resolution to follow a reasonable analysis. We used these DEMs for topographic profiles

transecting each main graben trough and taking measurements of the morphology of the fault (displacement, width).

DEMs and LORRI images were processed in the Java Mission-planning and Analysis for Remote Sensing (JMARS) software (version 4.0.10) and to measure scarp heights and lengths. Caution was taken to measure the maximum vertical relief, as this would correspond to a minimum magnitude of erosion and deposition of materials on the hanging walls (Polit et al. 2009). Although the main trough of Virgil Fossae was studied in this report, the complex strike-slip grabens in the center of the fossae were taken under consideration. We estimated the displacement error by the standard error of the widths and heights (Table 1) taken from > 10 topographic profiles at each fault site. Figure 3 shows an example of a topographic profile obtained from JMARS and subsequently used for our measurements.

Table 1: Standard errors for displacement and width measurements.

Fault site	No. Topographic Profiles	Width Standard Error (km)	Displacement Standard Error (km)
Virgil	15	0.52	0.18
Beatrice	15	0.54	0.17
Hermod	13	0.63	0.10
Kaknú	11	0.95	0.11

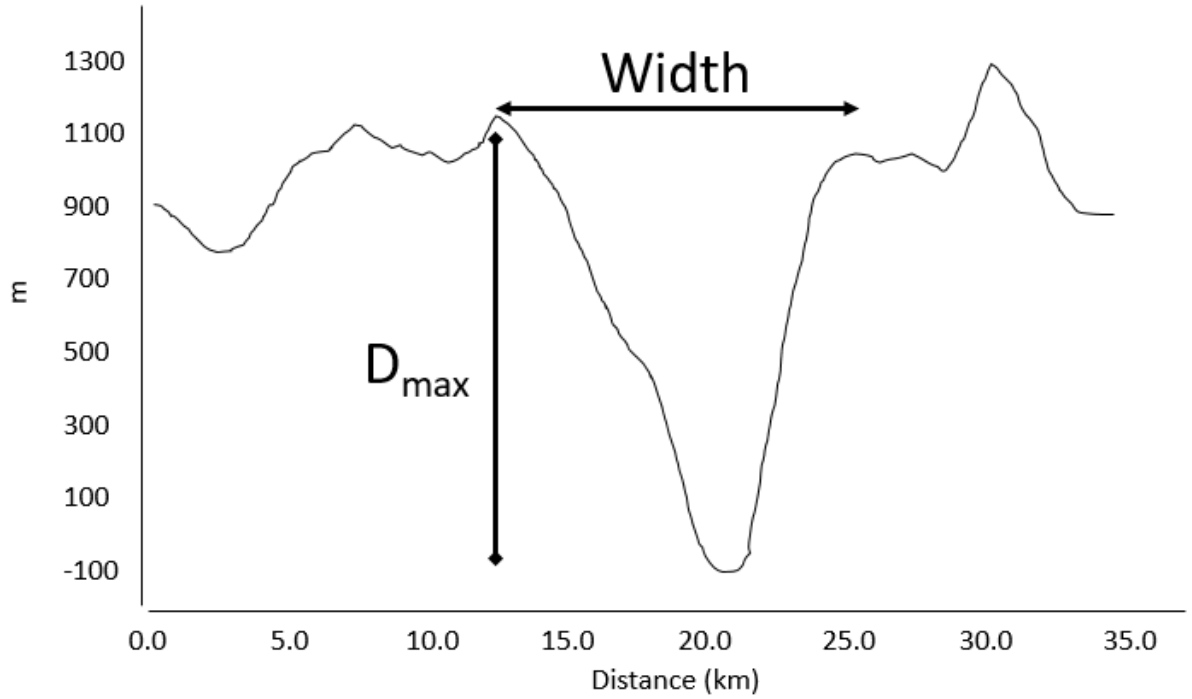

Figure 3: Example of acquired DEM profile used in this study. We do take note of the asymmetry of some profiles acquired and consistently measure the highest wall face of the fault.

Fault length needs to be measured consistently to construct D_{max}-L ratio comparisons. However, most grabens, like those on Earth and Mars, occur in echelon structures, which gives clues as to fault interactions. Faults in such close proximity to each other mechanically interact, mainly through stress fields and impeding (or promoting) fault growth, compared to an isolated fault (Willemse et al., 1996; Willemse, 1997; Gupta and Scholz, 2000; Kattenhorn and Pollard, 2001). Soft-linked faults are mechanically interactive, but not physically "bridged" by a connecting fault, whereas hard-linked faults are physically linked. In this study, faults that are soft-linked are separate faults, with the acknowledgement that they may be physically linked in the subsurface (e.g. Soliva et al., 2008; Polit et al. 2009). We identify fault terminations (location along the fault where displacement equals zero) within the resolution of the data.

The strength of faults supporting graben-valley topography may also be estimated from the morphometry if the elastic thickness of the lithosphere is known. The elastic thickness, *Te*, is the effective thickness in which the lithosphere can support elastic stresses over geologic timescales (Barnett and Nimmo 2002). An upper bound of Pluto's heat flux from a previous study by Conrad et al. (2019) estimated *Te* at 10 km, which we used in our study. Following a previous study by Barnett and Nimmo (2002), the fault block topography was approximated to a cosine curve, predicting maximum resolved shear stresses σ_{max}. From Jackson and White (1989), the value of σ_{max} is given by

$$\sigma_{max} = \frac{\rho_c g h}{2e} \; if \; \frac{\lambda}{T_e} < \frac{\pi}{2} \qquad (1)$$

Where ρ_c is the density of the basement material (in this case, Pluto's crustal density = 1.854 g/cm^3), g is the gravitational acceleration (0.62 m/s^2), h is the maximum vertical displacement of the fault, e is the base of natural logarithms, and λ is the wavelength of the faulting (i.e. widths). Observations from previous preliminary studies show that western close-encounter hemisphere faults on Pluto can be formed in low stress regimes, typically averaging < 300 kPa (Conrad et al. 2019).

If we assume, following Hyndman and Weichert (1983) and Willoughby and Hyndman (2005) that some level of seismicity occurs along the fault during fault growth, we can calculate the slippage rate, or the rate at which the fault sides are slipping relative to each other. Estimating deformation implicitly assumes that most deformation occurs over a defined fault cross-sectional area. For a single event over a fault of area A, the slope length d is related to the seismic moment by

$$M_0 = \mu A d \qquad (2)$$

Where μ is the shear modulus, which we set as 3.33 x 10^9 N/m^2 for water ice compositions. The slip rate *s* [mm/yr] is proportional to the rate of moment release in that

$$s = \frac{2M_0}{\mu l^2} \quad (3)$$

Where *l* is the length of the fault segment. An upper bound of 10^9 years was given following Cruikshank et al. 2019 to estimate the slippage rate.

The seismic moment M_0 is used to estimate fault roughness scaling. The M_0 value may be influenced by many factors, including dynamic interactions, geometric variations, and structural heterogeneity (e.g., fault roughness) and stress distributions. From Kanamori (1977):

$$M_w = \frac{2}{3} log M_0 - 10.73 \quad (4)$$

Where *Mw* is the moment magnitude, this variable then gives us an array of simulated seismic magnitudes across a fault line. The magnitudes are then plotted by cumulative frequency of the magnitudes, giving us a slope value, the *b-value*, following the Gutenberg-Richter law:

$$\log_{10} N = a - bM_w \quad (5)$$

Where *N* is the number of events having a magnitude ≥ Mw and *a* is a constant. In this study, *N* is the number of data points traversed across each fault. This *b*-value, similar to terrestrial earthquake studies tells us the proportion of relatively smaller to larger sized magnitudes (Gutenberg and Richter 1954). The *b*-value is the measured slope between the average of the of the magnitudes vs frequency of events and the larger magnitudes (so as to not have a large bias with smaller, more frequent magnitudes (Gutenberg and Richter 1954). Following the technique of Goebel et al. (2017), the *b*-value is connected to a correlation dimension D_2 (King 1983; Wyss et al. 2004) in that

$$D_2 = 2b \quad (6)$$

Where the linear relationship gives us an observed range of fault roughness, where the higher *b*-value slopes indicate a more fractured, unrestricted fault and a relatively younger age (Goebel et al. 2017).

9.5 Results

9.5.1 Virgil Fossae

The main branch of Virgil Fossae is 798.3 km long (Figure 4a), spanning from (7.13°S, 105.97°E) to (12.59°N, 135.81°E) in a SW-NE orientation. 15 topographic profiles were obtained and measured from the DEMs. Caution was taken to retrieve topographic profiles from the main branch, and not from the strike-slip-complex in the center of the main branch (Figure 4b). From the collective topographic profiles, the main branch appeared fairly symmetric at the southwestern portion, becoming more asymmetric with a higher southern wall going east toward Elliot Crater.

From initial observation, fault lengths < 8 km showed a different trend in D_{max}-L ratios than those > 8 km (Table 2; Figure 5). The D_{max}-L ratio for the larger lengths average to 0.128, whereas the smaller faults have a D_{max}-L ratio of 0.137. Plotting the D_{max}-L ratios for these larger versus smaller lengths (Figure 5), the slope coefficient $\gamma = 0.61$ for lengths < 8 km and $\gamma = 0.38$ for > 8 km faults.

Taking the *h* and λ from the elevation profiles into equation 1, the maximum shear stresses ranged from 91.8 – 471.1 kPa, within range of Conrad et al. (2019) low stress regime from their study of the Inanna faults. These maximum shear stresses resolve to be higher to the east of the strike-slip-complex and north toward Elliot crater.

The slippage rate at Virgil Fossae ranged from 10^{-3} – 10^{-2} mm/yr. It is interesting to note from observations that Virgil Fossae showed an increase in slippage rate from west to east. From

105.97°E – 125.56°E, the average slip rate is 0.17 mm/yr. East of this range to 135.81°E, the average slip rate increases to 0.49 mm/yr. We note that this increase in slippage rate arises just east of the strike-slip-complex.

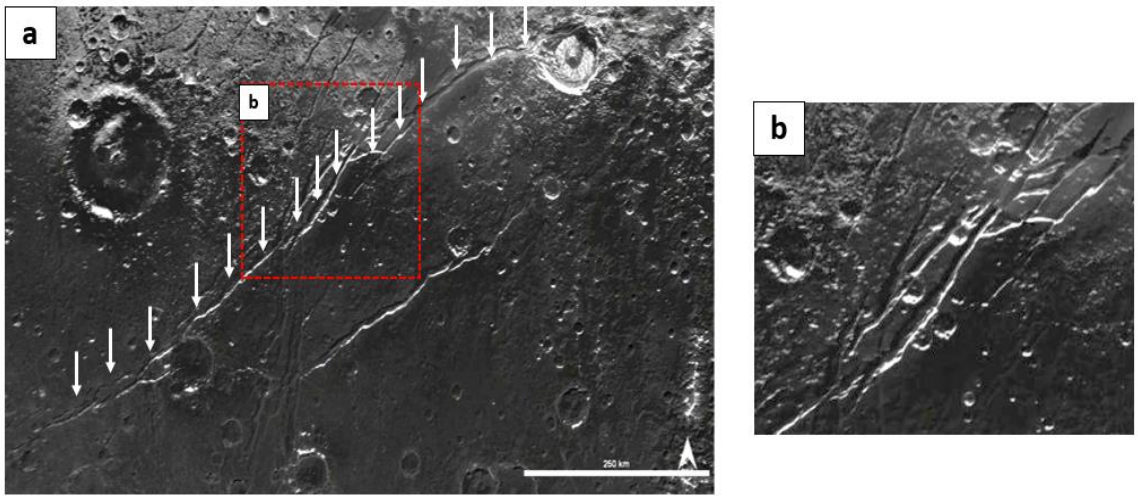

Figure 4: Virgil Fossae with main branch indicated by white arrows. Scale bar at 250 km. Arrow points north. Subsection (b) shows the complex strike-slip faults in the central Virgil Fossae branch.

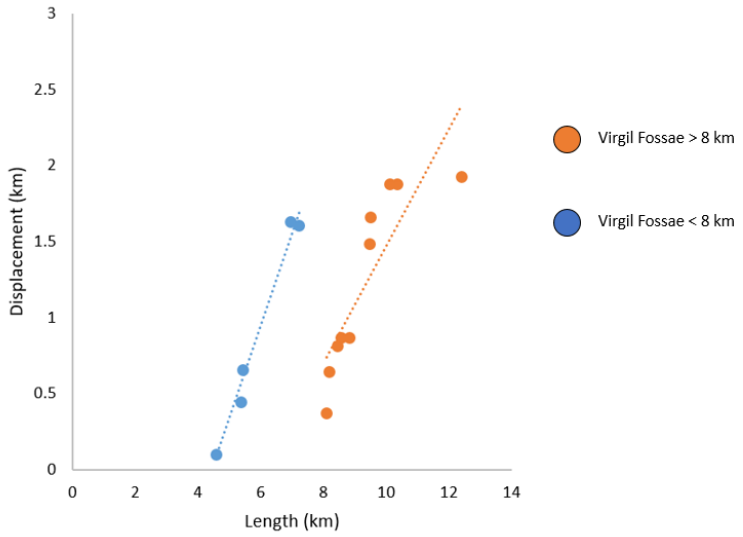

Figure 5: Virgil Fossae segments distinguishing smaller (< 8 km) versus larger (> 8 km) lengths. The slope coefficient is $\gamma = 0.61$ for lengths < 8 km and $\gamma = 0.38$ for > 8 km faults.

9.5.2 Beatrice Fossa

Beatrice Fossa is 358.7 km long (Figure 6), from (4.5°S, 121.16°E) to (3.25°N, 134.28°E) in a SW-NE orientation, practically subparallel to its neighbor, Virgil Fossae. The topographic profiles showed that Beatrice is uniformly symmetric in fault morphology, and there is a physical fault segment present at Beatrice near an impact crater. 15 DEMs were obtained and measured. The average D_{max}-L ratio from Table 2 was 0.13 and the linear slope $\gamma = 0.26$, a higher trend than the Virgil Fossae.

The maximum shear stresses calculated from Equation 1 ranged from 49.9 – 507 kPa, higher than the expected lower stresses estimated from Conrad et al. (2019). These maximum shear stresses resolve to be higher in the center of the fault branch. The slippage rate at Virgil Fossae ranged from $10^{-2} – 10^{0}$ mm/yr. Beatrice Fossa was observed to have an increased slippage rate also within the center of the fault length.

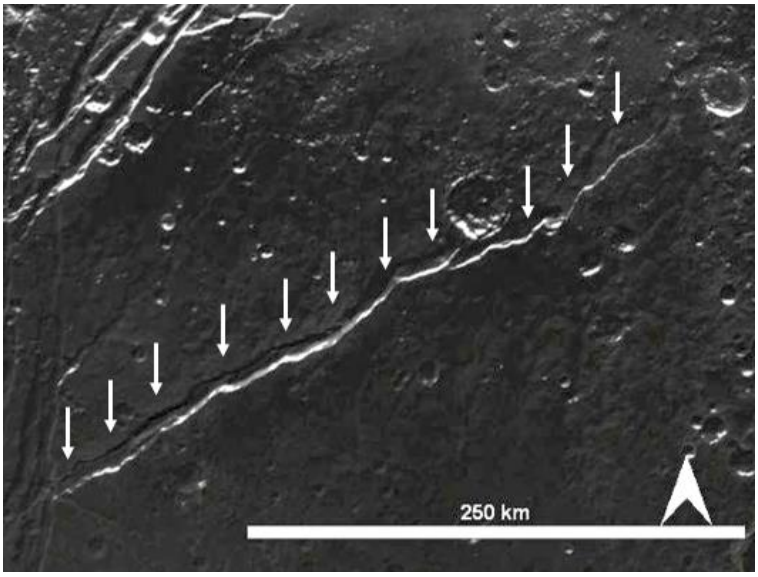

Figure 6: Beatrice Fossa with main branch indicated by white arrows. Scale bar at 250 km. Arrow points north.

9.5.3 Hermod Fossae

Hermod Fossae is 712.1 km in length and transects Virgil Fossae to the north (Figure 7), traversing from (14.88°S, 116.22°E) to (5.53°N, 121.56°E), nearly vertical in a N-S orientation, and has two branches. We focused on the longer, western branch. 13 DEMs were measured and was observed to be more asymmetric in the fault walls, becoming more symmetric going south. The D_{max}-L ratios from Table 2 average at 0.07 and has a linear slope of $\gamma = 0.044$, a much shallower trend than Virgil and Beatrice.

Maximum shear stresses ranged from 48.9 – 284.4 kPa, well within the Conrad et al. (2019) stress regime. The higher maximum shear stresses calculated were observed to be in the southern portion of the fault. The slippage rates ranged from 10^{-2} – 10^{-1} mm/yr. It is interesting to note that Hermod Fossae has two main areas of increased slippage rates, discussed later in Section 4.6.

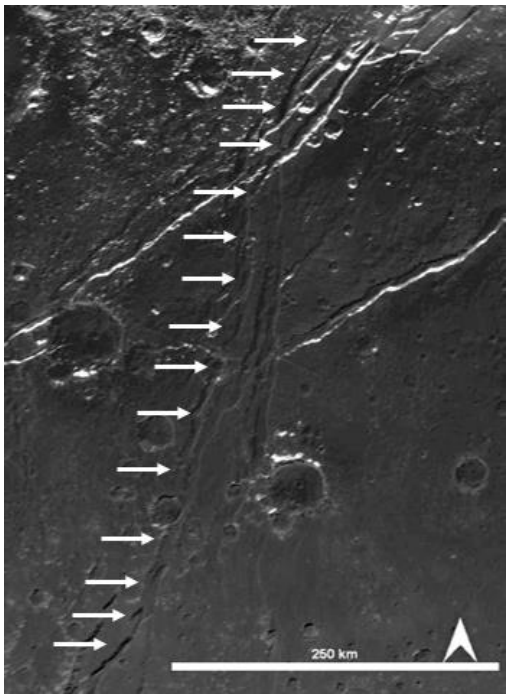

Figure 7: Hermod Fossae with main branch indicated by white arrows. Scale bar at 250 km. Arrow points north.

9.5.4 Kaknú Fossa

Kaknú Fossa is a notable southern Cthulhu Macula fault at 259.1 km in length (Figure 8), from (29.28°S, 115.56°E) to (31.72°S, 128.34°E), following a more SE-NW trend than the other Cthulhu Macula sites. 11 DEMs were measured for length, width, and height. Kaknú was observed to have wider graben floors than the other fossae and slightly higher northern walls in the western portion of the fault. The D_{max}-L ratios follow a $\gamma = 0.065$ linear fit, similar to Hermod in lower slope, and average at 0.072.

The maximum shear stresses along Kaknú Fossa range from 39.8 – 271.9 kPa, similar range of shear stresses as Hermod Fossae and within the low stress regime as stated by Conrad et al. (2019). These maximum shear stresses are observed to be uniform across the fault, decreasing in stress to the east at the conjunction of a small impact crater. The slippage rate ranged from 10^{-2} – 10^{0} mm/yr. Slippage rates increase toward the east until the most easterly portion, where slippage rates drastically decrease by a magnitude of 2.

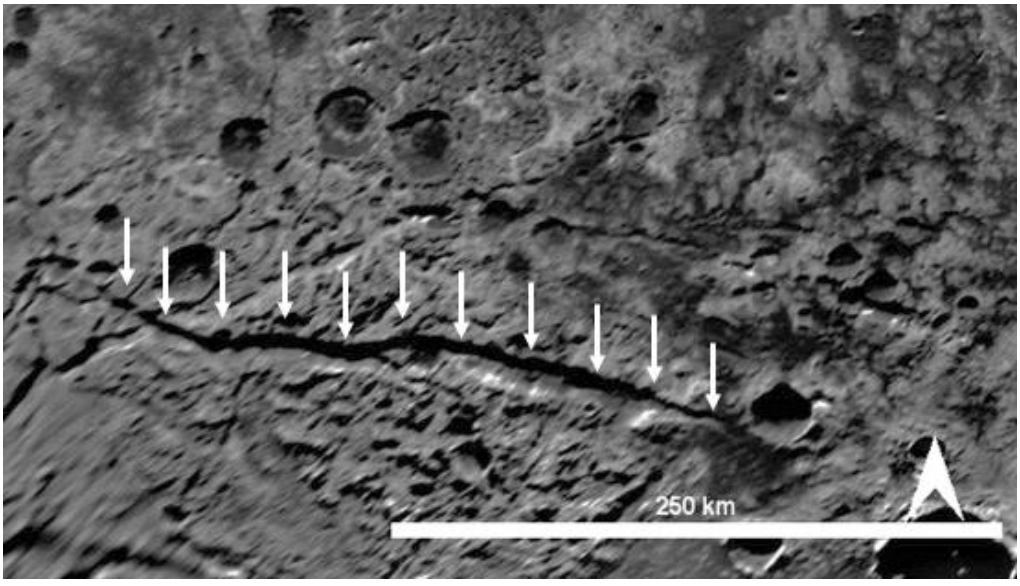

Figure 8: Kaknú Fossa indicated by white arrows. Scale bar at 250 km. Arrow points north.

Table 2: D_{max} and Length measurements at each study site

Study Area	Fault	Length L (km)	D_{max} (m)	D_{max}/L
Virgil	A	8.19	649.3	0.0792
	B	8.09	376.2	0.0465
	C	5.36	447.9	0.0835
	D	9.50	1664.9	0.175
	E	8.83	870.8	0.098
	F	8.55	873.1	0.102
	G	9.48	1489	0.157
	H	5.43	658.9	0.121
	I	8.45	818.4	0.0968
	J	4.57	100.2	0.022
	K	6.95	1633.8	0.235
	L	12.4	1929.4	0.155
	M	7.22	1607.3	0.222
	N	10.3	1882.1	0.182
	O	10.1	1880.5	0.186
Beatrice	A	10.4	626.3	0.060
	B	9.9	753.2	0.0761
	C	12.25	1580.7	0.129
	D	10.67	1014.3	0.095
	E	11.7	1858.8	0.158
	F	13.2	2076.7	0.157
	G	11.35	1255.7	0.111
	H	11.63	1762.9	0.152
	I	13.63	1819.1	0.133
	J	12.26	1928.4	0.157
	K	9.1	1214.5	0.133
	L	5.82	555.3	0.068
	M	8.98	1286.5	0.143
	N	8.44	204.3	0.024
	O	13.6	801	0.068
Hermod	A	8.79	759.7	0.086
	B	9.65	939.4	0.097
	C	7.8	200.4	0.026
	D	11.5	461.9	0.040
	E	11.4	767.3	0.067
	F	13.1	825.0	0.063
	G	6.38	245.1	0.038
	H	12.5	325.0	0.026
	I	12.6	943.9	0.075
	J	9.0	662.1	0.074
	K	13.0	786.3	0.060
	L	11.2	1164.7	0.104
	M	6.7	798.8	0.119

Table 2 Cont.: D_{max} and Length measurements at each study site

Study Area	Fault	Length L (km)	D_{max} (m)	D_{max}/L
Kaknú	A	6.5	624.0	0.096
	B	5.31	283.2	0.053
	C	8.4	796.7	0.095
	D	9.23	977.6	0.11
	E	11.6	1113.7	0.096
	F	14.1	769	0.054
	G	13.87	913.8	0.066
	H	13	505.2	0.039
	I	11.9	1194.1	0.10
	J	6.6	163.1	0.025
	K	6.2	345.6	0.056

9.5.5 Displacement-length ratio comparison

We analyzed the topographic expressions of four fault systems in central Cthulhu Macula, with a total of 54 elevation profiles, to derive height and width of fault segments. The resultant maximum displacements and their corresponding lengths (e.g. Virgil and Hermod main branches were studied, not including associated graben) were then used to derive the D_{max}-L statistic. The D_{max}-L ratio shows a large scatter in the data between 4 – 14 km lengths, with maximum displacements from as low as 0.1 to as much as 2 km (Figure 9). Following the regression approach by Clark and Cox (1996) and Polit et al. (2009), we computed the best fits for the investigated fault sites. Results show that Virgil and Beatrice have higher trend scaling. According to Polit et al. (2009), these steep slope trends refer to less restricted fault growth. Hermod and Kaknú Fossae have very shallow trends and poorer R^2 fit to linearity, thus implying restriction of growth, possibly from environmental and mechanical influences.

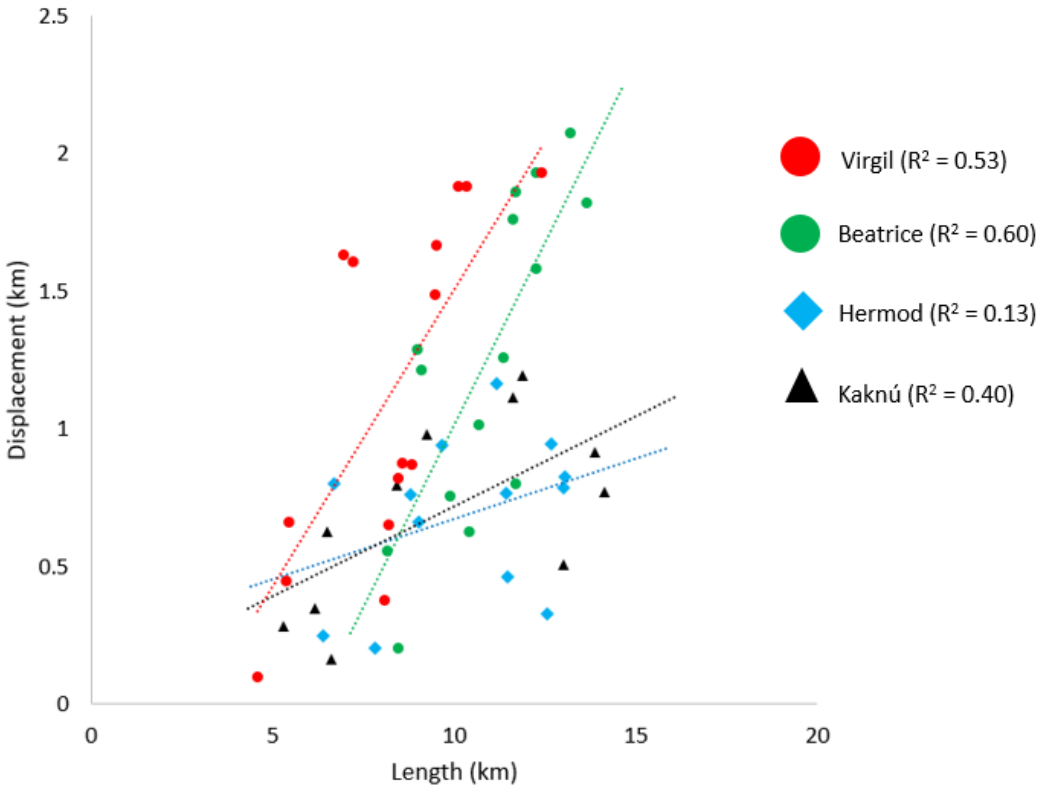

Figure 9: D_{max}-L ratios of the study sites. Note that Virgil and Beatrice show similar high slopes than Hermod and Kaknú. This gives us a clue to their unrestricted or restricted growth behavior as influenced by their environment of emplacement and subsurface material.

9.5.6 Shear Stresses and Slippage Rates

We also used the maximum vertical displacement and width of the faults to derive maximum shear stresses at each of the 54 elevation profiles using Equation 1. The resulting shear stresses were then colorized as a scale from the minimum stress (5 kPa) to the maximum (436 kPa), as shown in Figure 10 a-d. Slippage rates calculated from Equation 3 were used to determine the fault wall dynamics across the main fossae branches. Virgil Fossae shows two distinct clusters in shear stress versus slippage rates plot (Figure 11). The higher shear stress and faster slippage rates, ranging from 0.006 mm/yr in the western portion of the main branch and increases to 0.86 mm/yr toward Elliott Crater. Beatrice Fossa shows a much variable range in having a higher shear

stress and slippage rate than its neighbor Virgil. The shear stress and slippage rates, ranging from 0.09 – 2.3 mm/yr are observably more in the center of the fault. Hermod and Kaknú Fossae show similarities in that both show lack of variability in shear stresses across the entirety of their faults. Hermod Fossae shear stresses are below 350 kPa, with higher shear stresses toward the southern portion, and slippage rates between 0.03 – 0.5 mm/yr. Kaknú Fossa has shear stresses below 300 kPa with slippage rates from 0.06 – 1.6 mm/yr.

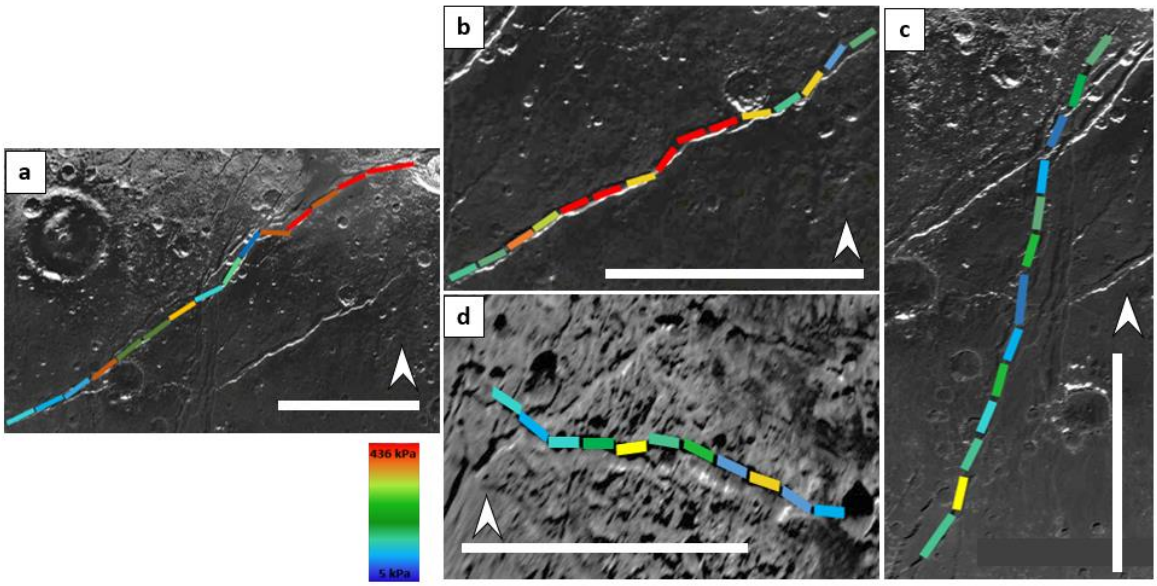

Figure 10: Colorized maps of maximum shear stresses across each traverse at each of the study sites. Color bar scales from 5 kPa to 436 kPa. Scale bars at 250 km. Arrow points north.

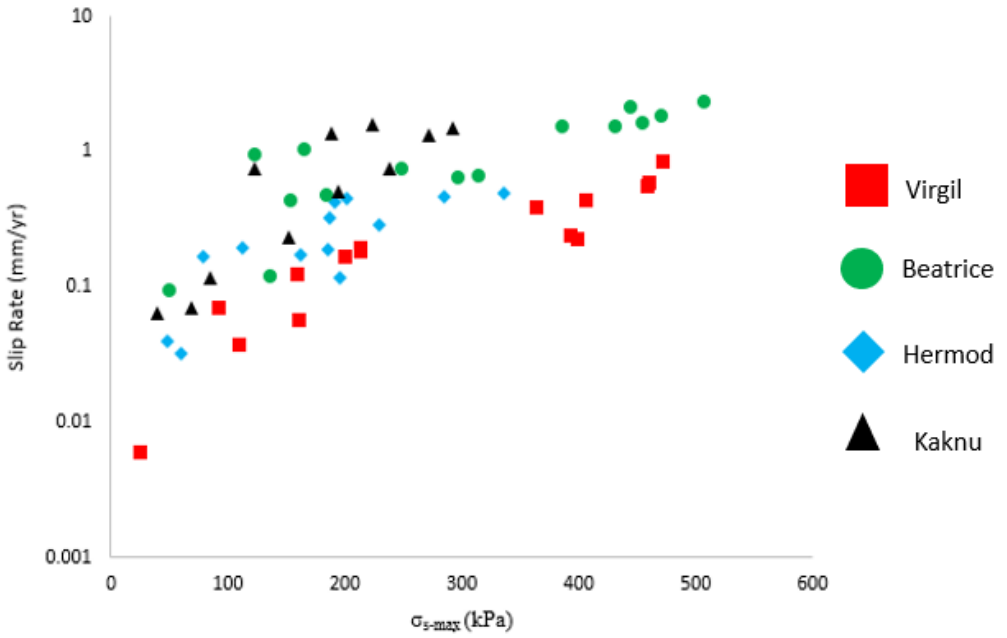

Figure 11: Maximum shear stress versus slippage rates at each study site. Note that Virgil Fossae displays two distinct clusters, discussed previously in Section 4.1.

9.5.7 Roughness Scaling from Slip Magnitudes

Recalling Equation 5, b-values are controlled by the geometry of the fault and any surrounding fault network (e.g. dynamics of interacting faults; King, 1983; Burridge and Knopoff 1967). The geometry of faults, on a basic level, is shaped by dynamic rupture events and, conversely, dynamic interactions are controlled by the distribution of stresses, which may easily be perturbed by fractures and roughness (e.g., Scholz, 1968; Goebel et al. 2017).

At each transect taken across the fault, we assume that is an "event" of some magnitude to produce the current morphology over a maximum period of 10^9 years (Keane et al. 2016). The seismic moment magnitudes across the fault boundaries are evaluated and plotted by cumulative frequency of the magnitudes, producing a similar sloped shape to those of terrestrial earthquakes (Gutenberg and Richter 1954). Following the technique by (Okal and Romanowicz 1994), we take the slope of the cumulative frequency starting at the average magnitude (which helps us avoid the

larger proportion of smaller magnitude events). This slope gives us our b-value, as seen in Figure 12.

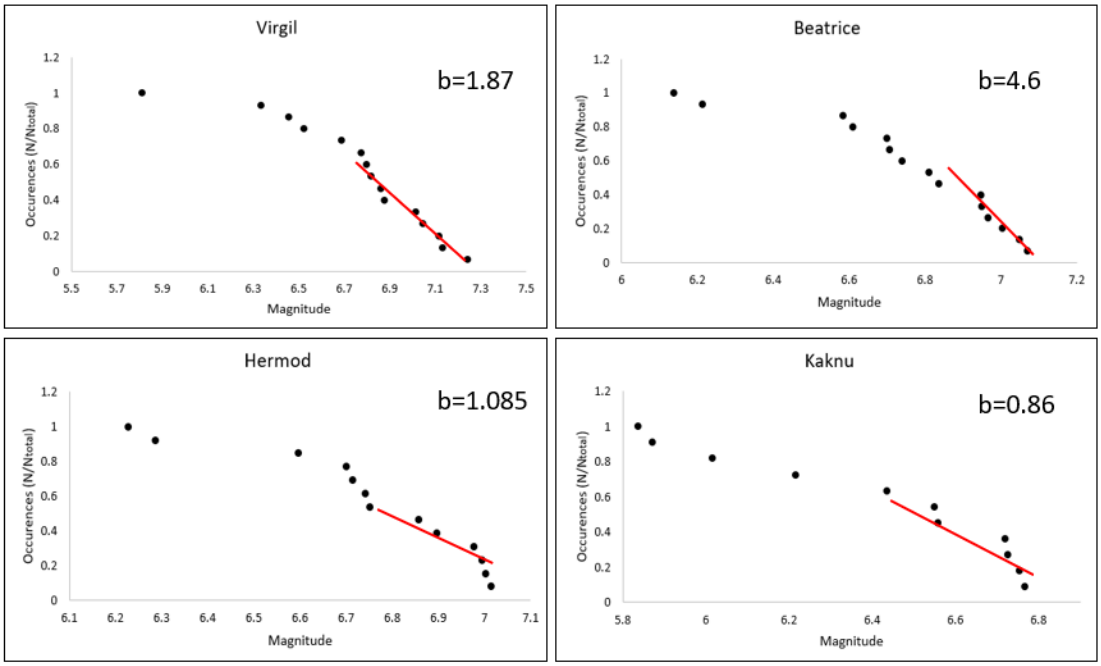

Figure 12: Simulated magnitudes versus cumulative occurrences at each study site. Red lines take the average of the magnitudes to find the slope value (b-value, as shown).

9.6 Discussion and Implications

The faults in the central Cthulhu Macula region on Pluto analyzed in this study possess remarkable structural morphologies. Kaknú and Beatrice Fossae involve a single or a few segmented faults within a main branch, while multiple, complex branches accompany Virgil and Hermod Fossae. These faults mainly dominate this central area of Cthulhu Macula and do not show any similar arrangements to the mountain ranges in southeast Cthulhu Macula. Virgil and Beatrice do show similar orientations to Inanna and Dumuzi Fossae to the northeast, outside the bounds of Cthulhu Macula and surrounding the northwestern lobe of Sputnik Planitia. Faults across Pluto would show similar characteristics in the asymmetry of the graben walls, but the amount of depth, width of the fault floor, and complexity of the fossa in its entirety can give us insight as to the

environment in how these faults interact and grow. Cthulhu Macula is considered to be an ancient terrain (Moore et al. 2016), so the evolution of such faults may have a longer evolution of dynamic fault processes.

The origins of these faults remain unknown, although there are several hypotheses, such as global contraction (Hammond et al. 2016), heat flux (Conrad et al. 2019), and regional loading or polar wander influences (Keane et al. 2016). We suggest a combination of such processes would have to take place to concern the differing orientations and relative ages seen in this region of Pluto.

The analyzed faults may have grown as part of different faulting mechanisms throughout Pluto's geologic history, so the structures may not have adapted strains with the same structural styles as assumed here. Furthermore, interactions among other faults (e.g. Hermod Fossae being observably overlapped by Virgil Fossae) and associated graben systems, may have contributed to growth behavior. The fault growth may also be influenced by regional variations in the lithospheric properties (Peacock 1991; Conrad et al. 2019), such as cryovolcanic interactions (Cruikshank et al. 2019) or flexure loading from Sputnik Planitia (Nimmo et al. 2016). Although we identified the D_{max}-L ratios to suggest variations in fault growth, no single reason listed here can be identified as the main cause of the large variations in D_{max}-L ratios, but rather a combination on a localized scale within the Cthulhu Macula region.

Comparing these fault systems to those of Mars and Earth (Figure 13) show that the Plutonian fossae have steeper D_{max}-L slopes than the terrestrial counterparts. This gives us an interesting insight to how icy surfaces would behave differently than rocky surfaces. That is, the steeper slopes of the D_{max}-L ratios from Pluto imply less restrictive mechanisms toward fault growth than rocky bodies. Although water ice acts like rhyolitic rock at such extremely cold

temperatures (Kargel 1998), fault production and shear forces through ice have yet been constrained for Pluto.

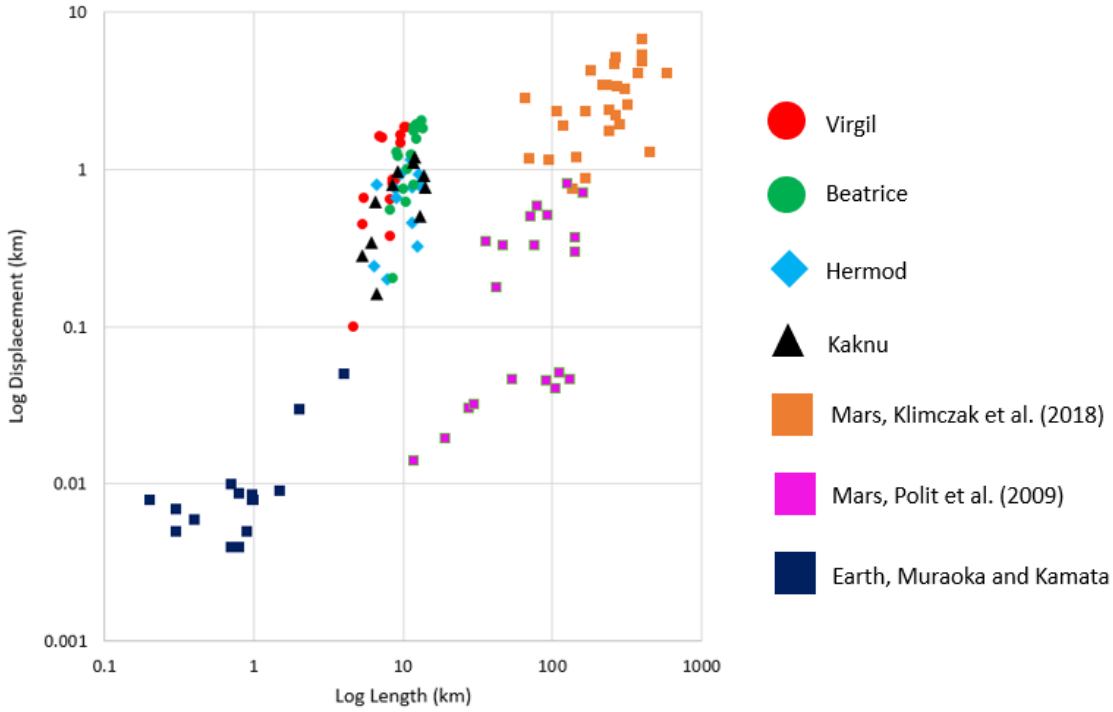

Figure 13: Compilation of D_{max}-L data for this study compared to Martian and terrestrial normal faults. Data for Mars from Klimczak et al. (2018) and Polit et al. (2009). Terrestrial data from Muraoka and Kamata plotted from Figure 12 in Polit et al. (2009).

Virgil and Beatrice Fossae show a higher variability of shear stresses and slippage rates across their fault boundaries. It has been noted that Virgil and Beatrice have a similar localized heat flux response from their topography (Conrad et al. 2019), however, their shear stresses across each fossae show a difference. Virgil Fossae shows an increase in shear stress and slippage nearing Elliott Crater, which has been noted to be a prime suspect in cryovolcanic activity and seepage of ammonia-type material (Cruikshank et al. 2019). From this, subsurface materials could influence the behavior of fault wall movement and overall growth behavior. Beatrice Fossa shows more stress and slippage toward the center of the fault, quite possibly from the same reasoning as Virgil

in that subsurface material is upwelling in the center of the fault, but the detection of ammonia-like material on the surface of Pluto has yet been fully understood. While Hermod and Kaknú share similarities in the lack of stress and slippage variability, the morphology and location of these faults are vastly different. Hermod Fossae is underlying Virgil Fossae with less fault wall sharpness, so we suspect that Hermod is relatively older than Virgil Fossae. Also, Hermod intersects Virgil at an almost perpendicular angle. We hypothesize that previous tectonic events may have happened across Cthulhu Macula, even before the creation of Sputnik Planitia and the consequences of polar wandering (Keane et al. 2016). Kaknú Fossa is located on the southern portion of Cthulhu Macula that has similarly oriented graben, but also has an observably more complex environment with craters and mottled terrain. This terrain can give us clues to Kaknú's restrictive fault growth and subdued shear stresses.

Previous studies in a terrestrial setting have correlated b-values to a relative age of the fault environment (King 1983; Wyss et al. 2004; Goebel et al. 2017). D, the fractal correlation dimension from Equation 6, increases from polished (smoother, homogenized faults) to more fractured surfaces. Observations on the geometric complexity and roughness showed that higher slip rates relate to younger, rougher faults that produce a higher degree of source-mechanism heterogeneity (Bailey et al., 2010; Powers and Jordan, 2010; Goebel et al., 2014). Goebel et al. (2017) observes that fault roughness decreases with age and cumulative slip, suggesting a maturity level for smoother faults (e.g., more homogenized stress fields), more localized seismicity (e.g., rather than regional or global influences), and lower b-values (Goebel et al. 2013).

Higher b-values relates to younger faulting mechanisms and slippage comes from deeper, lower differential stress settings (Schorlemmer 2005). From the D-b relation, Beatrice is a highly fractured fault system and relatively younger than the other faults in this study (Figure 14a). This

observation is justified by the higher shear stress variability (Figure 14b), higher slippage rates, and a larger D_{max}-L ratio (e.g., less restricted in fault growth). Virgil Fossae has the next highest b-value, a less fractured system than its sub-parallel neighbor, Beatrice. It also has comparable shear stress variability, slippage rate range, and D_{max}-L ratio, though considered relatively older by the D-b relation. Hermod and Kaknú Fossae have the lower b-values, relating to more polished, smoother fault systems. That is, the surface setting in which these faults are found are more homogenous, lesser shear stresses and variability in slippage, thus relatively older than Beatrice and Virgil.

Relating roughness scales and ultimately ages to these faults gives us insight to the growth behavior of the fault and the environment at which it propagated. Since Beatrice and Virgil Fossae are oriented in a similar fashion and located in the same portion of Cthulhu Macula, it can be assumed that these originated from a similar regional event, possibly a similar heat flux response or polar wandering influence (Keane et al. 2016; Conrad et al. 2019).

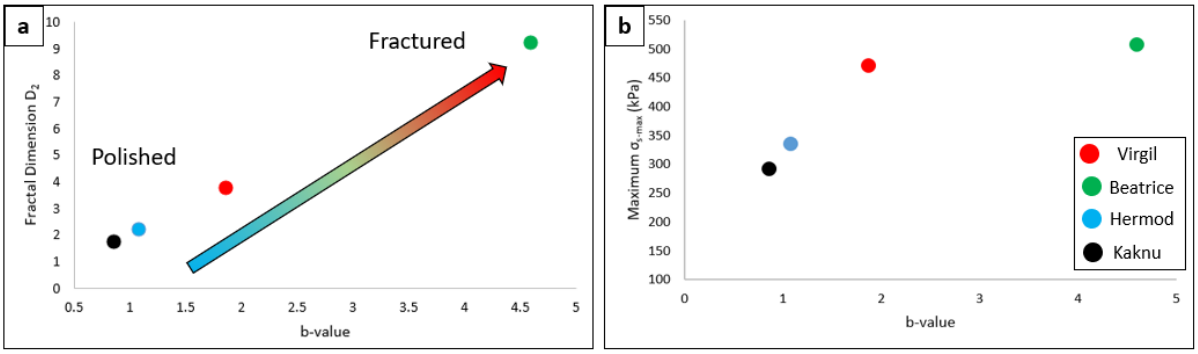

Figure 14: Fractal dimension of roughness as determined by the b-value. Different roughness scales (a) show that Virgil and Beatrice Fossae are more fractured than Hermod and Kaknú Fossae. These b-values are plotted against the calculated maximum shear stress (b) to show a similar pattern from (a).

9.7 Conclusions

Measurements of faults within the central Cthulhu Macula region reveal differences in displacement and maximum shear stress distribution and roughness that imply spatial and possibly temporal variations in the strain and magnitudes of slippage. Using an assortment of techniques, including fault morphometry and fault displacements, slippage rates, and fractal dimension scaling for roughness relations, we suggest that the Beatrice and Virgil Fossae are relatively younger than Hermod and Kaknú, with Beatrice Fossa having the largest shear stress and highest roughness. This may correspond to a heterogeneity in the crustal thickness and material, along with a relatively more variable stress field. The Virgil Fossae displays similar extremes as Beatrice, but revealing lesser variation in stresses, implying the interactions of surrounding underlying faults (i.e. Hermod Fossae) and surrounding geology (possible ammonia-induced cryovolcanism) can influence the localized mechanisms of fault growth. The displacement-length ratios of the faults show that Beatrice and Virgil follow a more power-law scaling for localized scale-invariant faulting regimes compared to Hermod and Kaknú having an exponential D_{max}-L ratio trend, implying these as vertically restricted faults. The different fault characteristics from the northern portion of Cthulhu Macula compared to the southern portion reveal that Kaknú and Hermod are from a much older geologic time in Pluto's geologic history and the different orientations of these fossae are still to be explored. The variation in stress behavior and morphology thus represents the active geologic evolution of Cthulhu Macula, particularly in localized areas with varying fault regimes.

9.8 Acknowledgements

This work was supported by the Pluto System After New Horizons Workshop (2019) and appreciated feedback from workshop attendees. We gratefully thank the NASA New Horizons

team for their successful mission and data return so that we may continue to explore Pluto's fascinating surface.

9.9 Data Availability

The LORRI images are archived in the Planetary Data System (PDS) Small Bodies Node at https://pds-smallbodies.astro.umd.edu/holdings/nh-p-lorri-2-pluto-v3.0/dataset.html.

9.10 References

Bailey, I., Ben-Zion, Y., Becker, T.W., and Holschneider, M., 2010. Quantifying focal mechanism heterogeneity for fault zones in central and southern California: Geophysical Journal International, v. 183, p. 433–450, doi:10.1111/j.1365-246X.2010.04745.x.

Barnett, D., Nimmo, F., 2002. Strength of faults on Mars from MOLA topography. Icarus, 157, 34-42. doi:10.1006/icar.2002.6817

Burridge, R., and Knopoff, L., 1967. Model and theoretical seismicity: Bulletin of the Seismological Society of America, v. 57, p. 341–371.

Clark, R. M., & Cox, S., 1996. A modern regression approach to determining fault displacement-length scaling relationships. Journal of Structural Geology, 18(2–3), 147–152. https://doi.org/10.1016/S0191-8141(96)80040-X

Conrad, J., Nimmo, F., Schenk, P., et al., 2019. An upper bound on Pluto's heat flux from a lack of flexure response of its normal faults. Icarus, 328, 210-217. https://doi.org/10.1016/j.icarus.2019.03.028

Cowie, P.A., Scholz, C.H., 1992a. Physical explanation for the displacement–length relationship of faults using a post-yield fracture mechanics model. Journal of Structural Geology 14, 1133–1148. https://doi.org/10.1016/0191-8141(92)90065-5

Cowie, P.A., Scholz, C.H.,1992b. Displacement–length scaling relationships for faults: data synthesis and discussion. Journal of Structural Geology 14, 1149–1156. https://doi.org/10.1016/0191-8141(92)90066-6

Cruikshank, D. P., Imanaka, H., and Dalle Ore, C. M. 2005. Tholins as coloring agents on outer Solar System bodies. Adv. Space Res. 36, 178-183. https://doi.org/10.1016/j.asr.2005.07.026

Cruikshank, D., Umurhan, O., Beyer, R., et al., 2019. Recent cryovolcanism in Virgil Fossae on Pluto. Icarus, 330, 155-168. 10.1016/j.icarus.2019.04.023

Dawers, N.H., Anders, M.H., Scholz, C.H., 1993. Growth of normal faults: displacement–length scaling. Geology 21, 1107–1110. https://doi.org/10.1130/0091-7613(1993)021%3C1107:GONFDL%3E2.3.CO;2

Goebel, T., Schorlemmer, D., Becker, T., Dresen, G., and Sammis, C.G., 2013. Acoustic emissions document stress changes over many seismic cycles in stick-slip experiments: Geophysical Research Letters, v. 40, p. 2049–2054, doi:10.1002/grl.50507.

Goebel, T., Candela, T., Sammis, C., Becker, T., Dresen, G., and Schorlemmer, D., 2014. Seismic event distributions and off-fault damage during frictional sliding of saw-cut surfaces with pre-defined roughness: Geophysical Journal International, v. 196, p. 612–625, doi:10.1093/gji/ggt401.

Goebel, T., Kwiatek, G., Becker, T., Brodsky, E., Dresen, G., 2017. What allows seismic events to grow big?: Insights from b-value and fault roughness analysis in laboratory stick-slip experiments. Geology, 45 (9), 815-818. doi:10.1130/G39147.1

Gross, M.R., Gutierrez-Alonso, G., Bai, T., Wacker, M.A., Collinsworth, K.B., Behl, R.J., 1997. Influence of mechanical stratigraphy and kinematics on fault scaling relations. Journal of Structural Geology 19, 171–183. https://doi.org/10.1016/S0191-8141(96)00085-5

Grundy, W., Bertrand, T., Binzel, R., et al., 2018. Pluto's haze as a surface material. Icarus, 314, 232-245. https://doi.org/10.1016/j.icarus.2018.05.019

Gupta, A., Scholz, C.H., 2000. A model of normal fault interaction based on observations and theory. Journal of Structural Geology 22, 865–879. https://doi.org/10.1016/S0191-8141(00)00011-0

Gutenberg, B. and Richter, C.F, 1954. *Seismicity of the Earth and Associataed Phenomena*, Princeton University Press, Princeton, NJ, USA.

Hammond, N. P., Barr, A. C., Parmentier, E. M. 2016. Recent tectonic activity on Pluto driven by phase changes in the ice shell. Geophys. Res. Lett. 10.1002/2016GL069220.

Hyndman, R.D., D.H. Weichert, 1983. Seismicity and rates of relative motion on the plate boundaries of western North America, Geophys. J. R. Astron. Soc., 72, 59-82. https://doi.org/10.1111/j.1365-246X.1983.tb02804.x

Imanaka, H., Khare, B. N., Elsila, J. E., Bakes, E. L. O., McKay, C. P., Cruikshank, D. P., Sugita, S., Matsui, T., and Zare, R. N. 2004. Laboratory experiments of Titan tholin formed in cold plasma at various pressures: Implications for nitrogen-containing polycyclic aromatic compounds in Titan haze. Icarus 168, 344-366. https://doi.org/10.1016/j.icarus.2003.12.014

Jackson, J. A., and N. J. White 1989. Normal faulting in the upper continental crust: Observations from regions of active extension. J. Struct. Geol. 11, 15–36. https://doi.org/10.1016/0191-8141(89)90033-3

Kanamori, H., 1977. The energy release in great earthquakes. JGR, 82 (20), 2981-2987. https://doi.org/10.1029/JB082i020p02981

Kargel, J., 1998. Physical chemistry of ices in the outer solar system. In: Solar System Ices (B. Schmitt et al., eds.), 3-32. Astrophysics and Space Science Library, v227.

Kattenhorn, S.A., Pollard, D.D., 2001. Integrating 3D seismic data, field analogs and mechanical models in the analysis of segmented normal faults in the Wytch Farm oil field, southern England. AAPG Bulletin 85, 1183–1210. https://doi.org/10.1306/8626CA91-173B-11D7-8645000102C1865D

Keane, J., Matsuyama, I., Kamata, S., Steckloff, J., 2016. Reorientation and faulting of Pluto due to volatile loading within Sputnik Planitia. Nature, 540, 90-93. doi:10.1038/nature20120

King, G., 1983. The accommodation of large strains in the upper lithosphere of the Earth and other solids by self-similar fault systems: The geometrical origin of b-value: Pure and Applied Geophysics, v. 121, p. 761–815, doi:10.1007/BF02590182.

Klimczak, C., Kling, C., Byrne, P., 2018. Topographic expressions of large thrust faults on Mars. JGR: Planets, 123, 1973-1995. https://doi.org/10.1029/2017JE005448

Materese, C. K., Cruikshank, D. P., Sandford, S. A.,Imanaka, H., Nuevo, M. 2015. Ice chemistry on outer solar system bodies: Electron radiolysis of N2-, CH4-, and CO- containing ices. Astrophys. J. 812:150 (9pp). October 20. https://doi.org/10.1088/0004-637X/812/2/150

Moore, J., et al., 2016. The geology of Pluto and Charon through the eyes of new horizons. Science 351, 1284–1293. https://doi.org/10.1126/science.aad7055.

Nimmo, F., Hamilton, D. P., McKinnon, W. B. et al. 2016. Reorientation of Sputnik Planitia implies a subsurface ocean on Pluto. Nature 540, 94-96. https://doi.org/10.1038/nature20148

Okal, E., Romanowicz, B., 1994. On the variation of b-values with earthquake size. Physics of the Earth and Planetary Interiors, 87, 55-76. https://doi.org/10.1016/0031-9201(94)90021-3

Peacock, D.C.P., 1991. Displacements and segment linkage in strike-slip-fault zones. Journal of Structural Geology 13, 1025–1035. doi.org/10.1016/0191-8141(91)90054-M

Polit, A., Schultz, R., Soliva, R., 2009. Geometry, displacement-length scaling, and extensional strain of normal faults on Mars with inferences on mechanical stratigraphy of the martian crust. Journal of Structural Geology, 31, 662-673. doi:10.1016/j.jsg.2009.03.016

Powers, P., and Jordan, T., 2010. Distribution of seismicity across strike-slip faults in California: Journal of Geophysical Research, v. 115, B05305, doi:10.1029/2008JB006234.

Robbins, S. J., Singer, K. N., Bray, V. J., et al. 2017. Craters of the Pluto-Charon system. Icarus 287, 187-206. https://doi.org/10.1016/j.icarus.2016.09.027

Schenk, P., Beyer, R., McKinnon, W., et al., 2018. Basins, fractures and volcanoes: Global cartography and topography of Pluto from New Horizons. Icarus, 314, 400-433. https://doi.org/10.1016/j.icarus.2018.06.008

Schlische, R.W., Young, S.S., Ackermann, R.V., Gupta, A., 1996. Geometry and scaling relations of a population of very small rift related normal faults. Geology 24, 683–686. https://doi.org/10.1130/0091-7613(1996)024%3C0683:GASROA%3E2.3.CO;2

Schorlemmer, D., Wiemer, S., and Wyss, M., 2005. Variations in earthquake-size distribution across different stress regimes: Nature, v. 437, p. 539–542, doi:10.1038/nature04094.

Scholz, C., 1968. The frequency-magnitude relation of microfracturing in rock and its relation to earthquakes: Bulletin of the Seismological Society of America, v. 58, p. 399–415.

Scholz, C.H., 1997. Earthquake and fault populations and the calculation of brittle strain. Geowissenschaften 15, 124–130. https://doi.org/10.2312/geowissenschaften.1997.15.124

Scholz, C.H., 2002. The Mechanics of Earthquakes and Faulting, second ed. Cambridge University Press, 471 pp.

Scholz, C.H., Dawers, N.H., Yu, J.Z., Anders, M.H., Cowie, P.A., 1993. Fault growth and fault scaling laws – preliminary results. Journal of Geophysical Research 98, 21951–21961. https://doi.org/10.1029/93JB01008

Schultz, R.A., 1999. Understanding the process of faulting: selected challenges and opportunities at the edge of the 21st century. Journal of Structural Geology 21, 985–993. https://doi.org/10.1016/S0191-8141(99)00025-5

Schultz, R.A., Fossen, H., 2002. Displacement–length scaling in three dimensions: the importance of aspect ratio and application to deformation bands. Journal of Structural Geology 24, 1389–1411. https://doi.org/10.1016/S0191-8141(01)00146-8

Schultz, R.A., Okubo, C.H., Wilkins, S.J., 2006. Displacement–length scaling relations for faults on the terrestrial planets. Journal of Structural Geology 28, 2182–2193. https://doi.org/10.1016/j.jsg.2006.03.034

Schultz, R.A., Soliva, R., Fossen, H., Okubo, C.H., Reeves, D.M., 2008. Dependence of displacement–length scaling relations for fractures and deformation bands on the volumetric changes across them. Journal of Structural Geology 30, 1405–1411. https://doi.org/10.1016/j.jsg.2008.08.001

Segall, P., and Pollard, D., 1980. Mechanics of discontinuous faults: Journal of Geophysical Research, v. 85, p. 4337–4350, doi:10.1029/JB085iB08p04337

Singer, K. N., White, O. L., Schenk, P. M. et al. 2016. Pluto's putative cryovolcanic constructs. 47th LPSC abstract 2276.pdf.

Soliva, R., Benedicto, A., 2005. Geometry, scaling relations and spacing of vertically restricted normal faults. Journal of Structural Geology 27, 317–325. https://doi.org/10.1016/j.jsg.2004.08.010

Soliva, R., Schultz, R.A., 2008. Distributed and localized faulting in extensional settings: insight from the North Ethiopian rift – Afar transition area. Tectonics 27, TC2003. doi:10.1029/2007TC002148.

Wilkins, S.J., Gross, M.R., 2002. Normal fault growth in layered rocks at Split Mountain, Utah. Journal of Structural Geology 24, 1413–1429. https://doi.org/10.1016/S0191-8141(01)00154-7

Willemse, E.J.M., Pollard, D.D., Aydin, A., 1996. Three-dimensional analyses of slip distributions on normal fault arrays with consequences for fault scaling. Journal of Structural Geology 18, 295–309. https://doi.org/10.1016/S0191-8141(96)80051-4

Willemse, E.J.M., 1997. Segmented normal faults: correspondence between three dimensional mechanical models and field data. Journal of Geophysical Research 102, 675–692. https://doi.org/10.1029/96JB01651

Willoughby, E., Hyndman, R., 2005. Earthquake rate, slip rate, and the effective seismic thickness for oceanic transform faults of the Juan de Fuca plate system. Geophysical Journal International, 160 (3), 855-868. 10.1111/j.1365-246X.2005.02523.x

Wyss, M., Sammis, C., Nadeau, R., and Wiemer, S., 2004. Fractal dimension and b-value on creeping and locked patches of the San Andreas fault near Parkfield, California: Bulletin of the Seismological Society of America, v. 94, p. 410–421, doi:10.1785/0120030054.

Chapter 10

Conclusions

10.1 Summary of Results

Since the first images and surficial spectral data retrieved from the New Horizons mission in 2015, researchers have attempted to explain its icy composition variability in several ways, namely (i) spectroscopic phases and how those ices change on a localized versus global scale; (ii) temporal evolution of these ices in different seasonal/climatological conditions; and (iii) surface evolution of these ices in differing geophysical conditions. In this project we investigate each of these themes through experimentation of CH_4, N_2, and CO ices in binary or ternary mixtures at a simulated range of 10 – 50 K to encompass Pluto's seasonal extremes, and then investigate certain icy geophysical surface processes, such as glacial folding and fault extensions, while understanding the phases that may play a role in those processes.

In Chapter 3 we investigated the spectral interactions of the binary mixture CH_4-N_2. We were able to recreate previous experimental work at comparably higher spectral resolution. We also observed the transitions of CH_4-α to CH_4-β at ~21 K with a previously unidentified residual band change at ~24 K. The identification of the 1.485 μm CH_4 band (with a possible 1.458 μm mode transition at > 40 K) and the appearance of the 2.185 and 2.194 μm CH_4 bands when in mixture with N_2 implies a spectral relationship with the concentration of N_2 present in the ice sample.

In Chapter 4, in the N_2-CO binary mixtures, we report that lack of certain CO spectral bands confirmed the hcp + cubic phase transition at ~40K. We identify a previously unknown phase change with the 2.318 and 2.38 μm CO bands within the specific conditions of ≤ 20 K and ≤ 30 mol% CO, including a physical fractured pattern of the ice sample, which lack the 2.239 and

2.337 μm bands indicative of the cubic phase. We propose this section of the phase diagram to be a polycrystalline structure between N_2 and CO.

For Chapter 5 in the CO-CH_4 mixtures, we created a CO-CH_4 binary phase diagram, which does not currently exist, for the near-IR wavelengths and low temperatures < 50 K relevant to Pluto and the outer Solar System. We have found that there are five distinct phase regimes, each displaying certain spectral bands, especially the 1.243 μm CH_4 band, which is only present in the β-CH_4 crystalline phase at molar concentrations of < 60 mol% CO. Furthermore, we found that molar ratios ≥ 70 mol% display the 2.32 μm CH_4 and 2.38 μm CO bands at all recorded temperature conditions, which we have labeled as Phase III.

In Chapter 6, we combined CH_4, N_2, and CO at varying molar concentrations to get a preliminary view of the ternary phase diagram and investigate the interactions of these ices from 15 – 50 K. We explored the phases within CH_4-, N_2-, and CO-dominant ices (where dominance is ≥ 50 mol%). Our created ternary phase diagram shows separate CH_4 and CO dominant phase regimes, along with three different CH_4-N_2-CO- mixture phases depending on the spectral bands present and molar concentrations of the dominant ice. Comparing our study to obtained ground-based spectra, the CH_4-dominant mixtures matched certain spectral bands found in Pluto spectra, whereas N_2-dominant mixtures were more relevant to Triton spectra. This newly defined ternary phase diagram can be helpful toward understanding dominant ice mixtures from ground-based and mission fly-by spectra.

Focusing on the Baret Montes glacier on Sputnik Planitia, Pluto in Chapter 7, we found a comparable ridge analysis done on Europa to extrapolate this technique to the glacial ridges observed on Baret Montes. While the origin of this glacier still remains unknown, the folding patterns observed were analyzed for relative duration of the folds, which is estimated to be a

maximum 5.53 My. Based on geomorphologic and spectral observations, we infer the folded terrain observed on Baret Montes to be the remnants of a previous compressional stress process evidenced by the localization of those folds and implications of a thin upper-folding crust of methane-water ice composition.

In Chapter 8, our measurements of the Hekla Cavus reveal differences in the maximum shear stress distribution that imply spatial variations in not only the entirety of the depression cavity, but in relation to a surrounding Uplifted Bulge system in the southeastern portion of Cthulhu Macula. Using an assortment of techniques, including morphometry and depression wall displacements, we suggest that Hekla Cavus is a subglacial cryo-volcanic collapse as part of the Uplifted Bulge complex of tectonic variety.

Finally, in Chapter 9, we survey four major fault systems within the Cthulhu Macula region on Pluto to reveal differences in displacement, maximum shear stress distribution, and a roughness scale that implies spatial and possibly temporal variations. We found that the Beatrice and Virgil Fossae are relatively younger than Hermod and Kaknú, with Beatrice Fossa having the largest shear stress and highest roughness. The displacement-length ratios of the faults show that Beatrice and Virgil follow a more power-law scaling for localized scale-invariant faulting regimes compared to Hermod and Kaknú having an exponential D_{max}-L ratio trend, implying these as vertically restricted faults.

10.2 Future Work

Several binary mixtures showed interesting, previously unidentified phases, especially the polycrystalline phase in the CO-N_2 binary, and the creation of a new CO-CH_4 phase diagram.

However, there are still several remaining questions and future works that are relevant to the expansion of these experimental studies, such as:

(i) The experiments in these works involved intimate mixtures of the gases, but the spectral properties should be investigated when the ices are condensed at different times (i.e., layered ices, not intimately mixed prior to freezing). This would be relevant to Pluto and other KBOs/TNOs in that volatile transport of ices (such as CH_4 and CO) could seasonally condense as a top layer.

(ii) These experiments utilized near-IR techniques, though should be replicated and analyzed in the mid-IR (where more CH_4 and CO spectral bands reside) and Raman spectroscopy for more in-depth studies of the crystalline structures, especially the polycrystalline phase in the N2-CO binary system.

(iii) These binary systems could expand our knowledge of Plutonian ices further by adding a water ice component, namely, to observe if water ice would enhance (or saturate) CH_4, N_2, or CO spectral signatures.

(iv) Adding a water ice component could also help create a quaternary phase diagram when combined with CH_4-N_2-CO mixtures. This could also be expanded to test the amorphous water ice phases (e.g., ~77 K is the transition between high-density and low-density amorphous phases).

There are also remaining future investigations regarding the geologies presented here, such as:

(i) Investigate other faulted areas across Pluto, especially Cthulhu Macula faults being water ice dominant with methane. How do these faults compare with the Sleipnir Fossae area (CH_4-N_2 ices) or Djanggawul Fossae (N_2-CO ices)?

(ii) Cryovolcanism as a subsurface geological process can be expanded to investigate key factors, such as differences in lithosphere thickness could influence the surface geology and evolution of the putative Wright and Piccard Mons volcanoes.

(iii) For the Baret Montes folds, this leads to promising future work on ice rheology and ice mechanics of different viscosities at extremely low temperature conditions.

(iv) Glaciers across Pluto, namely the western lobe of Sputnik Planitia, display a variety of morphologies, which begs the questions as to why there is a variability of morphologies on these glaciers and the differences in formation mechanisms across Sputnik Planitia.

Overall, the experimental work on ices and theoretical research on the cryogeology of Pluto both have a wealth of future investigations. I hope that the work presented here can be a steppingstone for these future endeavors, as well as insight to the complexities of these experimental undertakings to understand the spectral behaviors of ice mixtures at simulated Plutonian conditions.